

EXPERIMENTAL AEROACOUSTICS STUDY ON JET
NOISE REDUCTION USING TANGENTIAL
AIR INJECTION

Arsalan Ahmad

Supervisors

Dr. Eldad Avital, Prof. Chris Lawn & Dr. John Cater

A thesis submitted for the degree of
DOCTOR OF PHILOSOPHY

to the

University of London

School of Engineering and Materials Science
Queen Mary, University of London,

September 2011

ABSTRACT

Aircraft jet exhausts are a source of undesirable noise and continue to be an area of investigation driven by increasingly stringent regulation. The noise is produced by the unsteady mixing of the jet with the surrounding air and is dominated by the effects of the shear layer. In this study, the mechanisms of noise suppression are investigated on an unheated Mach 1.3 jet through three distinct control techniques. The first consists of tangential steady flow injectors located upstream of the nozzle exit whereas the second involves an equal number of control jets spaced further downstream around the nozzle exit. The third technique pulses air tangential into the shear layer at a frequency coinciding with the preferred modes of the jet ($St \sim 0.17$, $f \sim 2\text{kHz}$).

Near and far-field acoustic measurements were made in anechoic chamber with an array of 10 free-field microphones. All three forms of tangential air injection induced reductions in overall sound pressure levels (OASPL) across a range of observer angles. External tangential injection was found to be the most efficient technique, as it produced comparably similar noise reductions at only a fraction of the injection mass flow ratio. The most significant acoustic benefit was an 8dB SPL reduction at the sideline observer angle, subsequently eliminating both screech and broadband shock noise at Strouhal numbers of $St \sim 0.74$ ($f \sim 9.6\text{kHz}$) and $St \sim 1$ ($f \sim 13\text{kHz}$) respectively. An OASPL reduction of up to 5dB was also recorded at a downstream angle of 15° . However, the low-frequency noise benefits from these control jets came at the expense of increased high frequency noise beyond $St > 2$ ($f \sim 26\text{kHz}$).

The flow-fields of the jet were observed using stereoscopic Particle Image Velocimetry (PIV). The introduction of a swirling component of velocity downstream of the nozzle exit was found to have a stabilizing effect on the jet shear layer. Reductions in turbulence intensity and Reynolds stress were recorded towards the end of the potential core by up to 18% and 25% respectively. The ultimate objective of this study was to develop an injection configuration that is effective at reducing jet noise whilst minimising penalties in weight and thrust.

ACKNOWLEDGEMENTS

“All praise is for Allah, the Lord of all that exists, the most gracious, the most merciful and the owner of the day of recompense”. Quran [1: 2-4]

I would like to especially thank Dr John Cater for his guidance and support through the first year of my research degree, his enthusiasm enabled me to contribute towards and present an AIAA conference paper in Vancouver, Canada. The finances that he arranged enabled me to travel to numerous other conferences over the past three years.

Dr Darren Luff's initial guidance in the experimental set-up and operation of the PIV system was invaluable. His hard and dedicated work in building the anechoic chamber and test facility enabled me to begin my experimental phase from day one.

I am grateful to my current supervisors Dr Eldad Avital and Professor Chris Lawn for their continual support and guidance in ensuring my progress for the major part of this research training.

The joint scholarship awarded by Queen Mary, University of London and the Engineering & Physical Sciences Research Council, funded this work and is gratefully acknowledged.

This thesis would not have been possible without my father Aziz Ahmad's endless love and encouragement. I hope I will be able to fulfil his dream by successfully completing this degree.

Last, and by no means least, I would like to deeply thank my beloved wife for her continual patience and support.

LIST OF CONTENTS

ABSTRACT.....	2
ACKNOWLEDGEMENTS	3
LIST OF CONTENTS	4
LIST OF TABLES	8
LIST OF FIGURES	9
LIST OF SYMBOLS	17
1 INTRODUCTION	19
1.1 Motivation	19
1.2 Aims & Objectives	22
1.3 Achievements & Contribution.....	23
1.4 Thesis Structure	24
2 LITERATURE REVIEW	25
2.1 Acoustic Analogy Theory.....	25
2.2 Experimental Aeroacoustics	28
2.3 Jet Flow Structure.....	29
2.4 Sources of Jet Noise	31
2.4.1 Turbulent Mixing Noise	31
2.4.2 Mach Wave Radiation	34
2.4.3 Screech Noise	35
2.4.4 Broadband Shock Noise	36
2.5 Passive Methods for Jet Noise Reduction	38
2.5.1 Swirling Jets.....	38
2.5.2 Mechanical Chevrons	41
2.6 Active Methods for Jet Noise Reduction.....	42

2.6.1	Fluidic Injection.....	42
2.7	Human Perception and Response to Noise.....	46
2.8	Summary.....	48
3	INSTRUMENTATION AND FLOW CONFIGURATIONS	50
3.1	Acoustic Chamber	50
3.2	Experimental Jet Apparatus.....	51
3.3	Mach 1.3 Nozzle.....	54
3.3.1	Theoretical Jet Flow Parameters.....	54
3.3.2	Converging-Diverging Section Design.....	56
3.3.3	Primary Jet Flow Parameters	57
3.4	Tangential Injection Configurations.....	58
3.4.1	Internal Tangential Injection (ITI).....	58
3.4.2	External Tangential Injection (ETI).....	61
3.4.3	Pulsating Tangential Injection (PTI)	63
3.5	Acoustic Instrumentation and Data Acquisition.....	65
3.6	Near and Far-Field Microphone Arrays	67
3.7	Signal Processing & Spectral Analysis	69
3.7.1	Fast Fourier Transform (FFT)	69
3.7.2	Sound Pressure Level (SPL).....	69
3.7.3	Strouhal Number.....	70
3.7.4	Amplitude Calibration	71
3.7.5	Distance Calibration	71
3.7.6	Autocorrelation	74
3.7.7	Cross-Correlation & Time Lag.....	74
3.8	Particle Image Velocimetry (PIV).....	77
3.8.1	Digital Imaging.....	77

3.8.2	Laser Light Source.....	78
3.8.3	Seeding Particles.....	79
3.8.4	Velocity Vector Processing	83
3.8.5	Post-Processing Parameters	85
3.8.6	Stereoscopic PIV	86
3.9	Jet Thrust	89
4	ACOUSTIC FIELD RESULTS	90
4.1	Far-Field Sound Pressure Level	90
4.1.1	Primary Jet	90
4.1.2	Internal Tangential Injection (ITI).....	97
4.1.3	External Tangential Injection (ETI).....	101
4.1.4	Pulsating Tangential Injection (PTI)	105
4.1.5	Comparison of Optimal Configurations	109
4.2	Autocorrelation.....	113
4.3	Cross-Correlation	116
4.4	Cross-Spectral Time Lag	121
4.5	Noise Source Location.....	123
4.6	Near Field Sound Pressure Level	129
4.7	Summary of Acoustic Results	133
5	FLOW FIELD RESULTS.....	134
5.1	Axial Velocity	134
5.2	Tangential Velocity	144
5.3	Turbulence Intensity	148
5.4	Reynolds Stress	151
5.5	Vorticity.....	154
5.6	Summary of Flow-Field Results.....	158

6	DISCUSSION	159
6.1	Shock Associated Noise Reductions	159
6.2	Turbulent Mixing Noise Sources and Structures.....	161
6.3	Mechanisms for Low Frequency Noise Reductions.....	162
6.4	Mechanisms for Increased High Frequency Noise.....	165
6.5	Error and Uncertainty	167
6.6	Optimal Noise Reduction Technique	168
6.7	Back to the Beginning	171
7	CONCLUSIONS & FUTURE WORK.....	174
7.1	Conclusions	174
7.2	Future Work.....	177
	REFERENCES.....	179
	APPENDIX A	190

LIST OF TABLES

Table 2.1: Summary of Noise Reductions from Passive & Active Methods.....	49
Table 3.1: Ambient Air Properties and Plenum Parameters	57
Table 3.2: Main Jet Exit Flow Parameters.....	57
Table 3.3: Theoretical Internal Injection Flow Parameters.....	60
Table 3.4: Theoretical External Injection Flow Parameters.....	61
Table 3.5: Measured External Injection Flow Parameters	61
Table 3.6: Measured Pneumatic Drill Rotary Speeds with Respect to Supply Pressure...	64
Table 3.7: Measured Pulsating Injection Flow Parameters.....	64
Table 3.8: Distance Calibration Factors with Respect to Noise Source Origin at the Nozzle	72
Table 3.9: Distance Calibration Factors with Respect to Noise Source Origin at $x/D=5$.	73
Table 4.1: Comparison of Noise Reductions from all Air Injection Techniques.....	110
Table 4.2: Noise Source Structure Sizes Approximated from Peak Correlation Time Lags	113
Table 4.3: 2kHz Noise Source Location (x/D_J) based on Peak Cross-Correlation Time Lag	123
Table 4.4: 6.3kHz Noise Source Location (x/D_J) based on Peak Cross-Correlation Time Lag	124
Table 4.5: 9.6kHz Noise Source Location (x/D_J) based on Peak Cross-Correlation Time Lag	124
Table 4.6: 13kHz Noise Source Location (x/D_J) based on Peak Cross-Correlation Time Lag	124
Table 4.7: Noise Source Location (x/D_J) based on Contours of Near-Field SPL	130
Table 5.1: Variation in Jet Thrust with Type of Injection based on 165N for the Primary Jet.....	135
Table 5.2: Effect of Air Injection Technique on Lengths of Potential and Supersonic Cores	140
Table 5.3: Swirl Numbers Generated by each Tangential Air Injection Technique	144

LIST OF FIGURES

Figure 2.1: Diagram illustrating the dynamic and acoustic regions that constitute a supersonic round jet. The turbulent mixing noise description is based on Tam's (2008) two-source model, whereas the shock associated noise description is based on the work of Powel (1953).....	30
Figure 2.2: Similarity acoustic spectra for the two components of turbulent mixing noise: <i>F-spectra</i> characteristic of large-scale turbulence structure noise (—) and <i>G-spectra</i> characteristic of fine-scale turbulence structure noise (– –) as proposed by Tam et al. (1996).....	32
Figure 2.3: Acoustic spectra acquired at an upstream angle of 150° with respect to streamwise axis of a Mach 2 jet, showing the three main sources of supersonic jet noise (reproduced from Tam, 1995).....	37
Figure 2.4: Illustration of a serrated chevron nozzles being used by NASA (2006), The Boeing Company (2007) and Alkisar et al., (2008).....	41
Figure 2.5: Illustrations of various azimuthal spaced, axially impinging microjet configurations. (a) 8 water injectors by Krothapalli et al., (2003), (b) 8 air injectors by Alkisar et al., (2007), (c) 18 air injectors by Alkisar et al., (2008) and (d) 18 air injectors by Castelain et al., (2008).	42
Figure 3.1: A schematic plan view of the acoustic chamber and experimental jet apparatus, which was commissioned in 2007 at the Department of Engineering of Queen Mary, University of London.	50
Figure 3.2: Three-dimensional cut-out view of the acoustic chamber with wall and floor surfaces covered with anechoic foam wedges. During acoustic measurements, the nozzle and microphone support beam were covered with 70mm thick foam sheets.	51
Figure 3.3: Cross-section of the plenum chamber showing the flow straightening devices as well as the converging-diverging nozzle. All dimensions are in mm (Luff et al, 2008).....	52
Figure 3.4: CAD assembly drawing of the experimental jet apparatus, with a Mach 1.3 converging-diverging nozzle. The pressure transducer used to regulate the plenum pressure is located downstream of the honeycomb and wire meshes.	53

Figure 3.5: Schematic of the cross-section for the internal tangential air injection configurations.	58
Figure 3.6: CAD assembly drawing of the upstream internal tangential air injection configuration.	59
Figure 3.7: Eight-way manifold used to distribute the secondary air supply to the injectors.	59
Figure 3.8: Schematic of the cross-section of the External Tangential Injection configuration.	62
Figure 3.9: Illustration of the External Tangential Injection configuration. The supply reservoir and control system is identical to the internal tangential injection system.	62
Figure 3.10: CAD assembly drawing of the siren design used to produce 2kHz pulsating flows.	63
Figure 3.11: Components of a condenser microphone, the like of which was used in the present study. The diagram was adapted from PCB Piezotronics, Microphone handbook (2009).	65
Figure 3.12: CAD assembly drawing of the near-field microphone array covering x-axis locations between $-2 < x/D <$ and y-axis between $6 < y/D < 12$ from the nozzle exit.	67
Figure 3.13: The far-field acoustic array, parallel to the streamwise jet axis. The microphone observer angles ranged from 90° - 15° , whilst all pointing towards the expected primary noise source, the nozzle.	68
Figure 3.14: Diagram showing how the physical position of the microphones can be simulated as effectively being placed on a radial arc using the distance calibration factor. (Drawing not to scale)	72
Figure 3.15: Effective positions of the microphone (red circles) using the distance calibration with the new noise source origin 5 nozzle diameters along the potential core. (Drawing not to scale).	73
Figure 3.16: CAD assembly drawing of the 2D PIV experimental configuration, for 2-component velocity measurements of the axisymmetric plane of the jet.	78

Figure 3.17: Instantaneous PIV images from 2D measurements. The square images on the left correspond to a physical size of 205mm, covering the first 6.5 nozzle diameters of the axial jet from the nozzle exit, followed by the next 205mm ($6.5D_J - 13 D_J$) of the jet on the right. Primary jet (top), internal injection at 40% IMFR (centre) and external injection at 1% IMFR (bottom)..... 82

Figure 3.18: CAD assembly drawing of the experimental configuration for stereoscopic 3D PIV, for three-component velocity measurements of the end-on plane, perpendicular to the jet axis. 87

Figure 3.19: Instantaneous PIV images from both cameras during stereoscopic 3D measurements. The field of view corresponds to a physical size of 50mm×50mm. Primary Jet (top), internal injection at 40% IMFR (centre) and external injection at 1% IMFR (bottom). 88

Figure 4.1: Comparison of SPL spectra, scaled to 40 nozzle diameters, at various observer angles from the unmodified Mach 1.3 primary jet. 92

Figure 4.2: Comparison of SPL spectra, scaled to 40 nozzle diameters from jet exit, with variation in observer angles from the streamwise primary jet axis. 93

Figure 4.3: Comparison of SPL spectra between the primary jet (—), Tam’s (1996) similarity *G-spectra* for fine-scale turbulence noise (••) & *F-spectra* for large-scale turbulence noise (- -). 94

Figure 4.4: OASPL at various observer angles for the primary, Mach 1.3, jet with measurements scaled to a distance of 40 nozzle diameters from $x/D=0$. Error bars indicate standard deviation of 0.2dB, which is less than 1% of the peak $OASPL_{RMS}$ value. 96

Figure 4.5: Comparison of OASPL at various observer angles for the primary jet using distance calibration factors based on a noise source origin at $x/D=0$ (—■—) and $x/D=5$ (—◆—) from the nozzle exit. 96

Figure 4.6: Comparison of SPL spectra at various observer angles for internal tangential injection at mass flow ratios of 10% (- -), 40% (···) & 50% (-.-) against the primary jet (—). 98

Figure 4.7: Comparison of SPL spectra at various observer angles for the best performing configuration of internal tangential injection; at a mass flow ratio of 40%... 99

Figure 4.8: Comparison of OASPL at various observer angles for internal tangential injection at mass flow ratios of 10 % (—◆—), 40 % (-▲-) & 50% (··●··) against the primary jet (—■—). 100

Figure 4.9: Comparison of jet noise reduction using internal tangential injection technique at injection mass flow ratios of 10% (—◆—), 40% (-▲-) and 50% (··●··) with respect to OASPL of the primary jet..... 100

Figure 4.10: Comparison of SPL spectra at various observer angles for external tangential injection at mass flow ratios of 0.7% (--), 1% (··) & 1.3% (-.-) against the primary jet (—). 102

Figure 4.11: Comparison of SPL spectra at various observer angles for the best performing configuration of external tangential injection; at a mass flow ratio of 1% . . 103

Figure 4.12: Comparison of OASPL at various observer angles for external tangential injection at mass flow ratios of 0.7% (—◆—), 1% (-▲-), & 1.3% (··●··) against the primary jet (—■—). 104

Figure 4.13: Comparison of jet noise reduction using the external tangential injection technique with injection mass flow ratios of 0.7% (—◆—), 1% (-▲-) and 1.3% (··●··) with respect to OASPL of the primary jet..... 104

Figure 4.14: Comparison of SPL spectra at various observer angles for 2kHz pulsating injection at mass flow ratios of 0.5% (--), 0.7% (··) & 0.9% (-.-) against the primary jet (—). 106

Figure 4.15: Comparison of SPL spectra at various observer angles for the best performing configuration of 2kHz pulsating injection; at a mass flow ratio of 0.7%..... 107

Figure 4.16: Comparison of OASPL at various observer angles for 2kHz pulsating tangential injection at mass flow ratios of 0.5% (—◆—), 0.7% (-▲-), & 0.9% (··●··) against the primary jet (—■—). 107

Figure 4.17: Comparison of OASPL at various observer angles for pulsating tangential injection at mass flow ratios of 0.7% and pulsating frequencies of 1kHz (—◆—) and 2kHz (-▲-) against the primary jet (—■—). 108

Figure 4.18: Comparison of jet noise reduction using the pulsating tangential injection technique at pulsating frequencies of 1kHz at 0.7% IMFR (—◆—) and 2kHz at 0.7% IMFR (-▲-) with respect to OASPL of the primary jet. 108

Figure 4.19: Comparison of SPL spectra for the optimal noise reducing configuration of each technique; internal injection at 40% mass flow ratio (--), external injection at 1% mass flow ratio (···) & 2kHz pulsating at 0.7% mass flow ratio (-.-) against the primary jet (—). 111

Figure 4.20: Comparison of OASPL at various observer angles for the optimal noise reduction configurations of each technique. Primary jet (—■—), external injection at 1.1% mass flow ratio (-▲-), internal injection at 40% mass flow ratio (-◆-) & 2kHz pulsating injection at 0.7% mass flow ratio (··●··). 112

Figure 4.21: Comparison of jet noise reduction for the optimal noise reduction configurations of each technique; external injection at 1.1% mass flow ratio (-▲-), internal injection at 40% mass flow ratio (-◆-) & 2kHz pulsating injection at 0.7% mass flow ratio (··●··) with reference to the primary jet. 112

Figure 4.22: Comparison of the normalised autocorrelation of pressure signals at various observer angles for the primary jet (—), internal injection at 40% mass flow ratio (--), external injection at 1% mass flow ratio (···) & 2kHz pulsating injection at 0.7% mass flow ratios (-.-). 115

Figure 4.23: Comparison of normalised cross-correlation of pressure signal with fixed microphone at 30°; primary jet (—), internal at 40% IMFR (--), external at 1% IMFR (···) & 2kHz pulsating at 0.7% IMFR (-.-). 117

Figure 4.24: Comparison of cross-correlation of pressure signals from adjacent microphones with respect to the one at 80°; primary jet (—), internal injection at 40% IMFR (--), external injection 1% IMFR (···) & 2kHz pulsating injection at 0.7% IMFR (-.-). 118

Figure 4.25: Comparison of cross-correlation of pressure signals from adjacent microphones with respect to the one at 50°; primary jet (—), internal injection at 40% IMFR (--), external injection at 1% IMFR (···) & 2kHz pulsating injection at 0.7% IMFR (-.-). 119

Figure 4.26: Comparison of cross-correlation of pressure signals from adjacent microphones with respect to the one at 30°; primary jet (—), internal injection at 40%

IMFR (--), external injection at 1% IMFR (···) & 2kHz pulsating injection at 0.7% IMFR (-.-). 120

Figure 4.27: Comparison of normalised acoustic power spectra at various angles and frequencies; auto-spectra of signal 1 (—), auto-spectra of signal 2 (—), cross-spectra of adjacent signals 1 & 2 (—) and the time lag corresponding to the peak correlation value of the cross-spectra (—). 122

Figure 4.28: Noise source location for 2kHz ($St \sim 0.17$) noise based on error convergence between the theoretical and experimental cross-correlation time lags between microphones at 90° , 80° (—), 80° , 70° , (—) 70° , 60° (—), 60° , 50° (—), 50° , 40° (—), 40° , 30° (--), 30° , 25° (--), 25° , 20° (--), 20° , 15° (--). 125

Figure 4.29: Noise source location for 6.3kHz ($St \sim 0.49$) noise based on error convergence between the theoretical and experimental cross-correlation time lags between microphones at 90° , 80° (—), 80° , 70° , (—) 70° , 60° (—), 60° , 50° (—), 50° , 40° (—), 40° , 30° (--), 30° , 25° (--), 25° , 20° (--), 20° , 15° (--). 126

Figure 4.30: Noise source location for 9.6kHz ($St \sim 0.75$) noise based on error convergence between the theoretical and experimental cross-correlation time lags between microphones at 90° , 80° (—), 80° , 70° , (—) 70° , 60° (—), 60° , 50° (—), 50° , 40° (—), 40° , 30° (--), 30° , 25° (--), 25° , 20° (--), 20° , 15° (--). 127

Figure 4.31: Noise source location for 13kHz ($St \sim 1$) noise based on error convergence between the theoretical and experimental cross-correlation time lags between microphones at 90° , 80° (—), 80° , 70° , (—) 70° , 60° (—), 60° , 50° (—), 50° , 40° (—), 40° , 30° (--), 30° , 25° (--), 25° , 20° (--), 20° , 15° (--). 128

Figure 4.32: Contours of near field OASPL (dB) for the primary jet (top) and external injection at 1% IMFR (bottom). 130

Figure 4.33: Contour plots of near-field SPL (dB) at 2kHz ($St = 0.17$), corresponding to the Kelvin Helmholtz roll-up frequency of the primary jet (top) & external injection at 1% IMFR (bottom). 131

Figure 4.34: Contour plots of near-field SPL (dB) at 6.3 kHz ($St = 0.49$) corresponding to the fundamental mode of screech for the primary jet (top) & external injection at 1% IMFR (bottom). 131

Figure 4.35: Contour plots of near field SPL (dB) at 9.6kHz ($St=0.74$) corresponding to the harmonic mode of screech for the primary jet (top) & external injection at 1% IMFR (bottom).....	132
Figure 4.36: Contour plots of near field SPL (dB) at 13kHz ($St=1$) corresponding to the broadband shock peak for the primary jet (top) and external injection at 1% IMFR (bottom).	132
Figure 5.1: Comparison of axial velocity profiles at $x/D=0.6$ for internal tangential injection at mass flow ratios of 0% (■), 10% (◆), 40% (▲) & 50% (●).	136
Figure 5.2: Comparison of axial velocity profiles at $x/D=0.6$ for external tangential injection at mass flow ratios of 0% (■), 0.7% (◆), 1% (▲) & 1.3% (●).	136
Figure 5.3: Comparison of velocity profiles at $x/D=0.6$ between the best performing configurations; internal tangential injection at 40% mass flow ratio (◆) , external injection tangential at 1.0% mass flow ratio (▲) against the primary jet (■)....	137
Figure 5.4: Variation on axial velocity profile with streamwise distance from the nozzle exit for primary jet (top), ITI at 40% mass flow ratio (centre) and ETI at 1% mass flow ratio (bottom)	138
Figure 5.5: Comparison of axial velocity profiles at various streamwise locations for primary jet (■), internal injection at 40% mass flow ratio (◆) and external injection at 1% mass flow ratio (▲).....	139
Figure 5.6: Comparison of axial velocity contours between the primary jet, internal tangential air injection at 40% mass flow ratio and external tangential air injection at 1% mass flow ratio.....	141
Figure 5.7: Comparison of axial velocity profiles at various streamwise locations for primary jet (■), internal injection at 40% IMFR (◆) and external injection at 1% IMFR (▲). Second order polynomials have been used to demonstrate the trend of data points.	142
Figure 5.8: Comparison of axial velocity contours from 3D stereoscopic PIV at $x/D=0.6$ for the primary jet, internal tangential injection at 40% mass flow ratio & external tangential injection at 1% mass flow ratio. The corresponding contour lines are spaced at regular intervals of 20 m/s.....	143

Figure 5.9: Comparison of tangential velocity profiles at $x/D=0.6$ for internal tangential injection at mass flow ratios of 0% (■), 10% (◆), 40% (▲) & 50% (●)..... 146

Figure 5.10: Comparison of tangential velocity profiles at $x/D=0.6$ for external tangential injection at mass flow ratios of 0% (■), 0.7% (◆), 1% (▲) & 1.3% (●)..... 146

Figure 5.11: Comparison of tangential velocity profiles at $x/D=0.6$ between the best performing configurations; internal tangential injection at 40% mass flow ratio (◆), external injection tangential at 1.0% mass flow ratio (▲) against the primary jet (■).... 147

Figure 5.12: Variation in normalised turbulence intensity with streamwise distance from the nozzle exit for the primary jet (top), internal injection at 40% IMFR (centre) and external injection at 1% IMFR (bottom)..... 149

Figure 5.13: Comparison of axial turbulence intensity profiles at various streamwise locations for primary jet (■), internal injection at 40% IMFR (◆) and external injection at 1% IMFR (▲)..... 150

Figure 5.14: Variation in normalised Reynolds Stress with streamwise distance from the nozzle exit for the primary jet (top), internal injection at 40% IMFR (centre) and external injection at 1% IMFR (bottom)..... 152

Figure 5.15: Comparison of normalised Reynolds Stress profiles at various streamwise locations for the primary jet (■), internal injection at 40% IMFR (◆) and external injection at 1% IMFR (▲)..... 153

Figure 5.16: Contours of time averaged, non-dimensionalised out-of-plane vorticity, $\omega_x D_J / U_J$, from stereoscopic PIV at $x/D=0.6$ of the primary jet (top), internal tangential injection at 40% mass flow ratio (centre) & external tangential injection at 1% mass flow ratio. Lines are spaced at intervals of 0.5 for positive (—) & negative (···) values. 155

Figure 5.17: Three-dimensional view of non-dimensionalised out-of-plane vorticity, $\omega_x D_J / U_J$, for primary jet (top), internal injection at 40% IMFR (centre) & external injection at 1% IMFR..... 156

Figure 5.18: Contours of time averaged, non-dimensionalised out-of-plane tangential vorticity, $\omega_\theta D_J / U_J$, from 2D mono PIV of the primary jet (top), internal injection at 40% IMFR (centre) & external injection at 1% IMFR (bottom). 157

LIST OF SYMBOLS

a	=	Speed of Sound under Ambient Conditions	(m/s)
α	=	Observer Angle from Downstream Jet Axis	(°)
A_P	=	Acoustic Power	(Pa ²)
C_m	=	Microphone Calibration Constant	(Pa/V)
C_D	=	Distance Calibrations Factor	
D_J	=	Main Jet Diameter at Nozzle Exit	(m)
δ_{BL}	=	Boundary Layer Thickness	(m)
$\delta_{i,j}$	=	Kronecker Delta Function	
f	=	Frequency	(Hz)
f_F	=	Fundamental Screech Frequency	(Hz)
f_H	=	Harmonic Screech Frequency	(Hz)
G_θ	=	Rotational Momentum	(N)
I	=	Acoustic Intensity	(W/m ²)
K	=	Kleinstein Proportionality Constant	
L_C	=	Spatial Correlation Length Scale	(m)
l	=	turbulent length scale	(m)
M	=	Mach Number of the Flow	
M_S	=	Swirl Mach Number	
\dot{m}	=	Mass Flow Rate	(kg/s)
Pa	=	Ambient Pressure	(Pa)
P	=	Static Pressure	(Pa)
P_O	=	Stagnation Pressure	(Pa)
P_{ref}	=	Reference Pressure for Air	(Pa)
ρ	=	Air density	(kg/m ³)
ϕ_{peak}	=	Peak Mach Wave Radiation	(°)
Q	=	Volumetric Discharge	(m ³ /s)
Re	=	Reynolds Number	
R_J	=	Main Jet Radius at Nozzle Exit	(m)
R_{AC}	=	Normalised Autocorrelation	
R_{CC}	=	Normalised Cross-Correlation	
R_S	=	Reynolds Stress	(m ² /s ²)
s	=	Shock Cell Spacing	(m)
S_N	=	Jet Swirl Number	
s_m	=	Microphone Sensitivity	(V/Pa)
St	=	Strouhal Number Based on Main Jet Diameter and Velocity	

t	=	Time	(s)
T_J	=	Static Jet Temperature	(K)
T_I	=	Turbulence Intensity	
T_o	=	Stagnation Temperature	(K)
T_x	=	Axial Thrust	(N)
τ_o	=	Time Lag for Peak Autocorrelation	(s)
τ_{max}	=	Time Lag for Peak Negative Autocorrelation	(s)
τ_{peak}	=	Time Lag for Peak Cross-correlation	(s)
τ_S	=	Seeding Particle Relaxation Time	(s)
τ_ζ	=	Delay time for the second-order correlation to fall to $1/e$	(s)
μ	=	Dynamic Viscosity	(kg/ms)
u_x	=	Instantaneous Axial Velocity	(m/s)
u_r	=	Instantaneous Radial Velocity	(m/s)
u_θ	=	Instantaneous Tangential Velocity	(m/s)
u'_x	=	Fluctuation in Axial Velocity	(m/s)
\overline{U}_x	=	Time Averaged Axial Velocity	(m/s)
U_J	=	Weighted Mean Jet Velocity	(m/s)
U_C	=	Convective Jet Velocity	(m/s)
ω_x	=	Axial Vorticity	(1/s)
γ	=	Specific Heat Ratio for Air	(1/s)
x, y, z	=	Cartesian Co-ordinates of Microphones from the Nozzle	(m)
x, r, θ	=	Cylindrical Co-ordinate System for Velocity Components	(m)

1 INTRODUCTION

1.1 Motivation

Aircraft noise, after roadway traffic, is the second largest source of environmental noise pollution and therefore of considerable concern to urban areas surrounding most major airports (Smith, 2004). With the advances made in aerospace technology, air transportation is being used much more frequently than in the past and this continuing growth in the popularity of air travel has led to predictions by European aircraft manufacturer, Airbus, of an increase in global air passengers by almost 4.9% a year, with the freight industry also expected to grow by 5.8% annually. High levels of growth over the past decades have led to an increase in noise intensity around airport communities and have been met by stringent aircraft regulations and noise certification requirements to suppress them (Smith, 2004). In the light of this, the field of aeroacoustics has attracted much attention, with aircraft noise reduction becoming one of the most important areas of research.

The International Civil Aviation Organisation (ICAO) imposes regulations that limit the maximum noise exposure from aircraft at three crucial positions during its flight envelope (Jenkinson et al. 1999). For certification purposes these are: below the approach, to the sideline of the runway and under the take-off path of the aircraft. The noise measurement location for the approach phase is situated at ground level 2 km from the start of the runway below the approach trajectory of the aircraft. During the aircraft acceleration phase for take-off, the measurement point is 450m to the sideline of the runway, with the departure measuring point being just below the take-off path of the aircraft at approximately 6.5 km from the start of the runway. The noise limit for each of the three measurement points varies with respect to the aircraft take-off mass, but stands at a maximum allowable limit for aircraft heavier than 270 tonnes at 108 EPNdB (Jenkinson et al. 1999), which is the effective perceived noise level in decibels having taken into account the duration to its exposure and distance from its source (RAeS, 2004). The regulations introduced by ICAO (Annex 16, 1971) and FAR (part36, 1969) during the mid twentieth century did not pose a major threat to small aircraft, since their less powerful engines contributed less towards the overall noise produced by the aircraft. However, stricter limits were later imposed due to the increasingly higher frequency of their operation. For larger, more powerful, aircraft this limit led to the use of ‘hush kits’ in order to bring the engine noise down to acceptable limits. The extra weight and cost of these devices proved detrimental to airline economics, and hence led to a demand for quieter and more efficient jet engine designs.

In order to develop a technique for reducing aircraft noise we must first address the sources from which it originates. An aircraft's overall noise signature can be categorised into three main components: aerodynamic airframe noise, engine noise and aircraft systems noise. Airframe self-generated noise is a more significant factor during the approach phase of the aircraft and is a product of airflow over deliberately varied surfaces such as high-lift devices, engine intake and landing gear. However, during most of the aircraft's flight envelope it is secondary to the principle noise source, the jet engine. Noise generation is associated with sudden changes in air pressure; such situations are commonly found in and around aircraft turbojet engines where changes in pressure and temperature are required for the generation of thrust. Significant components of engine noise are generated by the compressor and turbine (Rolls-Royce, 1986). However, for turbojet engines, these are considered less significant compared to the exhaust jet noise during most operating conditions. Jet noise is caused by turbulent mixing of high speed exhaust gases with the atmosphere and is dominated by the effects of the steep velocity gradients in the shear layer (Rolls-Royce, 1986). Noise levels from the jet engine have been estimated to be proportional to the eighth power of the jet exit velocity (Lighthill, 1954). Hence a variation in jet noise, through varying jet velocity, will have a greater influence on the overall noise generated by the engine when compared to the compressor or turbine. Based on this comparison, the simplest form of reducing jet noise is through a reduction in jet exhaust velocity and hence aircraft speed (Jenkinson, 1999). On the other hand, the thrust generated from the engines is proportional to the square of the exit velocity and so a compromise must be made. In recent years noise reduction from aircraft engines has been achieved in the form of high by-pass ratio, turbofan engines, where a larger diameter slow speed fan streams cool air around the hotter inner core of the jet. A fan has been shown to be capable of reducing jet noise to levels below those found in low by-pass or pure jets, as well as modifying the directivity of jet noise from sideline to trailing downstream angles. However this modification results in the noise from the by-pass fan becoming the dominant component. For a pure jet, the principle of reducing jet noise is quite simple: induce rapid mixing within a short region and this will reduce low frequency noise but at an expense of increased higher frequency noise (Rolls-Royce, 1986). High frequency noise dissipates rapidly and is quickly absorbed into the atmosphere, whilst the component that manages to propagate to the listener is beyond the human audible range, hence giving the perception of a quieter engine.

The introduction and continual refinement of noise regulations over the last 60 years has resulted in reductions in perceived noise levels around most major airports. However, with predictions of increased levels of air traffic, airports will have to

accommodate increasingly larger aircraft, such as the Airbus A380. This will inevitably lead to increased noise pollution in the airport community and even more stringent regulations that will no doubt significantly influence the design and operation of future aircraft engines. One such example that shows the actions undertaken to tackle these concerns is that of the Advisory Council for Aeronautics Research in Europe (ACARE), which aims to reduce perceived external aircraft noise by 50% for 2020 (European Commission for Research, 2001). During take-off and landing, this corresponds to a reduction of about 10dB at the certification measurement points (RAeS, 2005).

The aim of this study is to investigate and develop a novel air injection control technique for the purpose of reducing the noise of a supersonic Mach 1.3 circular jet whilst minimising penalties in both weight and thrust. A major tool used in this project is the anechoic test chamber facility which was commissioned at the School of Engineering and Materials Sciences at Queen Mary, University of London in 2008. It was the result of dedicated work by Dr Darren Luff and Dr John Cater specifically for the purpose of investigating jet noise (Luff et al., 2008). The test chamber has an approximate working floor space of 6m², and is equipped with an axial array of 10 free-field microphones capable of measuring both the acoustic near and far-fields of supersonic jets in an anechoic environment.

1.2 Aims & Objectives

The aim of this experimental study is to investigate the aeroacoustics of a supersonic Mach 1.3 circular jet and to gain an understanding of how it is affected by the application of a range of novel air injection techniques for the purpose of jet noise reduction. A list of objectives has been derived in order to guide this work towards achieving the overall aim and is detailed below.

- Understand the acoustic near & far-field characteristics of the Mach 1.3 supersonic jet.
- Identify trends in the directivity of the sound field in the axial plane of the jet
- Understand the flow-field characteristics of the supersonic jet.
- Identify the sources and flow structures that are responsible for producing jet noise.
- Identify approximate locations for the sources of jet noise.
- Study the effects of internal tangential air injection on the jet's acoustic & flow fields
- Study the effects of external tangential air injection on the jet's acoustic & flow fields
- Study the effects of pulsating tangential injection on the jet's acoustic & flow fields
- Study the effects of synthetic mass-less injection on the jet's acoustic & flow fields
- Ultimately, highlight a configuration that is effective at reducing jet noise whilst minimising penalties in weight and thrust.

1.3 Achievements & Contribution

This section highlights the achievements of this experimental aeroacoustic study.

- The trends in the directivity of the sound field of a Mach 1.3 cold jet have been identified for a range of observer angles with respect to the axial centreline of the jet, with the peak noise angle also being confirmed.
- The differences between flow structures and their propagating characteristics were identified through measuring the acoustic noise spectrum at various observer angles to the jet axis.
- The spatial correlation length scales of the noise generating structures were estimated by identifying the autocorrelation of the microphone signals at various observer angles from the jet.
- Approximate locations for the sources of jet noise were identified through the cross-correlation of the far-field acoustic data and a comparison was made to the noise source locations derived from near-field acoustic measurements.
- The flow-field of the supersonic jet was measured using Particle Image Velocimetry and profiles for velocity, turbulence intensity, Reynolds stresses and vorticity were generated in 2D for the axial plane and 3D in order to extract information for the azimuthal plane.
- The novel external (ETI) and pulsating (PTI) tangential air injection techniques were designed & manufactured by the author specifically in relation to this study. The acoustic and flow-field effects of both these techniques on the primary jet were identified and the injection mass flow ratios required for optimal reductions in jet noise were also highlighted with respect to each technique.
- The optimal tangential air injection configuration was identified against a criterion that accounts for reductions in noise levels, penalties in thrust & weight as well as complexity of implementing the design.

1.4 Thesis Structure

This thesis reports on the investigation of three distinct forms of tangential injection on a circular Mach 1.3 supersonic jet. Chapter 2 begins by giving an overview of experimental aeroacoustics over recent decades and how the steep rate of technological advancement has led to the use of more sophisticated experimental techniques. It continues by giving some background about past and current understanding of the sources of jet noise, and reports on the success and shortcomings of various types of jet noise reduction techniques. The lack of knowledge in regards to active control of jet noise through tangential air injection is also highlighted in order to justify this study.

Chapter 3 provides a detailed account of the experimental apparatus and methodology used in this study. The chapter is divided so that the acoustic measurements are described prior to those of the flow-field. A theoretical background is provided to show the basis for the assumptions, models and predictions made for the purpose of comparison or validation of the results. The configuration and operation of the three distinctly different tangential injection techniques are presented and the details of the design and manufacture of various elements associated with the acoustic chamber, including the converging diverging nozzle, are also provided in this chapter.

Chapter 4 presents the findings from the acoustic measurements of the near and far-field regions of the Mach 1.3 jet. The acoustic spectra of the jet is analysed to distinguish the characteristics of the various mechanisms that exist within the jet regime. Autocorrelation and cross-correlation of the far-field data are used to estimate the size and approximate location of jet noise structures and sources respectively. The chapter continues by detailing the effects of the three types of tangential injection and aims to single out the most efficient configuration with respect to the criteria set out in the thesis aims.

Chapter 5 presents the findings from the Particle Image Velocimetry experiments and illustrates the jet's flow-field with and without the air injection through analysing the axial velocity, turbulence intensity, Reynolds stress and vorticity profiles. The effects on axial thrust levels of the jet are also estimated using the velocity profiles.

Chapter 6, perhaps the most important of the thesis, attempts to couple the results from chapters 4 and 5 in order to give an explanation of the physics behind the noise reductions from the tangential air injection techniques. It also links to chapter 2 through the comparison and validation of the experimental findings and conclusions with those established in the field.

Finally the whole thesis is summarised in chapter 7, which includes a section to suggest future work that could not be addressed during the course of this study, either due to financial or time constraints.

2 LITERATURE REVIEW

2.1 Acoustic Analogy Theory

One of the earliest pioneers in the field of aeroacoustics was Sir James Lighthill, who had a specific focus on the problem of aerodynamically generated sound. In order to develop a theory on jet noise, he based his preliminary work (Lighthill, 1952 & 1954) on identifying its noise sources, which led to the establishment of an Acoustic Analogy. It was observed that the exact equations of fluid motion can be represented in the form of an inhomogeneous wave equation, which contains all the non-linearities of the Navier-Stokes equations. This was a rearrangement of the compressible equations of motion such that it described an acoustic field in the form of freely propagating linear disturbances, with the non-linear terms being moved to the right hand side of equation (2.1).

$$\frac{\partial^2 \rho}{\partial t^2} - a_\infty^2 \frac{\partial^2 \rho}{\partial x_i^2} = \frac{\partial^2 T_{ij}}{\partial x_i \partial x_j} \quad (2.1)$$

$$T_{ij} = \underbrace{\rho v_i v_j}_{\text{ReynoldsStress}} - \underbrace{\tau_{ij}}_{\text{ViscousStress}} + \underbrace{(p - \rho a_\infty^2)}_{\text{Dissipation}} \delta_{ij} \quad (2.2)$$

where ρ is the density, a_∞ is the ambient speed of sound and T_{ij} is the Lighthill stress tensor in which v_i , p , τ_{ij} and δ_{ij} are the velocity fluctuation, pressure, viscous stress and Kronecker delta function respectively. Lighthill promoted the idea that if the left hand side of equation (2.1) describes the acoustic wave propagation then the right side should represent the sources that generate the noise field. These noise sources were described as quadrupoles; due to the fact that they had second spatial derivatives, and were thought to have a relationship to the turbulent eddies in the flow. An important assumption in the acoustic analogy is that for low speed flows the source in a free jet can be regarded as a stationary compact quadrupole source in all directions. This means the retarded time variation across the sound source can be neglected and the acoustic density fluctuation can be linearly related to the volume integration of the second time derivative of T_{ij} (Ahuja, 1972). Crighton (1975) stressed that for cold, high Reynolds number, free shear flows, the dominant term in T_{ij} is the Reynolds stress, pointing towards the fluctuations in the momentum as the sound source. The second term in T_{ij} , known as the viscous stress, was said to have an effect even smaller than that of an octupole and therefore could be neglected in the compact approximation of a free jet. The third term in Lighthill's stress

tensor, usually referred as the dissipation term, can be equated to an excessive density source if divided by a_∞^2 (Morfey, 1976). Morfey observed that for a cold jet this source could behave as a quadrupole due to a viscosity effect, which was estimated to be relatively small. Curle (1968) had earlier shown that this source was of the order of M^4 hence justifying its omission in basic sound radiation calculations for low speed flows. As a result, Lighthill's stress tensor is usually approximated by only its first term, known as the momentum effect, or fluctuating Reynolds stresses. It represents a convection momentum, ρv_i , being convected with velocity, v_j . For $M \ll 1$ the density may be replaced by the mean density with a relative error of order M^2 (Crighton, 1975), and so $\rho v_i v_j$ may be approximated as $\rho_0 v_i v_j$. This leaves the stress tensor as $T_{ij} = \rho_0 v_i v_j$, which is an appropriate approximation for most subsonic cold air jet applications. Lighthill stressed the importance of making these approximations after the exact equation has been derived and once the quadrupole nature of the source terms has been extracted.

Lighthill (1954) obtained a formal solution to his acoustic analogy equation by using the Green's function solution of the wave equation and upon applying dimensional analysis to this solution he derived an important finding. This was the establishment of the noise scaling law, which related the acoustic power, A_p , radiated by a subsonic jet to the eighth power of its exhaust velocity.

$$A_p \propto V_j^8 \quad (2.3)$$

Although Lighthill's work was impressive in its scope, it was not without limitations. It assumed that the ambient surroundings were stationary and did not account for local variations in the speed of sound in the jet flow. Additionally, due to the complex nature of the source terms, they are usually simplified with the use of various assumptions. This includes modelling the noise generation as an inviscid process, treating the jet as being isothermal, and assuming turbulence as being isotropic (Greska, 2005).

In the years after the work of Lighthill, there have been many attempts to modify or improve the Acoustic Analogy Theory approach. Many of these efforts involved modifying the wave propagation operator on the left side of equation (2.1). One good reason to modify the wave propagation operator is to account for the mean flow refraction effect. Since all the non-linearities of the flow equations are grouped in the right-hand-side of Lighthill's equation, the flow-acoustic interaction terms are effectively hidden in the source. Lighthill recognised this effect and derived an estimate for the convection effect of the source by using a Doppler factor depending on the convective Mach number of the source and the angle of sound propagation. Further discussion on flow-sound

interaction was raised by Ribner (1962) and was also experimentally observed by Atvars et al. (1965). Goldstein (1976) amongst others investigated the effects of flow-acoustic interaction by looking at the refraction of sound by the mean shear flow, highlighting the importance of that effect for jet noise. More notably, Lilley (1974) used a wave equation operator based on the Rayleigh instability equation. His acoustic equation is exact for a parallel mean shear flow but is also applicable to jet flows which exhibit only weak spreading. Lilley's equation was used successfully to explain the generation of a cone of silence at the downstream arc of the jet. This phenomenon was reported experimentally by Lush (1971) who found a zone downstream of the jet which lacked high frequency noise components. Lighthill's formulation of a compact source coupled with a Doppler convection factor could not explain the generation of that zone. However, Lilley's equation explicitly extracted the shear refraction term into the wave operator, which was used successfully to show it to be responsible for tilting high frequency components away from the flow and thus causing a cone of silence. As a sound wave propagates downstream it has to travel a greater distance inside the jet as compared to a wave propagating towards the sideline direction, causing it to be more affected by the jet's mean flow. When the wave length is at the same scale or shorter than the propagation distance inside the jet, a refraction effect occurs, thus the cone of silence is generated downstream of the jet.

Lighthill's formulation was later extended by Ffowcs Williams (1963) and Ribner (1969) to account for supersonic jet flow. In a subsonic regime, the fluctuation of the subsonically convecting eddies is responsible for generating sound, however the mere supersonic convection of the flow eddies generates intense sound waves called Mach waves. Ffowcs Williams (1963) corrected Lighthill's Doppler convection factor to account for the finite life span of these eddies and thus removing the singularity from Lighthill's original formulation in the Mach direction. Through the use of this modified formulation for supersonic jets, it was shown that the radiated acoustic power is proportional to the third power of the supersonic jet velocity, thus providing a more complete understanding of supersonic jet noise.

$$A_p \propto V_J^3 \quad (2.4)$$

Lighthill's widely used Acoustic Analogy has proved to be successful in predicting the general behaviour of the low frequency sound radiated by both subsonic and supersonic jets. A recent study on experimental jet noise data showed the acoustic power to be proportional to V_J^6 and V_J^8 for subsonic hot and cold jets respectively

(NASA, 2001), noting that for low subsonic regimes heated jets exhibit greater noise levels than colder jets; whereas for higher Mach numbers this trend is inverted. The relative simplicity of Lighthill's formulation has proven to be very attractive for the purpose of computational implementation, e.g. Avital et al. (2008). However, its simplicity was also its disadvantage, in failing to differentiate explicitly between the acoustic-mean flow interaction and nonlinear flow processes causing the sound generation. Thus, other acoustic equations such as that of Lilley's were subsequently derived in order to provide a better explanation to experimental phenomena such as the cone of silence, and to enhance our ability in predict jet noise with the use of incomplete information on the jet's turbulence. Nevertheless Lighthill's formulation remained popular and will also be used in this work to provide a qualitative explanation to the effect of the control jets.

2.2 Experimental Aeroacoustics

The science of aeroacoustics has seen a great deal of development over the past fifty years through a range of analysis strategies such as experimental diagnostics, numerical simulation and computational modelling. Numerical simulation techniques have seen recent progress in their ability to solve the flow equations in reasonable computational time. However, their application is limited due to the finite number of mesh points that can be selected around the extremely thin boundary of the initial shear layers and at capturing the small-scale structures as the jet develops. As a result, the range of Reynolds numbers that can be simulated is limited (Avital et al., 2008; Alonso & Avital, 2009), as well as the accuracy to which the turbulent motion of a heat-conducting, viscous, compressible flow can be resolved. This, coupled with the short run times, make it problematic to obtain full-scale converged solutions (Jordan & Gervais, 2008).

In the light of this, the experimental approach has the advantage of the flow equations being perfectly solved by the physical flow itself. Given that current techniques have progressively become more sophisticated due to the improvements in measurement technology, as well as increasingly innovative data extraction and analysis techniques, scientists have come closer to understanding the noise source mechanisms of turbulent jets. Experimental research in its earliest stages focused on measuring the fluctuation in a flow field with the use of hot-wires, hot-films and pitot- tubes. Seiner and Reethof (1974) used a hot-wire anemometer to investigate the velocity fluctuations of a Mach 0.32 jet in an attempt to highlight the contributions from shear noise; the interaction of the turbulent structures with the mean flow of the jet. It was found that this noise source is the dominant mechanism, with the transition region of the jet producing most of the noise.

However, experimental uncertainty was a serious concern when using such techniques due to the possibility of the in-flow probes producing greater sound than the actual source that they were designed to measure. This led to developments that aimed to minimise these additional noise sources through the use of non-intrusive measurements. Laser Doppler Velocimetry (LDV) was used by Schaffer (1979) to study the unbounded Mach 0.97 jet. The observations led to the conclusion that the majority of noise measured at the downstream angles between 20° to 30° to the jet axis is generated by the shear noise source mechanism in the transition region, 5 to 10 diameters downstream of the nozzle exit.

Microphones have provided an effective means of exploring the dynamics of experimental jet aeroacoustics. Arrays configured in both the axial and radially positioned azimuthal directions provide advantages in examining the large-scale coherent structures in the jet's near and far-field. Small-scale turbulent structures however, dissipate more rapidly and can be naturally filtered out before reaching the far-field microphones. Hence, it is complicated to correctly interpret the measured data, as it is not evident how much information is being filtered. The microphones pick up contributions from both the 'hydrodynamic' and 'acoustic' pressure fields from the turbulent flow and if these are not distinguished, the results may be misleading (Jordan & Gervais, 2008).

2.3 Jet Flow Structure

Figure 2.1 illustrates the regions that constitute a model for the structure of a free jet. The precise length of these regions is a function of the Reynolds number as well as the nozzle exit conditions (Lilley, 1958). The transition from subsonic to supersonic flow also affects the length of these regions due to formation of complex shock cells near the nozzle exit. The existence of a shock cell structure is a common feature of imperfectly expanded jet flows and will be further discussed in § 2.4.3. The region between the jet's core and ambient flow experiences the steepest velocity gradients within the jet structure and is defined as the shear layer. The shear layer is dominated by small-scale structures, which are highly dissipative in nature and responsible for producing aerodynamic sound due to their high frequency, small-amplitude oscillations. The highly unstable shear layer is also characterised by significantly higher levels of vorticity as compared to its core (Zaman & Hussain 1981).

Within the mixing region lies the potential core of the jet which is defined as a region of almost uniform mean centreline velocity from the nozzle exit (Lilley, 1958). The gradual decay of the potential core is due to the interaction between the jet and the surrounding stagnant or lower velocity atmosphere. A significant development occurred

in the understanding of turbulence through the studies carried out by Crow and Champagne (1971). Large-scale turbulent structures were found to be a more dominant factor in the overall mixing process of jets as compared to the small-scale turbulent structures. The frequencies at which these peak noise radiating structures propagate are known as the preferred modes of the jet (Tanna, 1977). When a jet is disturbed at its preferred mode it enhances the formation of these large-scale turbulent structures, particularly at the end of the potential core (Panda et al., 2002).

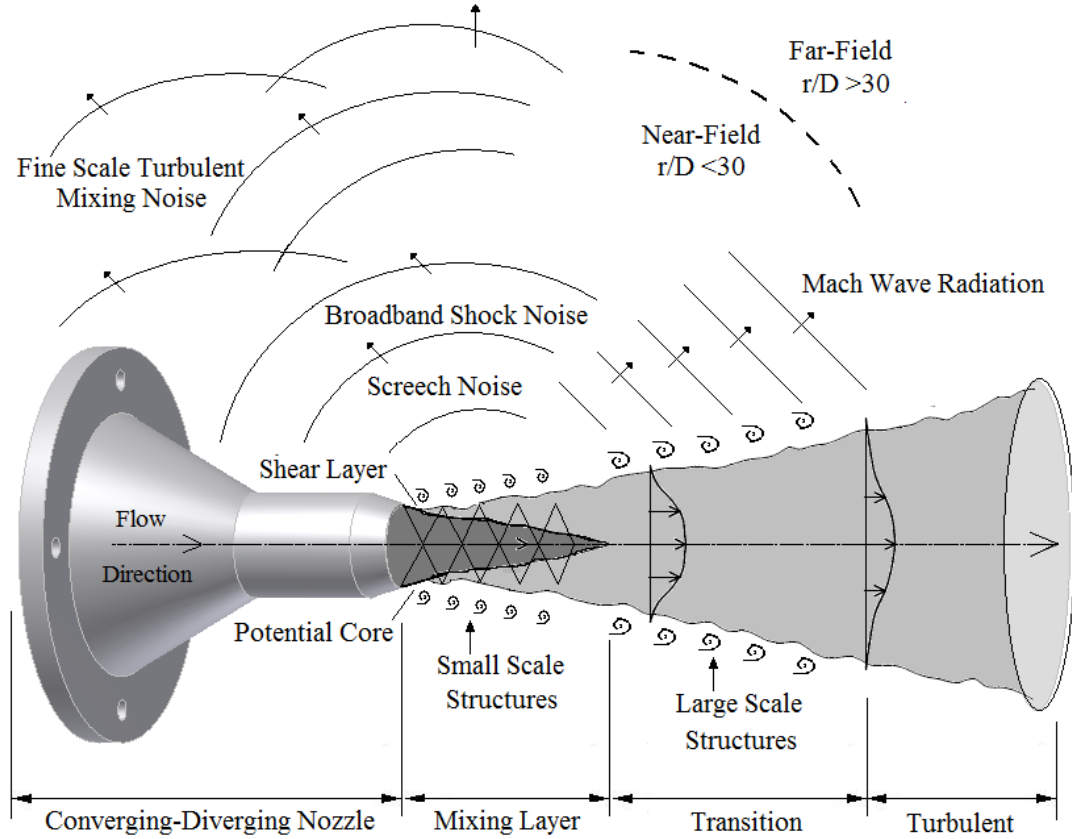


Figure 2.1: Diagram illustrating the dynamic and acoustic regions that constitute a supersonic round jet. The turbulent mixing noise description is based on Tam's (2008) two-source model, whereas the shock associated noise description is based on the work of Powel (1953).

Witze (1974) used an extensive compilation of experimental data on supersonic jets to derive a generalised equation for the centreline velocity decay of a jet. This can be re-arranged to give an expression for the length of the potential core:

$$\bar{x}_{CORE} = \frac{0.7}{k(\bar{\rho}_a)^{0.5}} \quad (2.5)$$

where the axial length, \bar{x} , is non-dimensionalised by the radius of the jet and the exit ambient density, $\bar{\rho}_a$, normalised by the density of the jet. The proportionality constant, k , is a function of the jet Mach number and for supersonic flows is denoted by;

$$k = 0.063(M_j^2 - 1)^{-0.15} \quad (2.6)$$

The acoustic near field of the jet is dominated by turbulent fluid motion which involves the conversion of the energy from rotational hydrodynamic modes to irrotational propagative modes, a process about which little is known (Jordon, 2005). Hydrodynamic modes and structures are characterised by non-linear and non-spherical propagation, in the near-field region, up to 30 nozzle diameters from the jet exit (Petitjean, 2003). These noise generating structures are believed to be non-localised, hence making it difficult to interpret the acoustic near-field. The region beyond this 30D boundary is referred to as the acoustic far-field, where the propagation of sound waves is spherical and the noise intensity is proportional to the inverse square of the radial distance from the jet (Petitjean, 2003).

2.4 Sources of Jet Noise

Many attempts have been made to derive a jet noise prediction theory since the birth of aeroacoustics in the 1950's. A literature survey will reveal many models and semi-empirical theories that aim to quantify jet noise. However its understanding is directly linked to the understanding of turbulence, which even to this day remains incomplete.

2.4.1 Turbulent Mixing Noise

The three accepted sources of noise produced from supersonic jets are turbulent mixing noise, Mach wave radiation and shock associated noise, which can either be broadband or a discrete screech tone (Crighton, 1977). Mixing noise is a product of the interaction between the flow structures in the shear layer region of the jet with the surrounding ambient air. Research on jet noise at NASA has highlighted that turbulent mixing noise of high-speed jets consists of two distinct components (Tam et al., 1996). This claim was supported by the fact that over 1900 measured frequency spectra from supersonic jets closely fitted the distinct spectral shape of the two principal noise sources as shown in Figure 2.2, regardless of the jet velocity, temperature, and direction of radiation. The first of these two distinct sources radiates principally in the downstream direction and is consistent with Mach wave radiation, due to the large-scale turbulence

structures or instability waves of the jet flow. The second component is dominant in the sideline and upstream directions suggesting it is noise from the fine-scale turbulence of the jet flow. It has more recently been shown that even the noise spectra of non-axisymmetric jets including jets from rectangular, elliptic, plug, and suppressor nozzles fits the same two experimentally determined spectra, indicating that the noise sources of these jets are similar to those of the circular jet (Tam 1998).

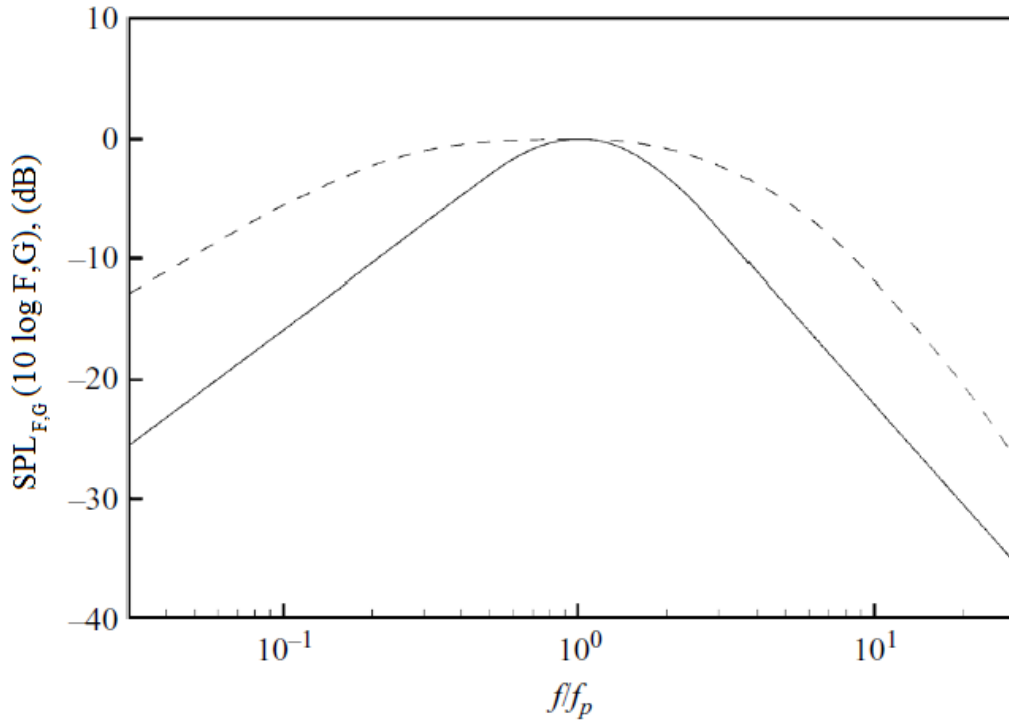


Figure 2.2: Similarity acoustic spectra for the two components of turbulent mixing noise: *F-spectra* characteristic of large-scale turbulence structure noise (—) and *G-spectra* characteristic of fine-scale turbulence structure noise (---) as proposed by Tam et al. (1996).

Experimental work on both round and bevelled nozzles by Viswanathan (2008) confirmed this pattern by demonstrating the sharp contrast in the nature of these dominant sources. The acoustic spectrum characteristic of the random incoherent sources radiating at 90° , was found to be somewhat flat, indicating low intensity noise from the rapidly dissipating fine-scale turbulence structures. Highly coherent, large-scale turbulent structures on the other hand were shown to be responsible for the peak noise events, which for a Mach 1.3 jet are known to radiate towards a downstream angle of 30° to the jet axis (Hileman et al., 2002). The intensity and directivity of the turbulent mixing noise of supersonic jets depends on the Mach number and the ratio of jet temperature to the ambient temperature (Tam, 1995).

Higher frequency turbulent mixing noise originates from the instabilities in the shear layer close to the nozzle exit, whereas noise related to lower frequencies originates from further downstream (Bishop et al., 1971). The locations of large noise events have been identified using a microphone array. It was estimated that 98% originated from between 1-12 diameters downstream from the nozzle exit. Flow visualization techniques have been used to illustrate that high amplitude noise events are characterised by large flow scales and that quiet periods coincided with smaller flow scales. Lower frequency noise events from large-scale turbulent eddies are found to correspond to Strouhal numbers of approximately 0.15-0.25 (Tanna, 1977; Tam, 1995; Panda et al., 2002), which equates to the Kelvin-Helmholtz roll-up frequency, also known as the preferred mode of a jet. Kelvin-Helmholtz instability waves, which occur between two parallel streams of varying velocity and density such as those that exist in the shear layer of a jet, can lead to Mach wave radiation when convected at supersonic speeds (Panda et al., 2002).

The noise generated from both large and fine-scale turbulent structures is highly directional in nature due to the effects of convection and refraction (Ribner, 1969; Tanna, 1975). Acoustic wave refraction occurs within the mixing region of the jet between the shear layer and the potential core of the jet. The higher flow velocity towards the core of the jet deflects the propagating sound waves, of wavelengths equal to or smaller than the jet diameter, away from the flow direction. This effect is more dominant in heated jets due to greater changes in temperature and hence density. This mean shear flow refraction reduces the amount of sound radiated in the direction of the jet flow and hence a results in relatively quieter area surrounding the jet axis which is called the 'cone of silence' (Tam 1998).

Emphasis on evaluating the contribution of large-scale structures on the sound field of supersonic jets is justified as the acoustic loads are a principal source of structural vibration (Petitjean et al., 2003) which may contribute to structural airframe fatigue and effect the operation of guidance and control systems and their supporting structure.

2.4.2 Mach Wave Radiation

Mach wave radiation is caused by the supersonic convection of turbulent large-scale eddies with respect to the surrounding ambient fluid (Kandula, 2008). The associated turbulence has a chaotic and random nature and hence in a stochastic sense, Mach waves can be described as travelling instability waves (Tam, 2009). Mach wave radiation is not associated with a single localised source, but an array of sources that extend along the axis of the jet from the nozzle exit to many exit diameters downstream (Tam, 2009). It is thought to originate at the nozzle exit but goes through a process of growth and decay as it propagates further downstream. In the near-field region, Mach wave radiation has shown to exhibit non-linear propagation effects (Punekar et al., 2010). Equation (2.7) can be used to calculate the peak Mach wave radiation angle, ϕ_{peak} , with respect to the downstream axis of the jet, using the local speed of sound, a_∞ , and the convective jet velocity, U_C .

$$\phi_{peak} = \cos^{-1}\left(\frac{a_\infty}{U_C}\right) \quad (2.7)$$

The convective Mach number refers to the speed of the propagating large-scale eddies and has been estimated for very high speed jets by Tam (2009) to be 80% of that of the main jet;

$$U_C = 0.8 U_J \quad (2.8)$$

However for cold supersonic laboratory jets with moderate Mach numbers of the order of $M=1.3$, a better empirical estimate is provided which yields a high subsonic convective Mach number (Tam, 2009).

$$U_C = 0.7 U_J \quad (2.9)$$

This estimate compares well with a much earlier one that claims the swirling large-scale structures in the shear layer region of the jet, known as eddies, to convect at around 60%-70% of the mean jet axial velocity (Bishop et al., 1971; Avital et al., 2008). Hence, for an ideally expanded Mach 1.3 jet, the convective Mach number would be high subsonic, thus inducing weak, if any, levels of Mach wave radiation (Hileman et al., 2001). A recent experimental study by Petitjean et al (2006) showed that, for a Mach 1.92 jet at a temperature ratio (T_J / T_o) of 0.58, the peak Mach wave radiation angle was towards a downstream direction at 30° to the streamwise axis of the jet. Since Mach wave radiation is associated with large-scale coherent structures, the resultant noise signature is dominated by low frequency noise.

2.4.3 Screech Noise

Shock cell structures are usually formed in imperfectly expanded supersonic jets, due to a mismatch of static pressures between the jet and surrounding atmosphere (Tam et al., 1995). The development of oblique shocks or expansion waves in the jet plume serves the purpose of balancing this difference of pressure for overexpanded or underexpanded flows respectively (Tam et al., 1995). Shock associated noise is considered to be a product of the interaction between the turbulent structures induced at the nozzle and the diamond shaped shock cell structure shown in Figure 2.1 (Henderson et al., 2008). In the presence of the shock cells, the jet emits two additional components of noise in addition to mixing noise, which are referred to as screech and broadband shock associated noise. Screech noise is generally observed in acoustic spectra acquired at upstream and sideline observation angles of cold laboratory jets (Henderson et al., 2008) and is a characteristic found in most imperfectly expanded jets. The screech tone component is discrete in nature, high in amplitude and is associated with various harmonics that are generated by an acoustic feedback of the disturbances at the nozzle lip. The associated harmonics move through the shock cell and are fed back to the nozzle lip through an external route outside the shock cells. As a result another disturbance is created which propagates downstream, hence giving a self-sustaining and repeating cycle (Neemah et al., 1999).

The pioneering work of Powell (1953) highlighted that there are two components of screech noise: its fundamental and secondary harmonic tones. He derived relationships that describe the directivity pattern of these tones by considering the shock cells as being adjacent stationary sources of equal strength and hence determining the phase between them. He found that the fundamental component peaked closer towards an upstream direction to the jet flow, as shown in Figure 2.3, whereas the harmonic component peaked closer to the sideline angle of 90°. Powell also presented an equation for quantifying the frequency of the fundamental component, f_F , of screech noise, shown in equation (2.10), where U_C is the convective speed of the hydrodynamic structures, s is the shock cell spacing and M_C the convective Mach number. The accuracy of this formula depends heavily on the shock cell spacing, s , which can be predicted numerically using the Prandtl-Pack formula shown in equation (2.11) (Singh & Chatterjee, 2007).

$$f_F = \frac{U_C}{s(1 + M_C)} \quad (2.10)$$

$$s = 0.8 \left(1.306D\sqrt{M_J^2 - 1} \right) \quad (2.11)$$

The frequency for the first harmonic component of screech noise, f_H , can be estimated as being twice that of the fundamental (Raman, 1999):

$$f_H = 2f_F \quad (2.12)$$

Earlier research in relation to shock associated noise was concentrated on screech tone abatement, due to its potential to cause structural damage if amplified to above a certain level. Several methods have been investigated for the purpose of screech tone abatement which include: porous plugs, co-annular jets, tabs and nozzle asymmetry. Even today, 60 years from the discovery of screech noise, it plays a vital role in the design of aircraft propulsion systems due to the ability of its harmonic component, which can reach as high as 170dB, to cause sonic fatigue failure as occurred on the British Aircraft Corporation VC-10 and on the F-15 and B1-B of the United States Air Force (Raman, 1999). The jet Mach number, temperature, nozzle lip thickness, and the existence of noise reflecting surfaces around the immediate vicinity of the jet have been all shown to have an effect on screech noise intensity. An increase in the nozzle lip thickness can increase screech intensity by up to 10dB (Norum, 1983), simply by acting as a sound-reflecting surface and hence amplifying the effects of the acoustic feedback loop from the shock cells. Acoustic measurements by Kaji et al., (1996) have provided evidence to suggest that shock noise is most intense somewhere between the third and fourth shock cell structures from the nozzle exit. However due to the non-linearity of the feedback loop, an empirical equation to describe the screech intensity is not yet available (Kandula, 2008).

2.4.4 Broadband Shock Noise

The characteristics of broadband shock associated noise have been explored for over 30 years since the pioneering work of Harper-Bourne and Fisher (1973) who developed the first empirical model for such noise. Converging-diverging nozzles, operating at design Mach number with fully and perfectly expanded supersonic jets, exhibit noise related to turbulent mixing only. For imperfectly expanded regimes however, there exist shock cell structures in the flow for the purpose of correcting the flow pressure as described earlier. The interaction of these shock cells with other structures in the mixing region of the jet, such as instability waves (Mach wave radiation) and small-scale turbulent eddies, leads to the amplification and generation of intense acoustic waves of which a component is broadband shock noise (Kandula, 2008). The resultant acoustic spectrum, like the one shown in Figure 2.3, highlights this interaction noise as sharp peaks at the sideline and upstream angles of a jets acoustic field.

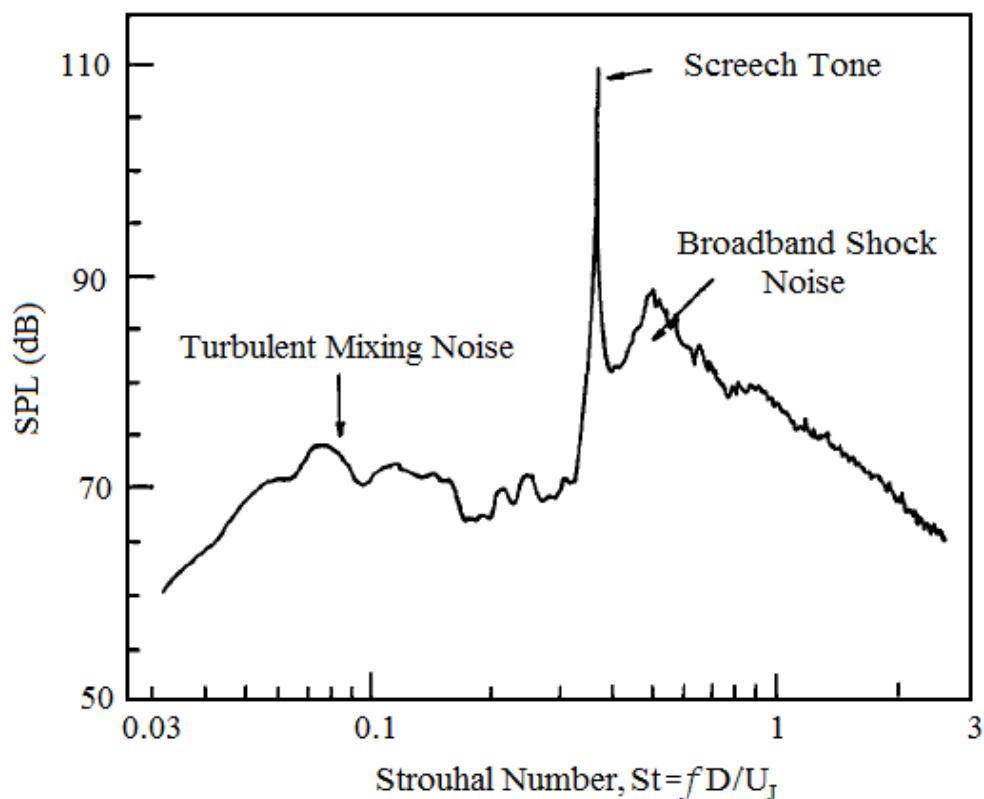


Figure 2.3: Acoustic spectra acquired at an upstream angle of 150° with respect to streamwise axis of a Mach 2 jet, showing the three main sources of supersonic jet noise (reproduced from Tam, 1995).

Broadband shock noise is evidently the dominant characteristic of the upstream spectra of a jet's acoustic field. Tam (1995) highlighted other distinct features of broadband shock noise based on experimental evidence from a converging-diverging Mach 1.67 jet by Norum and Seiner (1982). Firstly, the frequency that corresponds to the broadband shock peak, increases with the observer angle from the jet axis and is highest at the upstream angles. Secondly, the broadband peak consists of several sub-scaled mini peaks, which are most distinct at the sideline angle of 90° . Thirdly, the broadband shock noise spectral bandwidth increases with observer angle and is once again highest at the upstream angles beyond the sideline position. Finally, the sound pressure level of the broadband shock peak is independent of the jet temperature; however the corresponding frequency increases with an increase in jet temperature.

Recent experimental and theoretical work has shown that another type of broadband shock-noise, which radiates primarily in the downstream direction, is also present in dual stream (co-annular) supersonic jets. This form of the broadband shock cell noise has low intensity at the sideline (90°) observer angle and is believed to be generated by the interaction of large turbulence structures and the shock cells in the inner shear layer of the jet (Tam et al., 2008).

2.5 Passive Methods for Jet Noise Reduction

2.5.1 Swirling Jets

Before the 1980's the primary application of swirling jets was in combustion chambers for the purpose of enhancing mixing efficiency (Lilley, 1977). However, experimental studies on full-scale turbojet engines by Schwartz (1975) proposed the use of swirl as a potential application for jet noise reduction in an era coinciding with the Concorde noise reduction programme. Swirl was generated through stationary vanes circumferentially placed around an annular cross-section just upstream of the nozzle exit. Changes in overall sound pressure levels (OASPL) of -4dB and +1dB were recorded at angles of 30° and 90° to the downstream jet axis respectively, with 40% of the overall mass flow ratio of the jet passing through the swirl generating vanes. However, the mean centreline velocity of the supersonic jet (~650m/s) was reduced by the introduction of a tangential velocity component, equating to a loss of thrust by almost 2%. The interaction of centrifugal forces with free turbulent shear flows was found to increase proportionally with the strength of the swirl. The strength of swirl was controlled by changing blade angle of the swirl generating vanes from 40° to 60° to the flow axis, but no quantitative measure of its strength was presented.

Carpenter & Johannesen (1975) used the classical one-dimensional theory for choked, convergent–divergent nozzles and validated previous experiments in relation to swirl having a negative impact on engine performance. They also pointed out that “*the key to analysing swirling propulsive jets is the choice of which parameters to keep constant between swirling and non-swirling cases*” (Carpenter & Johannesen, 1975). It was convincingly argued that the nozzle pressure ratio be maintained such that the thrust parameter be fairly observed when the jet is subjected to swirl. This will therefore be taken as the justification for maintaining constant plenum pressure in this study. The Swirl number, S_N , is the parameter used to indicate the contribution of the tangential swirling component in an axial flow and can be defined as the ratio of the rotational to axial momentum as shown in equation (5.2) (Beer & Chigier, 1972). Relatively low levels of swirl, corresponding to $S_N < 0.1$ have shown to increase the entrainment and spreading rate of the jet, resulting in a reduction in the potential core length (Carpenter & Johannesen, 1975). For intermediate levels of swirl, $0.1 < S_N < 0.2$, the growth rate of the jet is seen to increase linearly with swirl number as pressure gradients along the axis are altered. Adding a substantial tangential component to the primary jet, $S_N > 0.4$ also results in a reduction of axial velocity and thus there is a thrust penalty to any system that attempts to control noise using bulk swirl of the primary jet. The production of a tangential velocity component in a round jet has been shown to radically affect the

characteristics of the shear layer and the production of noise (Carpenter & Johannesen, 1975).

Knowles and Carpenter (1988) developed and used a small perturbation theory to investigate the effects of swirl on a subsonic Mach 0.72 jet. A uniform swirl profile producing Swirl numbers of 0.1-0.15 was found to reduce thrust levels by nearly 3%.

Frank and Taghavi (1995) used small vanes, in plane and notched rectangular nozzles, for the purpose of introducing swirl specifically to the shear layer of a supersonic jet. At a downstream location of 9 nozzle diameters, the mass flow ratio of a circular jet with respect to the nozzle exit was found to be about 2, due to the surrounding air being entrained into the jet flow. For a rectangular jet, the mass flow ratio was found to be 30% higher, measuring 2.6. The introduction of swirl was demonstrated to enhance the mixing, entrainment and spreading rates of the jet by a further 15%, to a mass flow ratio of 3, to a level beyond that achieved by notches.

Neemah et al., (1999) used Schlieren photography for observing the impact of adding a rotational component of velocity to a supersonic Mach 1.3 circular jet, through an upstream vortex chamber for swirl generation. Results indicated that an increase in swirl yields a decrease in the length of the shock cell as well as a decrease in the number of cells. The result was attributed to increased levels of mixing with the surrounding atmosphere. In terms of acoustic findings, low swirl Mach numbers, $M_S = U_\theta / a_{critical}$, of about 0.3 were found to yield equally high reductions in spectral noise levels as compared to higher swirl Mach numbers of 0.5. The peak spectral noise reduction of up to 12 dB included the total elimination of screech noise.

DNS studies have shown that the dynamics of large-scale structures are strongly affected by the degree of swirl (Kollmann et al., 2001). This supports the concept of introducing swirl, as the resultant changes to shear layer dynamics should affect noise production. RANS and LES simulations have shown swirl to affect noise levels by increasing turbulent kinetic energy within the flow profile, as well as reducing the potential core length of the jet (Tucker et al., 2003).

Gilchrist & Naughton (2005) investigated the effect of swirl on the near-field flow of an incompressible swirling jet of Reynolds numbers $\sim 1.0 \times 10^5$. For low levels of swirl, characterised by Swirl numbers < 0.1 , no significant effect on the growth rate of the jet was recorded. Moderate degrees of swirl, $0.1 < S_N < 0.3$ were found to enhance the jet's growth rate and mixing, as compared to the non-swirling case. Gilchrist presented evidence for the enhanced growth rates to persist up to 20 nozzle diameters downstream of the jet exit, even though the swirl had decayed to a point at which it was barely detectable. Such changes in the flow characteristics in the near field would suggest that some turbulence structures of the swirling jet must persist far downstream.

Low Reynolds number flows ($Re \sim 1000$) have been investigated by Liang and Maxworthy (2005) with swirl being induced by an axisymmetric rotating pipe just upstream of the nozzle exit. Vortex roll-up in the shear layer of a jet was shown to occur at approximately two nozzle diameters downstream from the jet exit. These Kelvin-Helmholtz instabilities are known to be produced in the axial shear layer of the jet. Introducing a degree of tangential velocity or swirl into the axial jet can increase the dominance of the helical instability modes over the preferred modes of the jet. Vortex break-down was shown to occur for strongly swirling jets, characterised by Swirl numbers in excess of 0.6.

For supersonic jets, the application of a swirling component of velocity has been proven to successfully reduce screech noise, whereas for subsonic flow regimes, low levels of swirl have been found to be more efficient in reducing mixing noise and turbulence levels. However, most studies have focused on passive methods with fixed geometries such as guide vanes and vortex chambers for producing swirl. Consequently, there is a lack of numerical, experimental and computational results on active methods, such as tangential air injection for swirl generation in supersonic jets.

2.5.2 Mechanical Chevrons

Established methods of passive jet noise control such as lobed or chevroned nozzles are known to generate pairs of counter rotating, stream-wise vortices from each lobe and have been found to reduce low frequency noise at the expense of increased high frequency noise in the near-field (Callender et al., 2007). Mechanical chevrons were initially developed by Boeing, General Electric and NASA specifically for reducing jet noise from the aft angles towards the rear of the engine as shown in Figure 2.4. These devices suppress the overall noise by promoting rapid mixing of the propulsive jet with the surrounding flow (Knowles et al., 2005). However, alterations to the nozzle geometry such as these may incur a weight penalty, as well as increased drag and turbulence during cruise due to the induced mixing by the serrated shape of the nozzle. Hence, the design of compact, lightweight and actively controllable noise reduction methods is the focus of considerable recent research.

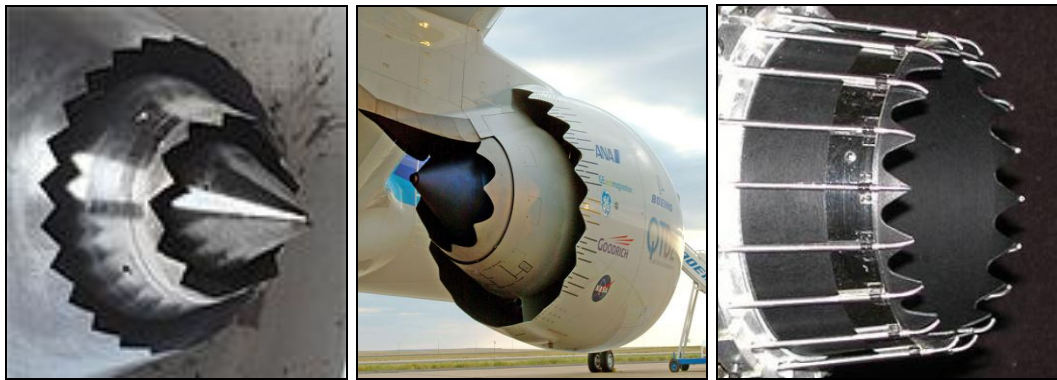


Figure 2.4: Illustration of a serrated chevron nozzles being used by NASA (2006), The Boeing Company (2007) and Alkislar et al., (2008).

An interesting three point criterion was suggested by Alkislar & Krothapalli (2007) to maximise the effectiveness of the stream-wise vortices on the aeroacoustics of the jet in terms of their location, strength and persistence.

- The strength of the vortices should be enough to disrupt only the large-scale coherent structures.
- Any additional turbulent kinetic energy produced by the vortices should be aimed mostly at the low-speed, outer edge of the shear layer.
- There are optimum values for the initial strength and separation of the streamwise vortices.

2.6 Active Methods for Jet Noise Reduction

2.6.1 Fluidic Injection

Microjets provide fluidic injection through small diameter injector nozzles arranged azimuthally around the main axial jet in order to disturb its immediate shear layer, as shown in Figure 2.5. Its application for active noise control on a supersonic Mach 1.2 jet has shown to suppress spectral noise levels by up to 1.2dB in the range of peak jet noise frequencies (Callender et al., 2007). Changes in mixing and turbulence levels due to the interaction of the microjets with the initial shear layer development region, have been shown to either impede or promote the formation of large-scale, coherent structures. This change in the flow structure of the jet can be used for far-field noise reductions across a greater range of frequencies when compared to mechanical chevrons (Callender et al., 2007). The other principal advantage of using fluidic injectors over passive methods is the on-demand nature of the control which can be activated or deactivated at will.

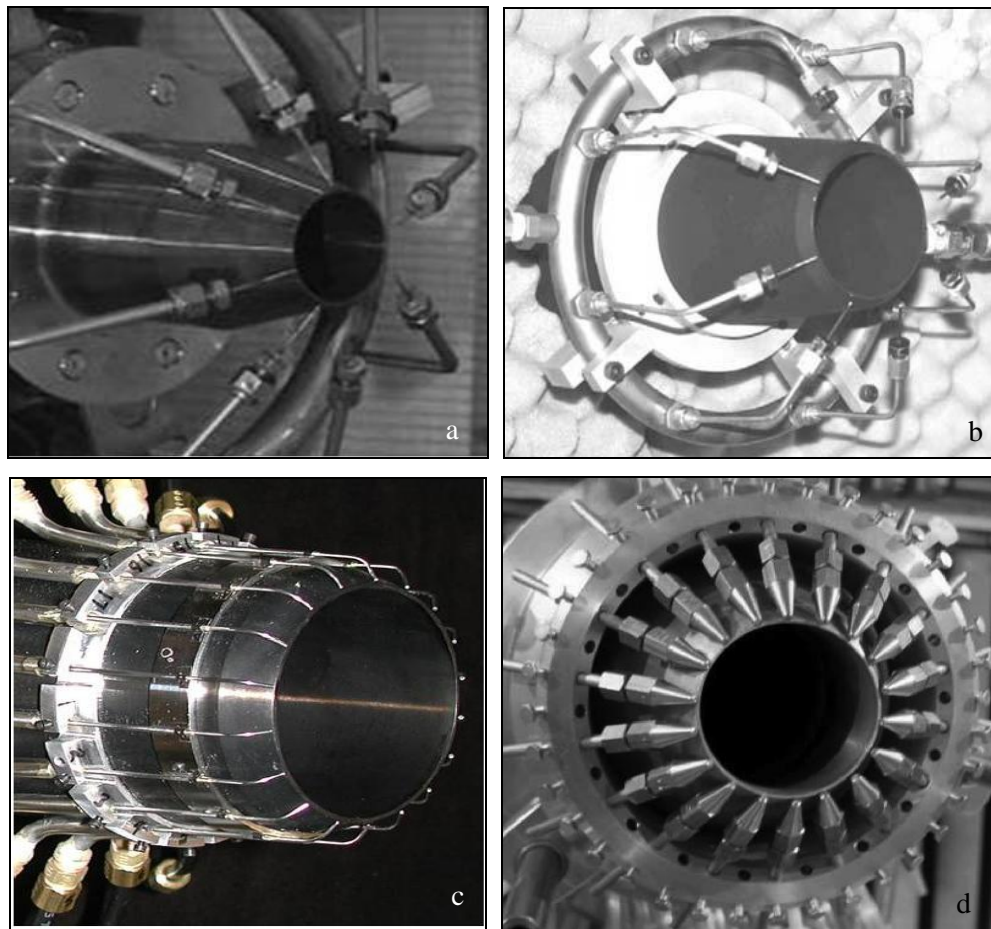


Figure 2.5: Illustrations of various azimuthal spaced, axially impinging microjet configurations. (a) 8 water injectors by Krothapalli et al., (2003), (b) 8 air injectors by Alkislar et al., (2007), (c) 18 air injectors by Alkislar et al., (2008) and (d) 18 air injectors by Castelain et al., (2008).

New and Tay (2004) investigated the effects of dual continuous control jets injecting radially upstream to a main jet. Using flow visualisation they found this configuration to have significantly weakened the formation of large-scale flow structures within the near-field region. This induces instability in the shear layer of the main jet, enhancing the production of small-scale turbulent structures as the rate of injection is increased. The fluid from the control jet is deflected into the main jet's core, resulting in the formation of a pair of counter-rotating vortices. For low control jet velocities, the main jet's shear layer is dominated by incoherent small-scale structures. For intermediate injection velocities the control jets penetrate into the main jet's core, showing minimal interaction with each other. However, the penetration induces another vortex roll-up region within the jet that interacts with the one within the main jet's shear layer, resulting in an early transition into turbulence. For high control jet velocities, the strength of each control jet is diminished due to the counter-rotating vortices penetrating too far into the core region, thus weakening their ability to alter the main jet.

A comparative study by Alkisar and Krothapalli (2007) aimed to highlight the role of streamwise vortices in a Mach 0.9 jet when subjected to two types of noise reducing mechanisms: mechanical chevrons and microjets (Figure 2.5). PIV measurements showed that microjets induce pairs of counter-rotating vortices near the inner, high-speed side of the initial shear layer. Mechanical chevrons were found to have produced vortices of much greater strength but in regions closer to the outer, low-speed side of the shear layer. Despite the chevrons inducing axial vorticity of higher strength, their effect upon the jet structure was confined to only a few diameters, due to a more rapid decay along the downstream axis. Entrainment levels as well as shear layer mixing were found to have increased with the use of both devices, which resulted in an increase in the production of small-scale structures, and hence turbulence levels in the near-field. Compared to the unaltered primary jet, chevrons induced a 30% increase in turbulence levels, peaking near the inner shear layer. This value was much lower for the microjets, causing a 10% increase near the low-speed outer edge of the shear layer. Acoustic spectra for both the near and far-fields showed an increase in high frequency SPL and this is attributed to the increase in turbulence levels near the nozzle exit on the high-speed inner side of the shear layer. However, low-frequency noise was reduced by the use of both devices, as the increased mixing diminished the growth of large-scale coherent structures near the nozzle exit. In contrast to the chevrons, microjets have a stabilising effect on the mean axial velocity profile of the jet, since they reduce the magnitude of the peak azimuthal vorticity in the shear layer (Alkisar and Krothapalli, 2007). Although the mechanical chevrons were able to reduce peak OASPL levels by up to 2dB as compared

to the modest 1dB with the microjets, the microjets were found to have performed better in terms of noise reduction for a wider range of observer angles to the jet nozzle exit.

Experimental work by Phalnikar et al., (2008) examined the flow properties of isolated free supersonic microjets with diameters ranging from 100–1,000 μm with exit velocities in the range of 300–500m/s. Similar microjets have been used in several applications which include active control of larger supersonic impinging jets for short takeoff and vertical landing (STOVL) aircraft (Lou et al., 2006), and flow separation (Kumar et al., 2006). Schlieren images were used to clearly show the characteristic shock cell structure typically observed in larger supersonic jets. Quantitative measurements of the jet's centreline velocity decay and spreading rates, as well as shock cell spacing, were obtained using a micro-pitot probe and a micro-Schlieren system. The mean flow features of free microjets were found to be similar to larger supersonic jets operating at higher Reynolds numbers (Phalnikar et al., 2008).

More recent experimental studies carried out by Henderson et al., (2008) focussed on the use of microjets combined with chevrons to azimuthally control broadband shock and mixing noises for both single and dual stream jets. The configuration was such that the control jets impinged directly into the core flow at a pitching angle of 50° to streamwise jet. The advantage of using fluidic injection lies in the ability to adjust the operation of such a device to match the conditions of the changing exhaust for high and low noise operations during the overall flight envelope. For low supersonic jets, screech tones at frequencies of approximately 3kHz have been recorded at angles further upstream than 90° . However, with slight air injection this is seen to disappear and is believed to be a result of the interruption of the feedback loop at the nozzle exit. A much broader peak in the spectrum at around 6kHz was attributed to broadband shock noise which was easily reduced by increasing the injection pressure ratio. This came at the expense of a slight increase in sound pressure levels at frequencies beyond 40kHz. Peak mixing noise was recorded at the downstream observer angles at low frequencies, with noise reductions becoming more visible as both the injection pressure and number of injector lines increased. The effect of varying the number of active control jets was also investigated whilst keeping the total mass and momentum of the injected air constant. The reductions in broadband shock noise were observed to be similar, of the order of 8dB, regardless of the number of active control jets. This reduction was found to be greater for higher injection pressures, corresponding to an injection mass flow ratio of 1.2% of that of the overall jet (Henderson et al., 2008). A supersonic, Mach 1.15 jet was also tested at a much higher temperature and the resultant acoustic spectra showed a broadband shock peak that was much less pronounced than with the colder jet. Hence, it was deduced that the shock noise is not affected as much by

air injection. However, the mixing noise was noted to have been reduced just as before (Henderson et al., 2008). The effect of fluidic injection on the core of a dual stream supersonic jet was also examined. In contrast to the single stream flow, no reductions in the broadband shock noise were recorded and this was attributed to the supersonic fan stream being at a much higher pressure ratio than the core, hence having a minimal effect on the shock cell structure (Henderson et al., 2008).

Castelain et al., (2008) used multiple impinging microjets of 1 mm diameter to demonstrate noise reductions on a subsonic Mach 0.9 jet as shown in Figure 2.5. Typical noise reduction of about 1 dB were recorded at the sideline (90°) and downstream (30°) angles to the jet axis for both configurations of 9 and 18 microjets equally spaced around the nozzle exit. The total mass flow ratio being discharged from the microjet system was approximately 1.2% of that of the main jet. The investigation highlighted that noise reduction is affected by several parameters, which include: the microjet velocity relative to the main jet velocity, the longitudinal distance between the point of injection and the nozzle exit, and by the number of microjets. Maximum noise reductions were obtained when the microjets were applied close to the jet exit such that they acted on the sensitive mixing layer. By increasing the number of microjets the interaction zone between the microjets and the main jet was increased, resulting in slightly greater noise reductions. Although higher injection velocities proved favourable, a balance must be met to minimise undesirable higher frequency noise generation from the microjets themselves.

Water injection for the purpose of reducing the mixing component of jet noise has also been investigated in the past. Krothapalli et al., (2003) used 8 microjets for water injection at mass flow ratios of about 5% to that of the primary Mach=1.4 flow. The mean flow structure of the jet was mostly unaltered as compared to the base case. However, a reduction in turbulence levels was measured and attributed to the water droplets breaking up upon interaction with the jet. Their results agreed with that of Arakeri et al., (2003) who showed air injection through microjets to cause a reduction in turbulence intensity associated with the shear layer with a subsequent increase in the length of the potential core as compared to an un-altered subsonic jet. In both cases a reduction in turbulence intensity was concluded to be the process responsible for the noise reductions. Kandula (2008) used a one-dimensional control volume formulation to determine the effects of water injection at higher mass flow ratios of about 10%. The reductions in noise were related directly to a reduction in the mean flow velocity due to momentum and heat transport between the injected water and the jet.

Several design parameters have been found to influence the effectiveness of noise reduction by fluid injection. Optimal reductions in jet noise will therefore require a careful compromise between these following variables:

1. Mass flow ratio between injection fluid and jet
2. Axial injection location relative to the nozzle exit
3. Fluid injection angle
4. Number of injectors
5. Method of injection i.e. pulse, spray, or jet like
6. Droplet size for liquid injection
7. Injection pressure
8. Injection temperature

2.7 Human Perception and Response to Noise

Understanding the human perception of noise is a complicated subject that involves the fields of physiology, psychology and acoustics. The human ear, one of the most intricately delicate parts our bodies, can be described as a “*sensitive broadband receiver and in conjunction with the nervous system it is a complex frequency analyser*” (Kinsler, 2000). The ear consists of three main parts- the outer, middle, and inner parts, all of which work in combination to give us the ability to perceive the pitch of a sound by detecting its wave frequency, and its loudness by the wave amplitude, in order to interpret complex sounds.

The International Organisation for Standardisation (ISO) outlines how the hearing thresholds of the population vary based on factors such as age. The average person can hear sounds in the frequency range of $20 \text{ Hz} < f < 20\text{kHz}$ (Cutnell, 1998). However, beyond the age of 30 years there is much variability recorded. In western cultures especially, for people that fall into the age band of 40 to 50 years, the upper bound of hearing is reduced to 15kHz, whereas for sounds below 1kHz the variability is found to be independent of age. In terms of the pressure level or energy of a sound the lower and upper thresholds of audibility for most people are 10dB and 120dB respectively (Cutnell, 1998). At the latter extreme, a tickling sensation is produced within the ear, whilst at 140dB this sensation become unbearable and is known as the threshold of pain (Cutnell, 1998).

The human ear reacts to loud sounds by adjusting its acoustic reflex or sensitivity and hence shifts up the threshold of audibility during exposure to noise. The amount by which the threshold shifts depends on the intensity and duration of exposure to the sound. Once the sound is removed the threshold begins to reduce and recovers to its original state such that there is no longer a shift present. This phenomenon is referred to temporary threshold shift (TTS) (Charron, 1998). The recovery time associated with such processes is proportional to the intensity and duration of exposure, and if these

parameters are too high then there may be incomplete recovery hence causing a permanent threshold shift (PTS). This is the result of permanent hair cell damage in the inner part of the ear (Charron, 1998).

It is very difficult to predict community response to environmental acoustics due to the vast range of variability in response amongst a population. One method used to do so by the ISO R1996 (1971) involves the use of the A-weighted sound pressure level, dBA, which is the most common unit of measuring for environmental noise. It adds a “weighting” to certain frequency components of sound in order for it to conform to the normal response of the human ear at conversational levels (RAeS, 2004). The method corrects the A-weighted sound pressure level from a noise source with respect its noise characteristics, like tone persistence, duration, timing and location. A community’s expected response is then categorised with respect to this corrected noise level and is as follows: <45 dBA no response, 45-55 dBA sporadic complaints, 50-60 dBA widespread complaints, 55-65dBA threats of community action and >65 dBA vigorous community action (Kinsler, 2000).

Exposure to unnaturally high levels of noise, such those usually associated with industrial workers and airport ground staff can bring the onset of noise induced hearing loss, which is of two types (Kinsler, 2000). Trauma is associated with a sudden event of high intensity sound, such as an explosion or jet engine, and causes the rupturing of the ear drum, damage to ossicles and sensory or hair cells. Chronic hearing loss, on the other hand, is due to repeated or prolonged exposure to high levels of noise (lower than that which causes trauma) which causes dysfunction of hair cells. It is particularly dangerous as the sufferer may not be aware of the slow and gradual process of hearing loss. With this in mind, the Occupational Safety and Health Act (1970), OSHA, prescribes permissible exposure limits for industrial workers to prevent PTS hearing loss for frequencies below 4kHz, those necessary for understanding speech. The exposure time limit is halved with every 5dBA increase in the sound pressure level: 2 hours~100dBA, 1 hour~105dBA and 30mins~110dBA. The recommended exposure time limits for non-occupational noise are much stricter and stand at: 15mins ~100dBA, 8min~105dBA and 4min~ 110dBA (Kinsler, 2000). With jet noise levels exceeding 105 dB up to several hundred metres from the runway during the departure phase of a passenger aircraft (RAeS, 2005), both occupational (airport ground staff) and non-occupational (passengers and local community) exposure time limits will be increasingly difficult to comply with, given the predicted growth in air traffic and aircraft size.

2.8 Summary

A literature review of past and present understanding of jet noise and the techniques used to reduce it, reveals the lack of experimental data in relation to tangential air injection for the purpose of active jet noise control, and hence makes an ideal starting point for the present study.

Jet noise is characterised by two principal noise sources, turbulent mixing noise and shock associated noise. It is accepted that turbulent mixing noise consists of two distinct noise components. The first is a product of rapidly dissipating fine-scale turbulent structures in the immediate shear layer of the jet that are highly radiative in the sideline and upstream directions. The second is a result of the growth of fine-scale disturbances into large-scale turbulent eddies that exist towards the end of the potential core and propagate towards the downstream aft angles, dominating the mixing process and far-field acoustic spectra.

Mach wave radiation occurs in the mixing region of a jet as a result of the supersonic convection of large-scale eddies, which for cold laboratory jets travel at approximately 70% of the jet exit velocity. Its directivity is highly dependent on the jet speed and temperature ratio. For a Mach 1.3 jet, that is to be studied in the present thesis, the intensity of Mach wave radiation is expected to be low.

Screech noise is a high amplitude discrete tone commonly found in imperfectly expanded jets and is a product of the feedback loop induced by the turbulence-shockwave interaction around the third to fourth shock cell in the potential core. It has fundamental and harmonic components both of which radiate in opposing directions and have been known to cause sonic fatigue failure. Broadband shock noise, thought to be sourced from the same turbulence-shockwave mechanism as screech noise, has a larger bandwidth and occurs at higher frequencies in both near and far-field upstream acoustic spectra.

Promoting enhanced levels of mixing within the shear layer disrupts the foundations of all noise source mechanisms and is shown to reduce jet noise. Active methods of jet noise control such as fluidic injection have the distinct advantage of adaptability to suit the various jet operating conditions throughout the flight envelope. As a result, penalties in weight, thrust and operational costs, through increased drag and specific fuel consumption, that are associated with current passive methods, can be avoided.

In supersonic jets the application of swirling component of velocity has been proven to successfully reduce screech noise, whereas for subsonic flow regimes, low levels of swirl have been found to be more efficient in reducing mixing noise and turbulence levels. However, most studies have focused on passive methods with fixed geometries such as guiding vanes and vortex chambers for producing swirl.

Consequently, the motivation for this study is in the lack of numerical, experimental and computational results on active control methods, such as tangential air injection for swirl generation in supersonic jets.

Tangential air injection is distinctly different from radial and impinging microjets in that they have a net swirl effect on the jet. The tangential injectors pitched at 90° to the axial jet, provide an optimal angle in favour of promoting swirl and hence shear layer mixing. Microjets are limited in the sense that they reach sonic velocities quickly for low injection mass flow ratios and hence are subject to parasitic self-generated high frequency noise. In the light of this, the injector nozzles in this study will have diameters of the order of millimetres as opposed to micrometers in order to avoid limitations in injection mass flow ratios. The noise reduction achieved through various passive and active jet noise control methods have been summarised in Table 2.1.

Table 2.1: Summary of Noise Reductions from Passive & Active Methods

Technique	Jet Mach No.	No.	Pitch	Mass Flow Ratio	Δ OASPL at 90°	Δ OASPL at 30°	Author
Swirl by Vanes	>1.5	-	60°	40%	+1dB	-4dB	Schwartz (1975)
Swirl, Vortex Gen	1.3	-	-	-	-3dB	-2.5dB	Neemah (1999)
Microjets	0.9	18	45°	1.1%	-2dB	-2dB	Arakeri (2003)
Microjets	1.2	16	30	-	-1.2dB	-0.8dB	Callender (2007)
Chevrans	0.9	8	60°	-	+1.5dB	-2 dB	Alkisslar (2007)
Microjets	0.9	8	60°	0.4%	-0.5dB	-1dB	Alkisslar (2007)
M ² jets + Chev's	1.2	8	50°	1.2%	-1 dB	-1 dB	Hendersn (2008)
Microjets	0.9	9	45°	1.2%	-0.9dB	-1dB	Castelain (2008)
Microjets	0.9	18	45°	1.2%	-1.2dB	-1dB	Castelain (2008)
Microjets	0.9	18	60°	0.4%	-0.5dB	-0.8dB	Alkisslar (2008)
Chevrans	0.9	18	60°	-	-0.6dB	-1.2dB	Akisslar (2008)
M ² jets + Chev's	0.9	18	60°	0.4%	-1.5dB	-2dB	Alkisslar (2008)

Based on these experimental findings, it would be reasonable to set noise reduction targets of approximately 1-2dB at sideline (90°) and downstream (30°) observer angles. In addition to this, the eight-point fluid injection criteria set out in §2.6 with regards to the design parameters that influence the effectiveness of noise reduction, will be explored to find an optimal configuration that balances noise reductions with penalties in weight, thrust and cost.

3 INSTRUMENTATION AND FLOW CONFIGURATIONS

3.1 Acoustic Chamber

The test apparatus was commissioned in 2007 at the Department of Engineering of Queen Mary, University of London. Its design and installation, by Luff & Cater (2008), was specific to the aim of investigating jet noise reduction techniques. The anechoic chamber has external dimensions of 3.5m×3.5m×2.5m as shown in Figure 3.1. Acoustic foam wedges are placed on the walls, ceiling and floor to produce an acoustically non-reflective environment for the jet study. The foam wedges measure 430 mm from base to tip and have cross-sectional base dimensions of 300mm×300mm. They are designed to produce a lower cut-off frequency of 200 Hz. All flat and non-porous acoustically reflective surfaces within the chamber, such as the exhaust funnel and the microphone support beam were covered in foam sheets. Internally, the chamber has wedge to wedge dimensions of 2.5m×2.5m×2.0m giving an approximate working floor space of 6m².

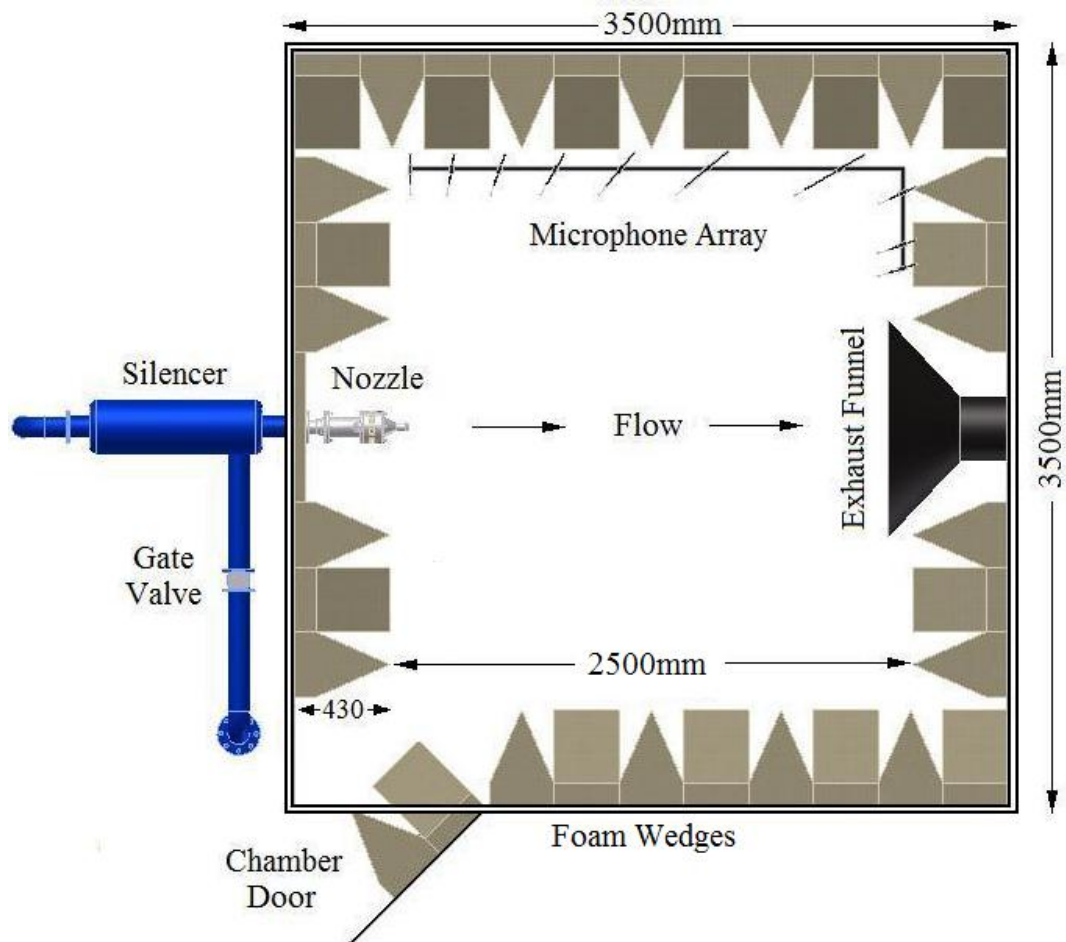


Figure 3.1: A schematic plan view of the acoustic chamber and experimental jet apparatus, which was commissioned in 2007 at the Department of Engineering of Queen Mary, University of London.

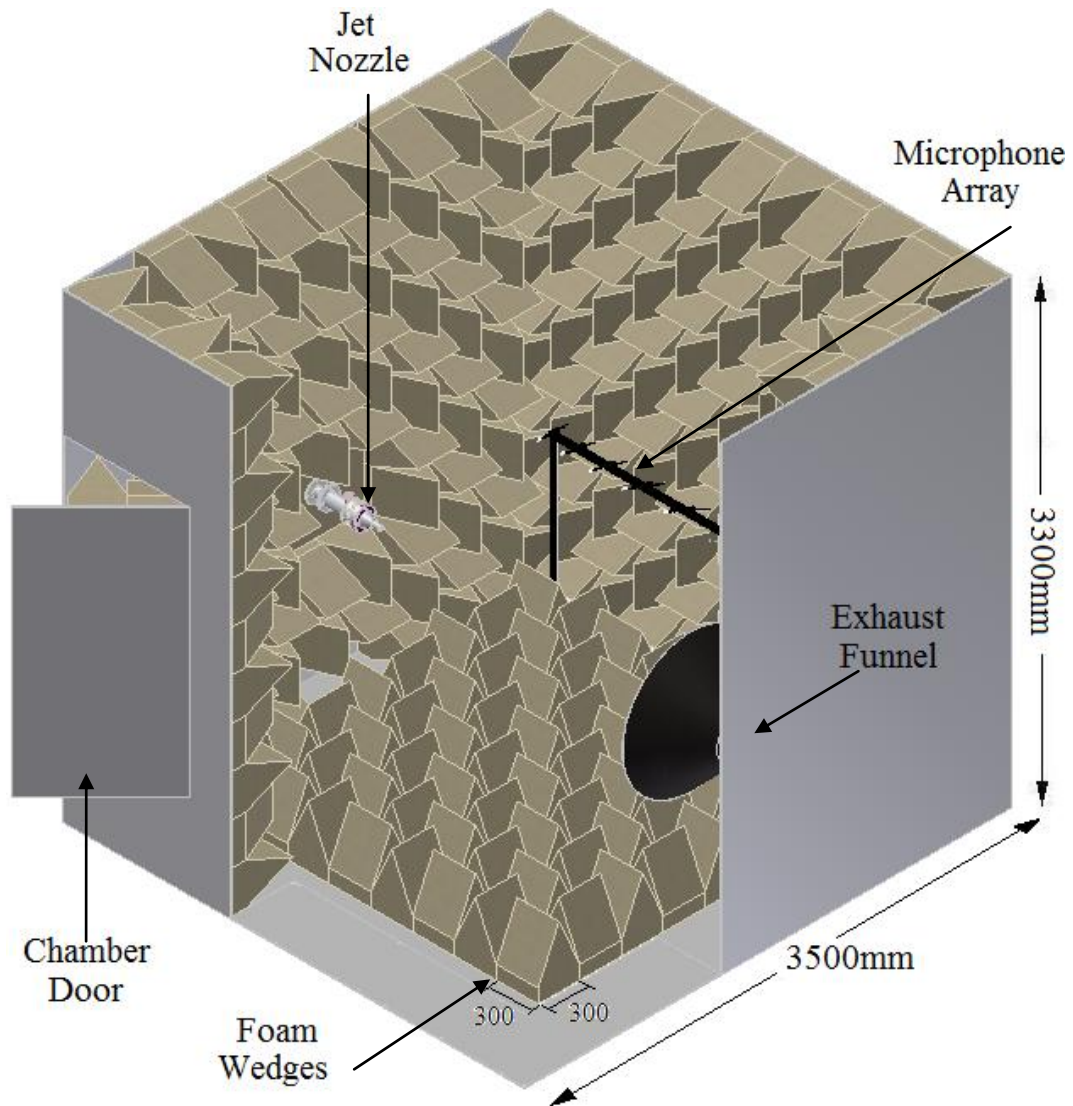


Figure 3.2: Three-dimensional cut-out view of the acoustic chamber with wall and floor surfaces covered with anechoic foam wedges. During acoustic measurements, the nozzle and microphone support beam were covered with 70mm thick foam sheets.

3.2 Experimental Jet Apparatus

Compressed air is supplied to the experimental apparatus by a reservoir with a capacity of approximately 50m^3 and at a pressure of 14bar (200psi). Before entering into the reservoir the air is first filtered and dried. The jet exits into initially still, ambient air with a nominal temperature of 293K. The flow is controlled with a pneumatically actuated gate valve, installed downstream of the reservoir, using a PID controller with an input signal from a pressure transducer located immediately upstream of the converging section of the nozzle. The pressure transducer's range was set so that 4mA was equal to zero bar gauge and 20mA equal to 4bar gauge. These values were selected to match the limits of both the transducers sensitivity range and gauge pressures that are expected in the plenum chamber. The PID controller scale is set to convert this range of mA values

into bar gauge which is displayed on a digital output. With this configuration the flow can be adjusted to maintain the desired nozzle pressure ratio to better than 1.6% precision, leading to an accuracy in velocity better than 0.8% (Luff et al., 2008). A Flo-Dyne silencer, designed to operate up to gauge pressures of 14bars and temperatures of 100°F (38°C), is located downstream of the gate valve to reduce the effect of apparatus generated flow noise on the acoustic measurements. The 82mm diameter plenum chamber is connected to the gate valve via 63mm (2.5in) internal diameter steel piping. The junction between the plenum chamber and steel piping is through an expansion section preceded by a 1m long silencer for the purpose of reducing internal noise from the compressor and gate valve (Tinney 2004). Once the flow has been expanded into the plenum chamber it then passes through a honeycomb and three wire meshes to condition the flow, by removing any swirl components and reducing turbulence levels. The wire meshes have blockage ratios less than 0.4. Each mesh is separated by 0.2 plenum chamber diameters, and the unit is designed to reduce the pressure by a factor of two (Mehta et al., 1979).

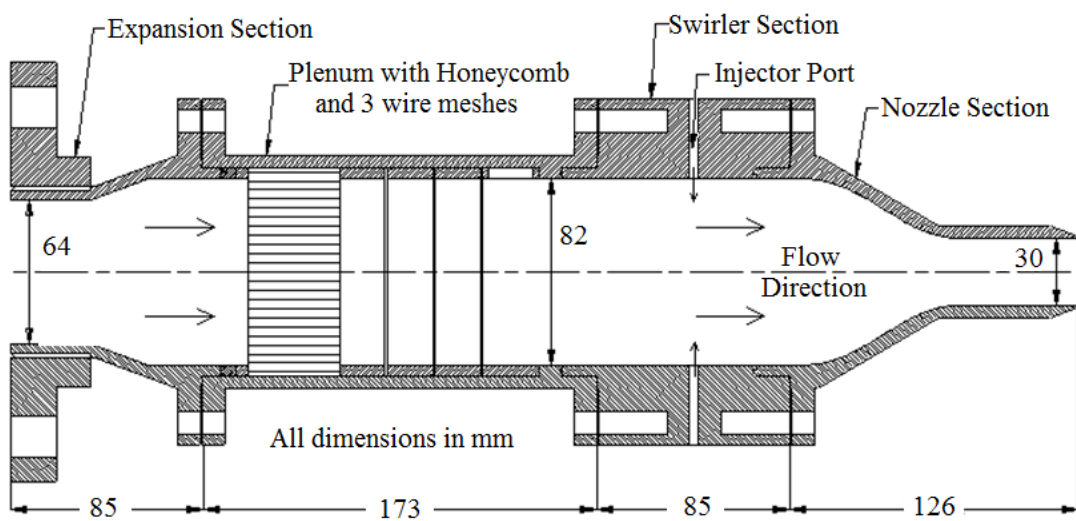


Figure 3.3: Cross-section of the plenum chamber showing the flow straightening devices as well as the converging-diverging nozzle. All dimensions are in mm (Luff et al, 2008).

The pressure transducer that regulates the plenum pressure is located downstream of the honeycomb and wire meshes and hence takes into account the pressure across them. The tangential injector ports are located downstream of the honeycomb, in order to prevent it from reducing the tangential velocity components within the flow. The entire system is mounted to an elevated steel stand such that the centre line flow axis is 1.3m above ground level. The circular exhaust funnel has an opening diameter of 1m contracting to an outlet of 0.3m followed by a 135 degree bend. Covering these funnel surfaces with foam allows the flow to be anechoically terminated to an atmospheric exhaust. The jet

apparatus intrudes 0.5m into anechoic chamber, equal to the length by which the exhaust funnel intrudes into the chamber at the opposite wall. This leaves 2.3m between them which equates to approximately 80 nozzle diameters. Based on this distance, the exhaust diameter of 1m is sufficiently large to capture a jet with a spreading angle of up to 12°. Tam (1995) highlighted that high-speed jets have very small spreading rates and Panda (1999) later quantified this angle as 5.7°. The main function of the exhaust duct is to ensure a constant ambient pressure within the chamber and prevent any re-circulation.

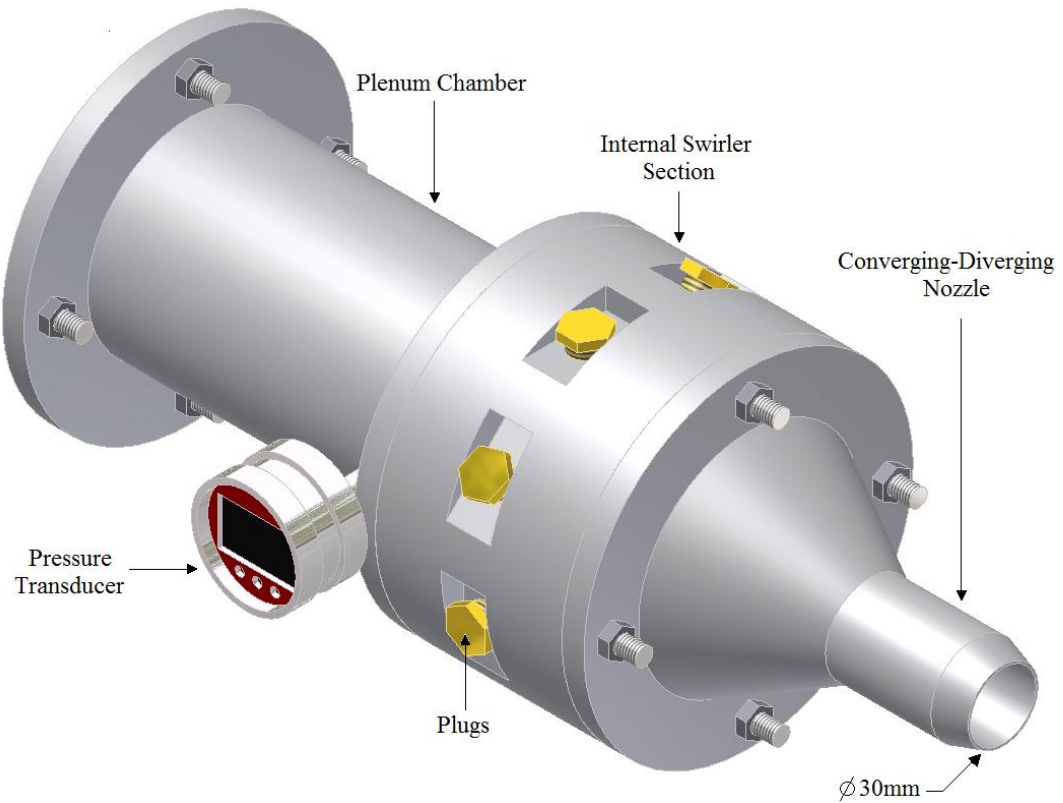


Figure 3.4: CAD assembly drawing of the experimental jet apparatus, with a Mach 1.3 converging-diverging nozzle. The pressure transducer used to regulate the plenum pressure is located downstream of the honeycomb and wire meshes.

3.3 Mach 1.3 Nozzle

3.3.1 Theoretical Jet Flow Parameters

It can be generalised from the second law of thermodynamics that a reversible flow is one that maintains a constant value of entropy (Zucrow & Hoffman, 1976). If a flow is gradually compressed through a decreasing volume and then gradually expanded through an increasing volume, the flow is able to return to its original state. Hence, the acceleration of air through a converging-diverging nozzle can be approximated as an isentropic process, given that the surface angles are small enough to prevent flow separation. The one-dimensional isentropic flow equations alongside the measured ambient properties can be used to calculate various plenum and nozzle exit parameters in order to control the jet's performance.

For fully expanded flows the jet exit pressure is equal to the ambient atmospheric pressure;

$$P_J = P_A \quad (3.1)$$

The stagnation pressure required in the plenum chamber in order to achieve a certain jet Mach number, M_J , can be calculated using the jet exit pressure, P_J , and the specific heat ratio for air, $\gamma=1.4$, (White, 2003);

$$P_o [Pa] = P_J \left(1 + \frac{\gamma - 1}{2} M_J^2 \right)^{\frac{\gamma}{\gamma - 1}} \quad (3.2)$$

The gauge stagnation pressure of the plenum chamber, P_g , can be found by subtracting the static atmospheric pressure from the absolute pressure;

$$P_g [Pa] = P_o - P_A \quad (3.3)$$

The stagnation plenum density can then be found using the measured stagnation temperature, T_o [K], and the ideal gas constant for air $R=287$ [J/kgK] (White, 2003);

$$\rho_o [kg/m^3] = \frac{P_o}{R T_o} \quad (3.4)$$

The speed of sound of an ideal gas at this given temperature and density is;

$$a_o [m/s] = \sqrt{\gamma RT_o} \quad (3.5)$$

Once the ambient and plenum properties are known the exhaust parameters of the jet can be calculated. The static density and temperature of the jet at the nozzle exit are calculated using the isentropic flow equations;

$$\rho_J [kg/m^3] = \rho_o \left(\frac{P_J}{P_o} \right)^{\frac{1}{\gamma}} \quad (3.6)$$

$$T_J [K] = T_o \left(\frac{P_J}{P_o} \right)^{\frac{\gamma-1}{\gamma}} \quad (3.7)$$

The local speed of sound with respect to the jet temperature is given by;

$$a_J [m/s] = \sqrt{\gamma RT_J} \quad (3.8)$$

Using the jet's Mach number, its exit velocity can be calculated;

$$V_J = a_J M_J \quad (3.9)$$

The mass flow rate can be found using laws of conservation;

$$\dot{m}_J [kg/s] = \rho_J A_J V_J \quad (3.10)$$

Assuming that this velocity is constant across the fully expanded jet, the thrust equates to;

$$T_X = V_J \dot{m}_J + A_J (P_J - P_A) \quad (3.11)$$

For a fully expanded jet, the jet pressure is equal to that of the atmosphere; hence the back pressure term can be assumed to be negligible. The Reynolds number is a dimensionless parameter used to correlate the viscous behaviour of a Newtonian fluid and defined by the ratio of its inertia to viscous forces (White, 2003).

$$\text{Re}_J = \frac{\rho_J V_J D}{\mu_J} \quad (3.12)$$

3.3.2 Converging-Diverging Section Design

For the purpose of this study a Mach 1.3 supersonic nozzle was designed and manufactured in-house by Luff et al., (2008). The convergent section of the nozzle was designed using a fifth order polynomial to reduce the internal boundary layer thickness and to provide a uniform velocity profile (Bell et al., 1988).

$$r = (r_I - r_E)(-6x'^5 + 15x'^4 - 10x'^3) + r_I \quad (3.13)$$

The fifth order polynomial gives the profile shape, r , with r_I being the contraction inlet radius (41mm), r_E the contraction exit radius (equal to the throat radius of 14.5mm) and x' the streamwise co-ordinate non-dimensionalised by the convergent section length of 80mm. The inner profile converges from a plenum diameter of 82mm to a throat diameter of 29mm giving a contraction ratio of 2.7:1. Usually if the contraction is too steep, the flow experiences flow separation at the throat, whereas if it is too gradual there may be an undesired growth in the boundary layer thickness, and hence a departure from isentropic flow (Tinney 2004). The profile of the divergent section of the nozzle was calculated by Luff et al., (2008) using the method of characteristics to reduce shock waves reflections within the nozzle (Zucrow & Hoffman, 1976). The Mach 1.3 nozzle has an exit diameter of 30 mm and a lip thickness of 0.5 mm. The nozzle, swirler section, plenum chamber and expansion section were all manufactured from free cutting aluminium alloy using a CNC lathe machine. The average surface roughness is approximately 0.2 microns. The nozzle is bolted onto the settling chamber section using eight M10 bolts, and is easily interchangeable with other nozzles as required.

3.3.3 Primary Jet Flow Parameters

Table 3.1 shows the ambient conditions which were used to calculate the primary jet's exit flow parameters shown in Table 3.2, using the isentropic flow equations described in § 3.3.1. The gauge pressure of the settling chamber was set at 1.75bar in order to achieve a Mach 1.3 jet. A table relating gauge plenum chambers pressures to desired exit Mach numbers was derived using the isentropic flow equations and is presented in the appendix A. Using this configuration of reservoir and nozzle, run times of approximately 1000 seconds can be achieved.

Table 3.1: Ambient Air Properties and Plenum Parameters

Plenum Gauge	Ambient Pressure	Stagnation Pressure	Stagnation Temp	Air Density	Sonic Speed
P_g [bar]	P_A [kPa]	P_o [kPa]	T_o (K)	ρ [kg/m ³]	a [m/s]
1.75	101.3	278.6	293	3.31	343

Table 3.2: Main Jet Exit Flow Parameters

Nozzle Pressure Ratio	Jet Mach Number	Jet Temperature	Nozzle Diameter	Mass Flow Rate	Reynolds Number
P_J/P_o	M_J	T_J [K]	D [m]	m_J [kg/s]	Re_J
0.36	1.29	219	0.03	0.44	1.25×10^6

3.4 Tangential Injection Configurations

3.4.1 Internal Tangential Injection (ITI)

A tangential flow was achieved by three different methods in this study. The first technique, in which air is injected internally and tangentially through eight 4mm internal diameter ports located in the plenum chamber directly upstream of the nozzle is called internal tangential injection and is illustrated in Figure 3.5 and Figure 3.6. Standard push-fit BSP connectors were used alongside 8mm internal diameter polyurethane tubing to create a network for simultaneous air injection across all ports. The flow rate to the air injectors was controlled by a manually operated valve and adjusted with reference to a digital display from a pressure transducer located downstream of the valve. Air to the injectors was equally distributed using an 8-way manifold as shown in Figure 3.7.

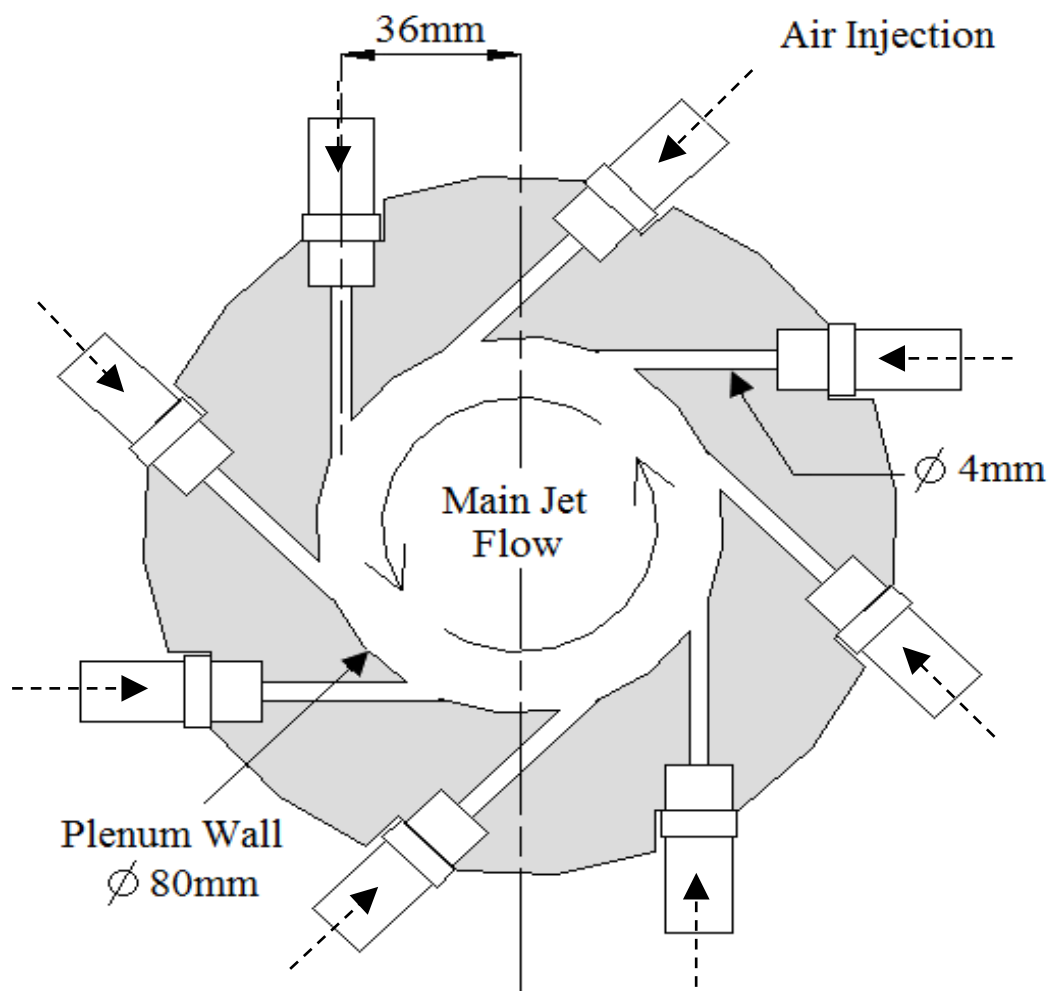


Figure 3.5: Schematic of the cross-section for the internal tangential air injection configurations.

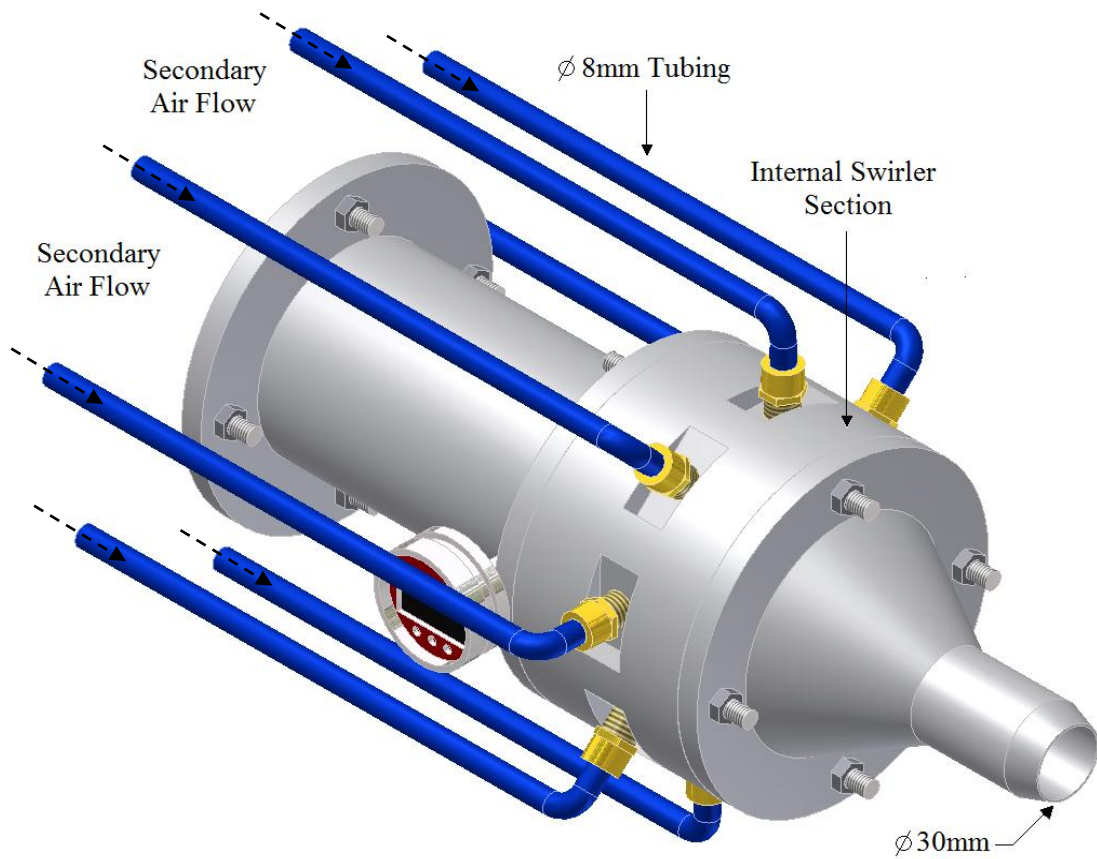


Figure 3.6: CAD assembly drawing of the upstream internal tangential air injection configuration.

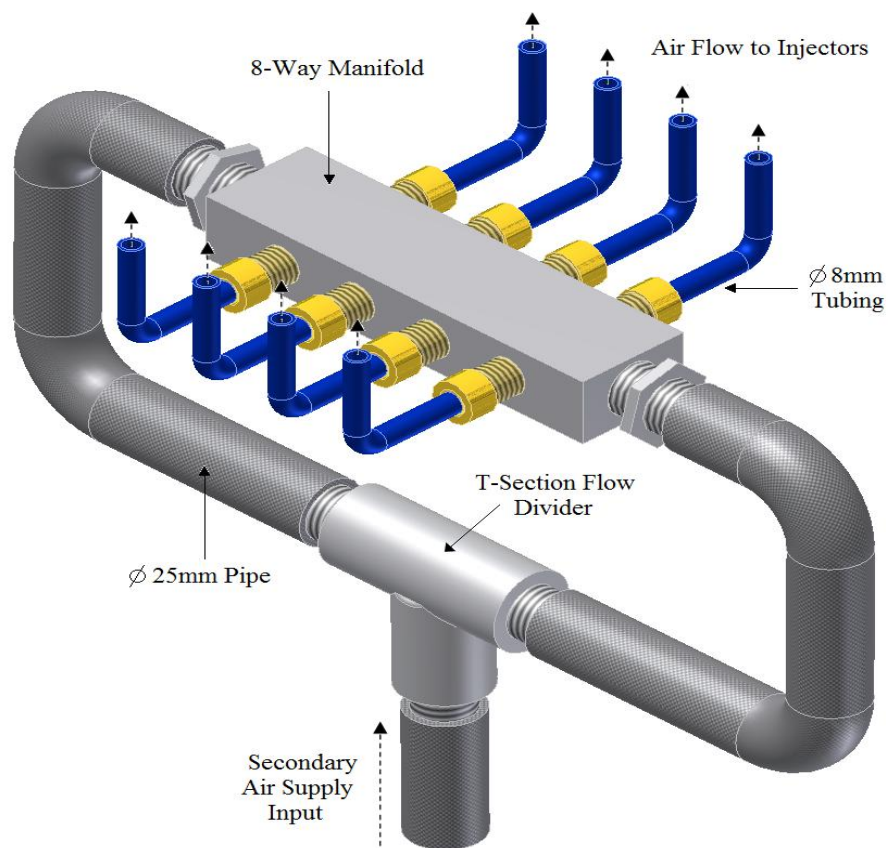


Figure 3.7: Eight-way manifold used to distribute the secondary air supply to the injectors.

The independently-controlled, secondary air supply to the tangential injectors was from a separate reservoir to the primary jet. Hence, it was possible to maintain the nozzle pressure ratio for a fair observation of jet thrust with variations in swirl (Carpenter and Johansen, 1975). Table 3.3 shows the estimated upstream swirling section flow conditions, using the isentropic flow equations. The mass flow ratio of the combined upstream injectors is defined in equation (3.14) as a percentage of the total mass flow rate of the jet. The total plenum pressure is conserved as the primary jet supply is decreased proportionally when upstream injection is used.

$$\frac{8\dot{m}_I}{\dot{m}_J} = \frac{\sum_1^8 \dot{m}_I}{\dot{m}_J} \quad (3.14)$$

Table 3.3: Theoretical Internal Injection Flow Parameters

Secondary Reservoir	Mach Number	Mass Flow Rate	Reynolds Number	Total Mass Flow Ratio
P_g [bar]	M_I	\dot{m}_I [kg/s]	Re_I	$8\dot{m}_I / \dot{m}_J$
2	0.35	0.006	9.2×10^4	10%
6	1.00	0.022	4.2×10^5	40%
8	1.00	0.027	5.4×10^5	50%

3.4.2 External Tangential Injection (ETI)

The second tangential air injection technique consists of eight 1.5 mm internal diameter tubes positioned downstream of the nozzle exit, offset by an axial distance of 1.5 mm ($x/D=0.05$), as illustrated in Figure 3.8 and Figure 3.9. The external injectors were configured as close as possible to the sensitive shear layer in order to yield maximum noise reductions (Castelain et al., 2008). Table 3.4 details the flow parameters used for ETI. The external jet size was selected such that the ratio of external injector to nozzle diameter (1.5/30) was equal to the ratio of internal injector to plenum diameter (4/80). This was done purely for the sake of maintaining some geometric similarity between the two configurations and is similar to the area ratios (1.5%) used in previous microjet studies (Callender, 2007). It is important to note that similar to the internal injection scenario, during external injection the mass flow rate of the primary jet is maintained as it is sourced from an independent reservoir.

Table 3.4: Theoretical External Injection Flow Parameters

Gauge Pressure	Mach No.	Mass Flow Rate	Reynolds No.	Mass Flow Ratio
P_g [bar]	M_E	\dot{m}_E [kg/s]	Re_E	$8\dot{m}_E / \dot{m}_J$
0.3	0.62	0.47×10^{-3}	2.3×10^4	0.9%
0.6	0.85	0.66×10^{-3}	3.4×10^4	1.2%
0.9	1.00	0.80×10^{-3}	4.3×10^4	1.5%

The injection mass flow rates were derived using isentropic flow equations. However, since the flow passes through several contractions from the point of supply to injection, it was necessary to approximate these frictional losses by validating the theoretical values through measurements. A rotometer capable of measuring flows up to 200 l/min (3.3×10^{-3} m³/s) was used for this purpose. Due to the limitations of the flow meter, the 0.9 bar gauge pressure scenario could not be tested and hence an error was estimated using the overall trend of preceding lower pressure measurements. The actual mass flow ratios were lower than those theoretically derived and are listed in Table 3.5.

Table 3.5: Measured External Injection Flow Parameters

Gauge Pressure	Theoretical Mass Flow Rate	Actual Mass Flow Rate	Error	Theoretical Mass Flow Ratio	Actual Mass Flow Ratio
P_g [bar]	$8\dot{m}_E$ [kg/s]	$8\dot{m}_E$ [kg/s]	%	$8\dot{m}_E / \dot{m}_J$	$8\dot{m}_E / \dot{m}_J$
0.3	3.8×10^{-3}	3.1×10^{-3}	22%	0.9%	0.7%
0.6	5.3×10^{-3}	4.5×10^{-3}	17%	1.2%	1.0%
0.9	6.4×10^{-3}	5.8×10^{-3}	11%	1.5%	1.3%

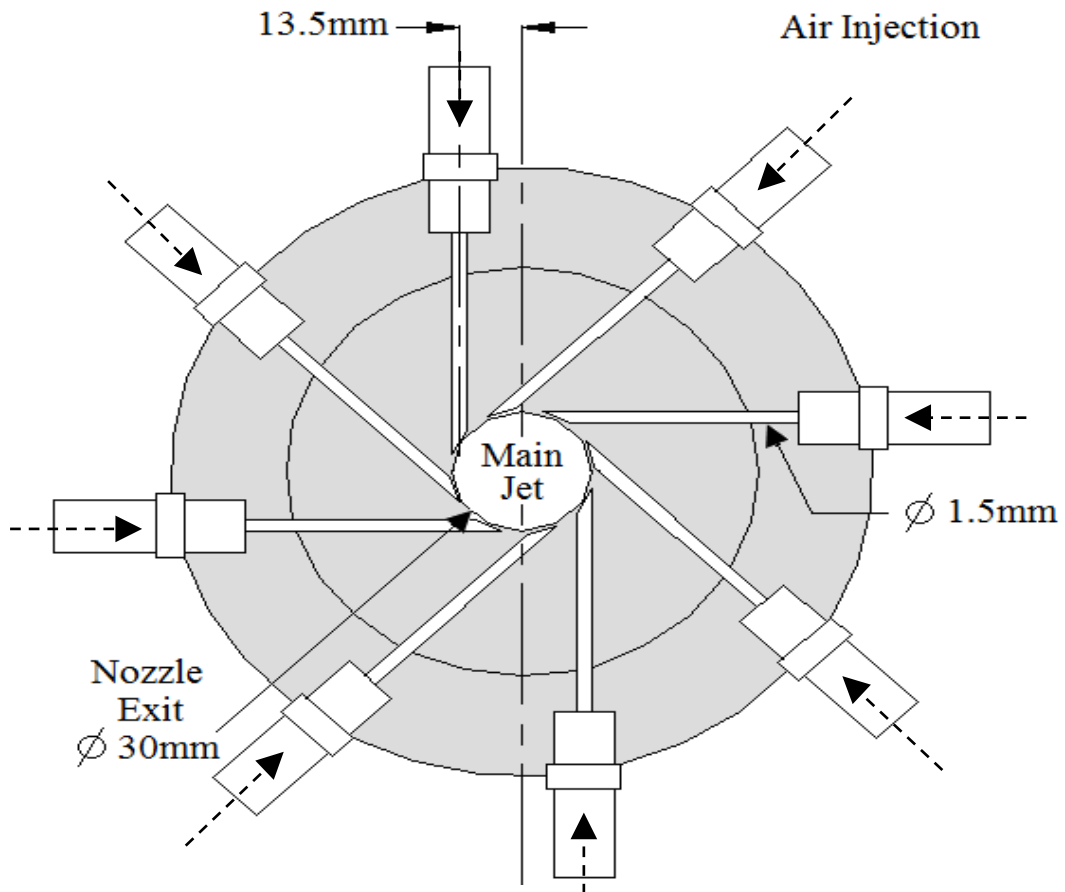


Figure 3.8: Schematic of the cross-section of the External Tangential Injection configuration.

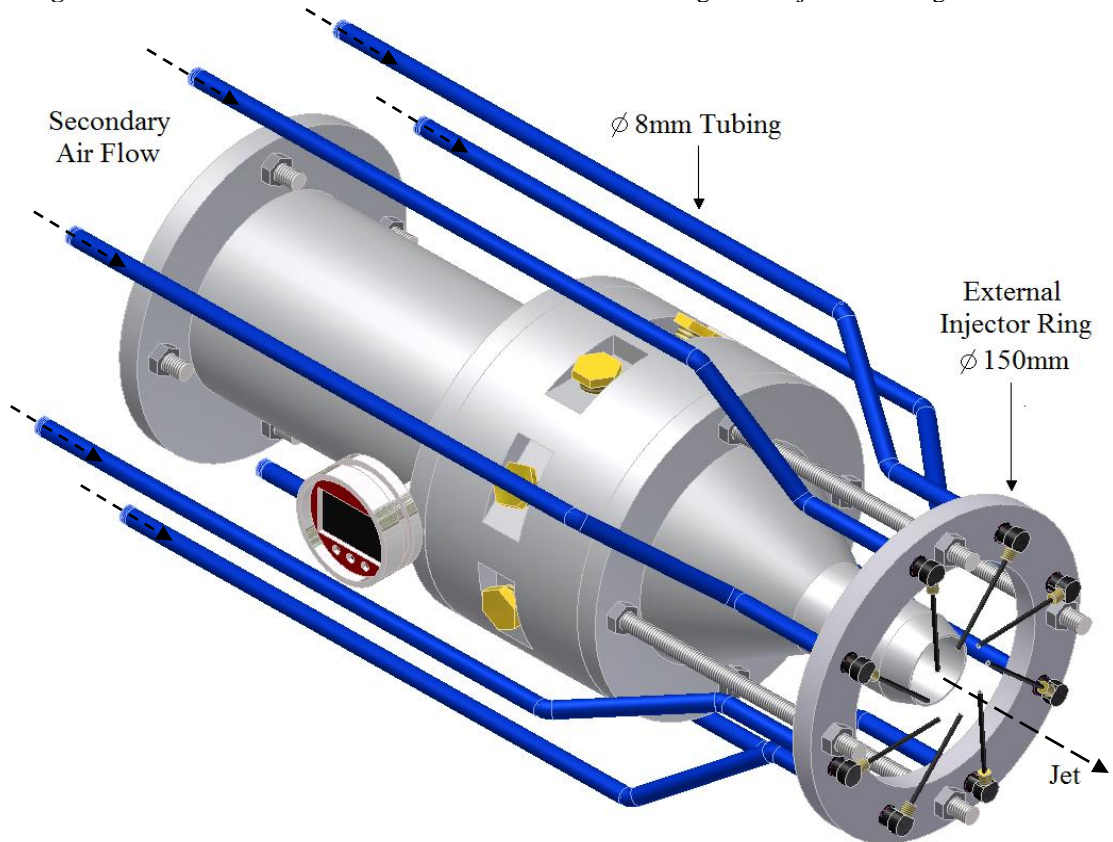


Figure 3.9: Illustration of the External Tangential Injection configuration. The supply reservoir and control system is identical to the internal tangential injection system.

3.4.3 Pulsating Tangential Injection (PTI)

The third tangential air injection technique uses an almost identical configuration to the external tangential injectors. However, the distinct difference is in the pulsating nature of the jets as opposed to the continuous steady injection used in the previous two techniques. Air is supplied and controlled from the same secondary reservoir and valve used in both the internal and external steady injection configurations. The pulsating effect is created by 120, 3mm diameter, holes on a 120mm radius aluminium disc rotated by a pneumatic drill, as shown in Figure 3.10. The holes were equally spaced by 6mm from centre to centre. A bearing manufactured from non-stick PTFE (Teflon) material was positioned such that air from the reservoir pipeline is able to pass through it to the manifold every time a hole on the disc is aligned to the single 3mm hole on the PTFE. The rate of pulsation is controlled by altering the rotary speed on the pneumatic drill which is rated at 1100rpm at a supply pressure of 6.5bar. Air to the pneumatic drill is also bled off the secondary reservoir pipeline using a T-section and monitored by a pressure gauge and a valve. A supply gauge pressure of 6bar to the pneumatic drill revolves the disc at 1000rpm yielding a 2kHz pulsating flow at the injectors, which operated in phase.

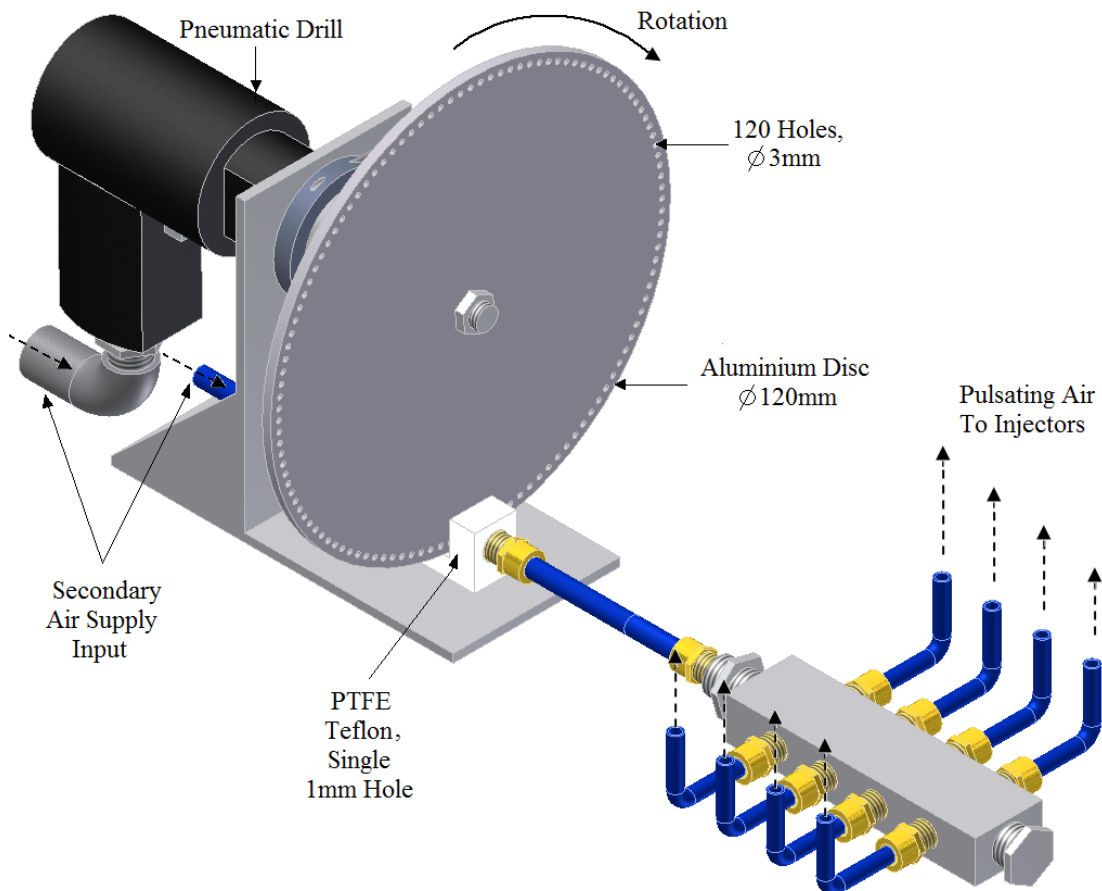


Figure 3.10: CAD assembly drawing of the siren design used to produce 2kHz pulsating flows

A digital tachometer was used to validate and calibrate the drill's rotary speed to its supply pressure with the corresponding parameters displayed in Table 3.6. The use of a rotormeter to measure the mass flow rate from the injectors would result in an inaccurate reading due to the pulsating nature of the injector fluid. Hence, by simply measuring the time taken for one of the injectors to fill a finite volume, the total mass flow rate could be measured and related to the supply pressure. The corresponding injection mass flow ratios for the pulsating injection technique were found to be of the order of those recorded for the external steady injectors and are presented in Table 3.7.

Table 3.6: Measured Pneumatic Drill Rotary Speeds with Respect to Supply Pressure

Supply Gauge Pressure	Rotary Speed	Pulsating Injection Frequency
P_g [bar]	V_r [rpm]	P_f [Hz]
1.8	500	1000
3.1	750	1500
6.0	1000	2000

Table 3.7: Measured Pulsating Injection Flow Parameters

Supply Gauge Pressure	Actual Mass Flow Rate	Actual Mass Flow Ratio
P_g [bar]	$8\dot{m}_E$ [kg/s]	$8\dot{m}_E/\dot{m}_J$
3	2.1×10^{-3}	0.5%
5	3.2×10^{-3}	0.7%
6	3.8×10^{-3}	0.9%

Considerably higher supply pressures are required to achieve pulsating mass flow ratios similar to those in steady external injection. This can be explained by a large pressure drop due to air leaks at the PTFE-to-aluminium interaction plane. A design with high quality air-tight bearings could certainly reduce the required supply pressure to the levels achieved in Table 3.5. Choutapalli (2009) used a motor powered, belt driven chopper disc to simulate a subsonic pulse jet through a 50mm diameter nozzle. In order to minimise the air leak between the rotating disk and the end cap of the stagnation chamber, a Teflon (PTFE) seal was attached to the rotating disk, however this improved seal design came at the expense of low pulsating jet frequencies of 250Hz. For the present study, one of the aims is to excite the jet through pulse jets at frequencies similar to the Kelvin Helmholtz roll-up structures ($\sim 2\text{kHz}$), also known as the preferred modes of the jet (Tam, 1995 and Panda, 2005). In order to reach such high pulsating frequencies a compromise had to be made in the quality of the slip surface bearing.

3.5 Acoustic Instrumentation and Data Acquisition

Microphones are designed, like the human ear, to transform pressure oscillations into electrical signals. A condenser microphone operates on basic transduction principles, whereby “*the incident sound pressure is translated into capacitance variations, which is then converted to an electrical voltage*” (Kinsler, 2000). A stretched, thin diaphragm is positioned at a small distance away from a stationary metal back plate which acts as a capacitor once voltage is applied. Oscillating pressure waves incident at the diaphragm cause it to vibrate hence changing the gap between it and the back plate. This results in an oscillating voltage from the capacitor, proportional to the original pressure oscillation.

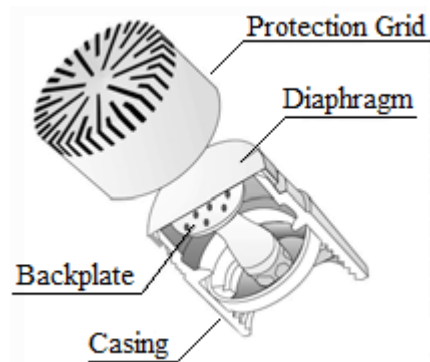


Figure 3.11: Components of a condenser microphone, the like of which was used in the present study. The diagram was adapted from PCB Piezotronics, Microphone handbook (2009).

Ten G.R.A.S (2003) type 40BF microphones were used to investigate the acoustic near and far-field of the jet. The 1/4 inch free-field condenser microphones were excited by the type 26AC pre-amplifiers and externally polarised to 200V by the type 12AN power modules. Condenser microphones are commonly used in free-field applications where there is a single noise source in an environment with minimised sound reflections (G.R.A.S, 2003). Their accuracy, especially at higher frequencies, is improved when their diaphragms are pointed directly (0° incidence) to the noise source, which in our case is the jet nozzle (Viswanathan, 2006). The microphone’s delicate diaphragm has a 6mm diameter and is encased by a protection grid that increases the microphone diameter to 7mm. In the acoustic field, higher frequency noise is associated with shorter wavelengths and when these are similar in size to the dimensions of the microphone head, it may cause an increase in the incident sound pressure due to diffraction effects (Kinsler, 2000). However, this is accounted for in the design of the microphone’s protection grid (G.R.A.S, 2003) and the resulting frequency response corrections. The 1/4 inch free-field microphones essentially measure sound pressure at the diaphragm as it would appear if the microphone were not present in the acoustic field. The microphones have a flat

frequency response up to 70kHz, with a tolerance of ± 2.0 dB and a dynamic range of 40dB to 174dB based on a reference pressure of 20 μ Pa. The operating temperature range is -40 °C to 150 °C. The calibration constant for each rear-vented microphone was derived from their sensitivities, s_m , which ranged from 3.45 to 3.67mV/Pa and were used as input data to compute the acoustic power spectra.

Microphone mounting is a critical component of the array design. Sound reflections from the horizontal support beam and individual holding clamps can noticeably contaminate the data, and affect the quality of acoustic spectra by altering its shape and smoothness (Petitjean, 2003). Perspex tubing with 8mm internal diameter was used to mount and extend the microphones away from the metal clamps fixtures at the array for the purpose of reducing sound reflections in and around microphones. All flat and non-porous surfaces were wrapped with foam for the absorption of high frequency sound pressure waves.

Data was acquired using a National Instruments NI-PXI-1033 multi-channel digital data acquisition system and controlled by a computer equipped with Labview 8.2 software. Two NI-PXI-6143, 16-bit, A/D acquisition boards were used with each comprising of 8 analogue input channels capable of acquiring 250k samples/s. Standard coaxial cables, which can be driven long distances without signal degradation, were used alongside BNC connectors throughout the setup. For the far-field tests, acoustic signals were sampled at 140kHz over 3 runs of 5 seconds, resulting in 2.1 million samples from each of the 10 channels, which were used for signal processing and spectral analysis in MATLAB.

Since the National Instruments data acquisition system does not have filtering characteristics, hardware filters were manufactured in-house to independently filter each microphone's signal across a band pass of 200Hz-70kHz before reaching the multi-channel acquisition boards. The lower filter limit was selected to coincide with the cut-off frequency of the foam wedges in the anechoic chamber. A software filter was specifically implemented to eliminate a discrete resonating internal electrical noise peak at 50Hz in the acoustic spectra. The fact that it was not eliminated by the hardware filters suggests that it originates from the computer or acquisition process itself. A Butterworth filter function was used in MATLAB to create a digital band pass between 200Hz-70kHz as before. Whilst computing the spectra, Fourier transforms were averaged over 2460 groups of 1024 data points. Based on the Nyquist frequency of 70kHz, the temporal resolution is 68Hz thus resulting in a narrowband spectra with 1024 points equally spaced over a frequency range of 200Hz-70kHz.

3.6 Near and Far-Field Microphone Arrays

The acoustic near-field of the jet, up to 30 nozzle diameters from the nozzle exit, is characterised by the non-linear and non-spherical propagation of hydrodynamic noise components (Petitjean, 2003). At such close range the non-compact nature of the noise sources eliminates the need to point the microphones at the nozzle exit. Figure 3.12 illustrates the near-fielded acoustic array, consisting of 10 equally spaced free-field condenser microphones (described later). A high precision electronically controlled traverse is used to axially traverse the array in increments of 7.5mm horizontally and 15mm vertically, which correspond to a $\frac{1}{4}$ and $\frac{1}{2}$ of the nozzle diameter respectively. Overall 780 data points are achieved by traversing the microphones axially from $-2 < x/D < 13$ and vertically from $6 < y/D < 12$.

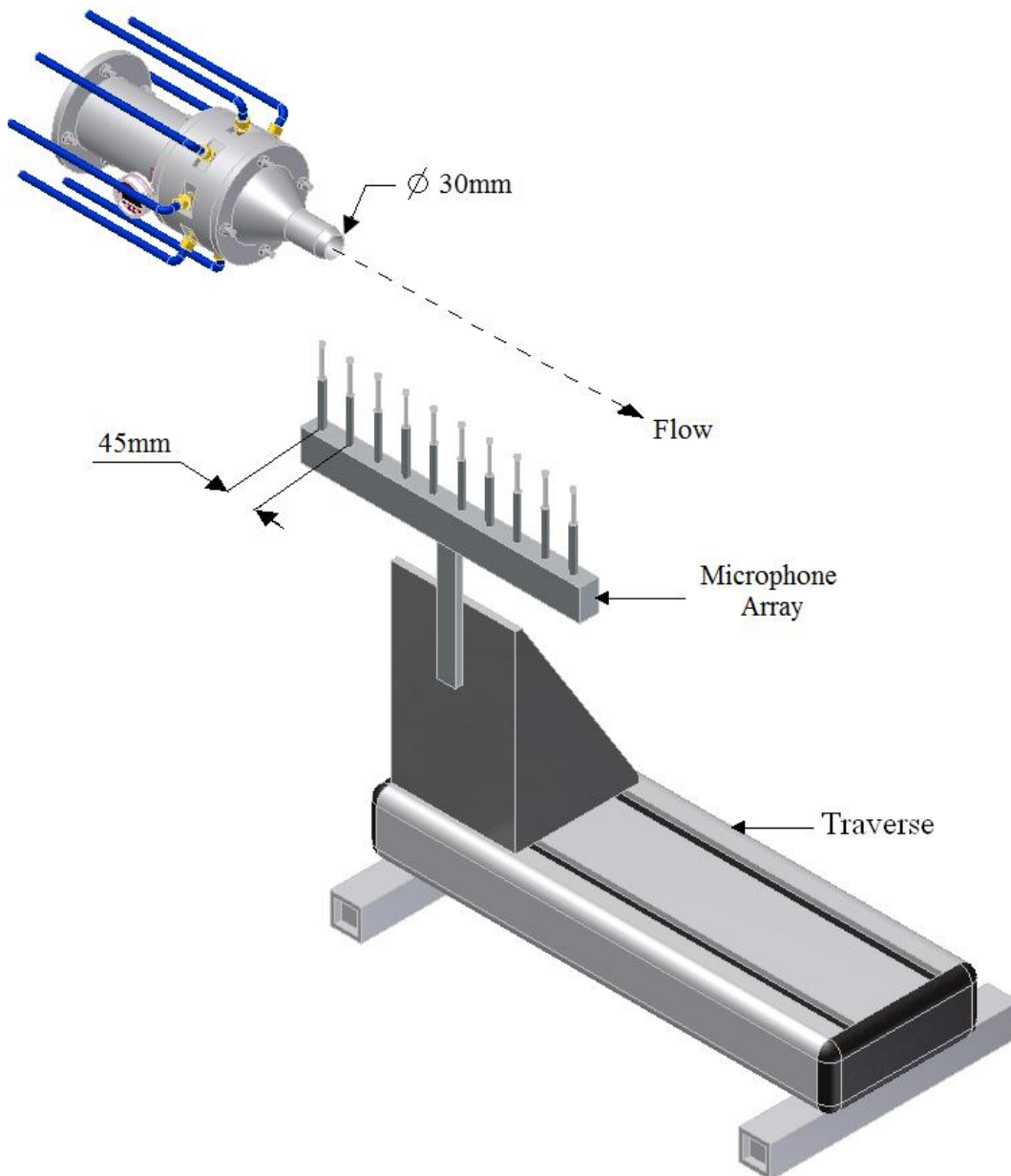


Figure 3.12: CAD assembly drawing of the near-field microphone array covering x-axis locations between $-2 < x/D < 13$ and y-axis between $6 < y/D < 12$ from the nozzle exit.

The region beyond $r/D=30$ from the nozzle is referred to as the acoustic far-field (Petitjean, 2003), where the propagation of sound waves is spherical and the noise intensity proportional to the inverse square of the radial distance from the source. Viswanathan (2006) showed that the accuracy in measuring the acoustic field is improved, especially at higher frequencies, by pointing the pressure transducers towards the noise source. Figure 3.13 illustrates the far-field axial array with 10 microphones positioned along a single plane at observer angles ranging from 90° to 15° relative to the downstream jet axis. Their distance from the jet exit ranges from 40 to 80 nozzle diameters ensuring that measurements are made in the acoustic far-field. A distance calibration was performed that effectively places the microphones on a radial array of radius $r/D=40$ from the nozzle exit, very similar to the physical far-field configuration used by Castelain (2008). This process will be described later in § 3.7.5.

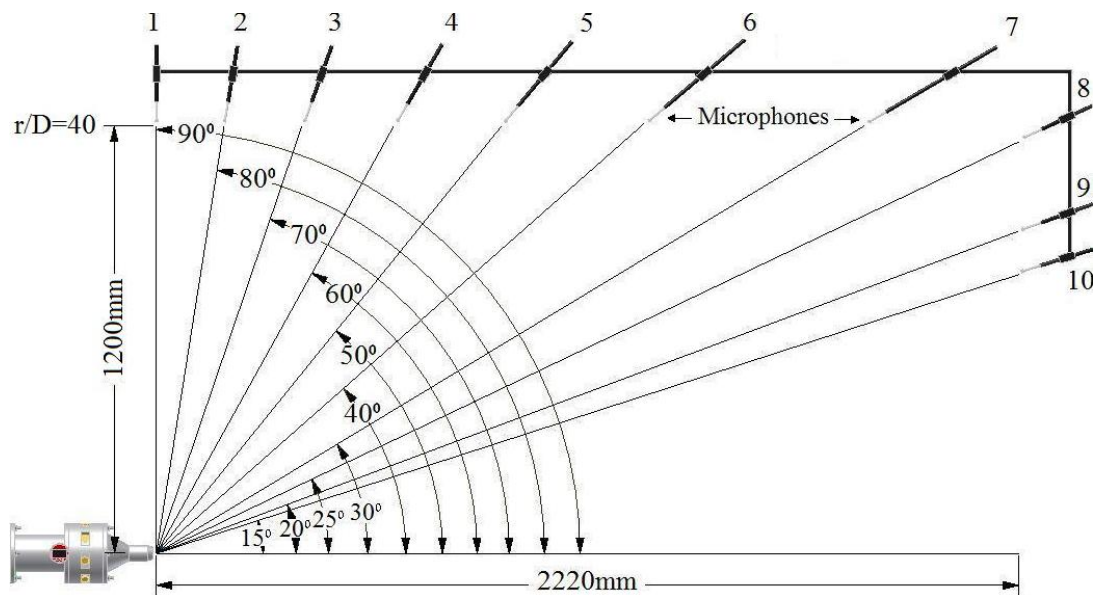


Figure 3.13: The far-field acoustic array, parallel to the streamwise jet axis. The microphone observer angles ranged from 90° - 15° , whilst all pointing towards the expected primary noise source, the nozzle.

The acoustic instrumentation was selected in the light of the frequency bandwidth and sound pressure level range established in previous experiments on supersonic jet noise. Krothapalli (2000) showed that a Mach 1.58 jet exhibits noise levels of up to 133dB at an observer angle of 45° to downstream jet axis. Tam's (2008) far-field measurements ($r/D=100$) of a Mach 1.5 jet also showed low frequency (1.5kHz) dynamic peaks of 135dB at 30° . Raman (1999) gave evidence of similar sound pressure levels for discrete screech tones beyond 10kHz in addition to Zaman (2010), who recorded broadband shock associated noise at frequencies beyond 10kHz for a Mach 1.2 jet. All these measurements are within the limitations of the acoustic signal measurement system.

3.7 Signal Processing & Spectral Analysis

3.7.1 Fast Fourier Transform (FFT)

The Fast Fourier Transform (FFT) is an efficient method of computing the Discrete Fourier Transform (DFT) and is an established tool for identifying the frequency components that make up a continuous waveform (Press et al., 1992). One of the main applications of the Fast Fourier Transform is to represent raw time-domain data in the frequency domain for analysing the spectral energy contained in data sampled at evenly-spaced time intervals. The FFT of the microphone's pressure signal returns a complex vector of real and imaginary parts and can be multiplied by the complex conjugate of its FFT to return the acoustic power spectrum with units Pa^2 . An FFT function was used in MATLAB 7.0 (Cooley & Tukey, 1965) to calculate the Fast Fourier Transform of a given pressure signal, p_1 , with an FFT of length N ;

$$F(p_1) = FFT(p_1, N) \quad (3.15)$$

An FFT of length 1024 was found to give a sufficient temporal resolution and smoother spectra as compared to 512 points. The acoustic power, A_p , which is effectively an autocorrelation of the pressure signal, can be expressed as;

$$A_p [Pa^2] = FFT(p_1) \times FFT^*(p_1) \quad (3.16)$$

$$(p_1)^* = conj(p_1) = real(p_1) - i \times imag(p_1) \quad (3.17)$$

3.7.2 Sound Pressure Level (SPL)

Sound pressure can be defined as the measure of the local pressure deviation from an equilibrium pressure as a result of a sound wave. It is generally measured using a microphone and has an SI unit of Pascal (Pa). The instantaneous sound pressure is the variation from local equilibrium as a result of a sound wave at a given instant in time, whereas the effective sound pressure, P_{rms} , is the root mean square (rms) of this instantaneous pressure over a given interval of time (Kinsler, 2000). The Sound Pressure Level (SPL) can be defined using logarithmic scales, since it suitably compresses the large range of numbers that are required to describe the wide range of intensities present in the environment. It is a measure of the effective sound pressure of a sound with respect to a reference pressure and is measured in decibels (dB) (Kinsler, 2000). This is consistent with the fact that humans judge the relative loudness of two sounds by their

intensities. To obtain the instantaneous sound pressure level, we can use the equation below, where P is an instantaneous pressure;

$$SPL(dB) = 20 \log_{10} \left(\frac{P}{P_{ref}} \right) \quad (3.18)$$

For sound measurements in air the reference pressure, P_{ref} , is equal to $20\mu\text{Pa}$. With this equation it can be deduced that for a sound pressure wave of 1Pa the SPL would correspond to 94dB . In order to calculate the Overall Sound Pressure Level (OASPL) over a period of time; equation (3.18), the instantaneous pressure, P , can be replaced with the root mean square of the pressure signal, P_{rms} , as shown in equation (3.20);

$$OASPL(dB) = 20 \log_{10} \left(\frac{P_{rms}}{P_{ref}} \right) \quad (3.19)$$

$$P_{rms} = \sqrt{\frac{\sum_1^N (P_n)^2}{N}} \quad (3.20)$$

However, to plot the SPL spectra, equation (3.18) can be modified by introducing the acoustic power signal, A_p , in Pa^2 ;

$$SPL(dB) = 10 \log_{10} \left(\frac{A_p}{P_{ref}^2} \right) \quad (3.21)$$

3.7.3 Strouhal Number

The Strouhal Number, which is a measure of the frequency of oscillation, can be defined as a ratio of the oscillation frequency to mean velocity (White, 2003);

$$St = \frac{f D_J}{V_J} \quad (3.22)$$

Where f , D_J and V_J represent the frequency [Hz], nozzle diameter and jet velocity respectively. Acoustic spectra are often plotted against the non-dimensional Strouhal number in place of frequency; this allows for comparison of results with those obtained from experiments with different nozzle diameters and jet velocities.

3.7.4 Amplitude Calibration

The microphones return a voltage signal in the time domain, coupled with the data acquisition and Labview 8.2 software. In order to convert to a pressure signal, the voltage signal is simply multiplied through by the respective microphone's unique calibration constant, C_m , which is derived from the manufacturer's laboratory tested sensitivity, s_m , of units Volts per Pascal;

$$C_m \left[\frac{Pa}{V} \right] = \frac{1}{s_m} \quad (3.23)$$

However, for validation purposes the calibration constant can be calculated by re-arranging the SPL equation with a substitution for P_{rms} :

$$SPL = 20 \log_{10} \left(\frac{C_m V_{rms}}{P_{ref}} \right) \quad (3.24)$$

This can be further re-arranged to make the microphone calibration constant the subject, which has units of [Pa/V]:

$$C_m = 10^{\left(\frac{SPL}{20}\right)} \times \left(\frac{P_{ref}}{V_{rms}} \right) \quad (3.25)$$

Hence, in order to find C_m , a standard laboratory amplitude calibrator can be used to generate a 1kHz tone at a sound pressure level of 94dB. The measured voltage signal from the microphone can then be used to derive the V_{rms} and hence find the only unknown parameter in equation (3.25).

3.7.5 Distance Calibration

The physical configuration of the axial microphone array results in all ten free-field microphone being positioned at a range of distances from the jet exit. The nozzle is selected as the origin since it is expected to be the primary noise source location. The microphones placed at a larger distance will record sound pressure levels that are reduced considerably compared with those closer to the source. In the light of this, a distance calibration factor can be used to compensate for this difference such that all microphones are effectively positioned at the same distance from the source in a radial arc of radius, $r=y_j$, as shown in Figure 3.14. Given the dimensions of the acoustic chamber, a radial array would have limited all ten microphones to a radial distance of $40D_j$, with the possibility of distorting the sound field. The axial array ensures that the microphones are

comfortably in the far-field (up to $r/D=80$), whilst creating space for other experimental equipment such as the PIV system for flow-field measurements.

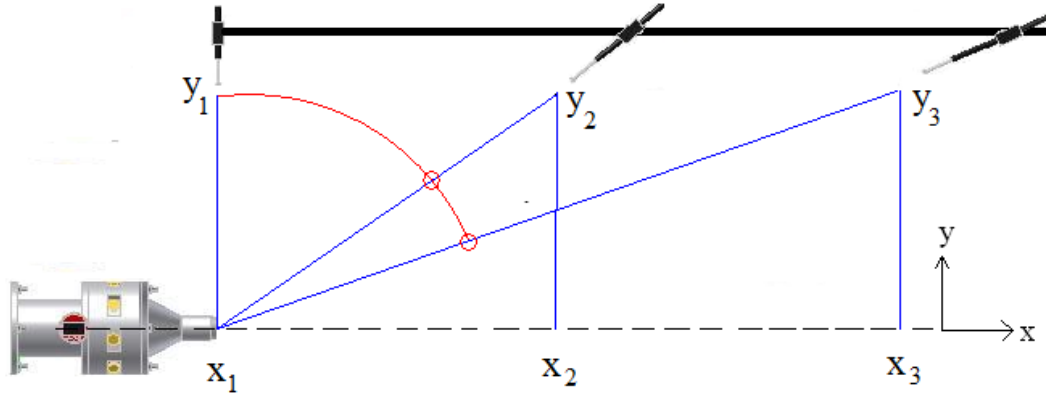


Figure 3.14: Diagram showing how the physical position of the microphones can be simulated as effectively being placed on a radial arc using the distance calibration factor. (Drawing not to scale)

The distance calibration factor, C_D , for each microphone is calculated with respect to its co-ordinates from the origin as shown in equation (3.26) and is displayed in Table 3.8.

$$C_D(i) = \frac{\sqrt{x_i^2 + y_i^2}}{y_1} \quad (3.26)$$

Table 3.8: Distance Calibration Factors with Respect to Noise Source Origin at the Nozzle

Microphone	M1	M2	M3	M4	M5	M6	M7	M8	M9	M10
α°	90	80	70	60	50	40	30	25	20	15
C_D	1.00	1.01	1.06	1.16	1.31	1.55	2.00	2.29	2.21	2.14
$20\log(C_D)$ [dB]	0	0.1	0.5	1.3	2.3	3.8	6	7.2	6.9	6.6

The corrected OASPL that accounts for the microphone's distance from the source is then given by equation (3.27). It must be emphasised that this process assumes the acoustic waves to propagate as spherical waves at a constant speed of sound, all the way from the source, with the noise intensity decaying proportional to the inverse square of the radial distance (Petijean, 2003).

$$OASPL(dB) = 20\log_{10}\left(\frac{P_{rms}}{P_{ref}}\right) + 20\log_{10}(C_D) \quad (3.27)$$

This approach can be used for investigating turbulent mixing noise in addition to Mach wave radiation noise, both of which have been shown to originate from the shear layer region through Schlieren photography (Krothopalli, 2000). However, Mach waves have been shown to have non-compact sources since their wavelengths are of the same length

scale as the source (Tam, 2009). Thus, sound may propagate as planar waves as opposed to spherical waves for a considerable distance, as illustrated in Figure 2.1. For the Mach 1.3 jet, the speed of the convective eddies is no greater than 70% of the jet speed (Bishop et al., 1971). Hence, without a supersonic noise source the possibility of the existence of Mach wave radiation is low (Hileman et al., 2001). Turbulent mixing noise sources of cold laboratory jets have also been shown to be non-compact in the near-field region of 15D to 30D from the nozzle exit, in which sound does not spread spherically (Petitjean et al., 2003). In the light of this, assuming a single compact source is fair, but not entirely correct. Although high frequency noise originates due to instabilities in the shear layer region close to the nozzle exit, the lower frequency noise originates from further downstream. Panda (2002) claimed that downstream radiating (20° - 30°) large-scale eddies; originate from the shear noise source mechanism in the transition region of 5 to 10 diameters away from the nozzle exit. Raman (1999) estimated that discrete screech tones originate from around the third to fourth shock cells, about 4 nozzle diameters along the potential core. Based on this evidence, the devised distance calibration will not be entirely correct for the purpose of investigating shock associated noise and subsonically generated noise that originates further downstream along the potential core. As a result the distance calibration factors for all microphones can be recalculated with the origin being set towards the end of the potential core ($x/D=5$). The angles of the microphones to the new noise source origin have been recalculated, as shown in Table 3.9.

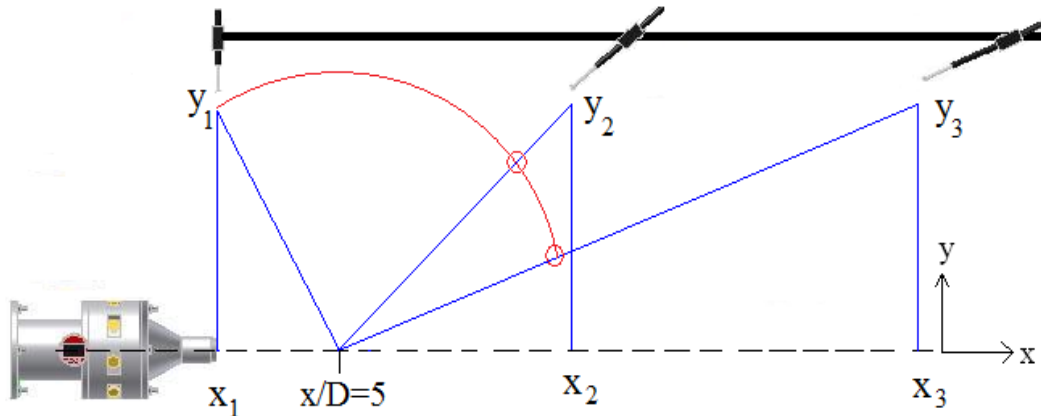


Figure 3.15: Effective positions of the microphone (red circles) using the distance calibration with the new noise source origin 5 nozzle diameters along the potential core. (Drawing not to scale)

Table 3.9: Distance Calibration Factors with Respect to Noise Source Origin at $x/D=5$

Microphone	M1	M2	M3	M4	M5	M6	M7	M8	M9	M10
α°	98	88	77	66	55	44	33	26	21	16
C_D	1.01	1.00	1.02	1.10	1.22	1.45	1.88	2.16	2.07	2.01
$20\log(C_D)$ [dB]	0.1	0.0	0.2	0.8	1.7	3.2	5.5	6.7	6.3	6.1

3.7.6 Autocorrelation

The autocorrelation function is the cross-correlation of a signal with itself and describes the degree of similarity of a value in the process at different points in time. It can also be described as a Fourier transform of the noise spectrum and is often used as a tool in spectral analysis to determine the time scale of coherence of the sound field (Tam, 2008).

$$R_{AC_{xx}}(\tau) = \frac{\sum_{i=1}^N (x_i - \bar{x})(x_{i+\tau} - \bar{x})}{\sum_{i=1}^N (x_i - \bar{x})^2} \quad (3.28)$$

Given that acoustic pressure waves propagate at the speed of sound, a , the resultant time lag for peak negative auto-correlation, τ_{max} , can be used to find the spatial correlation length, L_C (Tam, 2009). This equation will be used in § 4.2.

$$L_C[m] = a(2\tau_{max}) \quad (3.29)$$

3.7.7 Cross-Correlation & Time Lag

The normalised cross-correlation function is a non-dimensional parameter and can give information as to the best alignment or degree of similarity of two signals with respect to a set time lag, τ , between them (Tam, 2009).

$$R_{CC_{xy}}(\tau) = \frac{\sum_{i=1}^N (x_i - \bar{x})(y_{i+\tau} - \bar{y})}{\sqrt{\sum_{i=1}^N (x_i - \bar{x})^2} \sqrt{\sum_{i=1}^N (y_i - \bar{y})^2}} \quad (3.30)$$

The difference in the propagating distance between the two microphone signals is the reason for which a time lag is determined. The time lag, for which the cross-correlation between two pressure signals attains the highest positive value, indicates the overall time lag of the signals.

The normalised cross-correlation function can be used to find the time lag for which the signals are most aligned, as explained previously. However, in order to obtain the time lag of the signals with respect to the certain frequencies of the noise spectrum a

more detailed approach is required. In order to determine the phase lag between the signals, θ , of unit radians, the ‘*atan2*’ function can be used in MATLAB 7.0, which returns the four-quadrant inverse tangent (arctangent) of real parts of the two input variables (Press et al., 1992).

$$\theta[\text{rad}] = a \tan 2(\text{imag}(A_{P(1,2)}), \text{real}(A_{P(1,2)})) \quad (3.31)$$

The cross-power spectrum, $A_{P(1,2)}$, is the multiplication of the FFT of the first pressure signal by the complex conjugate of the FFT of the second.

$$A_{P1,2} [Pa^2] = FFT(p_1) \times FFT^*(p_2) \quad (3.32)$$

The frequency vector can be converted into angular frequency;

$$\omega \left[\frac{\text{rad}}{\text{s}} \right] = 2\pi f \quad (3.33)$$

Hence the experimental time lag, τ_{exp} , is the phase lag divided by the angular frequency;

$$\tau_{exp} [s] = \frac{\theta}{\omega} \quad (3.34)$$

In order to calculate the theoretical time lag between adjacent microphone signals, the exact co-ordinates of each microphone with respect to the noise source origin must be defined. The distance of the microphone tip from the origin can be derived using simple trigonometry:

$$C_1 [m] = \sqrt{x_1^2 + y_1^2} \quad (3.35)$$

Using the speed of sound we can deduce the time it takes for a pressure wave to reach the microphone from the point of origin:

$$t_1 \left[\frac{m}{s} \right] = \frac{C_1}{a} \quad (3.36)$$

The theoretical time lag, τ_{the} , is then the difference between the times it takes for a sound wave to reach the second and first microphones respectively.

$$\tau_{the}[s] = t_2 - t_1 \quad (3.37)$$

Using equations (3.35) to (3.37), a range of theoretical time lags can be derived for a corresponding range of theoretical noise source origins along the streamwise jet axis. Hence, through this trial and error approach, the approximate source of jet noise can be located by simply finding a match between the theoretical and experimental time lags. This process assumes the acoustic waves to propagate at a constant speed of sound, and will be used for noise source location in § 4.5.

3.8 Particle Image Velocimetry (PIV)

PIV is non-intrusive optical measurement technique, unlike traditional apparatus such as pitot tubes and hot wires that are placed directly in the flow stream. It is therefore suited to experimental applications such as supersonic jets involving shocks where the existence of probes would alter the flow pattern. It employs an indirect method for determining the flow velocity, by measuring the displacement of tracer particles within the flow from which the particle velocity is derived (Westerweel, 1993). The obvious advantage of using PIV is its unique feature that allows the observation of a large region of the flow field, unlike other methods, such as Laser Doppler Velocimetry (LDV), which measures the velocity at a specific point in the flow field. However, the advantage of a large spatial domain is coupled with a limited temporal resolution, the rate at which instantaneous images are captured, due to technological restrictions in digital image acquisition (Raffel, 1998). Instantaneous images of seeded flow can be used to derive information about spatial structures that exist in unsteady flows. However, flow characteristics such as velocity, vorticity, Reynolds stresses and turbulence are more accurately derived by time-averaging, hundreds of such instantaneous flow images. Modern cameras permit over 100 captures per minute, and the evaluation time for each image is of the order of a few seconds based on standard computers (Raffel, 1998).

3.8.1 Digital Imaging

Advances in electronic imaging systems have led to a widespread use of digital image cameras in place of the traditional photographic methods that involved chemical processes and slow development times. The solid state charge coupled device, also known as the CCD camera is an electronic device that converts light energy from photons into an electronic charge by the photoelectric effect in the semiconductor (Smits, 2000). The CCD element consists of micro-scale sub picture elements, called pixels, where this energy transfer occurs. The present study uses TSI's dual-camera PIV system equipped with two 12-bit CCD cameras with arrays of 2048×2048 pixels that were fitted with Nikon lenses of focal lengths of 50mm for 2D PIV and 105 mm for the 3D stereoscopic PIV measurements. The cameras were securely mounted on an extruded plate which itself was fixed to an axial traverse as illustrated in the CAD assembly drawing shown in Figure 3.16. This was done with the aim of investigating the local free-field conditions at various x/D locations along the axial jet direction. For the 2D configuration the camera resolution of 2048×2048 pixels equates to an image field of 205×205mm. Thus, a standard interrogation window of 64×64 pixels corresponds to a physical size of approximately 6mm×6mm. For the 3D stereoscopic setup the image field was of 50×50mm, equating the interrogation window to a physical size of 1.5mm×1.5mm.

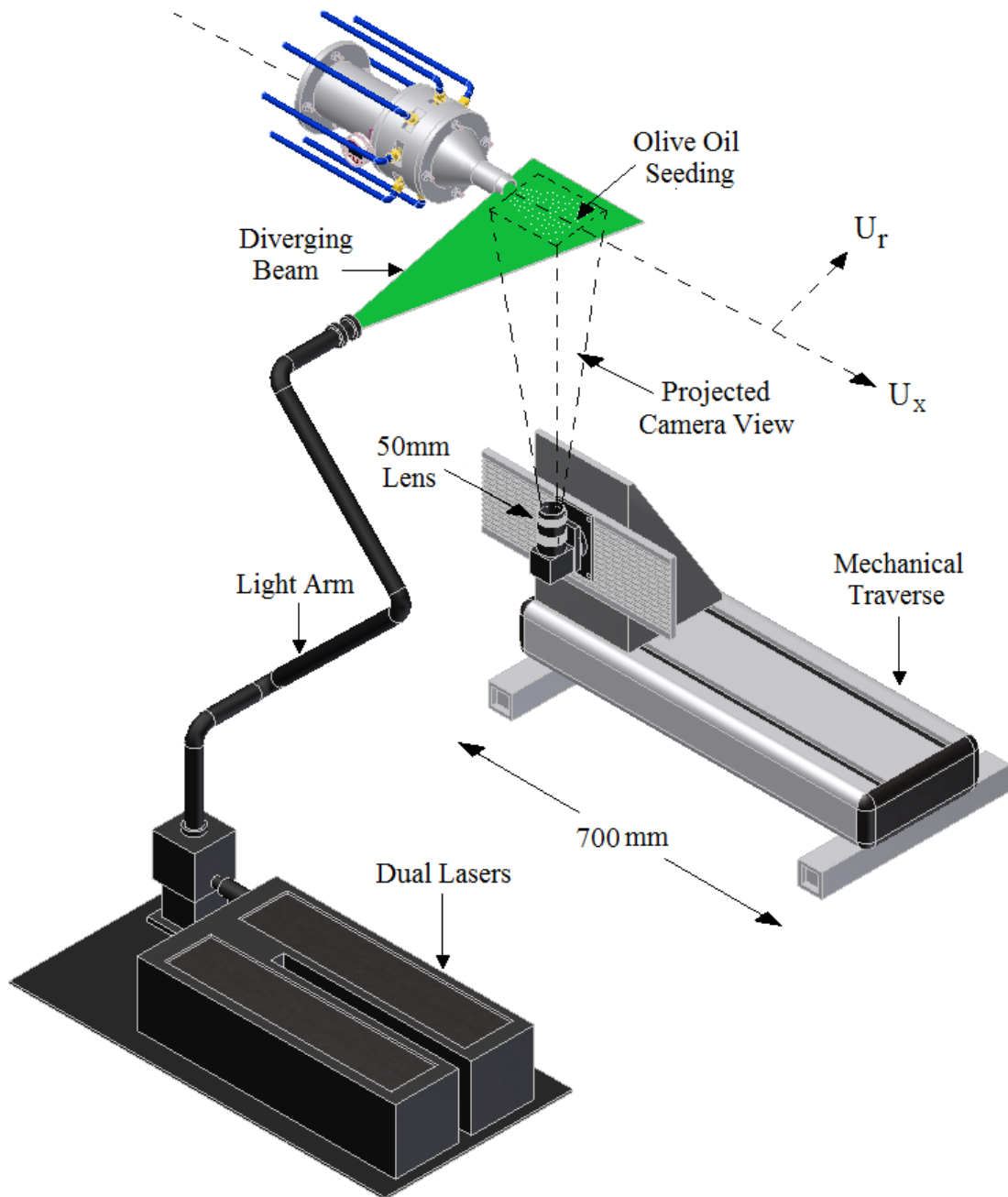


Figure 3.16: CAD assembly drawing of the 2D PIV experimental configuration, for 2-component velocity measurements of the axisymmetric plane of the jet.

3.8.2 Laser Light Source

The measurement plane was illuminated by a 190 mJ double pulse Nd:YAG laser (Neodym Nd^3 ions and yttrium-aluminium-garnet crystals), which produces monochromatic green light of wavelength 532nm. The laser and camera were synchronised using a PC running TSI's InSight 3G 9.0 software which acquires and processes double frame images. The software was capable of capturing double images in

straddle mode at a frequency of 7.25 Hz, which with respect to the flow speed of 380 m/s, provides a very low temporal resolution. For the 2D PIV configuration the 50mm lens were used to zoom into a square window measuring 205mm by 205mm, improving the spatial resolution at the expense of the overall domain size. The circular laser beam was manipulated using cylindrical collimating optics to produce a diverging light-sheet of about 2 mm in thickness. In order to prevent reflections from the aluminium nozzle, the light-sheet was trimmed at both ends beyond the field of view, whilst extra pieces of acoustic foam were utilised to cover any other reflective surfaces. This measure was also taken prevent subsequent damage through the over-exposure of the camera's CCD chip. At 70% power output the laser beam intensity was sufficient to illuminate the seeding particles for high contrast raw images without over-exposing the camera. The time delay between laser pulses was set in the range 0.5 μ s to 2 μ s, so that it was short enough to illuminate an instantaneous event that prevents particles escaping the plane of capture and long enough to determine the particle displacement between image pairs. During each 12 second capture phase, the PIV system captured 80 image pairs at a set frequency of 7.25 Hz. Hence, with multiple runs, a total of 240 instantaneous images were captured for processing.

3.8.3 Seeding Particles

Ideally, the seeding particles should follow the experimental fluid exactly without altering the flow regime and interacting amongst themselves (Westerweel, 1993). The degree to which the seeding particles follow the motion of the experimental fluid is called the velocity lag. Smaller particles are known to follow the flow better (Westerweel, 1994). The gravitational force acting on the seeding particles is a source of error in PIV measurements and is due to the mismatch between seeding particle and fluid densities. For a continuously accelerating fluid, the velocity lag, U_L , between the particle and fluid can be expressed as follows (Raffel, 1998):

$$U_L = U_p - U = d_p^2 \frac{(\rho_p - \rho)}{18\mu} a \quad (3.38)$$

Where U_p is the particle velocity, U the fluid velocity, with a , d_p , ρ_p , and μ being the constant gravitational acceleration (9.8 m/s²), particle diameter, particle density and dynamic viscosity of the fluid respectively. For olive oil particles with a diameter of 1 μ m, density 920 kg/m³ and a dynamic viscosity of the jet of 1.49 \times 10⁻⁵ kg/ms (based on the exit temperature of 219K), the particle velocity lag is approximately 7% of expected jet velocity. However, for high speed flows, such as a supersonic jet, the issue of particles

settling under the force of gravity is insignificant and hence the particle relaxation time, τ_s , to a step change in the fluid velocity is a more suitable measure of its ability to follow the flow (Raffel, 1998):

$$\tau_s = d_p^2 \frac{\rho_p}{18\mu} \quad (3.39)$$

Based on this expression the relaxation time for a 1 μm olive oil particle is 25 times smaller than that for a 5 μm particle, corresponding to values of 3.5 μs and 85 μs respectively. The timescale of PIV system can be obtained from the interrogation window length and local fluid velocity, l_{iw} / U_j . The timescale for the 2D PIV measurements, based on the physical interrogation window length of 6mm and peak jet velocity of 384m/s, is about 16 μs . For the 3D stereoscopic PIV configurations time scales are much smaller at 4 μs . Hence, a PIV laser pulse delay of 1.5 μs is sufficiently small to capture the flow changes, based on 1 μm olive oil relaxation times (3.5 μs) and PIV timescale (16 μs). At lower velocity regions, such as the shear layer, the local fluid velocity decreases with a consequent increase in the PIV timescale. Hence the particle velocity lag is not as crucial, as it will only be a fraction of the peak centreline velocity, given the overall range of velocities in the jet.

The exact location at which the seeding particles are introduced into the flow is critical, since their size and distribution may alter as they travel along the test chamber to the plane of illumination. Hence, it makes sense to determine the size and distribution of the seeding particles at the measurement plane and not before injection. In water measurements the seeding can be mixed into the flow prior to the tests, but in air flows it must be injected during measurements to prevent particles evaporating or settling before image capture. Olive oil droplets with a mean geometric diameter of approximately 0.5-5 μm were introduced into the flow just before the silencer, about 50 diameters upstream of the nozzle exit to allow sufficient mixing within the plenum chamber. The droplets were injected at gauge pressures between 2 to 3bar. For the purpose of injecting the seeding, a SCITEK LS-10 Remote Operation Liquid Droplet Seeder was used, which consists of 10 Laskin nozzle generators (SCITEK, 2006). Each Laskin nozzle operates near sonic conditions and has four 1mm holes that act as aerosols. The high shear region between the emerging air jets and seeding liquid atomises and entrains microscopic oil droplets into bubbles which release the seed on bursting at the free surface within the device (Raffel, 1998). A secondary phase of atomisation occurs when these bubbles collapse at escape from the liquid, yielding larger droplets, which are retained by an impactor plate at the top of the device. The smaller particles escape through the gap between the impactor plate and the side walls and reach the aerosol outlet. The

approximate seed output per jet is 10^8 particles per second. For gaseous experiments, health and safety issues, such as the experimentalists having to breathe the seeded air in open test configurations, must also be considered. When operated at its maximum production rate, the seeding device atomises the liquid at rates of approximately $1 \text{ mm}^3/\text{s}$ and so for a typical operation time of 100 seconds, the total volume of ejected seed is no more than 0.1 cm^3 . Therefore, this will not be a safety hazard since the exhaust funnel is designed to ventilate the flow away from the test chamber. Seeding was only included in the jet and not the surrounding entrained flow, which led to variations in seeding density. Homogeneous and steady seeding is necessary to avoid vector dropout, which is likely to increase the errors in the mean velocity. However, it was found that operating the jet for a short time led to an accumulation of particles in the chamber sufficient for PIV measurements outside the primary jet.

The quality and contrast of PIV images depends on the detection of the particles by the cameras and is directly related to the intensity of light being scattered off them. In gas flows, high powered lasers are required since only a fraction of that light intensity is reflected from the particles. Larger particles scatter more light but are not as capable of following the flow pattern as compared to smaller particles and hence a compromise is required (Melling, 1997). Therefore, choosing the correct type and size of seeding may be more economical than just increasing laser power. In liquid experiments, larger solid and liquid seeding particles are found to be able to follow the flow pattern better and so less powerful light sources can be utilised. For spherical seeding particles of olive oil, the peak light scattering angle is 180° with respect to the incident light with a fairly even radial scatter at all other angles (Raffel, 1998). Thus, it would be an advantage to capture images in forward scatter. However, this was not as easy to implement in stereoscopic PIV since having one camera in forward scatter would result in the other being in backward scatter thus giving a noticeably darker image. As a result, recording normal to the light-sheet is the more convenient arrangement. The intensity of light scattered by a $5 \mu\text{m}$ oil particle is several orders larger than that by a $1 \mu\text{m}$ particle (Melling, 1997), but once again a compromise must be met not to reduce the particle's ability to follow the flow. Since the laser light is not impeded by the particles, but actually distributed in all directions, particles are found to have an illuminating effect on neighbouring particles. The light scattering intensity of particles increases with the ratio of refractive indices between the particle and fluid and so justifies the use of oil in air. Figure 3.17 shows the field of view for the 2D PIV configuration through instantaneous flow images with indication of a homogeneous seeding density in and around the jet.

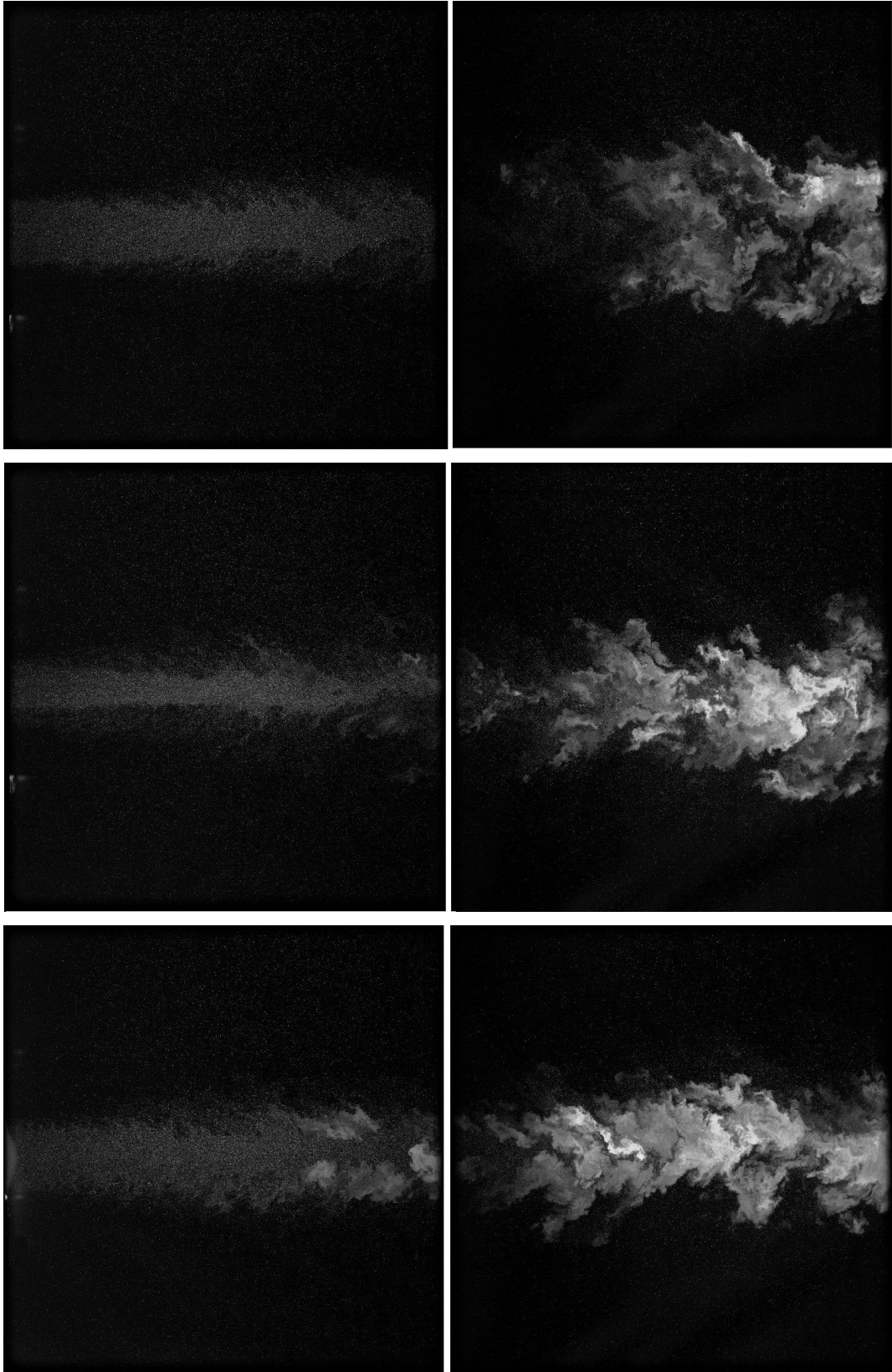


Figure 3.17: Instantaneous PIV images from 2D measurements. The images on the left correspond to a physical size of 205mm×205mm, covering the first 6.5 nozzle diameters of the axial jet from the nozzle exit, followed by the next 205mm ($6.5D_j - 13 D_j$) image of the jet on the right. Primary jet (top), internal injection at 40% IMFR (centre) and external injection at 1% IMFR (bottom).

3.8.4 Velocity Vector Processing

A statistical measure of the degree of similarity between a pair of images can be performed using the cross-correlation function, for which the correlation coefficient as a function of particle displacement is shown (Raffel, 1998):

$$C_c(dx, dy) = \sum_{x=0}^{x < M} \sum_{y=0}^{y < N} I_1(x, y) I_2(x + dx, y + dy) \quad (3.40)$$

Despite the simplicity of the approach it has deficiencies. Standard PIV evaluation images have resolutions of the order of a million pixels with displacement vectors ranging up to 20 pixels. To derive just a single correlation map using this two-dimensional technique would thus require a million calculations alone, a value that is proportional to the square of the sample size (Raffel et al., 1998). Considering that a single PIV image contains hundreds if not thousands of displacement vectors, a faster and more efficient way of calculating the cross-correlation is to produce the correlation map in the frequency domain and then transform it into the physical domain. This is done by utilising the correlation theorem, which states that the cross-correlation between two functions is equivalent to the Fourier transform of one function multiplied by the complex conjugate of the Fourier transform of the other (Press et al., 1992).

$$Corr(g, h) = FFT(g) \times FFT^*(h) \quad (3.41)$$

The correlation coefficient is then inverse-transformed to return to the cross-correlation map which has the same spatial dimensions, $N \times N$, as the input image pairs. This technique reduces the number of operations from N^4 to $N^2 \log_2 N$ and hence is up to fifty times faster in defining a correlation map than if performed in the physical domain (InSight 3G, 2008).

TSI's InSight3G 9.0 software was used to process the single exposure double frame PIV images. The processing grid engine breaks the input images up into smaller sizeable windows for the purpose of defining the vector field, either through a single or multi-pass cross-correlation algorithm. A multi-pass recursive Nyquist algorithm was selected as the grid engine with a first pass interrogation window size of 64×64 pixels. The refined second pass has an area of 32×32 pixels to allow for more accurate higher density flow measurements by reducing spurious vectors and increasing the spatial resolution (Fincham et al., 2000). The first processing pass computes the vector field using a 50% overlap between interrogation grids. The resultant vector field is then corrected based on the user defined pass validation settings. As mentioned earlier the time delay between laser pulses was set between 0.5-1.5us such that the displacement between

image pairs was no greater than 16 pixels, a quarter of the interrogation window (Raffel, 1998). The maximum allowable displacement of a particle between images was set to a third of the first pass interrogation window of 64x64pixels, so any vector displacement larger than 21 pixels is marked as void and is considered to be an outlier. The results of the first processing pass are used to optimize the particle displacements for the second processing pass. Interrogation windows of approximately 0.03 times the integral length of 30 mm, based on the nozzle diameter, are estimated to produce uncertainties in turbulence intensities of less than 2% (Høst-Madsen et al., 1995). The multi-pass cross-correlation technique coupled with an optimal seeding particle diameter of around 4 pixels has been shown to reduce the error in the individual interrogation window displacements by 7% (Westerweel et al., 1997). Using image deformation also increases the robustness and precision of vector evaluation by increasing the correlation peak between particle pairs by 10% (Fincham, 2000). It is accepted that the thickness of the shear layer near the nozzle exit in this study is of the order of the interrogation window size and that the velocity gradients in this region will be subject to a degree of spatial averaging (Luff et al., 2008).

The FFT correlator was selected as the correlation engine in order to compute the correlation function between image pairs. The highest correlation map pixel is assumed to be the particle image displacement peak caused by the contributions of many particle pairs, whereas other peaks are assumed to be noise peaks caused by the random pairings of images of different particles (InSight 3G, 2008). Correlation algorithms generate peaks with different sizes, shapes and slopes. The measurement accuracy may be improved by matching the peak algorithm to the correlation algorithm. A three-point Gaussian algorithm was selected as the peak engine to locate the correlation peak of the highest displacement pixel and its nearest neighbours with sub-pixel accuracy. The Gaussian peak was the recommended peak engine for use with FFT Correlation Engine (InSight 3G, 2008)

Systematic or bias errors are fixed errors in the measurement that remain throughout all image pairs, such as the misalignment of the light-sheet plane to the viewing plane or errors in perspective calibration. The errors relative to the actual displacement are expected to be largest in areas of lower velocity due to slower response time of particles in following the flow. Hence, the relative error in determining particle displacement between image pairs is most significant near the outer edge of the shear layers where the velocity approaches zero. For cross-correlation between singly exposed image pairs, Monte Carlo simulations were used to evaluate the measurement uncertainty with respect to particle size (Raffel, 1998). The root mean square random error was at an optimal low of 1% for particle image diameters of 3 pixels, based on an interrogation window size of 64x64 pixels. The error increases gradually to over 1.5% for image

diameters of 4 to 5 pixels, but increases much more sharply for those smaller than 3 pixels. When the particle image size becomes too small there is the introduction of peak locking, where the vector displacements are rounded to integer values and hence increases bias errors. The existence of peak locking can be easily detected by evaluation of histograms of vector displacement by the number of vectors, through multiple peaks, whereas a smooth single peaked histogram is what one should aim to achieve. Ensuring an average particle size of 4×4 pixels is a sufficient measure to avoid peak locking (Prasad et al., 1992). It is very difficult to avoid polydisperse flows and so for particles smaller than 1 pixel, the three-point Gaussian algorithm will result in narrow correlation peaks accurate to only a pixel and subject to peak locking. Whereas for much larger particles the correlation peak becomes too wide and hence makes the process of locating the zero gradient point less accurate (Prasad et al., 1992). Keane and Adrian (1991) showed that the vector evaluation process is most accurate when there are approximately 15-20 seeding particles per interrogation window for cross-correlation of the singly exposed image pairs. This condition was satisfied by regulation of the seeding density through varying the supply pressures between 2-3 bars. However, if there are too many particles their combined light scattering effect will illuminate those particles outside the plane of the light-sheet and hence augment the contribution of the out-of plane motion which should be limited to 25% (Keane, 1991).

3.8.5 Post-Processing Parameters

The vector evaluation process in modern PIV experiments is almost standardised, however, there exist visually inconsistent velocity vectors in the processed data field which can be validated and corrected using post-processing algorithms. The local median test is the most widely used local validation method which uses the vectors in the 3×3 pixel neighbourhood of each vector to calculate a reference value for validation (Westerweel, 1994). When the difference between the current vector and the reference vector's velocity magnitude is greater than the user-defined tolerance, which in this case was set to 2 pixel units, the vector in question is classified as invalid. Anomalous velocity vectors are most commonly located towards the edge of the illuminated field of view in drop-out areas with poor seeding density. They can also be characterised as singular sporadic events in an otherwise valid vector field. Once bad vectors have been highlighted a recursive filling method is used whereby the local mean of the 8 vectors in a 3×3 pixel neighbourhood is substituted as a replacement until all bad vectors are corrected. The 3G plot plug-in software from InSight was used in Tecplot 360 (2008) to calculate time averaged flow properties such as velocity, vorticity, Reynolds stresses and turbulence intensity based on 240 instantaneous vector fields.

3.8.6 Stereoscopic PIV

Despite all the advantages of the 2D PIV arrangement, the out-of-plane velocity component is lost in the measurements. One of the ways of recovering this third component is through introducing an additional camera with an angled viewing plane to the flow axis. This method is commonly known as stereoscopic PIV. The measurement precision of the third, out-of-plane component increases as the opening angle between the two cameras reaches 90° (Raffel, 2008). Hence for a symmetric setup, with both cameras on the same side of the light-sheet, the lens angle to the light-sheet plane should be close to 45° . For most lenses that are placed at an angle to the object plane there is a strong decrease in the modulation transfer function close to the edges of the field of view, which results in a distortion of the image plane (Raffel, 2008). In order to re-focus the edges of the image a Scheimpflug lens was placed between the lens and a slightly tilted CCD camera. This configuration is referred to as the angular lens displacement method with the Scheimpflug condition. For a lens angle of 45° to the light-sheet plane, it was difficult to focus onto the edges of the object plane even with the use of Scheimpflug lenses. Hence, a compromise was made and both lenses were placed at an angle of 30° . This is illustrated in the CAD assembly drawing of the experimental arrangement as shown in Figure 3.18.

In order to perform a perspective calibration between the viewing planes of both cameras, a 3D calibration plate was used which consisted of a central fiducial point surrounded by 1mm calibration spots equally spaced by 10mm on diagonal lines of alternating depths across the plate surface. Each of the two calibration grid images are cross-correlated in order to obtain the co-ordinates at which the spots superimpose. A resultant rectangular grid is then generated, which is the perspective calibration of the two viewing planes to the object plane. The advantage of the dual plane target is that it does not have to be traversed to multiple locations in order to gain a calibration. As described earlier, a 105mm focal length lens with aperture numbers between 4 and 8 was used to focus onto a 50×50 mm object field, thus equating each pixel to 24 μ m of physical space, resulting in an interrogation window that corresponds to a physical size of approximately 1.5mm. During each 6 second capture phase, the PIV system captured 40 stereoscopic image pairs at a set frequency of 7.25 Hz. With five such runs, a total of 200 instantaneous images were captured for processing. The processing and post-processing methods for the stereoscopic measurements were identical to those described for 2D PIV.

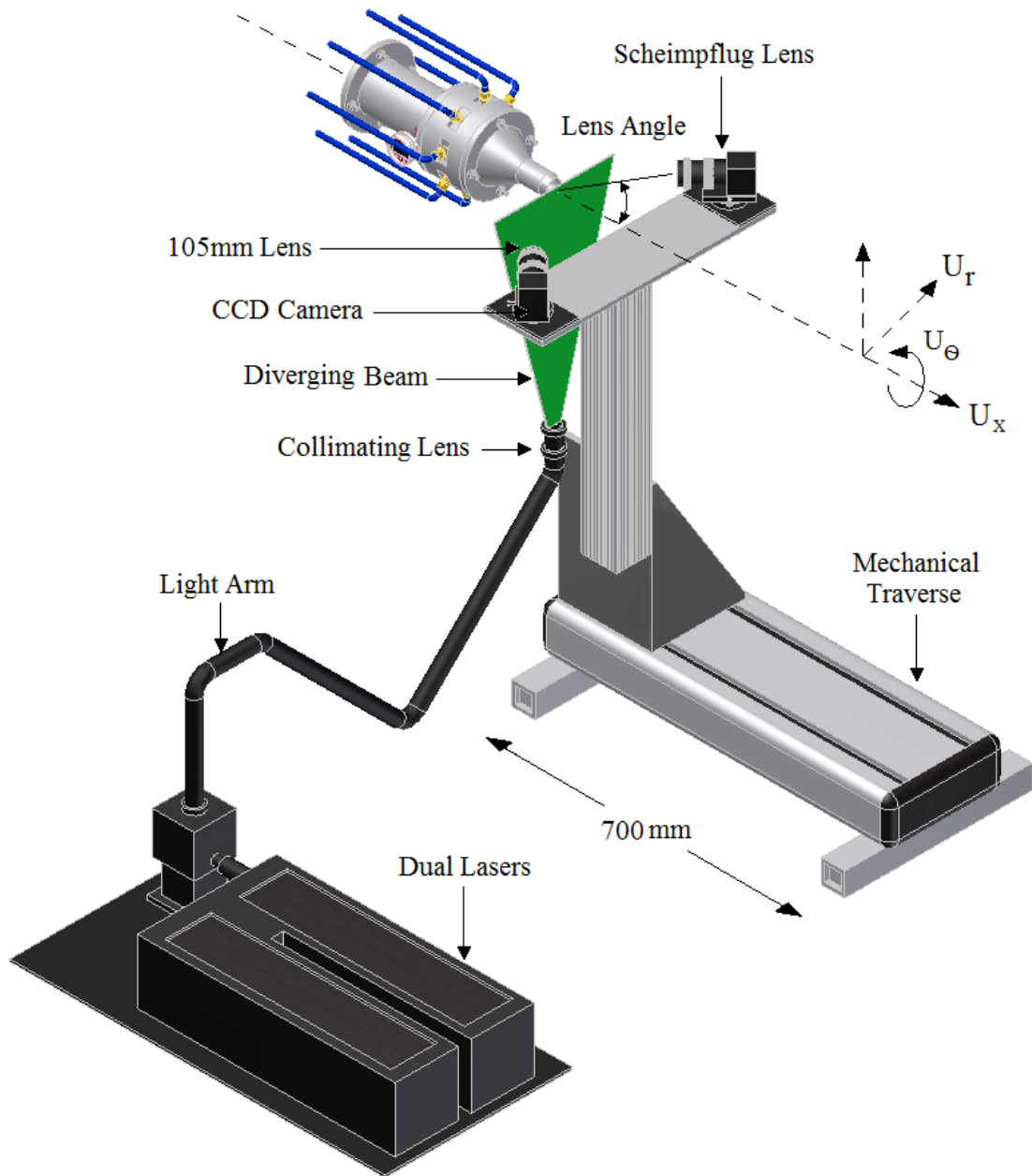


Figure 3.18: CAD assembly drawing of the experimental configuration for stereoscopic 3D PIV, for three-component velocity measurements of the end-on plane, perpendicular to the jet axis.

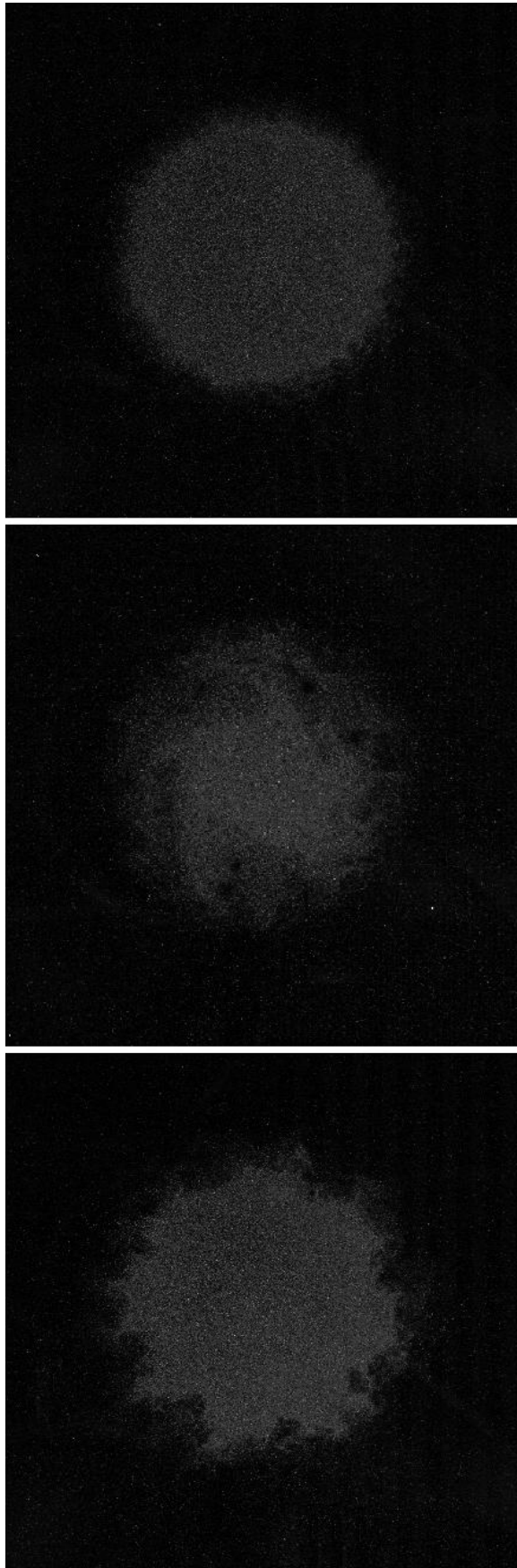


Figure 3.19: Instantaneous PIV images from the left camera during stereoscopic 3D measurements. The field of view corresponds to a physical size of 50mm×50mm for the primary jet (top), internal injection at 40% IMFR (centre) and external injection at 1% IMFR (bottom).

3.9 Jet Thrust

Directly measuring the thrust levels of a supersonic jet can be a difficult, especially when one considers the errors involved in the mechanism used to measure it, e.g. a thrust plate. However, the rate of momentum flux of a fully expanded jet can be estimated by the numerical integration of its axial velocity profile across the jet radius, which using the mean fluid properties at that plane, is equivalent to its thrust (White, 2003). The velocity profile can be obtained through traversing a pitot tube across the jet or by stereoscopic PIV. The momentum of a moving volume can be defined as a product of its mass and velocity hence the momentum flux is the rate of change of momentum;

$$M \left[\frac{kgm}{s^2} \right] = m \left(\frac{V}{t} \right) = V \left(\frac{m}{t} \right) = \dot{m} U_x \quad (3.42)$$

Since the mass flow rate is a product of the density, ρ , and volumetric discharge, Q , the momentum flux can be re-written as equation (3.43);

$$M = \rho Q U_x \quad (3.43)$$

In a cross-section of a jet, the mean velocity varies only with radial direction. Thus we can assume constant velocity across annular increments of the flow. These increments will have a ring area δA and an axial velocity U_x , and the increment of momentum flux transient through it can be expressed as;

$$\delta M = \rho \delta Q U_x \quad (3.44)$$

Using the following two substitutions for Q and A the momentum flux can be defined as;

$$\delta Q = U_x \delta A \quad (3.45)$$

$$\delta A = 2\pi r \delta r \quad (3.46)$$

$$\delta M = 2\pi \rho U_x^2 r \delta r \quad (3.47)$$

Finally, the total momentum flux or thrust of the jet is the definite integral equation (3.47), shown in equation (3.48) with limits R and 0, where R is infinite due to the boundary of the jet not being well-defined (Beer & Chigier, 1972). This is the technique used to calculate jet thrust later in the thesis.

$$M = T_x [N] = 2\pi \rho \int_0^R U_x^2 r \delta r \quad (3.48)$$

4 ACOUSTIC FIELD RESULTS

In this chapter the results related to the far-field acoustic measurements will be presented in order to illustrate the effects of all three tangential air injection techniques on the acoustics of the primary jet. These will be followed by the near-field microphone data for the purpose of better understanding the acoustic far-field. The results will be accompanied by a brief commentary, with the detailed discussion reserved for the penultimate chapter.

4.1 Far-Field Sound Pressure Level

4.1.1 Primary Jet

Figure 4.1 shows the sound pressure level (SPL) spectra at four specific observer angles relative to the streamwise axis of the unperturbed Mach 1.3 jet. All SPL measurements were scaled to 40 nozzle diameters from the jet exit using the distance calibration factor for each microphone with respect to its distance from the nozzle, as described in § 3.7.5. The acoustic spectrum at 90° is characterised by several distinct features, the most noticeable of which is the sharp, 118dB, peak at $St=0.74$ ($f=9.6\text{kHz}$). Using Powel's (1953) formula, as shown in equation (2.10), this 9.6kHz tone can be identified as a being the first harmonic component of screech noise since it occurs at a frequency that is exactly twice that of the fundamental component ($\sim 5\text{kHz}$). However, calculation requires knowledge of the shock cell spacing within the jet, and so will be discussed in more detail in § 6.1 with evidence from PIV measurements. Screech noise is a common feature of the acoustic spectra acquired upstream of imperfectly expanded supersonic jets (Powell, 1953). Samimy (2010) also noticed this strong SPL peak at $St=0.73$ at the 90° spectra of a Mach 1.3 jet, validating the present result. A much broader, secondary peak is present immediately next to the screech tone and has an amplitude of 116dB, centred at $St=1$ (13kHz), extending up to $St=1.6$ (20kHz). This broad shaped peak is also commonly found in upstream supersonic jet noise spectra and is well known as broadband shock noise (Harper-Bourne & Fisher, 1973). It is thought to originate from the same turbulence-shock interaction that produces screech noise. Apart from the two noise peaks, the sideline spectra is fairly flat at 113dB for the midrange frequencies between 1.3kHz to 9kHz ($St=0.1$ to 0.7 respectively). However, beyond $St=2$ (26kHz) the spectrum decays rapidly into ultrasonic frequencies.

The acoustic spectrum at an observer angle of 60° exhibits a fairly smooth, curved, shape devoid of sudden screech or broadband peaks. The highest noise level is recorded at 118dB for $St=0.2$ (2.5kHz) with the spectrum showing very similar decay properties at high frequencies to those at the sideline angle.

At 30° the spectrum is rather different to those upstream, in the sense that the noise peak is much larger, measuring at 132dB at $St=0.17$ (2.2kHz), followed by a more gradual and constant decay thenceforth. This trait was first noticed by Tanna (1977), who established $St=0.19$ as the value for peak jet noise. The peak noise frequency is found to coincide with the roll-up frequency of Kelvin Helmholtz instability waves, corresponding to $St=0.15-0.2$, which have experimentally been shown to exist near the end of the potential core (Panda et al., 2002).

The spectrum at 15° to the jet axis was recorded from the furthest location along the microphone array immediately adjacent to the exhaust funnel. It has a similar trend to that at 30°, apart from two distinct features. Firstly, the low frequency noise does not climb up to the spectral peak of 132dB, but rather maintains that level from $St=0.02$ up to 0.15 (250Hz to 2kHz respectively), signifying an increasing influence of low frequency noise from large-scale structures at the aft angles. Secondly, a discrete tone measuring 127dB occurs at $St=0.49$ (6.3kHz). Disturbances at the nozzle lip are known to generate several upstream propagating harmonic tones (Norum, 1983). However Neemah (1999) concluded that the process by which these harmonic disturbances travel upstream around the shock cells to the nozzle creates a secondary self sustained disturbance that propagates primarily in the downstream direction. According to this explanation, the tone in the 15° spectra could be the secondary disturbance from the screech generating mechanism. It could also be classified as the fundamental component of screech noise, since it matches closely to the 5kHz given by Powel's formula for fundamental screech equation (2.10) and is also much greater in amplitude (127dB), occurring at roughly half the frequency of the sideline propagating harmonic tone; 118dB at 9.6kHz. However, the fundamental component of screech noise is known to propagate in the upstream direction (Powel, 1953; Raman, 1999) and so this may be its reflection off the jet nozzle towards the downstream direction. Covering the nozzle and plenum apparatus with foam had shown to significantly reduce its amplitude as compared to preliminary acoustic spectra, adding evidence for the explanation that it may be a reflection. A similar discrete tone was documented by Samimy (2010) at $St=0.4$ for the downstream observer angles.

Figure 4.2, compares the SPL spectra from all ten microphone locations. The format chosen for presenting the data allows for the identification of the peak noise angle for the primary jet. At 134dB the peak noise angle of the jet is clearly at 25°, nearly 2dB higher than at 30° and 20°. This result agrees to an extent with that of Hileman (2002), who showed that for a Mach 1.3 jet, the noise peak radiates at an angle of 30° to jet axis.

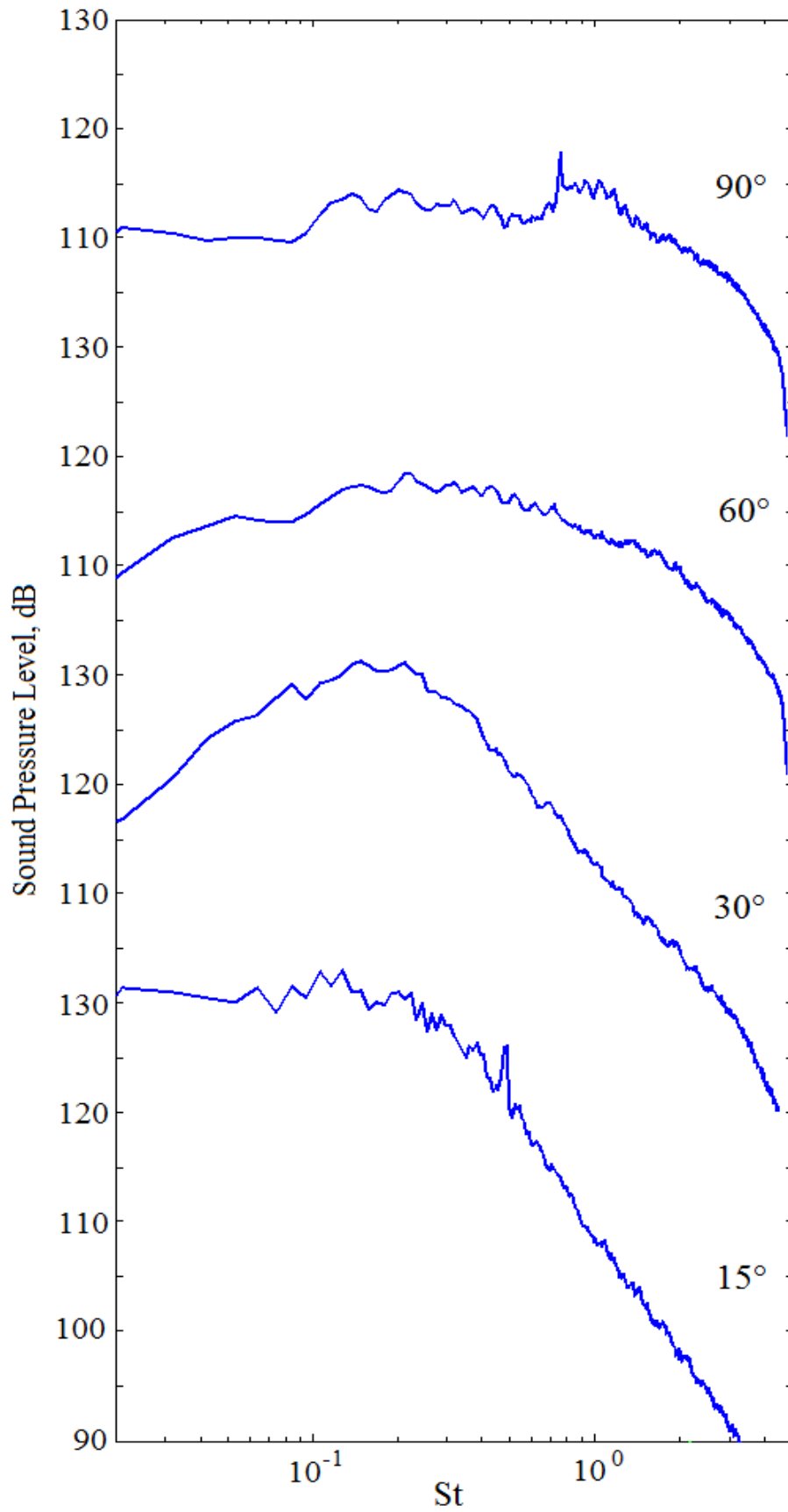


Figure 4.1: Comparison of SPL spectra, scaled to 40 nozzle diameters, at various observer angles from the unmodified Mach 1.3 primary jet.

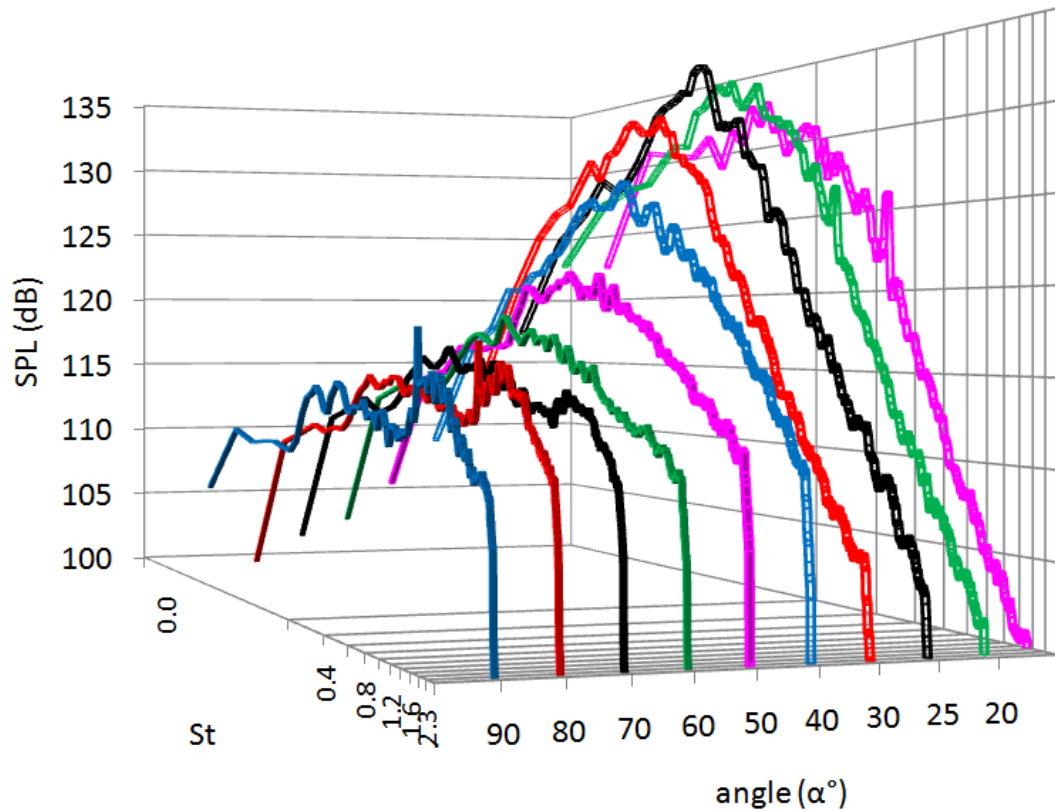


Figure 4.2: Comparison of SPL spectra, scaled to 40 nozzle diameters from jet exit, with variation in observer angles from the streamwise primary jet axis.

Tam (1996) surveyed over 1900 acoustic spectra from supersonic jets and found them to closely match two distinct similarity spectra regardless of the jet velocity and temperature. The first is called “*F-spectra*” which characterises noise from large-scale turbulent structures propagating in the downstream direction. The second is “*G-spectra*” which encompasses noise from fine-scale turbulent structures, highly directional towards the sideline and upstream angles. The *G* and *F-spectra* were shifted on both axes until they superimposed the primary jet’s spectral peak, after which a comparison could be made on the rate of growth and decay of the SPL, as shown in Figure 4.3. A distinct boundary is visible at 50° , which roughly separates the propagating angles for noise related to fine-scale (*G-spectra*) and large-scale structures (*F-spectra*). Noise at $f > 60\text{kHz}$ ($St > 4.6$) was filtered out using a Butterworth filter in MATLAB 7.0, as it was beyond the range of interest of this study. This is the reason for the sharp spectral fall-off beyond $St = 4.6$ for all observer angles. Although the primary jet’s acoustic spectra compares well with both *F* & *G similarity spectra* at the lower frequency range, the comparison is not as good in the higher frequency range at observer angles between 40° - 15° . A possible and most likely explanation for this occurrence is atmospheric attenuation, which is the gradual loss in acoustic intensity of sound waves propagating through a medium. Although attenuation through the spherical divergence aspect of the sound waves is

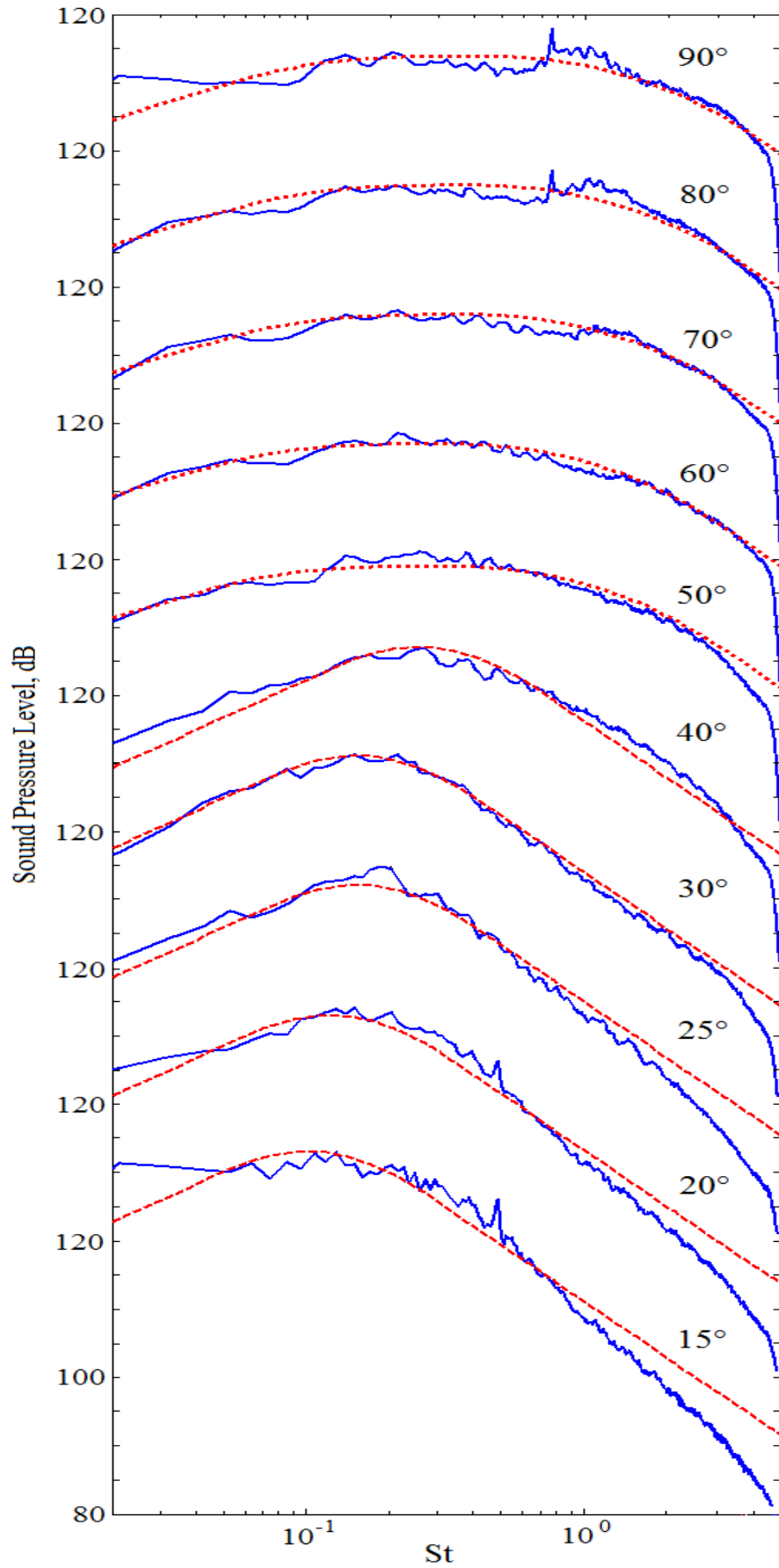


Figure 4.3: Comparison of SPL spectra between the primary jet (—), Tam's (1996) similarity *G*-spectra for fine-scale turbulence noise (••) & *F*-spectra for large-scale turbulence noise (--).

accounted for in the distance calibration factors already implemented in § 3.7.5, the air absorption effect is unaccounted for. Viswanathan (2008) evaluated the suitability of several different methods, before concluding the method of Shields and Bass (1977) to be the most accurate at the higher frequencies of interest in scaled laboratory tests. Their proposed atmospheric attenuation coefficient, AA , incorporates air temperature, relative humidity, spectral frequency and radial distance, r , of the microphone from the source. The magnitude of the atmospheric attenuation is shown to be as high as 3dB/m at a $f=70\text{kHz}$, whereas it is $<0.1\text{dB/m}$ for $f < 8\text{kHz}$ (Shields and Bass, 1977; Viswanathan, 2006). Since the downstream positioned microphone at 15° ($r/D \sim 80$) is twice as far from the nozzle exit as the sideline 90° ($r/D \sim 40$), the effects of air absorption are more visibly evident on its acoustic spectra. Introducing an atmospheric attenuation term, $+r[AA_{(testday)}]$, in equation (3.27) would result in a better comparison between the primary jet spectra and Tam's (1996) similarity F -spectra shown in Figure 4.3.

Figure 4.4 defines the directivity of the primary jet by showing the variation of the overall sound pressure level (OASPL) with respect to observer angle. The OASPL of the jet remains constant at 113.5dB for the sideline angles of 90° to 70° . It then begins to rise with decreasing observer angles for mid-range positions between 60° to 40° before peaking at 120.5dB at 25° for the downstream range of 30° - 15° . This result is consistent with the SPL spectra, suggesting that the large-scale eddies are more dominant and energetic than the fine-scale structures in the acoustic far-field of the jet. The error bars indicate a standard deviation 0.2dB in the data, which equates to less than 1% of the peak root mean square OASPL value. The error and uncertainty in the acoustic measurements will be discussed in § 6.5.

Figure 4.5 shows a comparison between the original SPL results against those with recalculated microphone distance calibration factors based on a noise source origin at $x/D=5$ along the streamwise axis of the jet. This required a minor modification of the microphone angles to the new noise source origin, without the need to physically change their positions. The derived results were not from a separate measurement to those used to calculate the SPL in Figure 4.4, but the same signals, with the only modification being the scaling of the distance calibration. The results for the extended noise source are identical to the original ones, for the mid range angles, but slightly reduced at both extreme measurement angles.

For the remainder of this study the scaling of SPL will be based on distance calibration factors calculated from a noise source origin at the nozzle (Table 3.8), as has been the case in numerous studies on jet noise reduction and locations (Panda 2005, Callender 2007, Alkislar 2008, Castelain 2008, Henderson 2008, Samimy 2010 & Zaman 2010). Petitjean (2003) used a scaling origin at $x/D=5$, considering it to be the main noise.

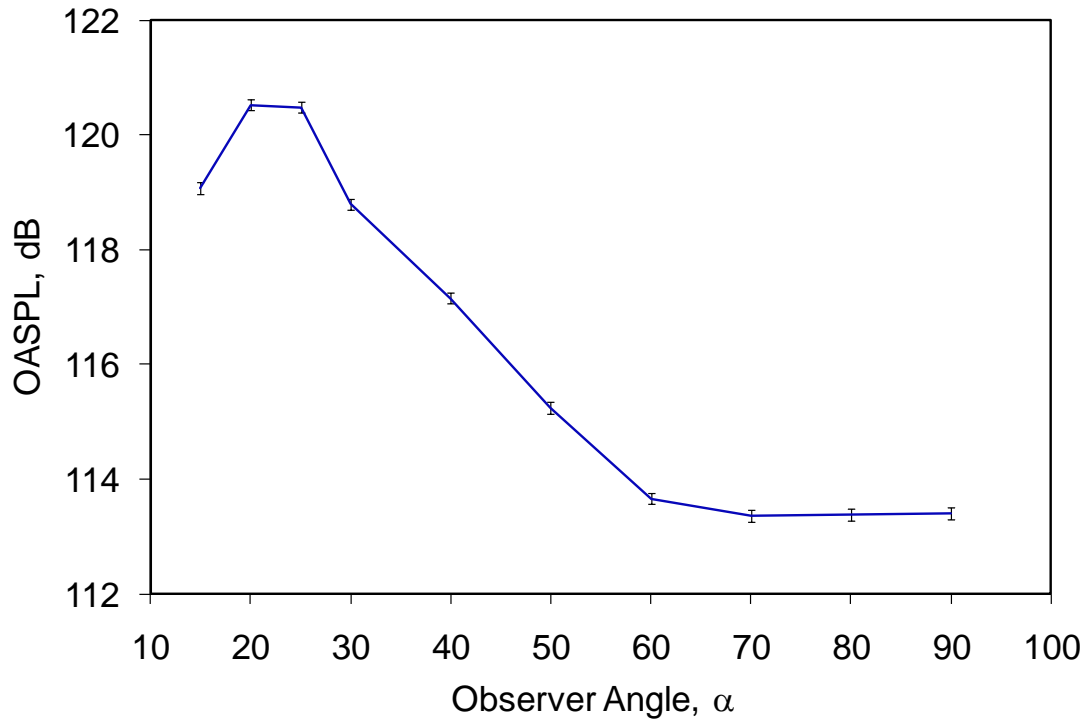


Figure 4.4: OASPL at various observer angles for the primary, Mach 1.3, jet with measurements scaled to a distance of 40 nozzle diameters from $x/D=0$. Error bars indicate standard deviation of 0.2dB, which is less than 1% of the peak $OASPL_{RMS}$ value.

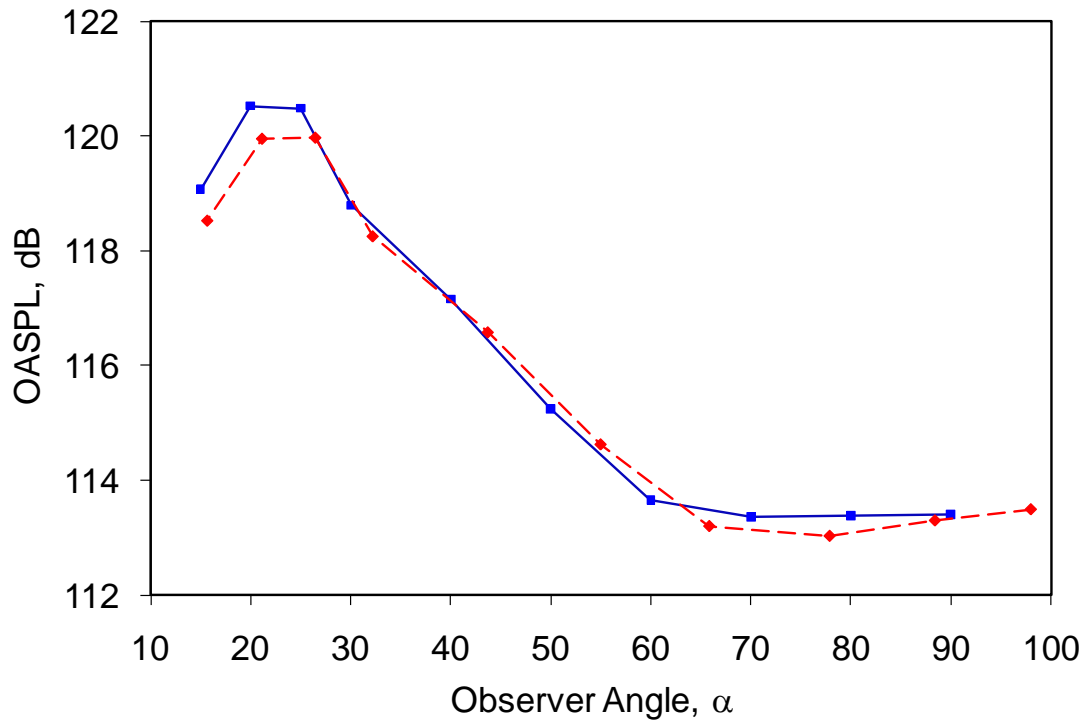


Figure 4.5: Comparison of OASPL at various observer angles for the primary jet using distance calibration factors based on a noise source origin at $x/D=0$ ($\text{---}\blacksquare\text{---}$) and $x/D=5$ ($\text{-}\blacklozenge\text{-}$) from the nozzle exit.

4.1.2 Internal Tangential Injection (ITI)

Figure 4.6 indicates how the SPL spectra of the primary jet are affected by the introduction of internal tangential air injection at various injection mass flow ratios (IMFR). At the sideline angle of 90° , an IMFR of 10% of that of the primary jet shows a slight reduction of the screech tone; however this is coupled with an adverse effect through an increase in both broadband shock and high frequency noise. Increasing the IMFR to 40% has two main effects. Firstly, and encouragingly, both the screech and broadband shock associated noise is totally eliminated through an SPL reduction of 6.4dB at $St=0.74$ (9.6kHz) and $St=1$ (13kHz) respectively. Secondly, there is evidence of increased noise outside the range $0.6 < St < 2$ ($8\text{kHz} < f < 26\text{kHz}$). The 40% IMFR configuration can be considered as optimal for this technique since an increase to 50% IMFR begins to counter effect the noise benefit through increased high frequency noise.

At 60° the noise reductions are moderate in comparison to those at 90° and are limited to Strouhal numbers lower than 1.5, with the same characteristic increase of higher frequency noise beyond, irrespective of IMFR. At an observer angle of 30° , the greatest noise reduction occurs at the spectral peak of $St=0.17$ and is proportional to the IMFR. The cross-over point to increased higher frequency noise occurs at $St=0.85$ (11kHz), which is lower than those observed at the upstream angles.

At the extreme downstream angle of 15° , the noise reduction pattern is distinctly different from all other angles, in that it is broadband and hence free of cross-over points. The downstream propagating component of screech noise at $St=0.49$ is completely abated by a 12dB SPL reduction using the 40% IMFR configuration. Increasing the IMFR to 50% results in only a slight broadband noise benefit and so may not be justified when considering the simultaneous increase in high frequency noise at the upstream observer angles.

Figure 4.7 shows the acoustic SPL spectra for all ten angles with the 40% IMFR configuration. In comparison to Figure 4.2, there is the absence of both screech and broadband shock noise at 90° , with the jet's peak noise radiation angle remaining unchanged.

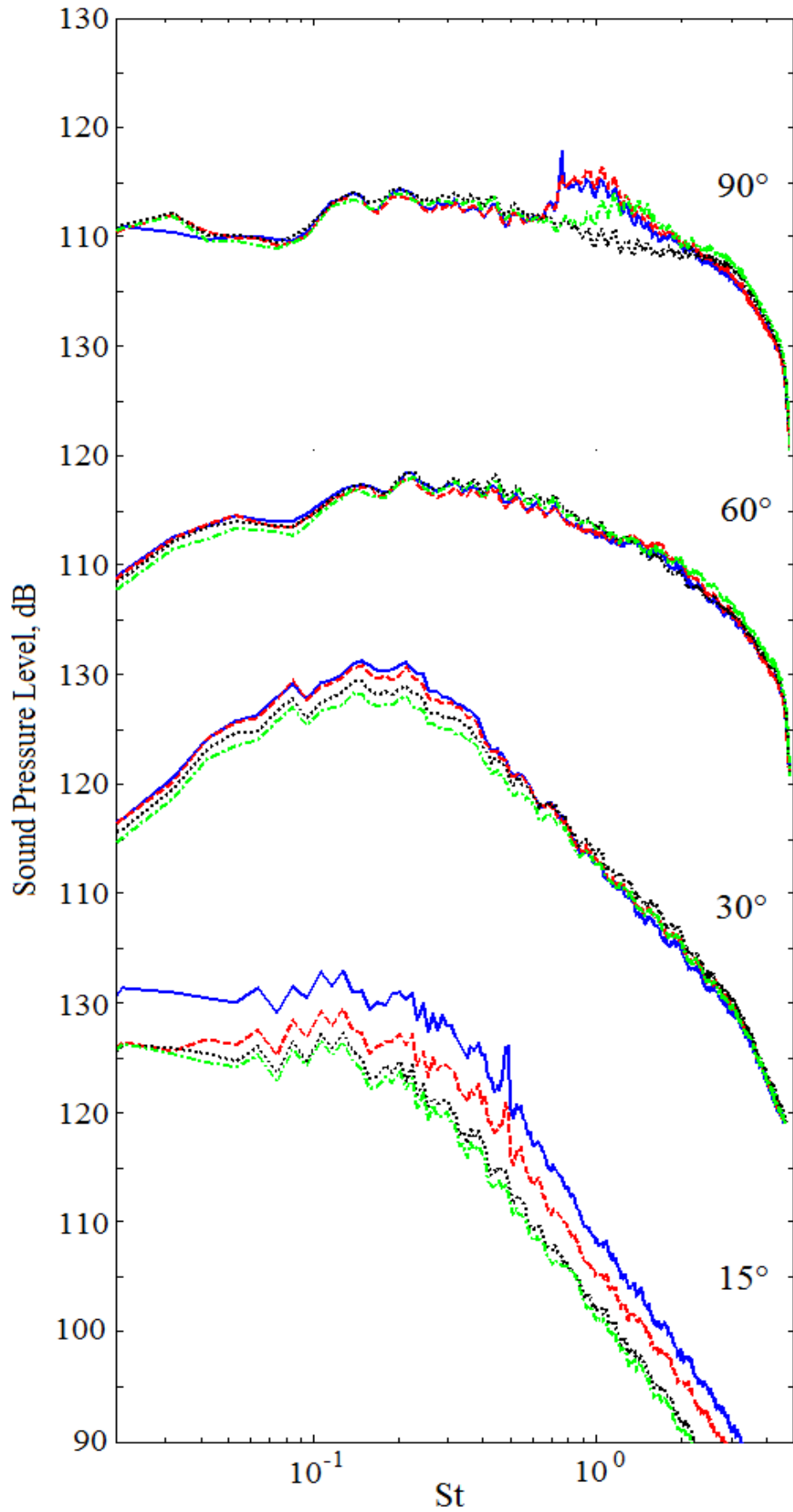


Figure 4.6: Comparison of SPL spectra at various observer angles for internal tangential injection at mass flow ratios of 10% (- -), 40% (···) & 50% (-.-) against the primary jet (—).

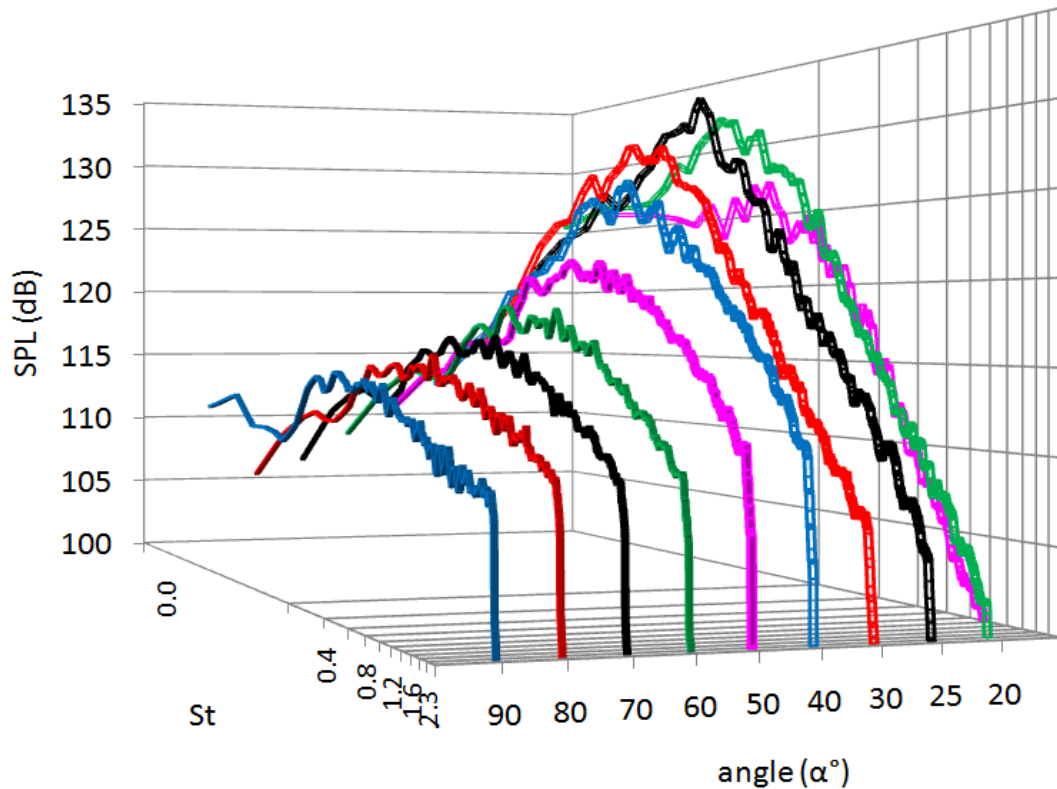


Figure 4.7: Comparison of SPL spectra at various observer angles for the best performing configuration of internal tangential injection; at a mass flow ratio of 40%.

Figure 4.8 shows the effect on the OASPL at various angles due to introducing different proportions of internal tangential injection to the primary jet. For an IMFR of 10% there is an increase in noise at the sideline and mid-range angles between 90° and 50°, with a corresponding reduction at the downstream angles. For 40% IMFR this trend changes, with both the sideline and downstream angles experiencing significant noise reductions, with the mid-range angles suffering slightly. For 50% IMFR, the enhanced reduction at the downstream angles is accompanied by a sharp increase in noise at all angles upstream of 50° to levels beyond those seen in the base case. Internal tangential injection in general seems to reduce low frequency noise in the downstream direction at the expense of increased higher frequency noise at the more forward angles, as shown in the SPL spectra. The 50° spectrum, which seems to be least affected by the injection, is the cross-over point for these opposing trends.

Figure 4.9 illustrates the effectiveness of this technique at the aft angles of the jet, with up to a 7dB reduction in OASPL at 15°. Neemah (1999) reported much lower peak noise reductions of approximately 2dB at an angle of 30°. However, a comparison of the magnitude of swirl cannot be made until the flow-field results are analysed in Chapter 5. Despite 50% IMFR showing greater noise benefit at lower angles, 40% IMFR seems the optimal configuration due to its showing the least, if any, adverse noise effects of the three IMFR configurations tested.

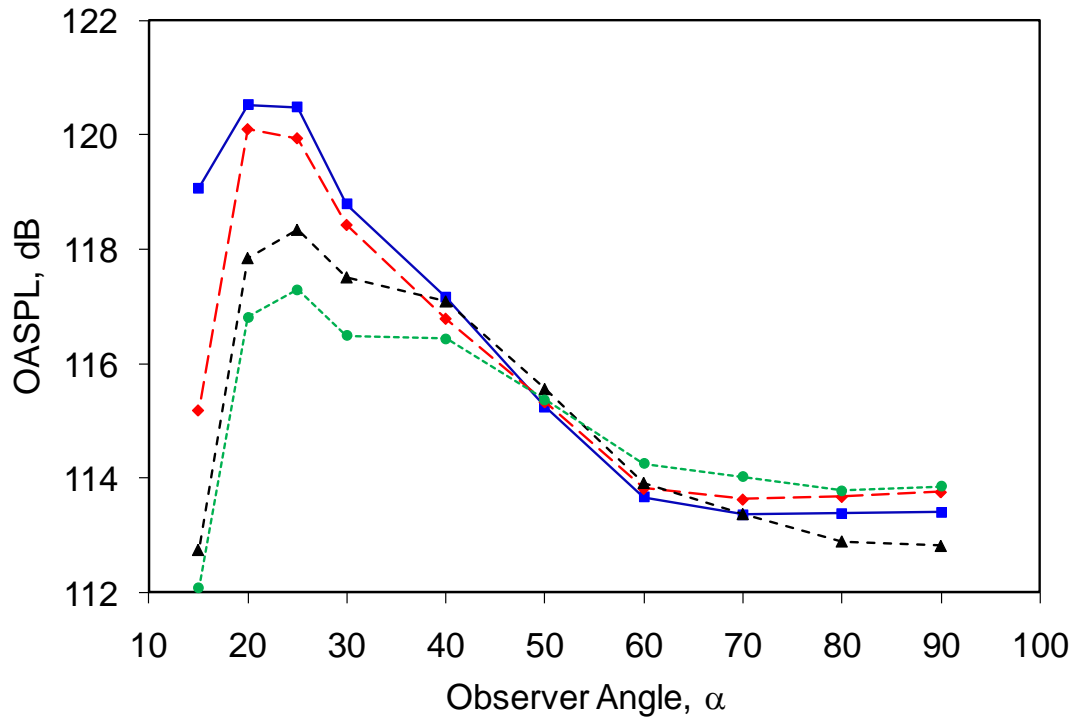


Figure 4.8: Comparison of OASPL at various observer angles for internal tangential injection at IMFRs of 10 % (—◆—), 40 % (—▲—) & 50% (---●---) against the primary jet (—■—).

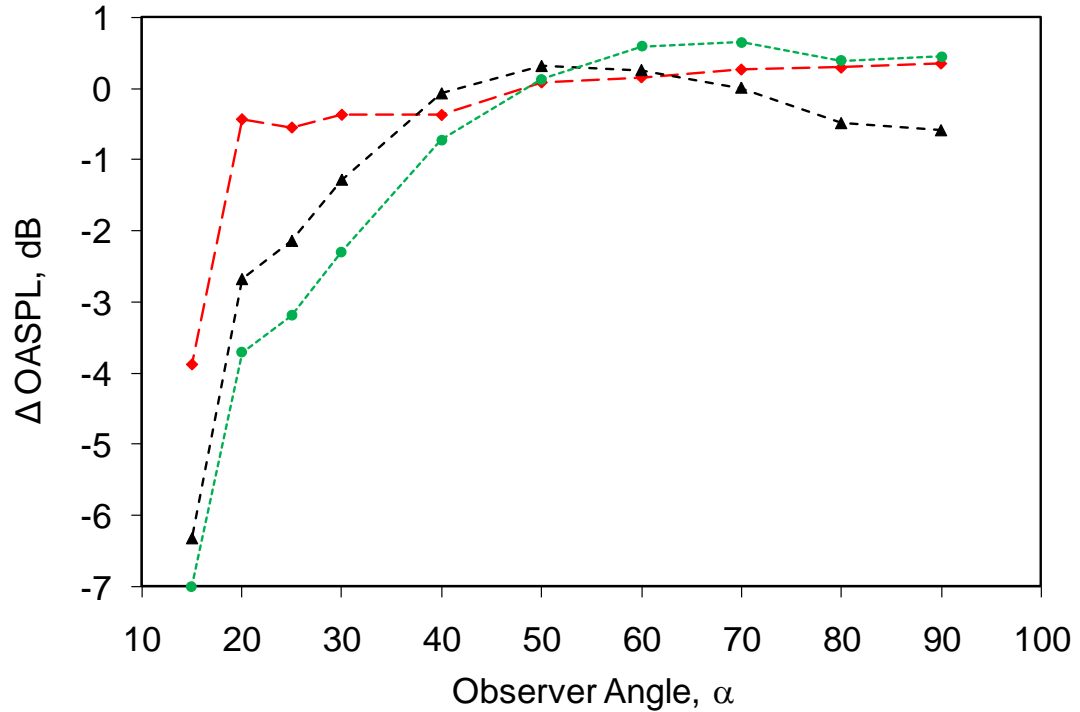


Figure 4.9: Comparison of jet noise reduction using internal tangential injection technique at IMFRs of 10% (—◆—), 40% (—▲—) and 50% (---●---) with respect to OASPL of the primary jet.

4.1.3 External Tangential Injection (ETI)

Figure 4.10 compares the effects of varying the strength of external tangential injection on the primary jet. Similar to internal tangential injection, the screech and broadband shock noise peaks at the 90° spectra are completely removed using external tangential injection. However, the startling contrast is in the amount of air required to do so. At only 1% IMFR, noise benefits are recorded below $St=2.5$ (32kHz) with a cross-over to increased ultrasonic noise beyond. It is interesting to note that the low-frequency noise reducing benefit in further increasing the IMFR from 1% to 1.3% is insignificant as compared to increasing it from 0% to 1%, for the 90° as well as the 60°, 30° and 15° observer angles. The principal effect of this amplified injection rate is a further increase in the higher frequency noise cross-over. Hence, the 1% IMFR configuration is regarded as optimal for this injection technique, beyond which there are diminishing returns in the acoustic spectra. The reduction of the harmonic screech tone by almost 7.5dB at an IMFR of 1% compares favourably with the experimental findings of Henderson (2008), who showed an 8dB reduction in broadband shock and screech noise with the use of fluidic chevrons (microjet-chevron combination) at an IMFR of 1.2% of that of the main jet. At 30°, the largest noise reduction of approximately 2 dB coincides with the spectral peak, with a 5dB abatement at the spectral peak for 15°. Although high frequency noise cross-over is a common feature of tangential air injection, the Strouhal numbers at which it occurs reduces with observer angle. For 90° it occurs at $St=2.5$ (32kHz), for 60° at $St=2$ (26kHz) and at 30° it occurs at $St=0.85$ (11kHz). Additionally, the cross-over effect is more pronounced at the downstream angle of 30°. Callender (2007) also observed this effect whilst using impinging microjets for noise reduction and found the cross-over frequency to be 10kHz, which compares favourably to the present finding. This increased high frequency noise can be attributed to the tangential jets themselves which are angled toward the sideline direction and have sonic exhaust conditions at the higher tested IMFR. This proposition will be further explored in Chapter 6.

Figure 4.11 shows the acoustic spectra at all the observer angles for the optimal noise reducing 1% IMFR configuration. The jet's peak noise angle seems to have shifted slightly towards 25°-20°, unlike the primary jet case in Figure 4.2 where 25° is clearly the jet noise peak angle. Slightly attenuated levels of broadband shock noise are still evident for the 90° and 80° spectra.

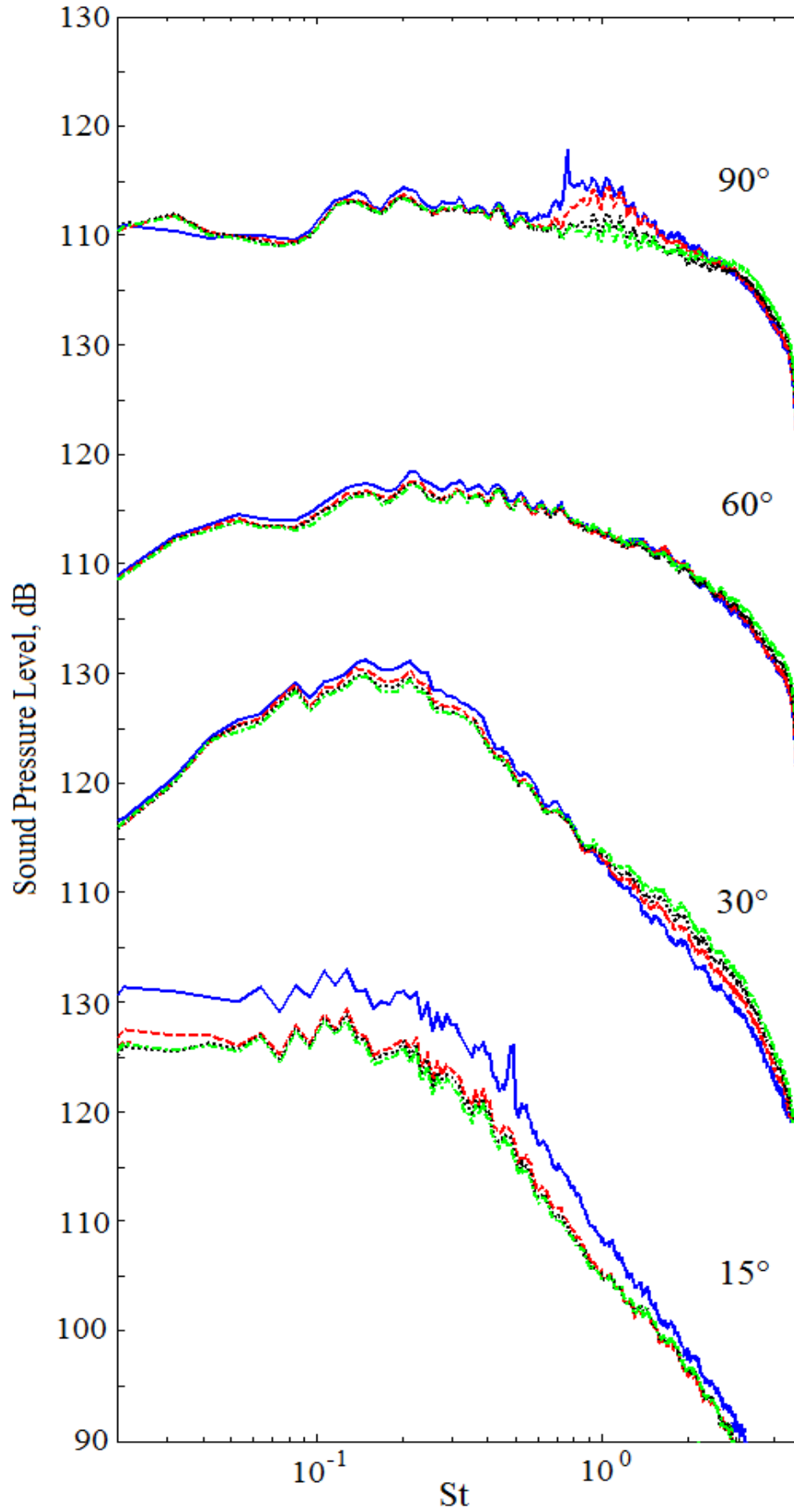


Figure 4.10: Comparison of SPL spectra at various observer angles for external tangential injection at mass flow ratios of 0.7% (- -), 1% (· · ·) & 1.3% (- · -) against the primary jet (—).

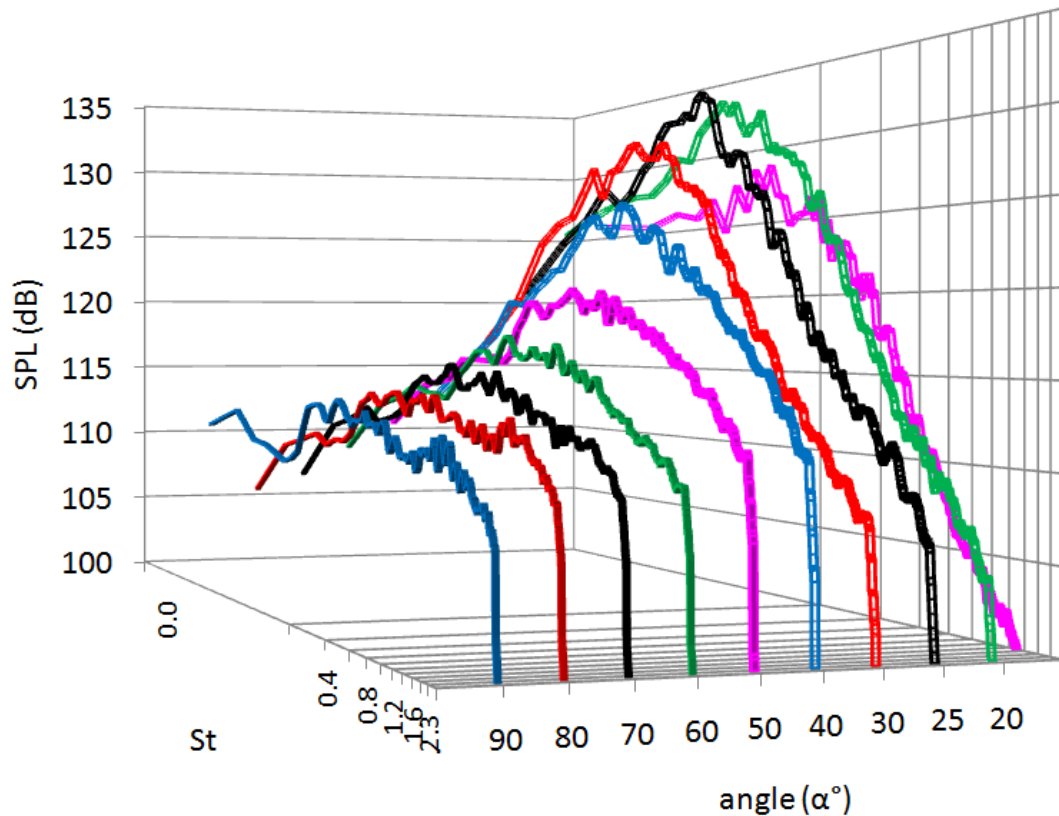


Figure 4.11: Comparison of SPL spectra at various observer angles for the best performing configuration of external tangential injection; at a mass flow ratio of 1%.

Figure 4.12 shows a comparison of the OASPL at various observer angles for different IMFR's of external tangential injection. At an IMFR of 0.7%, OASPL reductions are observed at all angles. The noise benefit at the extreme angles of the microphone array is further optimised by increasing the IMFR to 1% with minimal change at 50°. Further increasing the IMFR beyond 1% results in greater noise attenuation at the downstream angles, but at the expense of increased noise at the sideline angles. This diminishing return is consistent with the increased high frequency noise observed in the SPL spectra for sideline angles.

Figure 4.13 shows the 1% IMFR configuration to achieve a maximum noise benefit of 5dB at 15°, whilst the OASPL at the peak noise angle of 25° is reduced by 1.5 dB. It also shows it to be more consistent than the other two IMFR's across the majority of angles, hence making it the optimal noise reducing configuration. The result is promising considering that Castelain (2008) only managed to reduce 1.2dB off the peak radiating angle (30°) of a Mach 0.9 jet using a series of 18 azimuthally positioned impinging microjets, each with an injection mass flux ratio of 0.067% of that of that the main circular jet (total microjet system IMFR~1.2%).

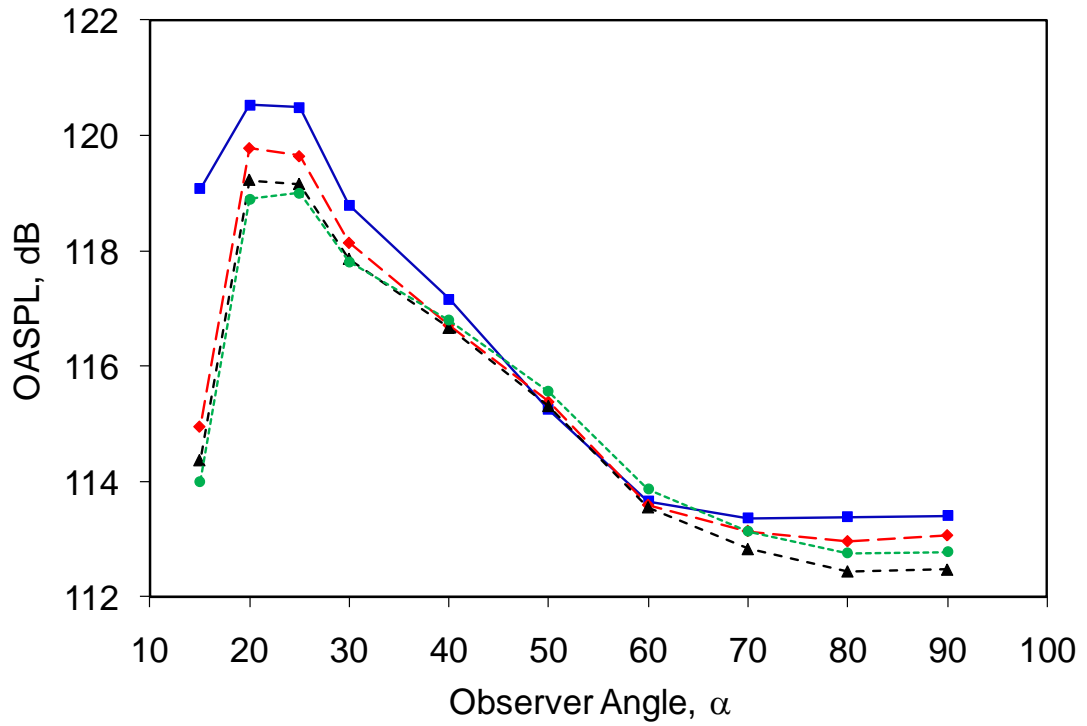


Figure 4.12: Comparison of OASPL at various observer angles for external tangential injection at mass flow ratios of 0.7% (-♦-), 1% (-▲-), & 1.3% (-●-) against the primary jet (—■—).

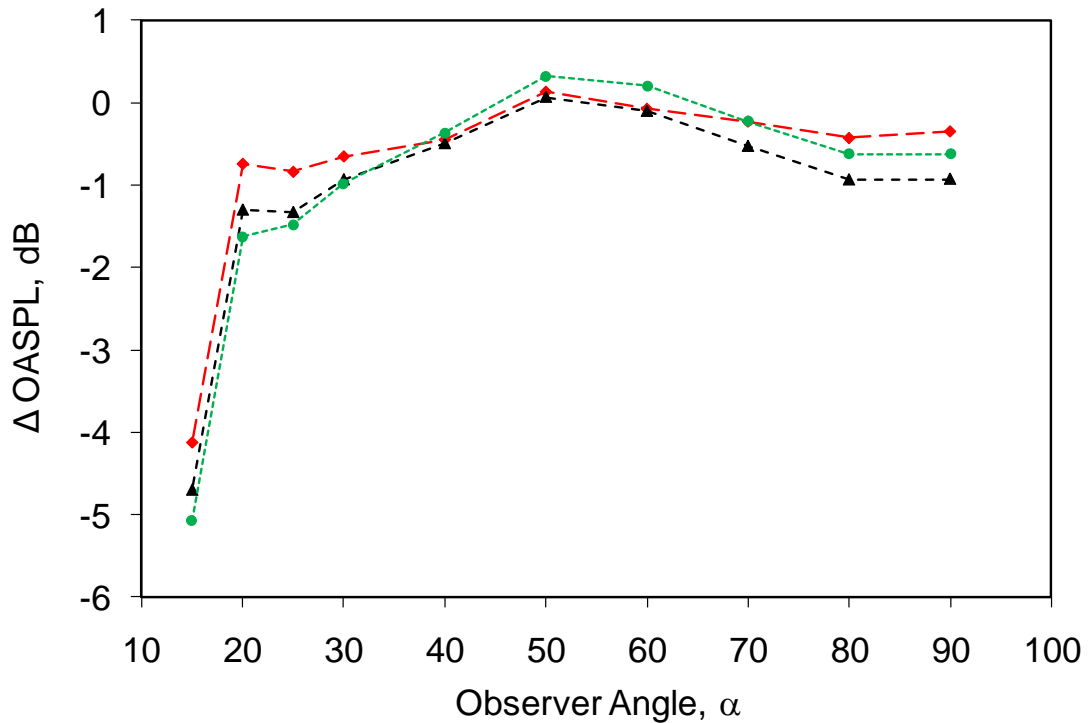


Figure 4.13: Comparison of jet noise reduction using the external tangential injection technique at IMFRs of 0.7% (-♦-), 1% (-▲-) and 1.3% (-●-) with respect to OASPL of the primary jet.

4.1.4 Pulsating Tangential Injection (PTI)

Figure 4.14 shows the effect of 2kHz pulsating tangential injection on the acoustic spectra of the primary jet. At 90°, with an IMFR of 0.5% the screech tone is eliminated and the broadband shock noise peak is reduced by 1.5 dB at $St=1$. Increasing the IMFR to 0.7% further reduces the broadband shock peak by another 1.5 dB, with noise reduction across the whole spectra. This result is interesting since there is an absence of the high frequency noise cross-over previously seen for the internal and external tangential injection cases. Further strengthening the IMFR to 0.9% results in the SPL spectra increasing back towards the level of the primary jet, especially at the higher Strouhal numbers. A similar trend is seen in the acoustic spectra at 60°, 30° and 15°, where the SPL is modestly reduced by increasing IMFR up to 0.7%, beyond which the noise benefit begins to diminish and the higher frequency noise cross-over effect becomes first evident. This result indicates that the 0.7% IMFR is the optimal configuration for this technique.

Figure 4.15 clearly shows broadband shock noise peaks at 90° and 80° highlighting the ineffectiveness of this technique in reducing them. The distinctiveness of the jet's peak noise radiation angle is also reduced compared to the primary jet case in Figure 4.2. Figure 4.16, in agreement with the corresponding SPL spectra in Figure 4.14 shows the 0.7% IMFR to be the optimal configuration, through constant and broadband reductions in OASPL. No cross-over to increased noise is present. Figure 4.17 and Figure 4.18 investigate the effect of the frequency of pulsation on the OASPL of the jet whilst keeping the IMFR constant at 0.7%. It shows the 2kHz configuration to be consistently quieter than the 1kHz injection by approximately 0.5dB across all angles. This result supports the initial justification for pulsating jets; that shear layer disturbances at frequencies close to the preferred mode (~2kHz) of the jet induce noise reductions.

At this point it would be appropriate to question the actual pulsating frequency of the PTI injectors given the adverse pressure gradients present in the complex network through which the flow needs to travel before exiting into the main jet (§ 3.4.3). For this purpose a microphone was positioned at an observer angle 30° to a single, 1.5mm diameter, isolated PTI injector at a radial distance $r/D=100$, in the absence of the primary jet flow. The resultant acoustic spectra presented in Figure A.2 of Appendix A shows a clear and relatively broad SPL peak at 2.2kHz with sharper harmonics at 4.4kHz, 6.6 kHz, 8.8 kHz & 11kHz, giving evidence in support of PTI operating close to its design frequency of 2kHz. Ideally, one would like to observe the effects of 3kHz pulsating injection on jet noise, before concluding the 2kHz configuration as being the optimal, however limitations of the pneumatic drill design do not permit this.

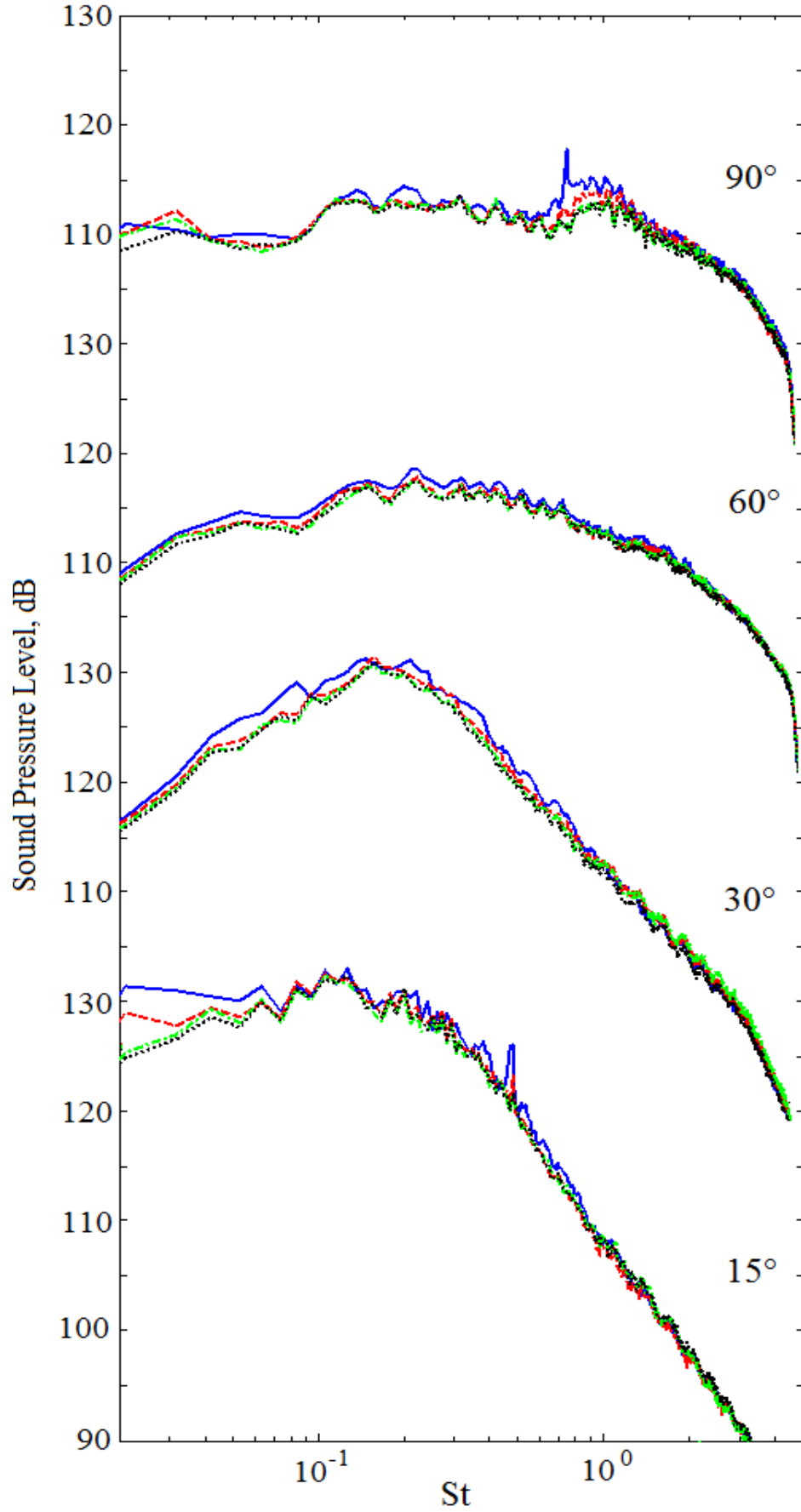


Figure 4.14: Comparison of SPL spectra at various observer angles for 2kHz pulsating injection at mass flow ratios of 0.5% (---), 0.7% (···) & 0.9% (-.-) against the primary jet (—).

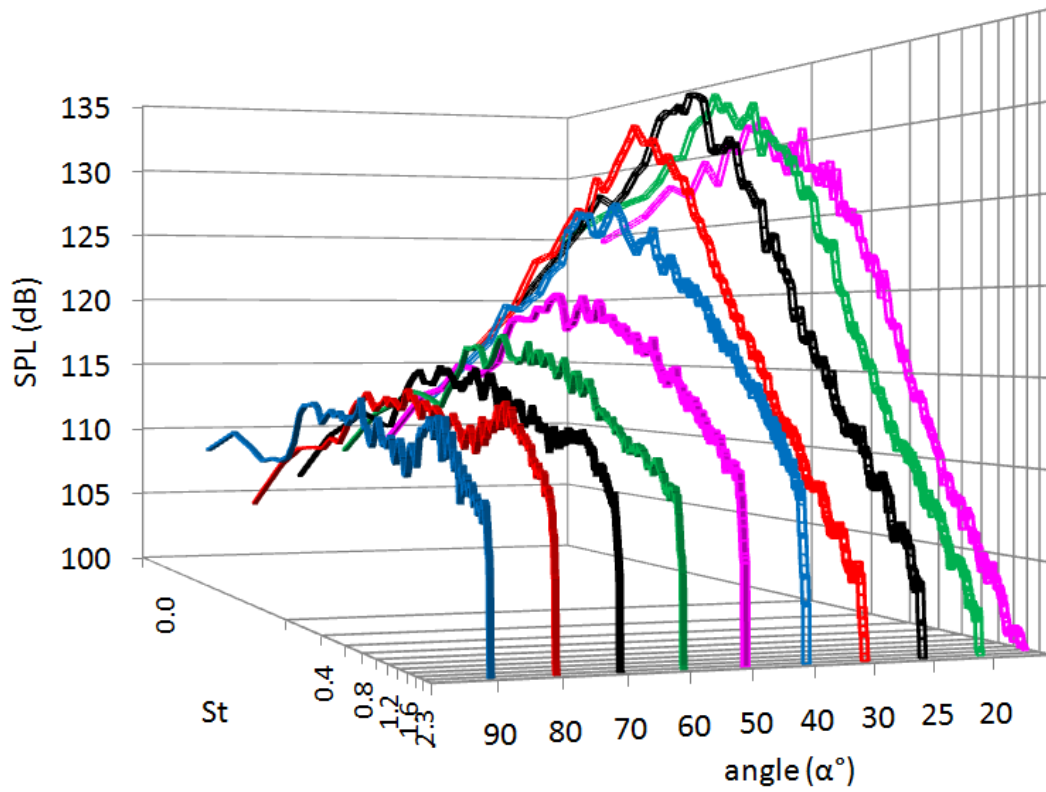


Figure 4.15: Comparison of SPL spectra at various observer angles for the best performing configuration of 2kHz pulsating injection; at a mass flow ratio of 0.7%.

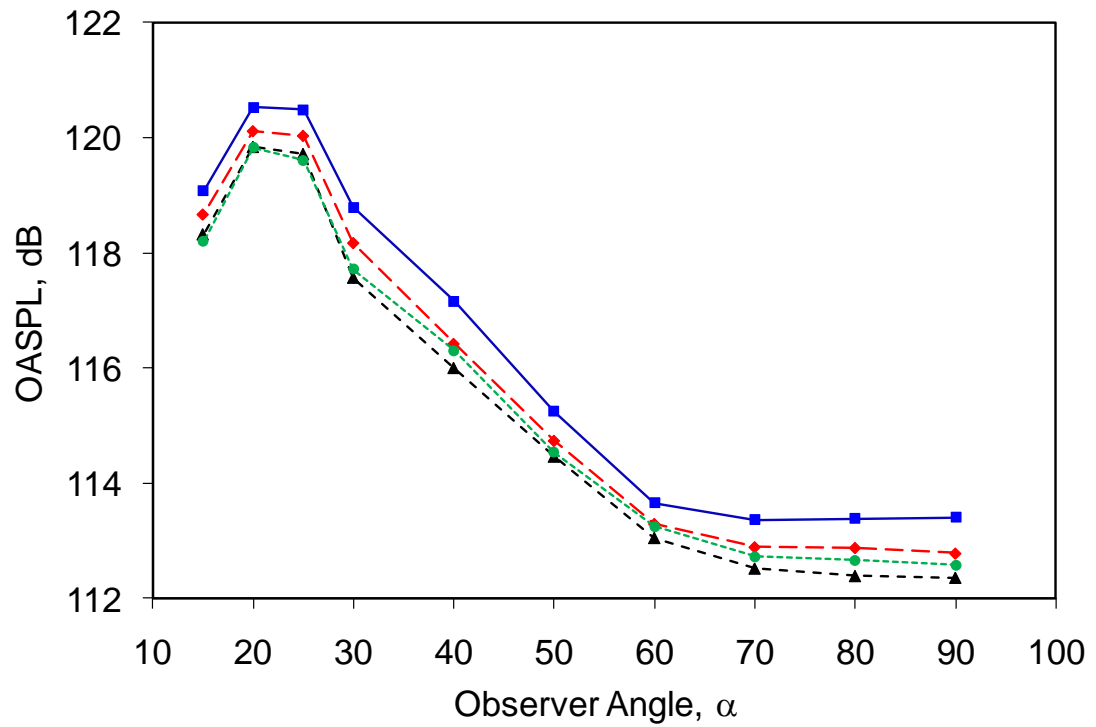


Figure 4.16: Comparison of OASPL at various observer angles for 2kHz pulsating tangential injection at IMFR of 0.5% (—◆—), 0.7% (—▲—), & 0.9% (·····●·····) against the primary jet (—■—).

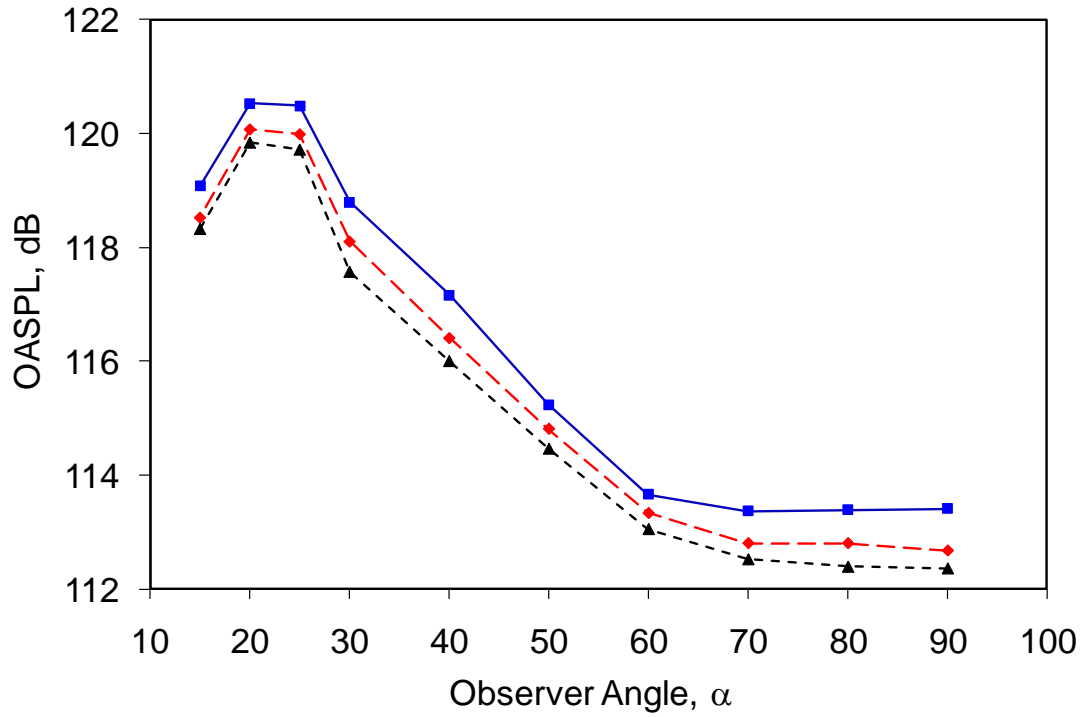


Figure 4.17: Comparison of OASPL at various observer angles for pulsating injection at IMFR of 0.7% and pulsating frequencies of 1kHz (—♦—) & 2kHz (—▲—) against the primary jet (—■—).

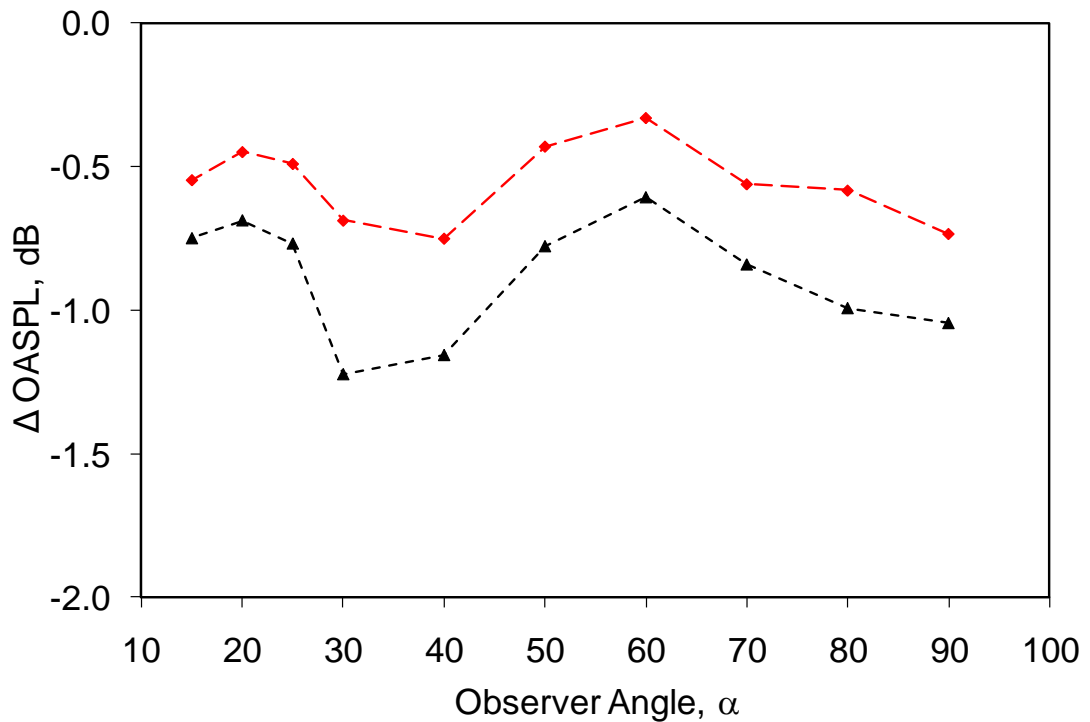


Figure 4.18: Comparison of jet noise reduction using the pulsating tangential injection technique at pulsating frequencies of 1kHz at 0.7% IMFR (—♦—) and 2kHz at 0.7% IMFR (—▲—) with respect to OASPL of the primary jet.

4.1.5 Comparison of Optimal Configurations

Figure 4.19 compares the SPL spectra for the best performing configurations from each of the three air injection techniques. Based upon the evidence of the preceding results, the IMFR's for optimal noise reductions were selected as: 40% for internal tangential injection (ITI), 1% for external tangential injection (ETI) and 0.7% for the 2kHz pulsating tangential injection (PTI). Figure 4.20 and Figure 4.21 compare the corresponding OASPL's for these techniques at various observer angles. Of the numerous possible comparisons that can be made between the noise reduction capabilities of the three air injection techniques the most interesting are summarised in Table 4.1.

At the sideline direction of 90°, ETI shows the highest screech tone reduction of 7.5dB, approximately 1dB better than the other two techniques. ITI shows the greatest noise benefit with respect to the broadband shock peak at $St=1$, but fails to maintain this trend throughout the spectra as seen by the increased higher and lower frequency noise in Figure 4.19. In terms of the OASPL, the 2kHz PTI at an IMFR of 0.7% performs the best with a 1dB decrease at 90°. It seems to be a surprising result, given that no major impact was observed in the corresponding SPL spectra. The key to deciphering the noise reduction mechanism is to understand the moderate, but constant noise reductions beyond $St\sim 1.5$.

At the mid-range observer angle of 60°, ETI at an IMFR of 1% attenuates the spectral noise peak by 0.9dB as compared to the 0.5dB by PTI. However, PTI was found to be the more effective technique when considering the OASPL reduction of 0.6dB, which dwarfs the 0.1dB by ETI. Once again this can be attributed to the broad-band reductions in SPL by PTI, unlike ETI, which reduces low frequency noise at the expense of increased ultrasound. In contrast to the success of these two techniques, ITI displayed no noise benefit at this angle with amplified peak SPL and OASPL values of 0.4dB and 0.3dB respectively.

At 30°, in the vicinity of the peak noise radiating angle of jet, all three techniques performed similarly with ITI and ETI having spectral peak ($St=0.17$) noise benefits of 1.8dB and 1.3dB respectively. ITI also proved to be the most effective overall at this angle with an OASPL reduction of 1.3dB. The SPL spectra for PTI once again was absent from any increase in high frequency noise, in contrast to the other two forms of injection.

At the most extreme downstream angle of 15°, ITI proved to be most successful technique with attenuations in the spectral peak and OASPL values by of 5.7dB and 6.3dB respectively. ETI followed closely with an OASPL reduction of 4.7dB. However the 0.7dB reduction by PTI was found to be relatively insignificant, rendering it ineffectual at this angle.

The Strouhal number, at which the spectral noise cross-over occurs, decreases with observer angle for both ITI & ETI. However it is a phenomenon that is non-existent for PTI. The spectral noise cross-over for ETI occurs at a higher Strouhal number than for ITI at any given observer angle, and will be further discussed in Chapter 6.

In conclusion, from Figure 4.20 and Figure 4.21, ITI is shown to be strongest at downstream angles of 30°-15° with adverse effects in the mid range angles of 70°-40°. ETI yields the greatest noise benefits at the sideline, 90°-80°, and downstream angles of 30-15° with moderate reductions elsewhere. PTI is totally different in nature, with an advantage over the other two techniques in the mid-range angles of 70°-40°. Two main distinctive features of the pulsating technique are that there is no crossover of noise at higher frequencies and that any reductions, albeit small, are consistent across all frequencies of the SPL spectra.

Table 4.1: Comparison of Noise Reductions from all Air Injection Techniques

INJECTION TECHNIQUE	PRIMARY	INTERNAL	EXTERNAL	PULSE
Injection Mass Flow Ratio	0%	40%	1%	0.7%
OBSERVER ANGLE 90°				
SPL, Screech Tone at $St=0.74, f=9600\text{Hz}$	117.8	111.4	110.3	111.3
ΔSPL of Screech Tone (dB)	-	-6.4	-7.5	-6.5
SPL, Broadband Shock at $St=1, f=13000\text{Hz}$	115.5	110.6	111.8	112.7
ΔSPL of B-Band Shock	-	-4.9	-3.7	-2.8
High f Noise Cross-Over (St)	-	2.0	2.5	-
ΔOASPL (dB)	-	-0.6	-0.9	-1.0
OBSERVER ANGLE 60°				
SPL of Noise Peak at $St=0.2, f=2600\text{Hz}$	117.7	118.1	116.8	117.2
ΔSPL of Noise Peak (dB)	-	+0.4	-0.9	-0.5
High f Noise Cross-Over (St)	-	1.3	2.1	-
ΔOASPL (dB)	-	+0.3	-0.1	-0.6
OBSERVER ANGLE 30°				
SPL, Preferred Mode at $St=0.17, f=2200\text{Hz}$	131.1	129.3	129.8	130.6
ΔSPL of Preferred Mode (dB)	-	-1.8	-1.3	-0.5
SPL of Ultrasound at $St=2.5, f=32000\text{Hz}$	101.4	102.8	104.1	101.3
ΔSPL of Ultrasound	-	+1.4	+2.7	-0.1
High f Noise Cross-Over (St)	-	0.6	0.9	-
ΔOASPL (dB)	-	-1.3	-0.9	-1.2
OBSERVER ANGLE 15°				
SPL of Noise Peak at $St=0.12, f=1500\text{Hz}$	132.9	127.2	128.2	132.3
ΔSPL of Noise Peak (dB)	-	-5.7	-4.7	-0.6
High f Noise Cross-Over (St)	-	-	-	0.9
ΔOASPL (dB)	-	-6.3	-4.7	-0.7
ALL ANGLES				
Peak OASPL Angle	25	25	25	25-20
Max ΔOASPL Angle	-	15°	15°	30°

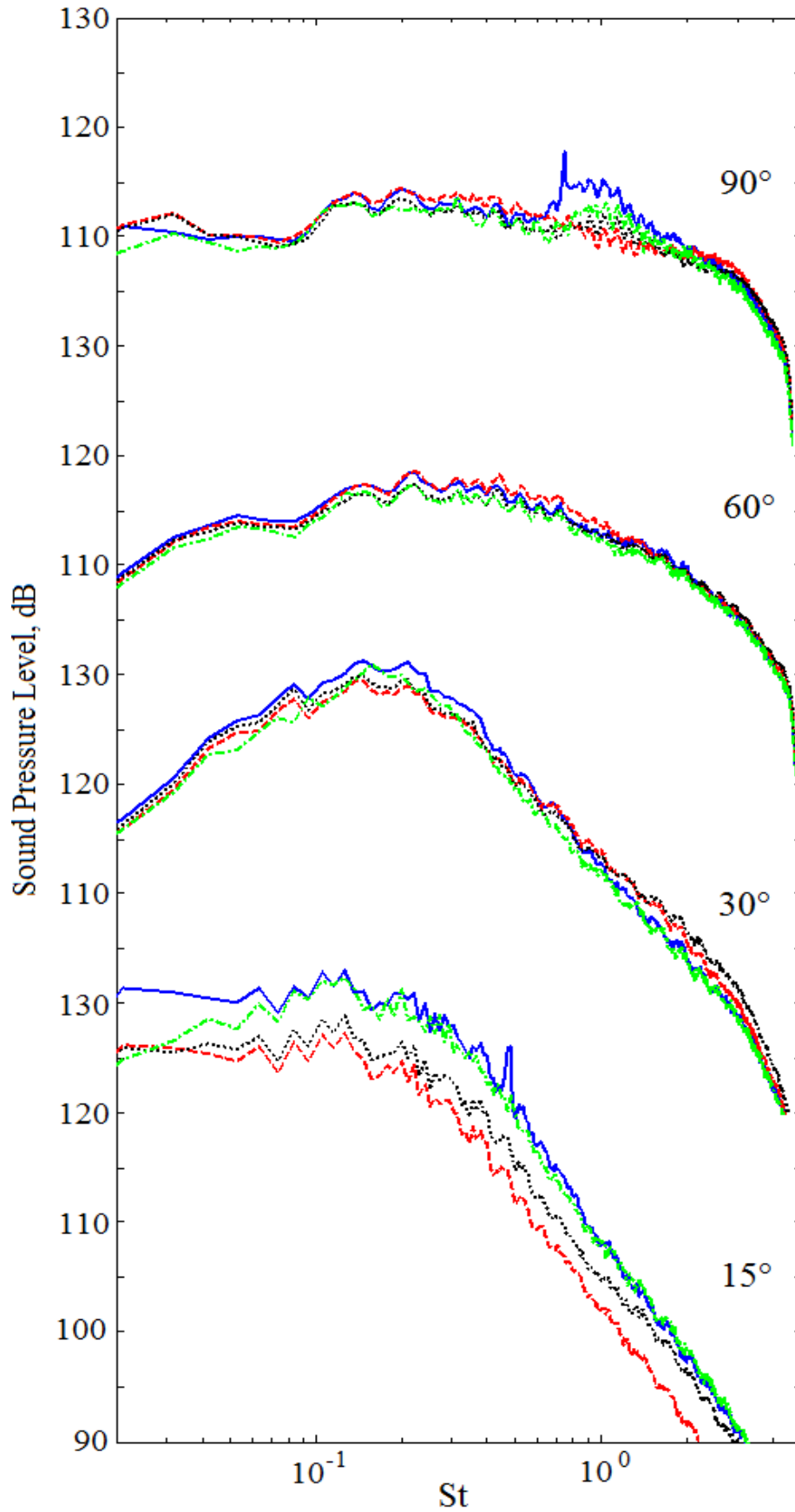


Figure 4.19: Comparison of SPL spectra for the optimal noise reducing configuration of each technique; internal injection at 40% IMFR (---), external injection at 1% IMFR (···) & 2kHz pulsating injection at 0.7% IMFR (-.-) against the primary jet (—).

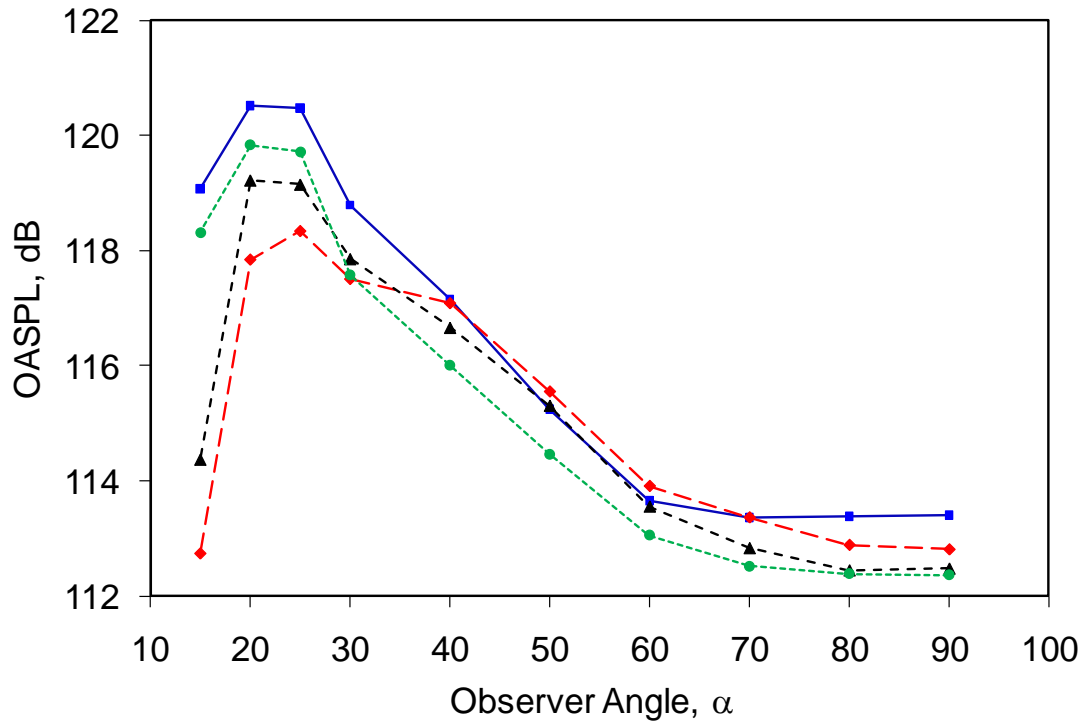


Figure 4.20: Comparison of OASPL at various observer angles for the optimal noise reduction configurations of each technique. Primary jet (—■—), external injection at 1.1% IMFR (-▲-), internal injection at 40% IMFR (-◆-) & 2kHz pulsating injection at 0.7% IMFR (-●-).

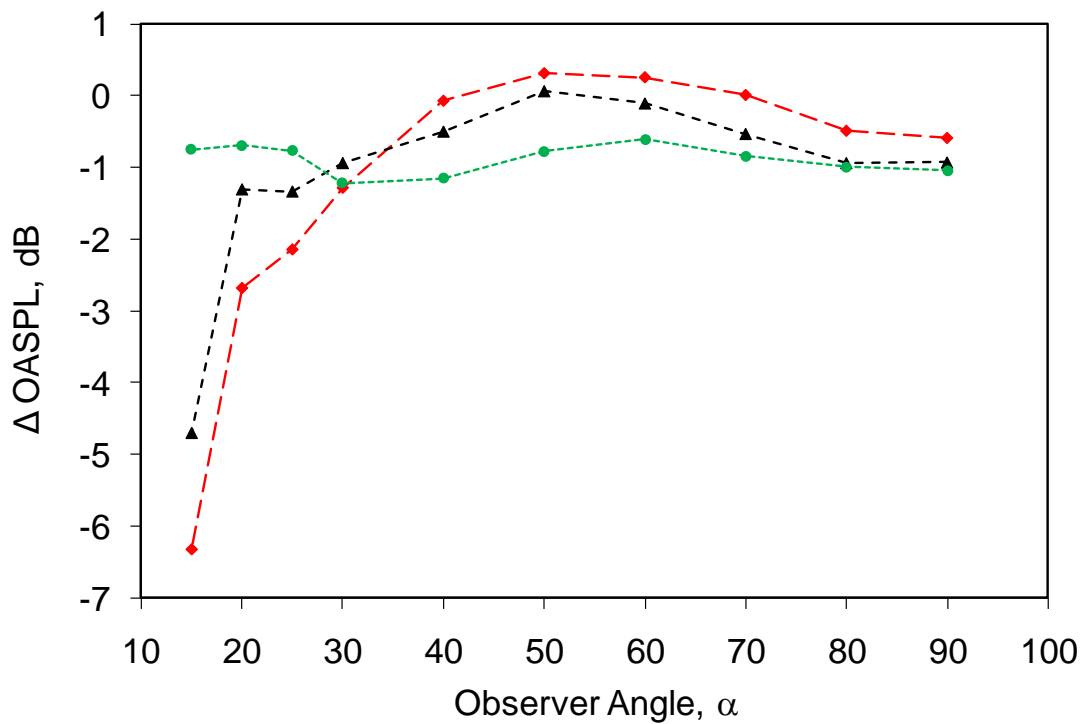


Figure 4.21: Comparison of jet noise reduction for the optimal noise reduction configurations of each technique; external injection at 1.1% IMFR (-▲-), internal injection at 40% IMFR (-◆-) & 2kHz pulsating injection at 0.7% IMFR (-●-) with reference to the primary jet.

4.2 Autocorrelation

Figure 4.22 shows a comparison of the normalised autocorrelation, R_{AC} , of the voltage signals from each of the 10 microphones. Upon visual inspection, the autocorrelations can instantly be divided into two groups based upon their peak correlation width ($2\tau_{max}$). The upstream and mid-range angles from 90°-50° are characterised by narrow correlation widths, whereas downstream angles from 30°-15° exhibit increasingly wider correlation peaks, with 40°-50° marking a clear transition between the two categories. Since the energetic small-scaled turbulent structures are known to dominate the sideline acoustic field of the jet, it is reasonable to accept the 90° autocorrelation function as a fair depiction of fine-scale structure noise, and similarly the 30° autocorrelation function as a representation of the noise from the large-scale turbulent structures. Through this definition it is evident that noise emitted from these two types of structures are distinctly different in nature. The minor fluctuations on either side of the correlation peaks of the sideline angles have been previously identified as products of low-amplitude reflections from the anechoic chamber walls and are considered insignificant.

The spatial correlation lengths existing within the acoustic field of the jet can be approximated by simply multiplying the normalised autocorrelation width, $2\tau_{max}$, by the propagating speed of the acoustic waves, a , which in equation (3.29) is assumed to be equal to that of the speed of sound (Tam, 2008). Based on the ambient temperature of 293K (Table 3.1), the sonic velocity ‘ a ’ is 343m/s. The correlation width ($2\tau_{max}$) is defined as twice the time lag at which the correlation peak reaches a maximum negative (R_{AC-max}), as shown in Figure 4.22. Based on this equation (3.29), the spatial correlation lengths or noise source structure sizes are listed with respect to their angle of propagation in Table 4.2.

Table 4.2: Noise Source Structure Sizes Approximated from Peak Correlation Time Lags

Microphone	90°	80°	70°	60°	50°	40°	30°	25°	20°	15°
$2\tau_{max}$ (ms)	0.01	0.02	0.03	0.04	0.1	0.2	0.3	0.31	0.32	0.33
Structure Size (mm)	3	7	10	14	34	68	102	105	109	112
Structure Size (D_j)	0.1	0.2	0.3	0.5	1.1	2.3	3.4	3.5	3.6	3.7

The noise structure sizes are shown to increase with decreasing observer angle up to the peak noise radiating angle of the jet (25°), beyond which there is a decay in the rate of growth. The radiation angle of the preferred modes of the jet ($St \sim 0.17$, $f \sim 2\text{kHz}$) is 30°. Based on the correlation peak at this angle, the radial (direction of propagation) length-scale of the Mach 1.3 jet is approximately 3 nozzle diameters. This compares relatively

well with the 2.6 nozzle diameters calculated for a Mach 1.67 jet, using a similar method (Tam, 2008).

The difference in the correlation pattern between air injection techniques becomes more apparent at angles downstream of 30°. The contrast in nature is a maximum at 15°, where despite the half-width time lags being the same, the correlation's negative peak depth is greater for the pulsating injection as compared to the primary jet. According to Tam (2008), one of the first influences of large-scale coherent structures on the measurements of the acoustic field is the deepening of negative auto-correlation peaks (R_{AC-max}). Hence, the opposing trend seen for the internal tangential injection technique may suggest the decay of influence from the large turbulent structures at this most extreme downstream angle. This aspect will be further discussed upon the availability of the flow-field data in the following chapter. The negative correlation peaks were first introduced at 40°, irrespective of air injection technique, justifying this choice as a transitional angle beyond which the effects of low-frequency noise from large-scale structures becomes a dominate feature of the acoustic spectra, as seen in the previous SPL results.

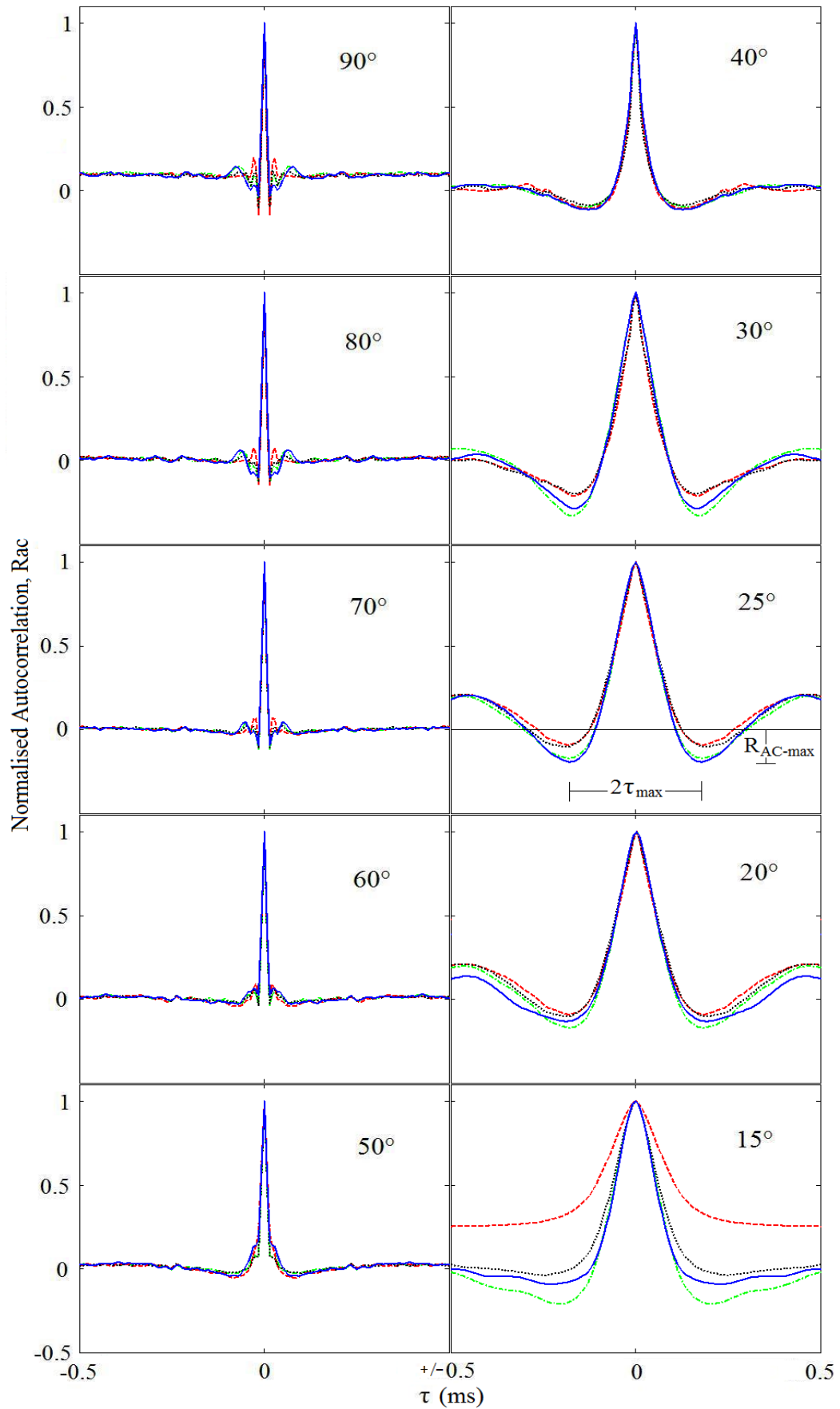


Figure 4.22: Comparison of the normalised autocorrelation of pressure signals at various observer angles for the primary jet (—), internal injection at 40% mass flow ratio (---), external injection at 1% mass flow ratio (···) & 2kHz pulsating injection at 0.7% mass flow ratios (-.-).

4.3 Cross-Correlation

Figure 4.23 shows the normalised cross-correlation, R_{CC} , between adjacent microphone signals as the separation angle between them is varied. By selecting the 30° angle microphone as the fixed reference, the second microphone location is varied from 90° - 15° in order to extract information on the coherence of noise structures in the acoustic far-field. The cross-correlations between microphone signals from the same location (30°), gives an effective autocorrelation, which has an expected value of unity for zero time separation. However, Figure 4.23 also indicates the lack of correlation when the second microphone is outside the Mach wave radiation cone of approximately 30° (Tam, 2009; Petitjean, 2006). In the case where both microphones are in the region of preferred radiation of large-scale structure noise (30° - 15°), the magnitude of the normalised cross-correlation is up to 0.8 (25°). Away from this region, the values of coherence drop sharply to zero with increasing separation angle. The observations are independent of the type of air injection when compared to the primary jet.

Figure 4.24 shows the cross-correlation between adjacent microphone signals with reference to the one at 80° . Despite a separation interval of only 10° to the immediate neighbouring microphone in the sideline direction, the correlation values are no more than 0.1, suggesting low spatial correlation and randomness of noise structures in this region. Figure 4.25 shows an increasing value of R_{CC} up to 0.2 between microphones at 40° and 50° based on a time lag of ~ 0.6 ms.

The extent to which the downstream propagating large-scale structures are coherent is confirmed by Figure 4.26 with a correlation peak of 0.8 at a time lag of 0.6ms between signals from microphones at 25° and 30° . Tam (2008) emphasised that the distinct disparity between the R_{CC} of the sound field radiated by the fine and large-scale turbulence structures is only the wavelength of the resultant sound waves and not their intensities. The pressure signals from the adjacent microphones are very similar, but due to the slight variation in propagation distance between them, the signals are misaligned in the time domain. Thus, by delaying the time lag, τ , between the signals from microphones 1 and 2 they can be aligned, resulting in a correlation product with a positive maximum value (Viswanathan, 2010).

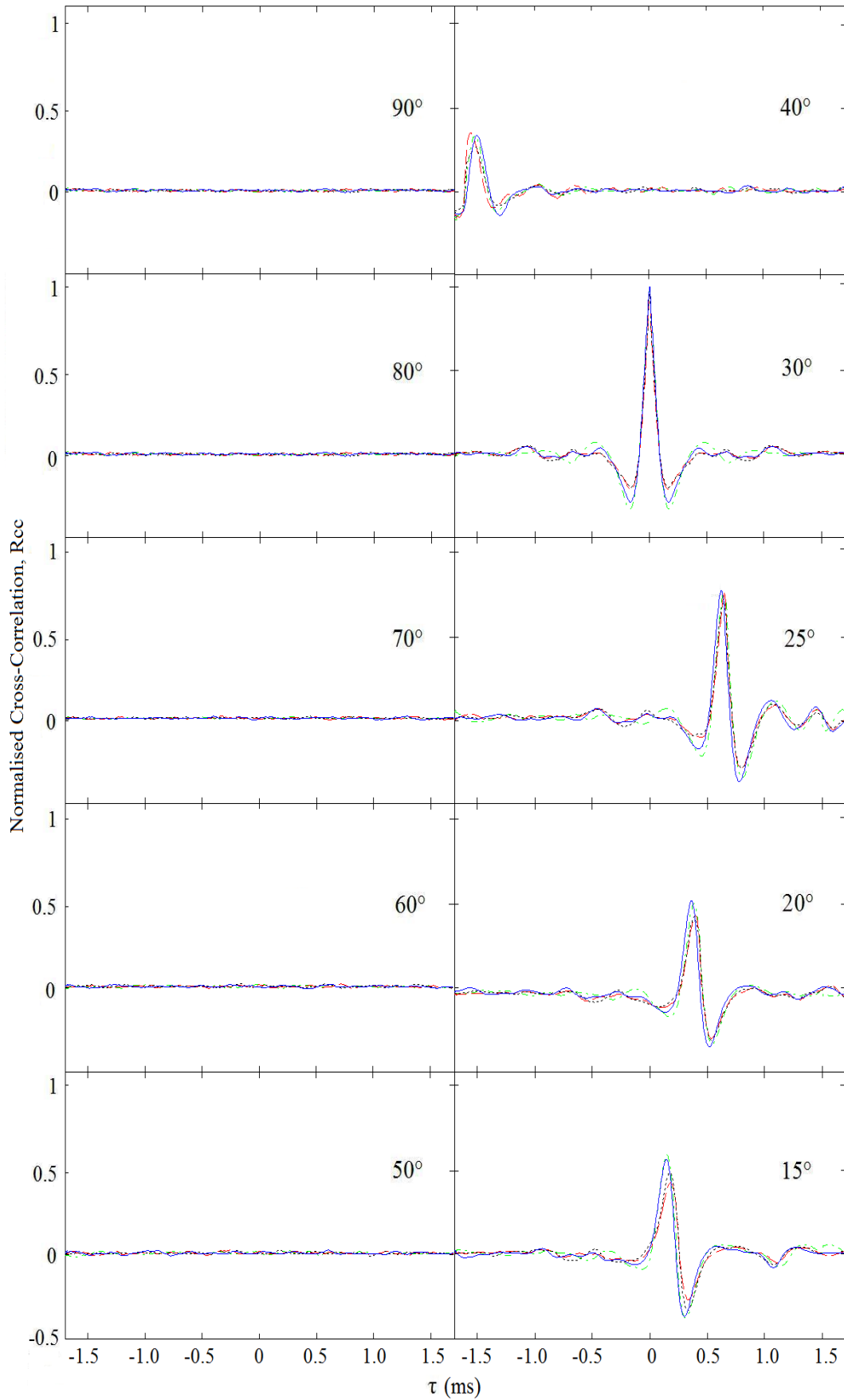


Figure 4.23: Comparison of normalised cross-correlation of pressure signal with fixed microphone at 30°; primary jet (—), internal at 40% IMFR (---), external at 1% IMFR (···) & 2kHz pulsating at 0.7% IMFR (-.-).

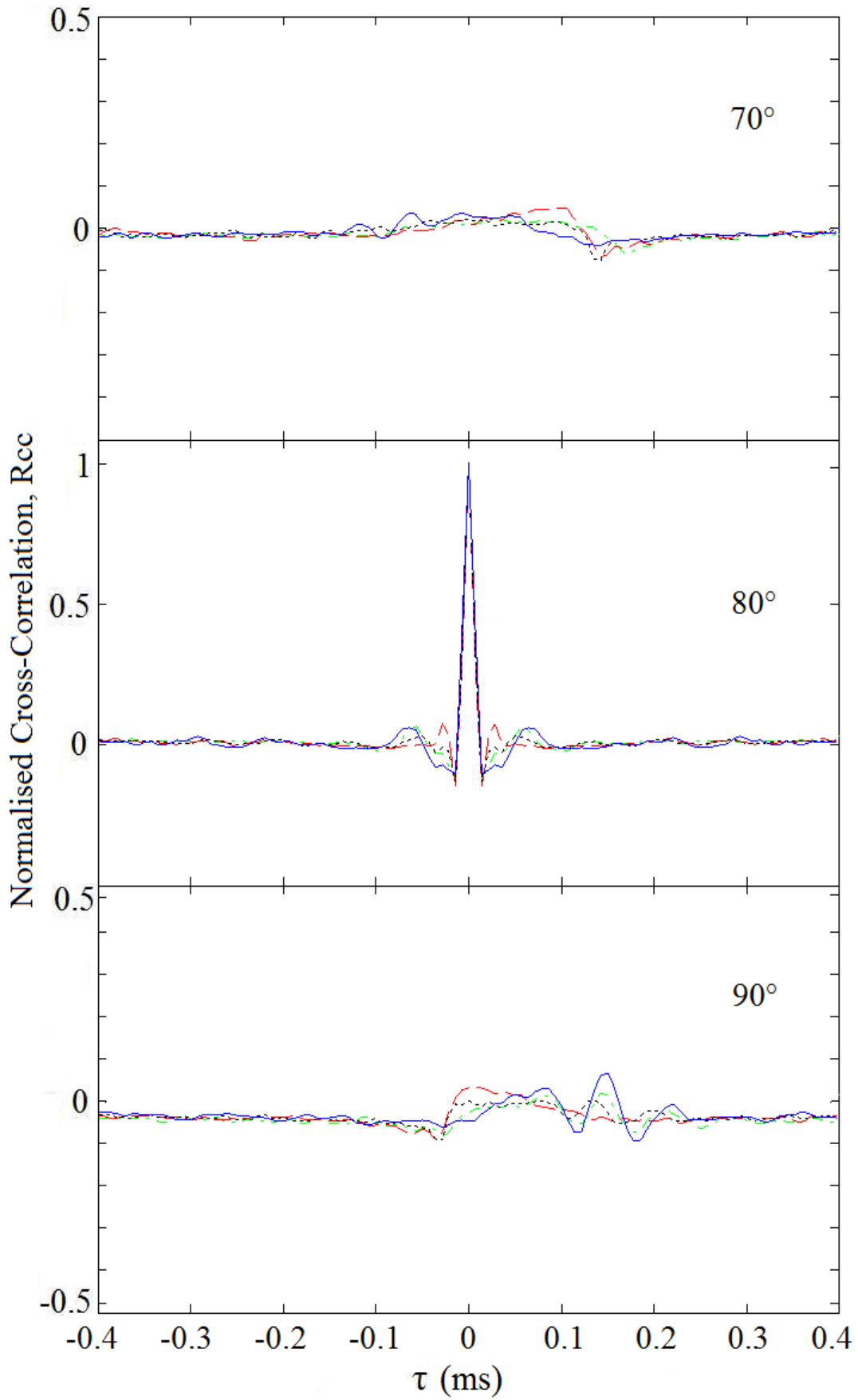


Figure 4.24: Comparison of cross-correlation of pressure signals from adjacent microphones with respect to the one at 80°; primary jet (—), internal injection at 40% IMFR (---), external injection 1% IMFR (···) & 2kHz pulsating injection at 0.7% IMFR (-.-).

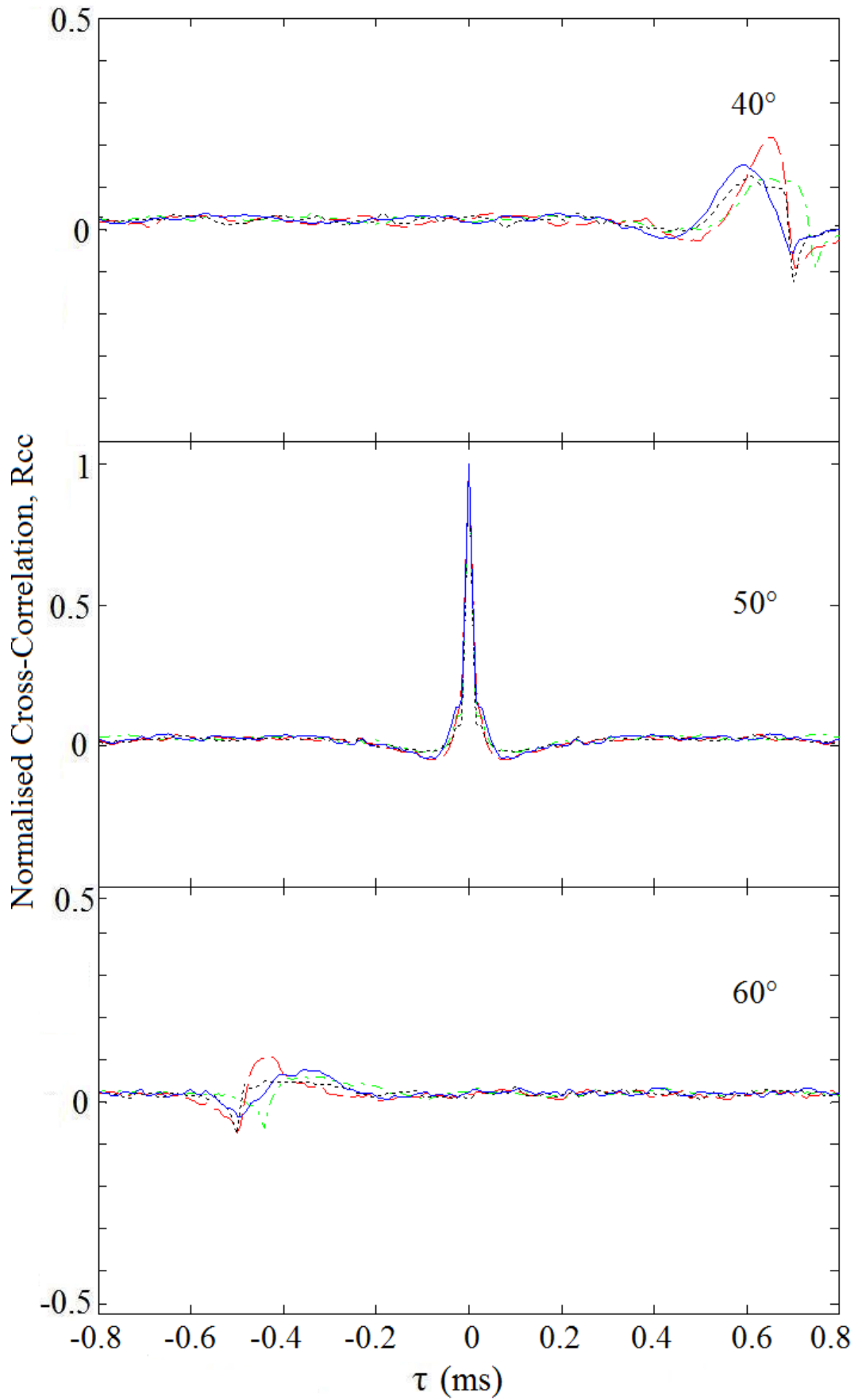


Figure 4.25: Comparison of cross-correlation of pressure signals from adjacent microphones with respect to the one at 50°; primary jet (—), internal injection at 40% IMFR (---), external injection at 1% IMFR (···) & 2kHz pulsating injection at 0.7% IMFR (-.-).

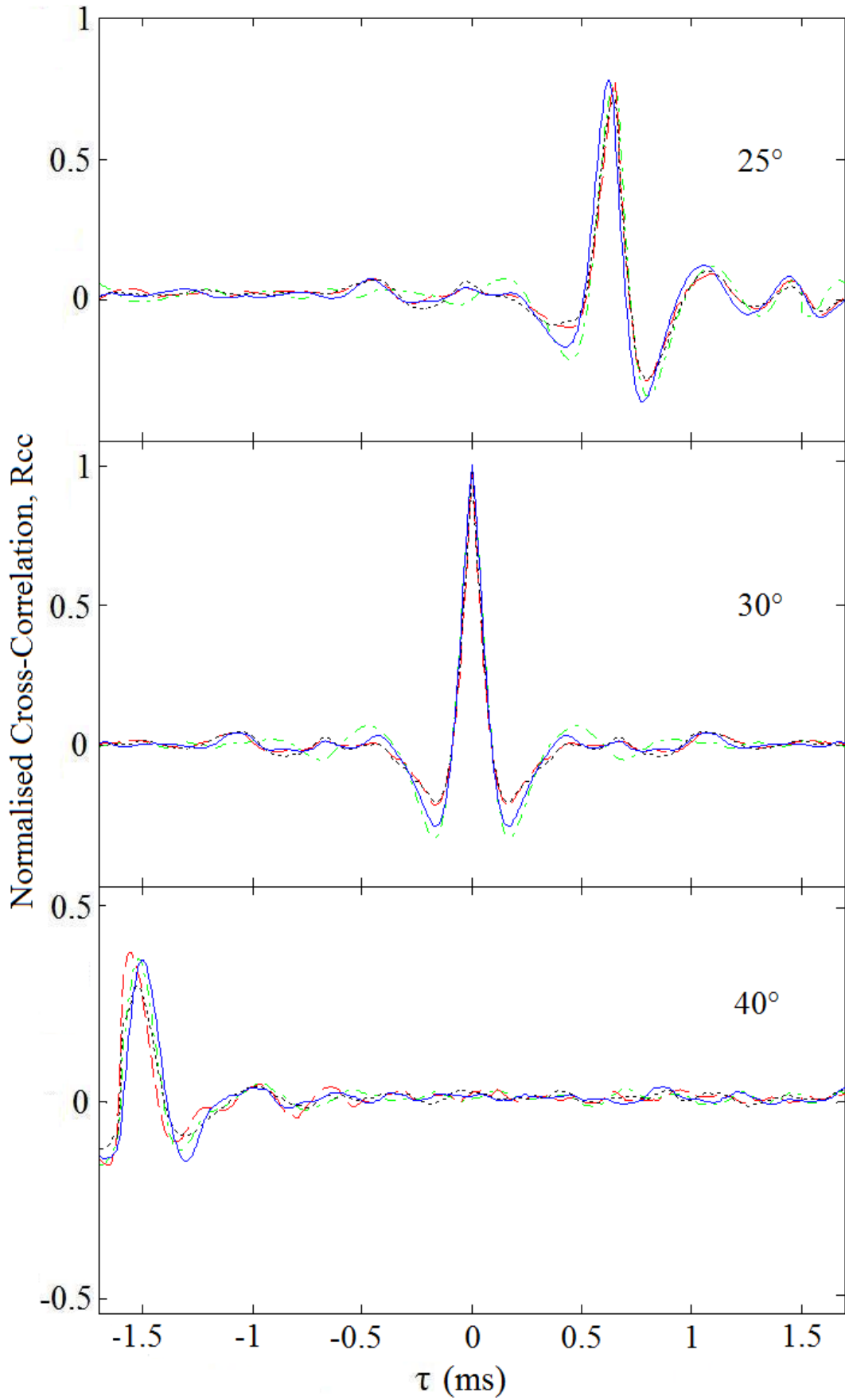


Figure 4.26: Comparison of cross-correlation of pressure signals from adjacent microphones with respect to the one at 30°; primary jet (—), internal injection at 40% IMFR (---), external injection at 1% IMFR (···) & 2kHz pulsating injection at 0.7% IMFR (-.-).

4.4 Cross-Spectral Time Lag

The normalised cross-correlation between adjacent microphone signals returns the time lag for peak correlation between the overall signals, making the process insensitive to frequency. It has already been shown that the noise peaks in the SPL spectra vary significantly with frequency and observer angle. Hence, in order to locate the source of structures radiating noise at a specific frequency, the cross-spectrum time-lags with respect to particular frequencies must first be obtained. The methodology outlined in § 3.7.7 will be used for this purpose.

Figure 4.27 shows how the acoustic power cross-spectra vary with frequency for three adjacent microphone pairings. The cross-spectra, as shown in equation (3.32), is the multiplication of the FFT of a pressure signal by its complex conjugate, and is denoted by the black line in Figure 4.27. The green line indicates the time lag, τ_{peak} , at which the peak cross-spectral correlation occurs with respect to frequency, and is derived using the phase lag between the signals, as shown in equation (3.31). It is evident that the peaks associated with shock noise in the far-field SPL spectra are also a feature of the corresponding cross-spectra pairing of 90° & 80° . The time lag for the sideline cross-spectra pairing remains fairly constant at $\tau=0.1\text{ms}$ for a broad range of frequencies. It begins to increase to about 0.3ms - 0.4ms for the 60° , 50° cross-spectra pairing and reaches a peak of 1.5ms for the 40° , 30° pairing at Kelvin-Helmholtz roll-up frequency of $\sim 2\text{kHz}$. The significantly larger time lags are due to larger propagation distances between adjacent microphone pairings in the downstream direction. The time lag derived from the cross-spectra, which is effectively the difference in time it takes for the same acoustic wave to reach the two microphones, matches very closely to those obtained from the normalised cross-correlation function (3.30), in Figure 4.24 to Figure 4.26, but with the added advantage of investigating the frequency dependence. These results will be exported to the following section to calculate the approximate noise source locations.

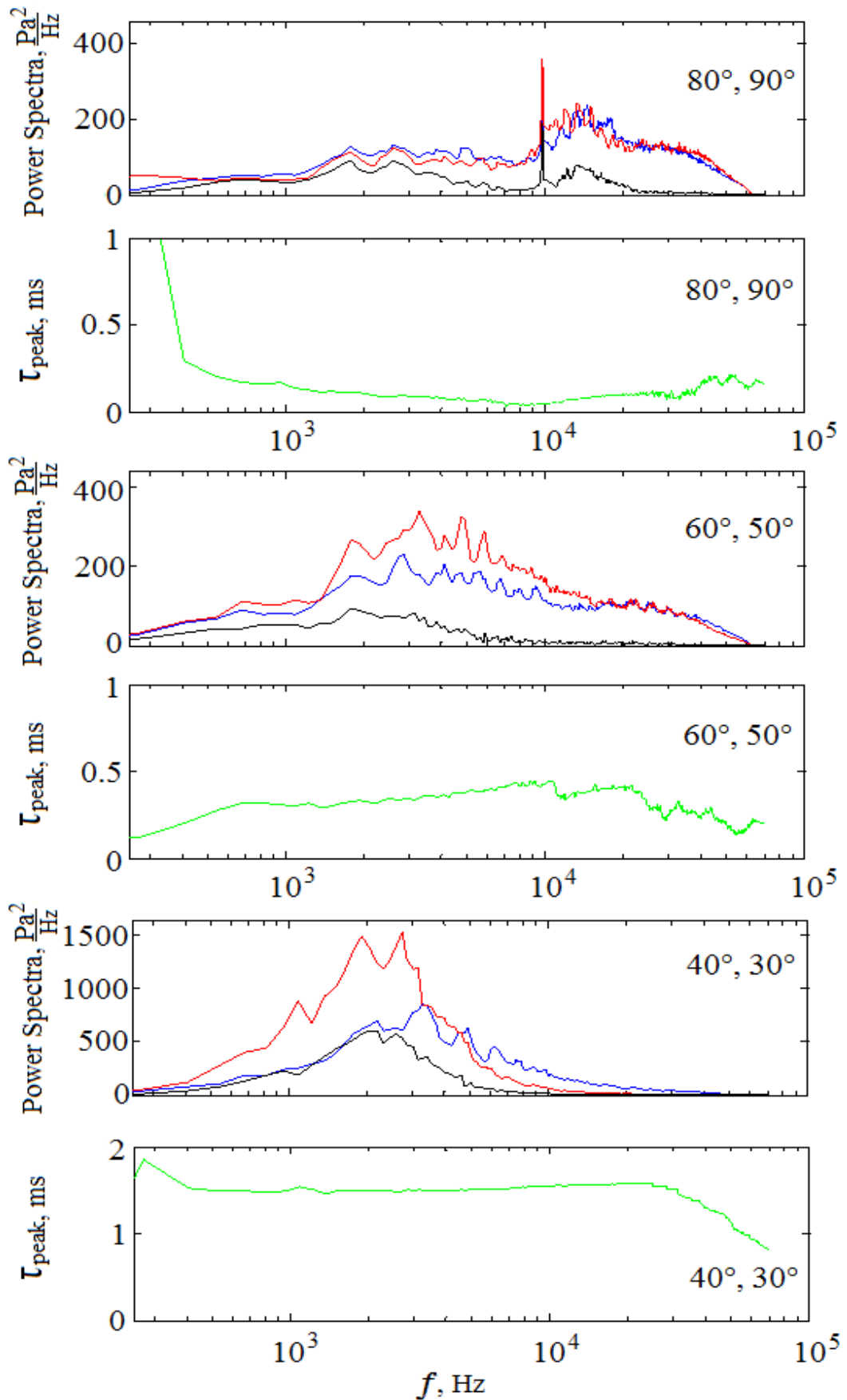


Figure 4.27: Comparison of normalised acoustic power spectra at various angles and frequencies; auto-spectra of signal 1 (—), auto-spectra of signal 2 (—), cross-spectra of adjacent signals 1 & 2 (—) and the time lag corresponding to the peak correlation value of the cross-spectra (—).

4.5 Noise Source Location

Theoretically, an acoustic time lag between two microphone locations can be derived using their co-ordinates, the location of the compact noise source origin along the streamwise axis, and the assumption that all acoustic waves propagate spherically at the constant speed of sound. This theoretical time lag can then be varied by changing the noise source location incrementally along the streamwise axis. The accepted noise source location is therefore the one for which the corresponding theoretical time lag most closely matches the experimental one, as described in the trial and error approach of § 3.7.7. Figure 4.28 shows the streamwise location in nozzle diameters at which the error between the theoretical and experimental time lags converges to zero. It also serves to compare the variation of the 2kHz source location with the introduction of each of the air injection techniques. Table 4.3 summarises the 2kHz source locations (x/D_j) with respect to the cross-correlation pairings from which the time lags were derived. The 2kHz source coincides with the preferred mode of the jet with a radiation angle of 30° as shown in Figure 4.1. For the primary jet there seems to be good agreement on source location, with all microphone pairings yielding an average location of $x/D=11.8$. The microphone pairings of $40^\circ-30^\circ$, $30^\circ-25^\circ$ & $25^\circ-20^\circ$ display a divergence in error between theoretical and experimental time lags with increasing input value of source location. For the purpose of further investigating this matter, the experiment was repeated with finer resolution in this downstream region with new microphone pairings of $40^\circ-35^\circ$, $35^\circ-30^\circ$, $30^\circ-28^\circ$, $28^\circ-25^\circ$ & $25^\circ-22^\circ$. Despite this, either divergence or a very slow rate of convergence was detected, so as to suggest a source location beyond $x/D=20$. For the sake of brevity those results are not presented. All the air injection techniques show a tendency to move the source location of large-scale structure noise closer to the nozzle exit, more so for ITI.

Table 4.3: 2kHz Noise Source Location (x/D_j) based on Peak Cross-Correlation Time Lag

Cross-Correlation	$90^\circ, 80^\circ$	$80^\circ, 70^\circ$	$70^\circ, 60^\circ$	$60^\circ, 50^\circ$	$50^\circ, 40^\circ$	$20^\circ, 15^\circ$	Mean
Primary Jet (x/D_j)	9.9	11.2	12.0	9.5	13.0	15.3	11.8
Internal Injection	7	8.2	7.8	5.2	11.5	12	8.6
External Injection	8.5	10.2	11.2	8.8	12.4	13	10.7
Pulsating Injection	9.1	8.6	10.5	11.4	9.2	17	11.0

Figure 4.29 makes a similar comparison of source location for the 6.3kHz source, which corresponds to the fundamental screech tone on the 15° spectra in Figure 4.1. Table 4.4 shows the source location to shift upstream for this higher frequency noise, which supports the view that high frequency, upstream radiating noise from fine-scale

turbulence, originates close to the nozzle, with lower frequency noise originating from beyond the potential core.

Table 4.4: 6.3kHz Noise Source Location (x/D_j) based on Peak Cross-Correlation Time Lag

Cross-Correlation	90°, 80°	80°, 70°	70°, 60°	60°, 50°	50°, 40°	20°, 15°	Mean
Primary Jet (x/D_j)	6.5	6.0	7.8	4.3	12.5	6.3	6.2
Internal Injection	4.4	4.4	4	2.2	10.2	2	3.4
External Injection	4.2	4.4	4.1	1.6	10.5	4.4	3.1
Pulsating Injection	5.8	2.9	4.5	6.4	8.4	10	5.9

Figure 4.30 suggests that the harmonic component of screech noise originates around $x/D=5$, which is further upstream from 6.3kHz fundamental screech and the 2kHz preferred modes. In Table 4.5 both internal and external tangential injection techniques have the effect of halving the source location from the nozzle exit in comparison to the primary jet. All three techniques were shown to totally eradicate the harmonic component of screech noise, as shown in Figure 4.19.

Table 4.5: 9.6kHz Noise Source Location (x/D_j) based on Peak Cross-Correlation Time Lag

Cross-Correlation	90°, 80°	80°, 70°	70°, 60°	60°, 50°	50°, 40°	20°, 15°	Mean
Primary Jet (x/D_j)	6.0	5.5	3.4	3.9	9.9	6.0	5.0
Internal Injection	3.5	3.5	3.2	0.6	9	1.2	2.5
External Injection	3.4	3.3	3	0.4	9	2.5	2.5
Pulsating Injection	5.1	1.2	9.4	5	5.8	9	5.9

Figure 4.31 is evidence that broadband shock noise originates around $x/D=6$, which is slightly downstream to the harmonic component of screech noise. Once again both the internal and external air injection techniques have been shown to have a similar mean effect of reducing the source location from the nozzle exit by half as shown in Table 4.6.

Table 4.6: 13kHz Noise Source Location (x/D_j) based on Peak Cross-Correlation Time Lag

Cross-Correlation	90°, 80°	80°, 70°	70°, 60°	60°, 50°	50°, 40°	20°, 15°	Mean
Primary Jet (x/D_j)	7.9	3.6	7.2	6.0	9.0	4.4	5.8
Internal Injection	3.1	3.1	2.2	0	8.2	0.5	1.8
External Injection	2.2	2.8	2.8	-0.5	8.1	1.2	1.7
Pulsating Injection	2.6	1.8	14.4	4.8	5.2	7.8	4.4

The noise source locations based on the 50°, 40° pairing consistently return higher values than the neighbouring pairings, irrespective of frequency. Hence the corresponding x/D values in each table have been regarded as an anomalous and are not accounted for in the mean noise source location calculations.

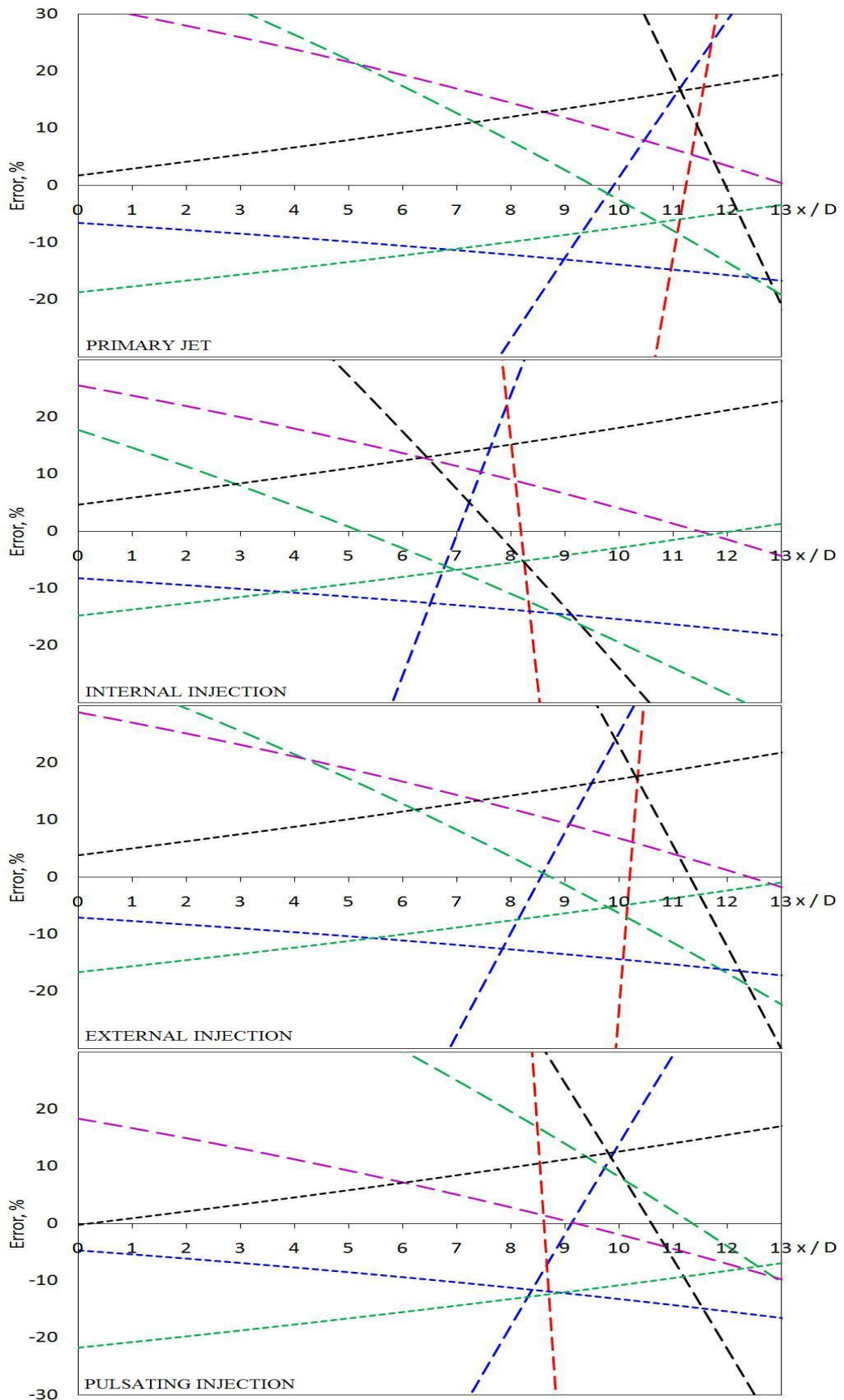


Figure 4.28: Noise source location for 2kHz ($St \sim 0.17$) noise based on error convergence between the theoretical and experimental cross-correlation time lags between microphones at $90^\circ, 80^\circ$ (—), $80^\circ, 70^\circ$ (—), $70^\circ, 60^\circ$ (—), $60^\circ, 50^\circ$ (—), $50^\circ, 40^\circ$ (—), $40^\circ, 30^\circ$ (—), $30^\circ, 25^\circ$ (—), $25^\circ, 20^\circ$ (—), $20^\circ, 15^\circ$ (—).

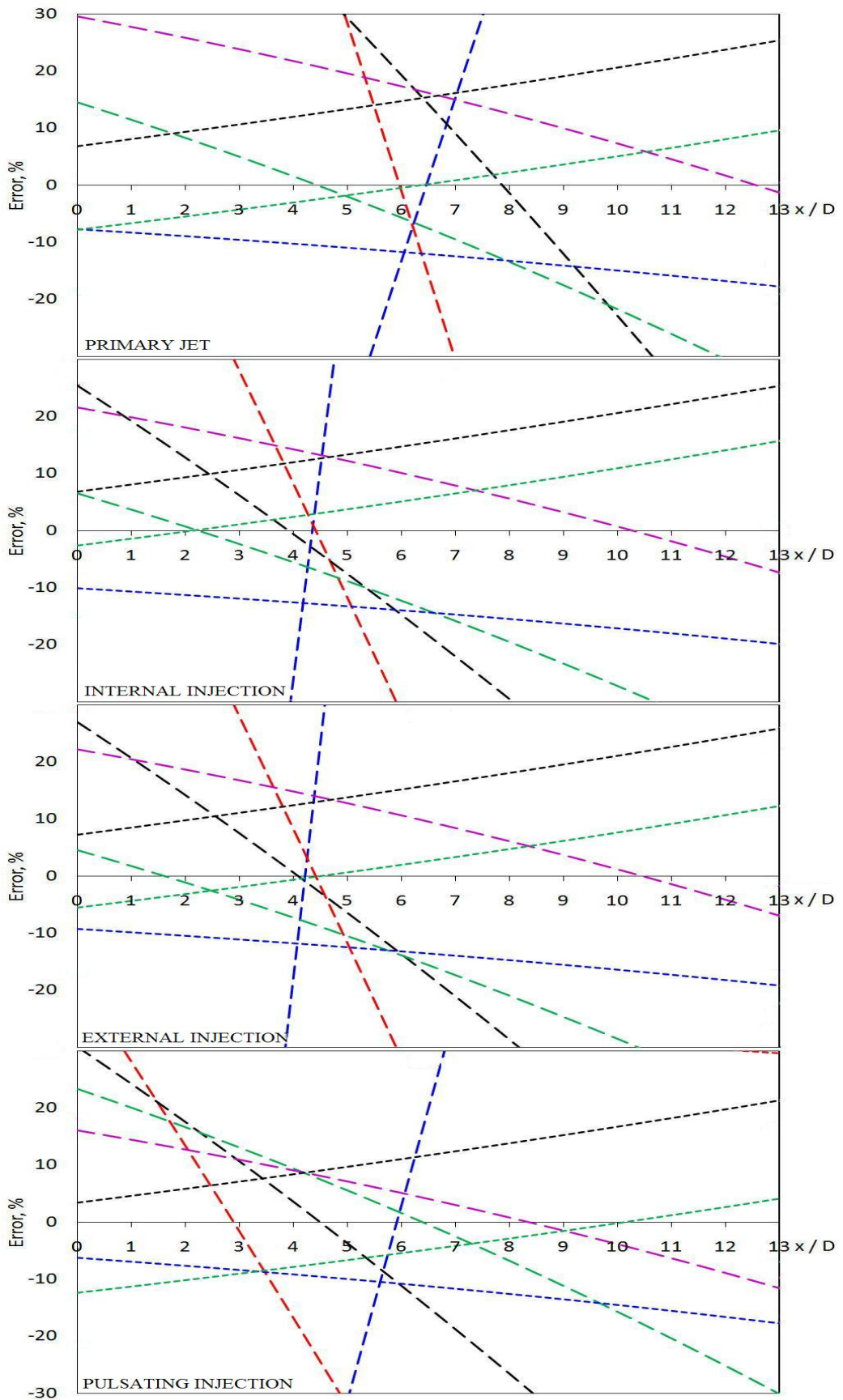


Figure 4.29: Noise source location for 6.3kHz ($St \sim 0.49$) noise based on error convergence between the theoretical and experimental cross-correlation time lags between microphones at 90° , 80° (—), 80° , 70° (—), 70° , 60° (—), 60° , 50° (—), 50° , 40° (—), 40° , 30° (—), 30° , 25° (—), 25° , 20° (—), 20° , 15° (—).

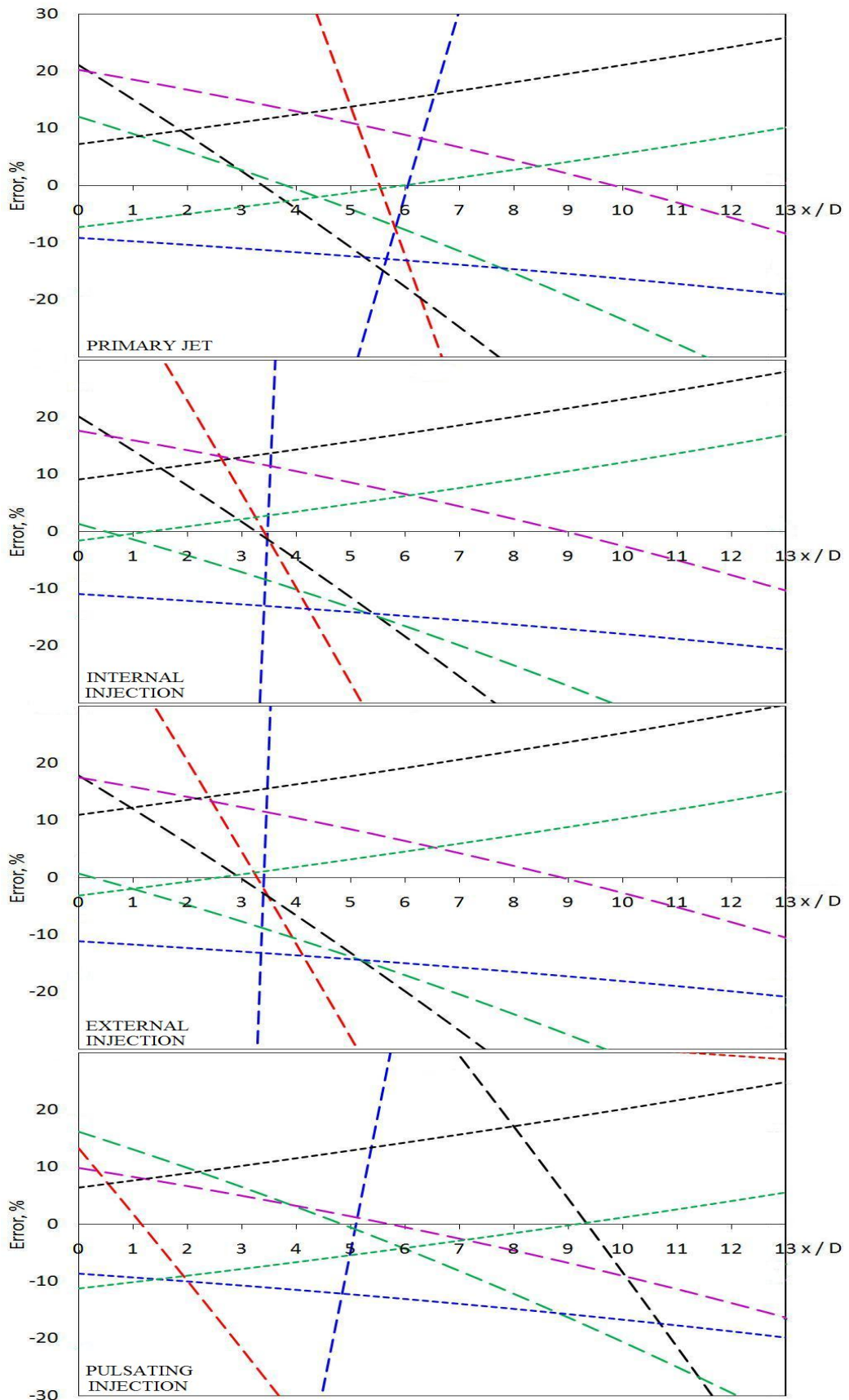


Figure 4.30: Noise source location for 9.6kHz ($St \sim 0.75$) noise based on error convergence between the theoretical and experimental cross-correlation time lags between microphones at 90° , 80° (—), $80^\circ, 70^\circ$ (—), $70^\circ, 60^\circ$ (—), $60^\circ, 50^\circ$ (—), $50^\circ, 40^\circ$ (—), $40^\circ, 30^\circ$ (—), $30^\circ, 25^\circ$ (—), $25^\circ, 20^\circ$ (—), $20^\circ, 15^\circ$ (—).

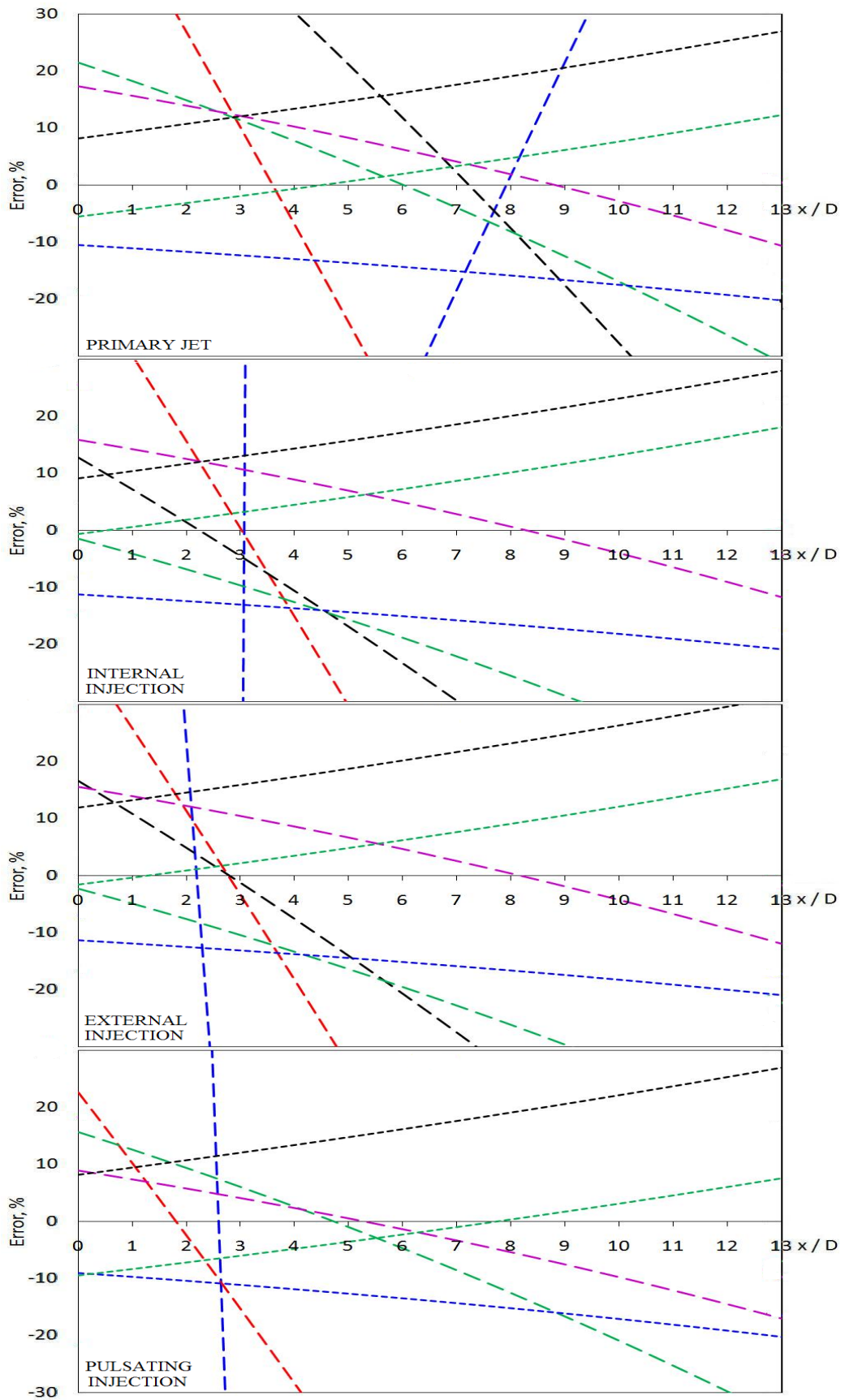


Figure 4.31: Noise source location for 13kHz ($St \sim 1$) noise based on error convergence between the theoretical and experimental cross-correlation time lags between microphones at 90° , 80° (—), 80° , 70° (—), 70° , 60° (—), 60° , 50° (—), 50° , 40° (—), 40° , 30° (—), 30° , 25° (—), 25° , 20° (—), 20° , 15° (—).

4.6 Near Field Sound Pressure Level

For the purpose of understanding the characteristics of the jet's acoustic far-field presented thus far, the impact of fluidic injection on the acoustic near-field is also examined. The SPLs were derived from the pressure signal measurements from a microphone grid spanning $2D_j$ upstream of the nozzle to $13D_j$ downstream along the streamwise jet axis. In the radial direction it extended from $6D_j$ to $12D_j$ in the same plane. The axial and radial resolutions of the grid were $\frac{1}{4}$ and $\frac{1}{2}$ nozzle diameters respectively. As explained in § 3.6, the near-field of the jet is characterised by non-spherical and probably non-linear sound propagation (Petitjean, 2003) and so there was no meaning in angling the microphones towards the nozzle or in applying a distance calibration.

Figure 4.32 shows contour plots of near-field OASPL with and without external tangential air injection. For both cases the spread of the contours has an oblong shape, suggesting an elliptic distribution of the acoustic field from the streamwise axis. This observation can be explained as the combined effect of an array of lower intensity sources with respect to the main source around $x/D=5.5$. As noted in Table 4.7, ETI does not affect the OASPL source location but does reduce noise by up to 2dB at most locations.

Figure 4.33 is evidence of near-field SPL reductions for 2kHz noise. The contour shape suggests this type of noise originates from around $13D_j$ from the nozzle exit, showing a precise match with the source location from the far-field cross-correlation between microphones at 50° and 40° as shown in Figure 4.28.

Figure 4.34 is particularly interesting since it suggests that the 6.3kHz noise has two source locations with the one at the nozzle exit being slightly weaker than the one at $x/D=13$. Introducing ETI at 1% reduces the SPL of the weaker source by 4-6dB with a slight reduction in SPL and source location from nozzle of the second noise source.

Figure 4.35 shows that the intense harmonic screech tone originates at $x/D=4.5$ with the contour distribution showing a clear propagation towards the sideline angle, through sustained SPL in that direction. With added ETI the screech tone is substantially reduced by up to 8dB near the source with a second, much weaker, source at $x/D=9$ becoming dominant. Once again the source location for screech shows excellent agreement with Figure 4.30 and Table 4.5.

Figure 4.36 shows that the broadband shock associated noise originates from $x/D=6$ with a distribution in a direction perpendicular to the axis of the jet. Even at this high frequency the source location agrees with far-field cross-correlation data of the primary jet in Table 4.6.

These near-field SPL results demonstrate strikingly similar characteristics to the extended near-field SPL measurements of a cold Mach 1.5 jet by Yu (1971). The pressure contour distribution for 2kHz noise peaked around 12 diameters downstream of the

nozzle, near the end of the supersonic core ($x/D=12.5$), which was found to be twice that of the potential core ($x/D=6.5$). More recent cross-correlation studies by Hileman (2004) and Self (2004) have also shown the 2kHz noise source to originate from $6 > x/D > 12$. Tam et al. (2009) concluded from Yu's (1971) data that low frequency (2kHz) noise sources responsible for peak noise radiation, are distributed over a substantial length of the jet, consistent with the nature of Mach wave radiation. The 10kHz noise, coinciding with the spectral peak of 138 dB, was shown to be non-localised, extending from $x/D=4.5$ up to 16. Very high frequency noise (up to 100kHz) was found to be fairly localised close to the nozzle exit at $x/D=4$, which is a typical feature of high frequency noise sources.

Table 4.7: Noise Source Location (x/D_j) based on Contours of Near-Field SPL

Noise Frequency	OASPL	2kHz SPL ($St=0.17$)	6.3kHz SPL ($St=0.49$)	9.6kHz SPL ($St=0.74$)	13kHz SPL ($St=1.0$)
Primary Jet	5.5	13	13 & 0	5.0	6
External Injection	5.5	13	12	2.6	6

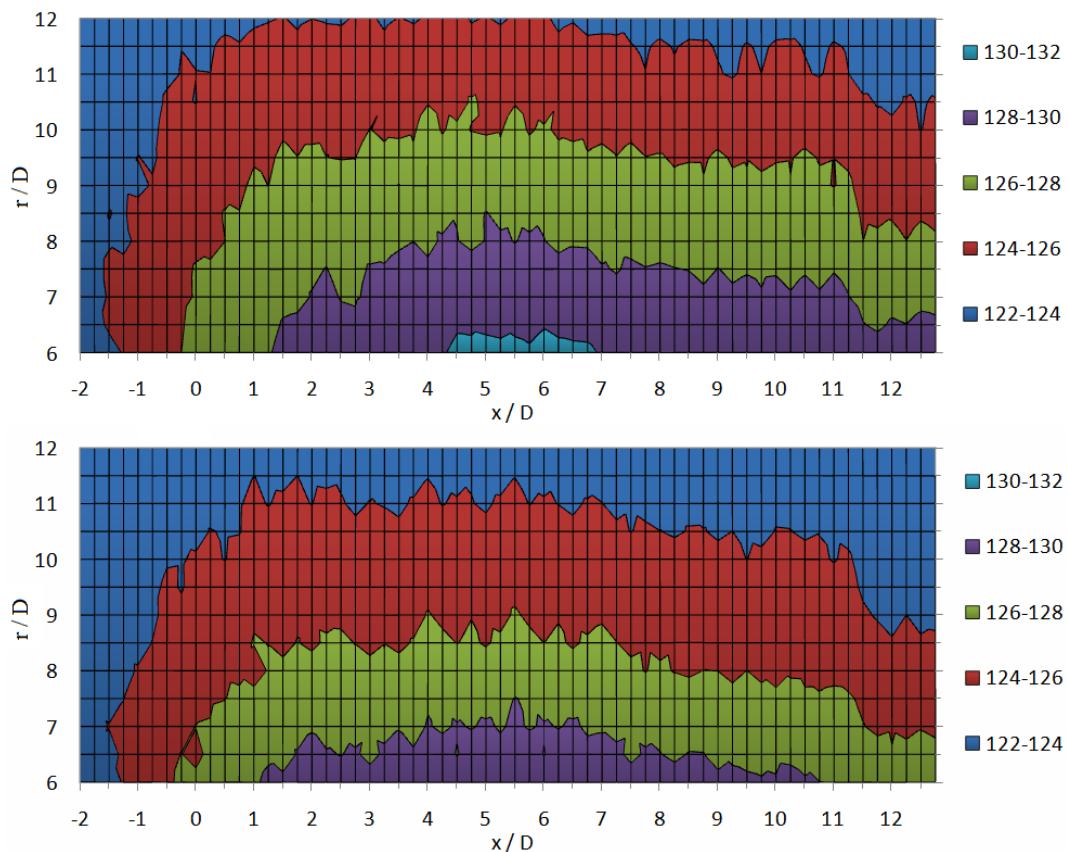


Figure 4.32: Contours of near field OASPL (dB) for the primary jet (top) and external injection at 1% IMFR (bottom).

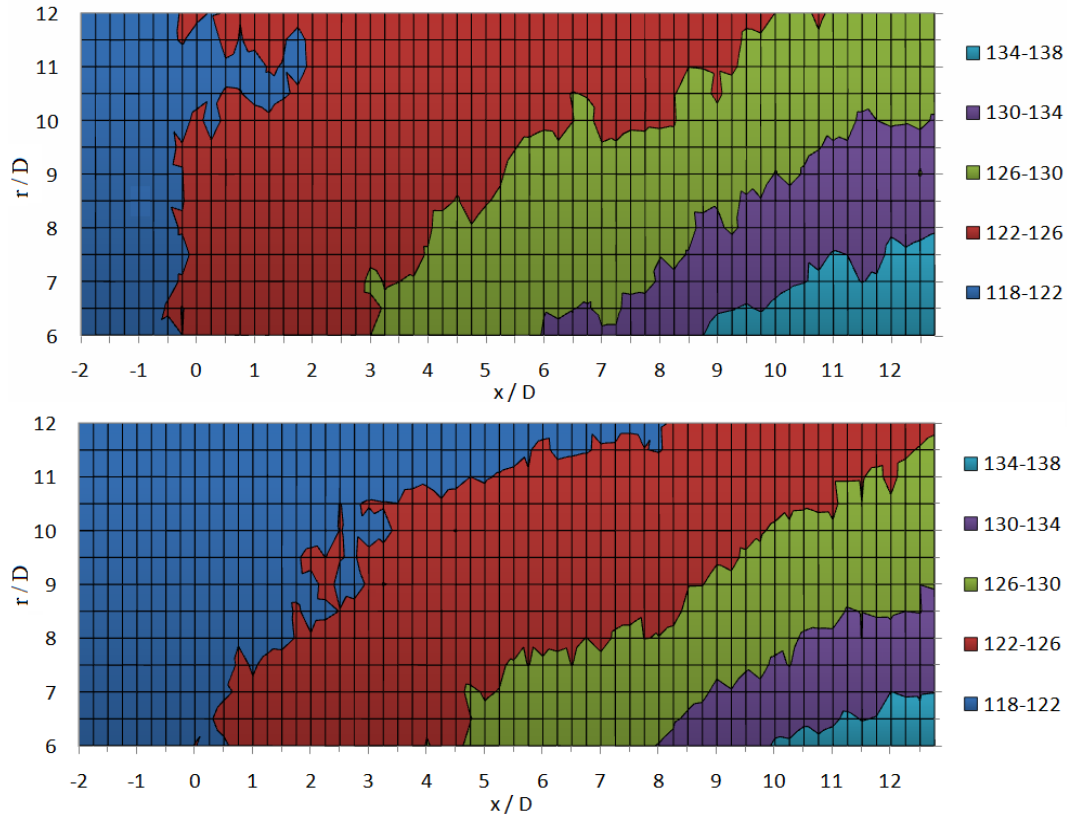


Figure 4.33: Contour plots of near-field SPL (dB) at 2kHz ($St=0.17$), corresponding to the Kelvin Helmholtz roll-up frequency of the primary jet (top) & external injection at 1% IMFR (bottom).

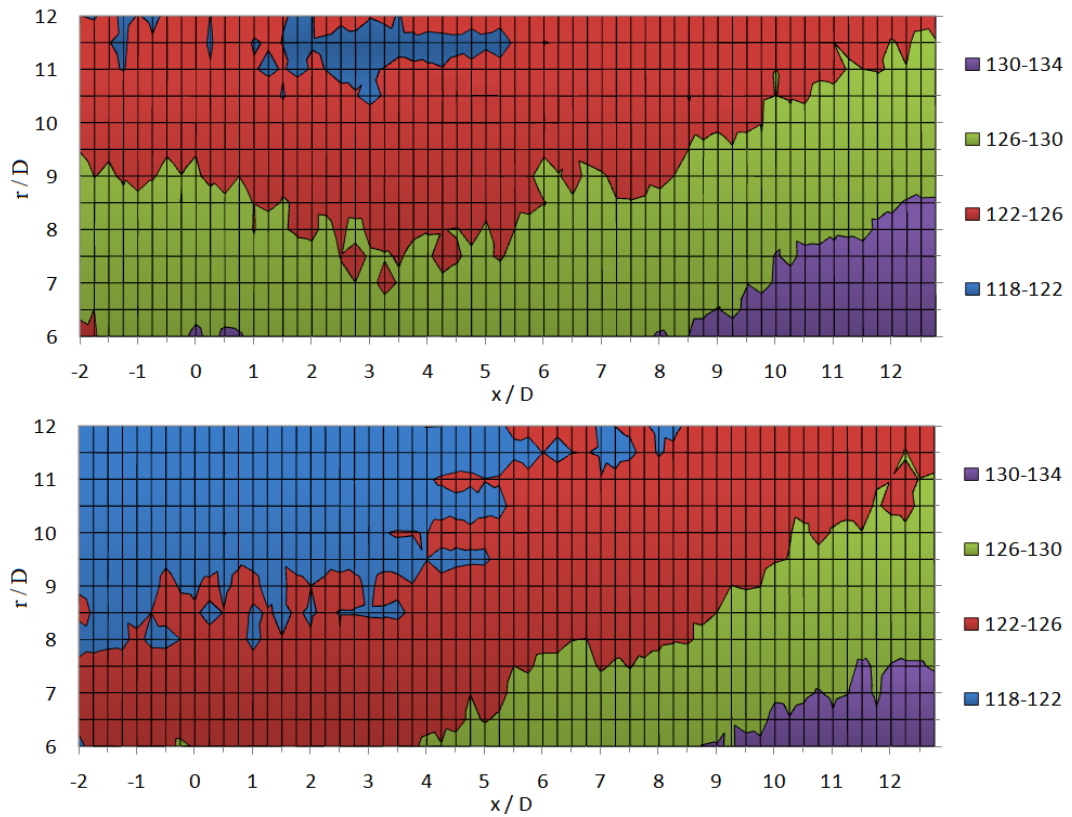


Figure 4.34: Contour plots of near-field SPL (dB) at 6.3 kHz ($St=0.49$) corresponding to the fundamental mode of screech for the primary jet (top) & external injection at 1% IMFR (bottom).

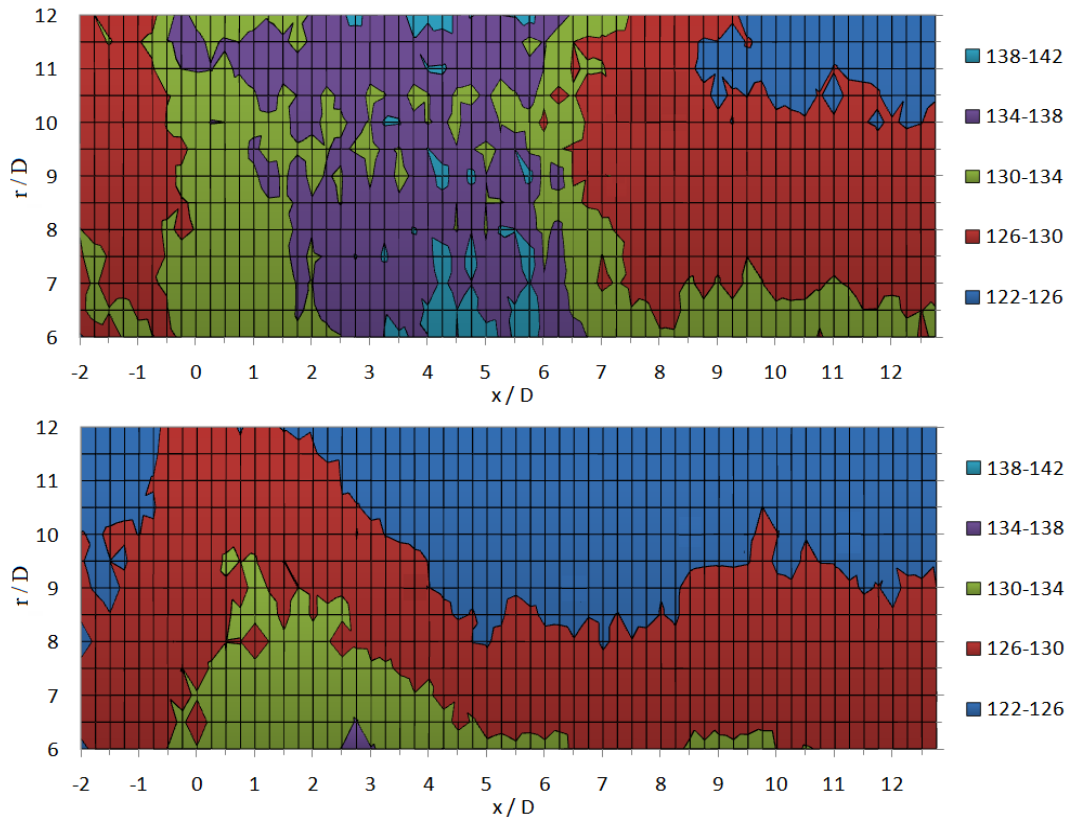


Figure 4.35: Contour plots of near field SPL (dB) at 9.6kHz ($St=0.74$) corresponding to the harmonic mode of screech for the primary jet (top) & external injection at 1% IMFR (bottom).

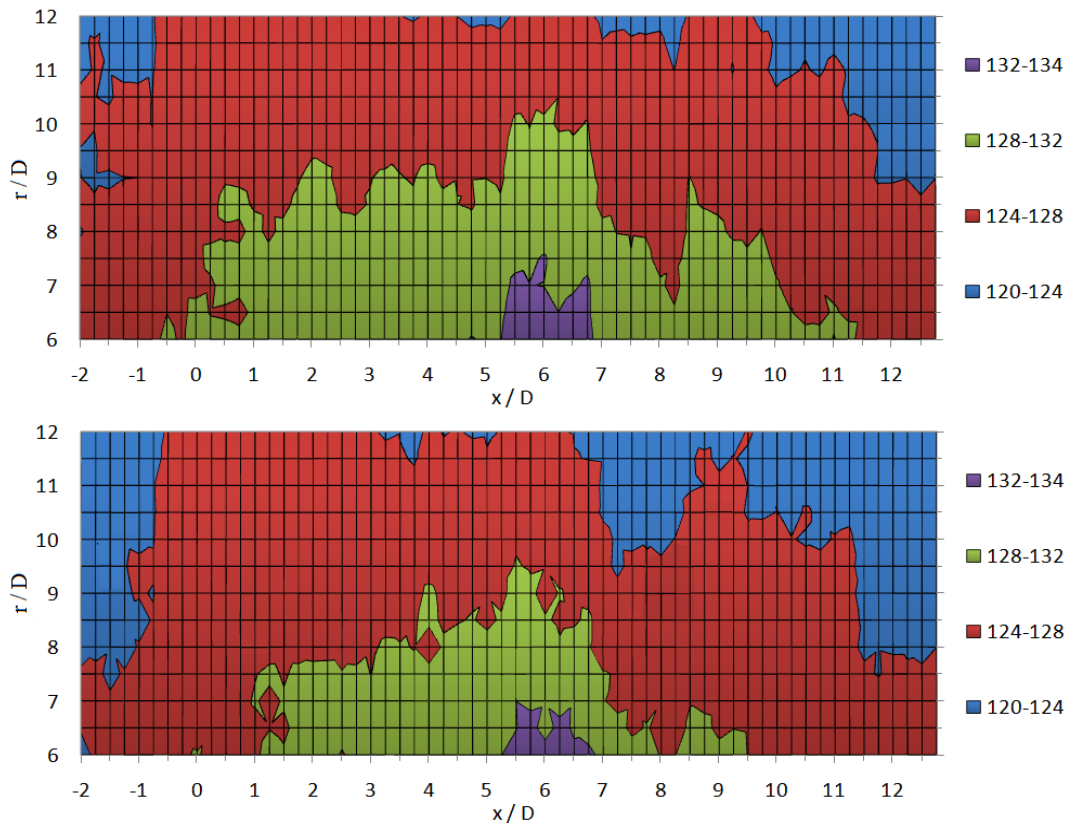


Figure 4.36: Contour plots of near field SPL (dB) at 13kHz ($St=1$) corresponding to the broadband shock peak for the primary jet (top) and external injection at 1% IMFR (bottom).

4.7 Summary of Acoustic Results

Mach 1.3 Primary Jet

- SPL results were scaled to $40D_j$, assuming the nozzle to be main noise source origin
- Relocating the scaling origin from $x/D=0$ to $x/D=5$ had negligible effect on OASPL
- The harmonic screech tone peaks at 118 dB for $St=0.74$ (9.6kHz) in the 90° spectra
- Broadband (BB) shock noise peaks at 116 dB for $St=1$ (13kHz) at 90°
- Preferred mode noise of the jet peaks at 132 dB for $St=0.17$ (2kHz) at 30°
- Upstream spectra (90° - 50°) conforms to similarity *G-spectra* for fine-scale turbulence
- Downstream spectra (40° - 15°) matches similarity *F-spectra* for large-scale turbulence
- Peak jet noise radiation at 25° with spectral & OASPL peaks of 134dB & 121 dB

Internal Tangential Injection

- An injection mass flow ratio of 40% to the main jet provides optimal noise reductions
- Reductions in Screech (6.4dB), BB shock peak (4.9dB) & Preferred mode (1.8dB)
- Optimal for downstream angles with an Δ OASPL of -6.3dB at 15°

External Tangential Injection

- An injection mass flow ratio of 1% to the main jet provides optimal noise reductions
- Reductions in Screech (7.5dB), BB shock peak (3.7dB) & Preferred mode (1.3dB)
- Optimal for 15° and 90° with Δ OASPL of -4.7dB and -1dB respectively

Pulsating Tangential Injection

- An injection mass flow ratio of 1% to the main jet provides optimal noise reductions
- Reductions in Screech (6.5dB), BB shock peak (2.8dB) & Preferred mode (0.5dB)
- Optimal at 40° - 70° with Δ OASPL of approximately -1dB

Noise Structure Size

- Normalised autocorrelation width increases with respect to reducing observer angle
- Spatial correlation length increases from $0.1D_j$ at 90° to a maximum $3.5D_j$ at 25°

Noise Structure propagation (Cross-correlation, R_{CC})

- High R_{CC} between downstream angles shows coherence of large-scale structures
- Low R_{CC} between upstream angles shows random distribution of fine-scale structures

Noise Source Location

- 2kHz, preferred mode noise originates from mean location of $x/D \sim 12$
- 6.3kHz, fundamental screech noise originates from mean location of $x/D \sim 6.2$
- 9.6kHz, harmonic screech noise originates from mean location of $x/D \sim 5$
- 13kHz, broadband shock noise originates from mean location of $x/D \sim 5.8$

Near-Field SPL

- Excellent noise source location comparison with far field cross-correlation data
- Detailed information on the non-localised nature of certain noise sources
- Evidence of SPL reductions at all frequencies through external air injection at 1%

5 FLOW FIELD RESULTS

The experimental findings from the acoustic measurements can be partially explained by examining the flow-field distributions of velocity, turbulence intensity, Reynolds stress and vorticity in the jet, and are presented in that order.

5.1 Axial Velocity

Figure 5.1 shows the effect of varying the IMFR of the internal tangential injection technique on the shape of the velocity profile of the jet, whilst maintaining pressure in the plenum chamber. The undisturbed profile of the primary jet is shown for comparison and is very close to the ‘top-hat’ type shape expected from a high Reynolds number exhaust with boundary layers reduced by the upstream contraction of the nozzle. For the primary jet case, the axial centreline velocity measures 375m/s, with peak velocities of 388m/s occurring towards the edges of the jet. A detailed discussion on the degree of expansion of the supersonic primary jet is provided in § 6.1. The primary effect of introducing ITI is the continual reduction in peak jet velocities towards the ‘top-hat’ edges with increasing IMFR’s. At IMFR’s of 10% & 40%, the centreline velocity is seen to increase beyond that of the primary jet, giving the profile a flatter shape within the diameter of the jet. The velocity profile shape becomes narrower for higher IMFR’s, suggesting an increasingly narrower jet core with thicker shear layers. For the 50% IMFR the profile is severely decayed at all r/D locations.

For a jet the axial momentum flux is conserved and hence its thrust, T_x , can be expressed as integral of the axial momentum across the cross-section of the jet, as shown in equation (3.48) (Beer & Chigier, 1972). The 165N of thrust derived by integrating the velocity profile across the jet compares favourably with the 168N of thrust previously calculated using the isentropic flow equation (3.11), based on the jet velocity of 384 m/s and mass flow rate of 0.437 kg/s.

Table 5.1 shows how the thrust levels of the jet are affected by the introduction of ITI. At an IMFR of 10% the jet’s thrust is increased by 1.5%, most probably due to the increased centreline velocity. For a 40% IMFR a 5% reduction in thrust is recorded and is attributed to the reductions in velocity, most prominently at the edges. Due to the nature of the cylindrical integration of equation (3.48), the fluid velocities closer to the edges of the jet have a larger radius and thus have a greater weighting on the overall thrust than those close to the centreline. Thus, despite the enhanced centreline velocity, reductions at the outer jet core have resulted in an overall loss of thrust. For the case where half of the overall mass flow is being injected tangentially, the jet’s performance is severely hampered through an 8% reduction in centreline velocity, which corresponds to a 12.5% loss of thrust. The reduction in centreline velocity can be validated by the findings of

Carpenter (1975) who showed that high levels of swirl create a significant change in the pressure gradients along the jet axis, inducing a lower centreline velocity. Although the pressure inside the plenum is designed to be constant despite the IMFR being introduced upstream of the nozzle, the actual swirling component seems to be responsible for the adverse pressure gradient along the jet, varying the nozzle's pressure ratio from the design condition.

Figure 5.2 shows the effect of the degree of external tangential injection on the axial velocity profile of the jet. The primary jet profile is shown for comparison. Again a slight reduction in velocity is recorded at the edges of the jet, relative to the increase in IMFR. However, there are two features that are distinctly different from those seen in the ITI velocity profiles. Firstly, the centreline velocity does not increase significantly beyond that of the primary jet although is seen to increase slightly when the IMFR is raised from 1% to 1.3%. Secondly, there is a noticeable increase in the profile width beyond the diameter of the jet ($-0.5 < r/D < 0.5$) that is proportional to the increase in IMFR. The overall effect of these wider shear layers translates to increased levels of thrust as shown in Table 5.1. The additional mass being introduced into the axial jet by the external tangential injectors is not thought to be the reason for the increased thrust, not only due to its relatively small quantity, but also because its plane of injection is perpendicular to that of the jet.

Table 5.1: Variation in Jet Thrust with Type of Injection based on 165N for the Primary Jet.

Injection Technique	Internal Tangential			External Tangential		
Injection Mass Flow Ratio	10%	40%	50%	0.7%	1.0%	1.3%
Δ Thrust	+1.5%	-5.0%	-12.5%	-0.7%	+0.8%	+1.1%

Figure 5.3 compares the velocity profiles from the best performing IMFR configurations of each technique as highlighted by the acoustic results. With reference to the primary jet's velocity profile, ETI at 1% IMFR evidently has a clear advantage over ITI at 40% IMFR, which can be summarised by the overall effects on performance in Table 5.1.

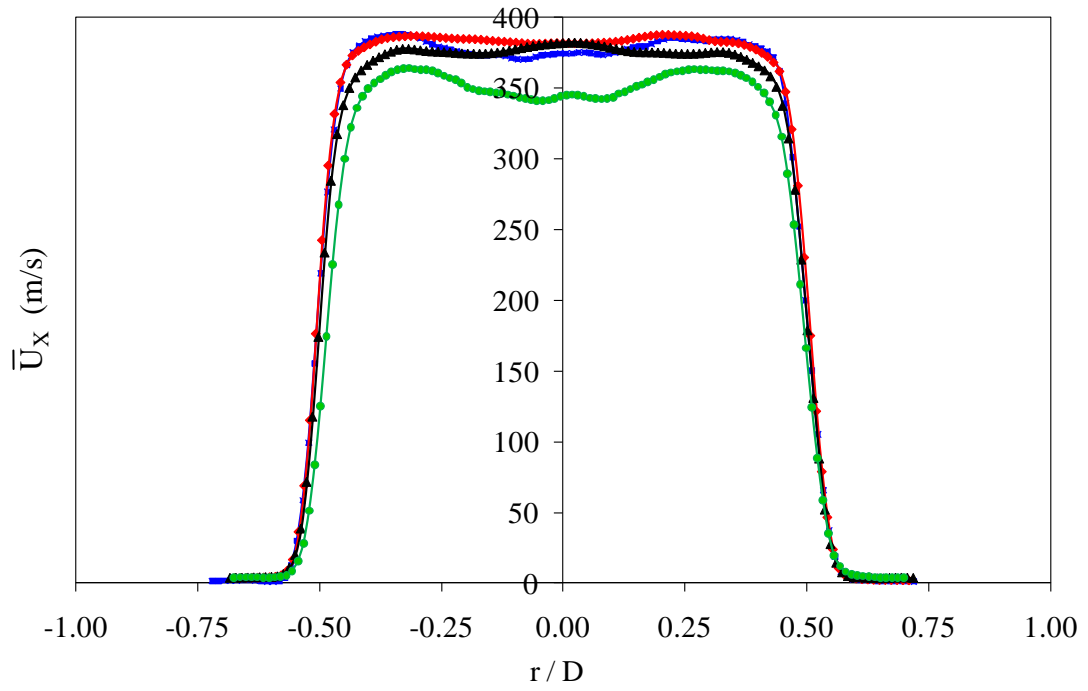


Figure 5.1: Comparison of axial velocity profiles at $x/D=0.6$ for internal tangential injection at mass flow ratios of 0% (■), 10% (◆), 40% (▲) & 50% (●).

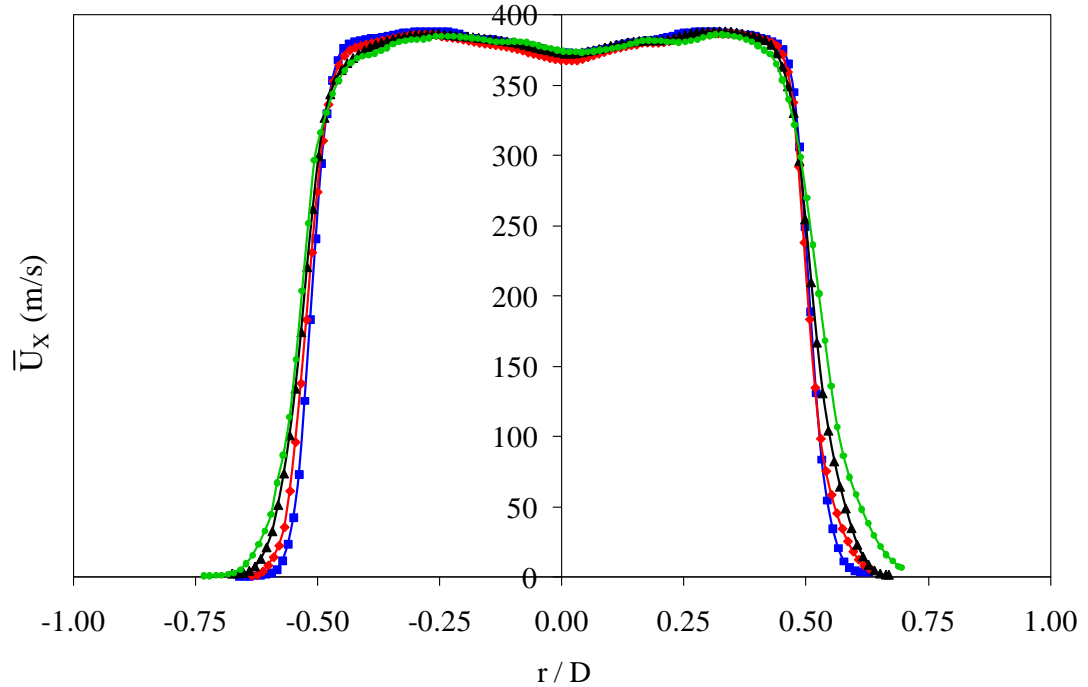


Figure 5.2: Comparison of axial velocity profiles at $x/D=0.6$ for external tangential injection at mass flow ratios of 0% (■), 0.7% (◆), 1% (▲) & 1.3% (●).

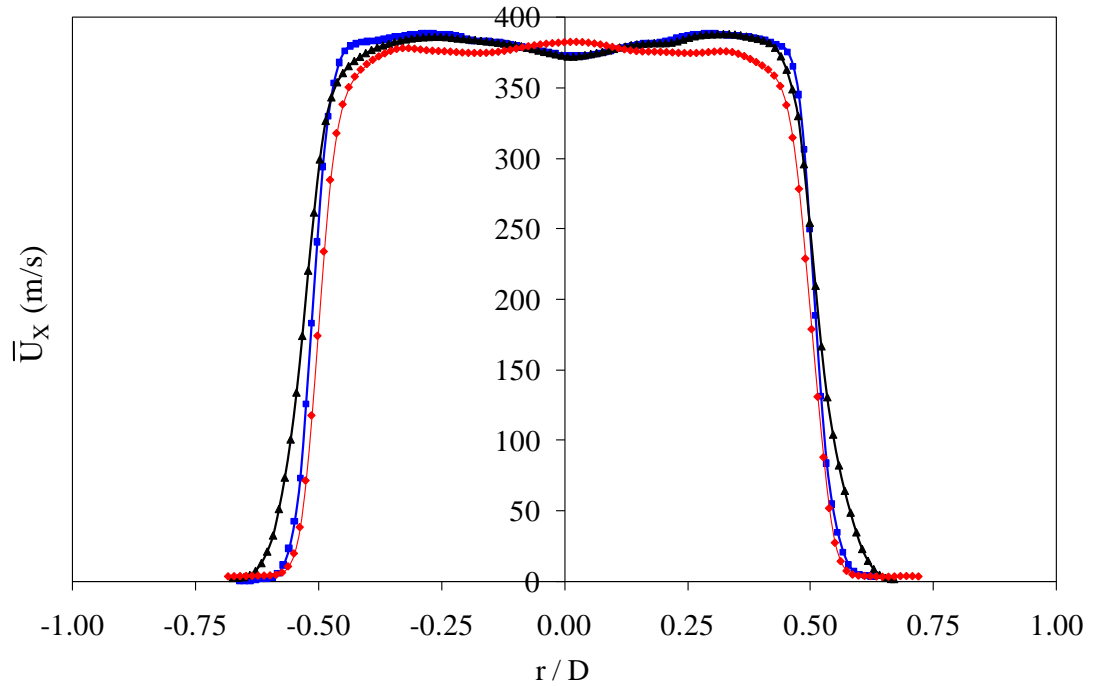


Figure 5.3: Comparison of velocity profiles at $x/D=0.6$ between the best performing configurations; internal tangential injection at 40% IMFR (\blacklozenge), external tangential injection at 1.0% IMFR (\blacktriangle) against the primary jet (\blacksquare).

Figure 5.4 serves the purpose of clearly illustrating the variations in the axial velocity profile with respect to streamwise location for ITI and ETI in comparison to the primary jet. Common to both techniques is the tendency of the centreline velocity to gradually decay with increasing streamwise direction with the shape of the profile also becoming wider. Figure 5.5 selects three streamwise locations of $x/D=0.6$, 6, & 12 at which a more detailed comparison of velocity profiles can be made. At $x/D=6$ the jet's centreline velocity and core diameters with ITI are shown to decay faster than with ETI, with the overall jet and shear layer showing a faster rate of spread. This trend is amplified for ITI even at $x/D=12$. However, ETI manifests an inverted trend relative to that of ITI, with a 40m/s increase in the centreline velocity as compared to the primary jet, a wider core and a very subtle reduction in the shear layer velocities in the region $-1 < r/D > 1$. This is strong evidence of the contrasting nature of the two techniques in altering the jet structure, through which the noise reductions are achieved.

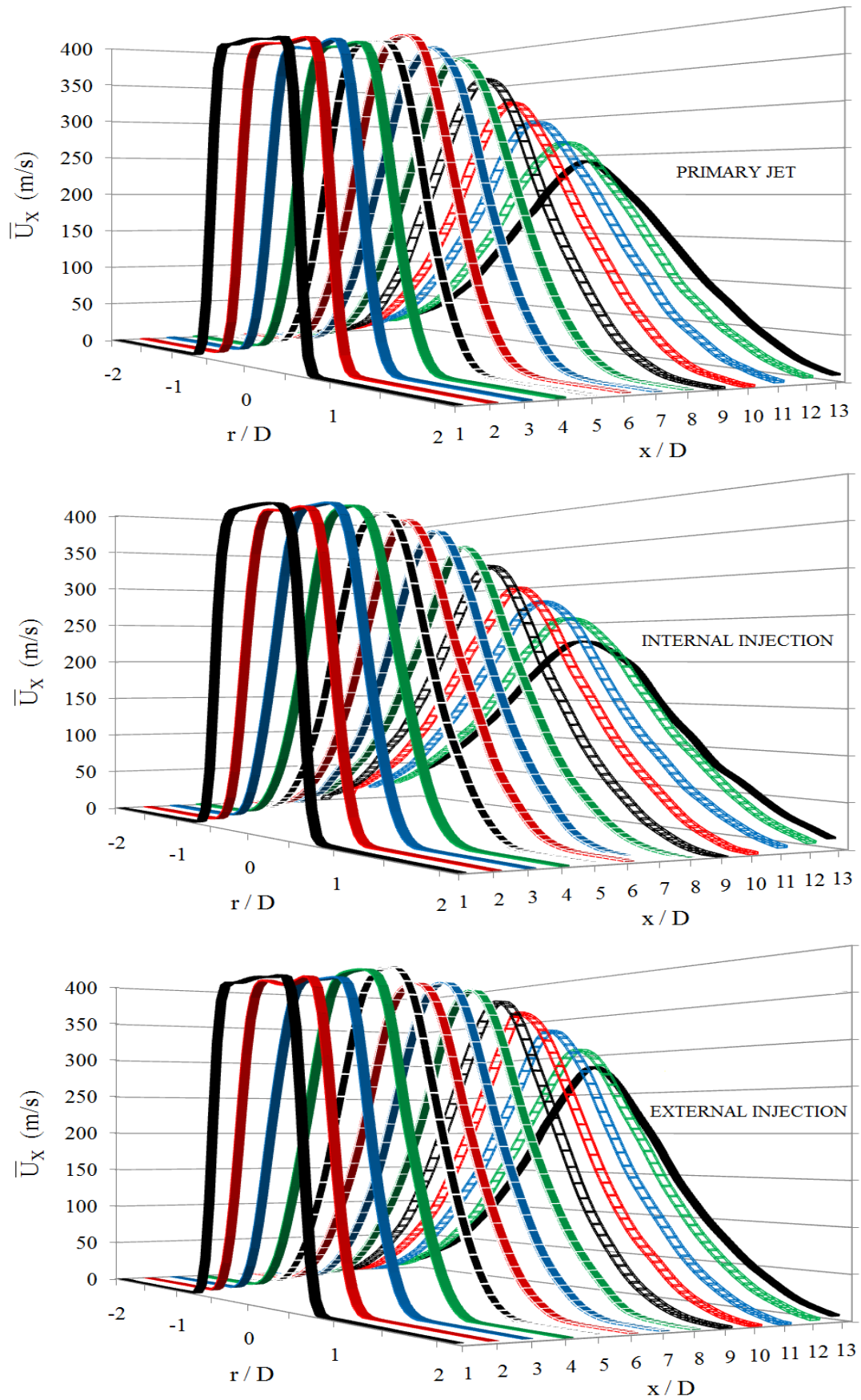


Figure 5.4: Variation on axial velocity profile with streamwise distance from the nozzle exit for primary jet (top), ITI at 40% IMFR (centre) and ETI at 1% IMFR (bottom).

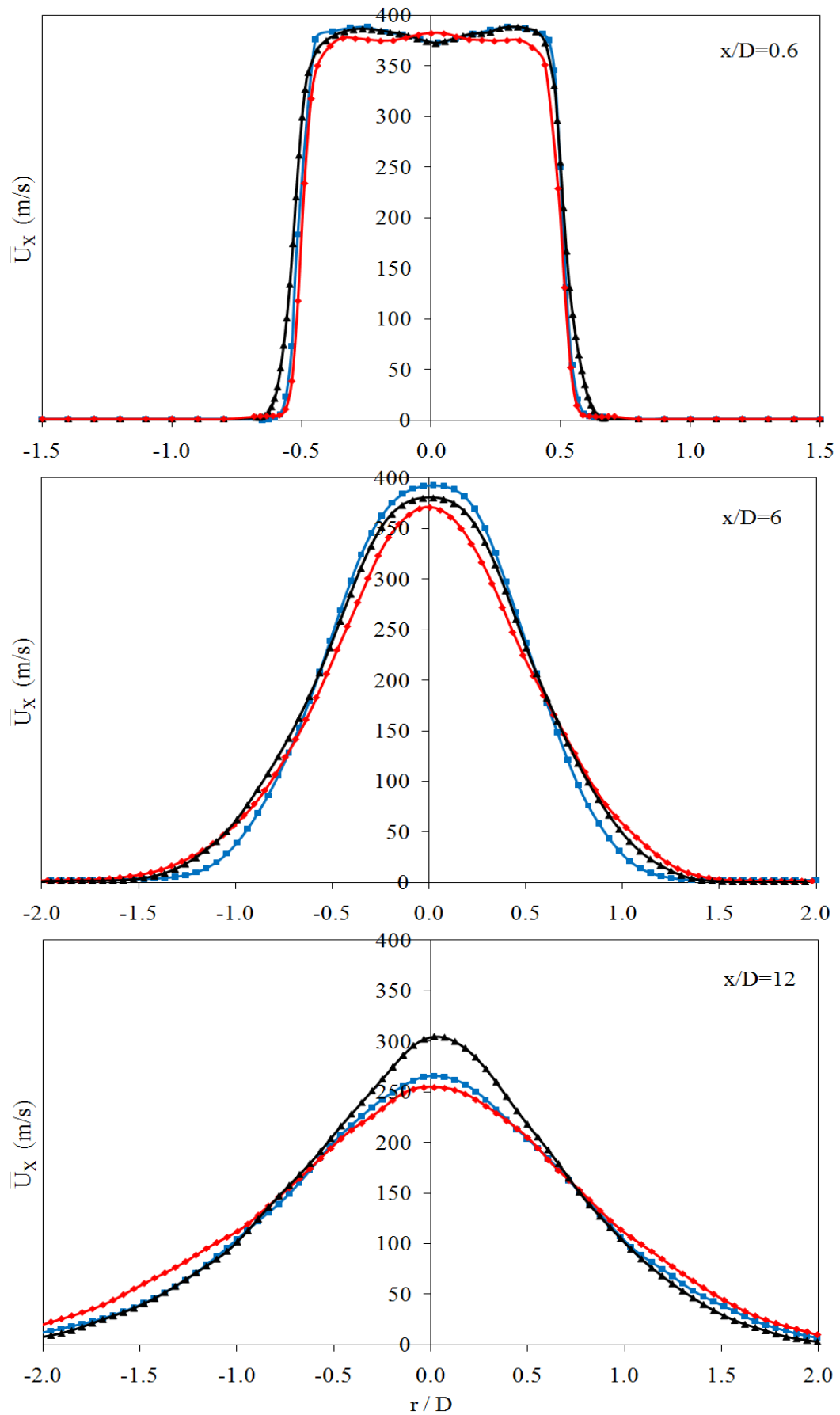


Figure 5.5: Comparison of axial velocity profiles at various streamwise locations for primary jet (■), internal tangential injection at 40% IMFR (◆) and external injection at 1% IMFR (▲).

Figure 5.6 shows contours of axial velocity obtained from the 2D PIV measurements whereas Figure 5.7 shows the variation in the centreline velocity in the streamwise direction. Several flow characteristics can be obtained from the sideline view of the jet and these are summarised in Table 5.2. The potential core is defined as the streamwise extent to which the centreline velocity is maintained (Lilley, 1958), and can be quantified as $U_x/U_J=1$ (Arakeri, 2003). Using Witze (1974) re-arranged expression for a jet's centreline velocity, the theoretical length of the potential core, shown in equation (2.5), is found to match perfectly to the experimental primary jet value of $6D_J$. The potential core is found to be reduced to $4D_J$ with ITI and increased to $6.5D_J$ for ETI. In agreement with the result of ITI, RANS and LES simulations have previously shown the introduction of swirl to reduce the length of the potential core (Tucker et al., 2003). The opposite effect of ETI agrees with the findings of Arakari et al. (2003), who showed that axially impinging microjets immediately downstream of the nozzle increase the length of the potential core by up to $1.5D_J$. The supersonic core, defined as the streamwise extent to which the centreline velocity is maintained at Mach 1 (Yu, 1971), is manipulated in a similar fashion to the potential core by both techniques.

The shock cell spacing, measured as the distance between the centres of the first two cells, is approximately 1.1 nozzle diameters for the primary jet. This value is not constant and is found to vary between shock cells further downstream. Hence, a better estimate would be the mean shock cell spacing, which can be found by specifying the average number of shock cells up to a distance of $x/D=6$. The mean shock cell spacing of $0.85D_J$ for the primary jet matches to within 2% of the $0.87D_J$ predicted numerically using the Prandtl-Pack shock cell spacing formula (2.11), based on a jet Mach number of 1.3. ITI reduces the mean shock cell spacing by $0.15D$, which subsequently reduces the total number of shock cells in the jet structure. ETI shows a modest reduction of $0.05D$; however, the total number of shock cells is greater than in the primary jet due to longer potential and supersonic cores. The results for ITI can be validated through the Schlieren experiments carried out by Neemah (1999). An increase in the rotational component of velocity (swirl) was shown to decrease the number and length of the shock cells and was attributed to increased mixing between the jet and the atmosphere.

Table 5.2: Effect of Air Injection Technique on Lengths of Potential and Supersonic Cores

Injection Technique	Primary Jet	Internal Tangential	External Tangential
Potential Core (x/D)	6	4	6.5
Supersonic Core (x/D)	11.1	10.2	12.3
1 st Shock cell pair spacing (D)	1.1	0.9	1.05
Mean Shock cell spacing (D)	0.85	0.7	0.8

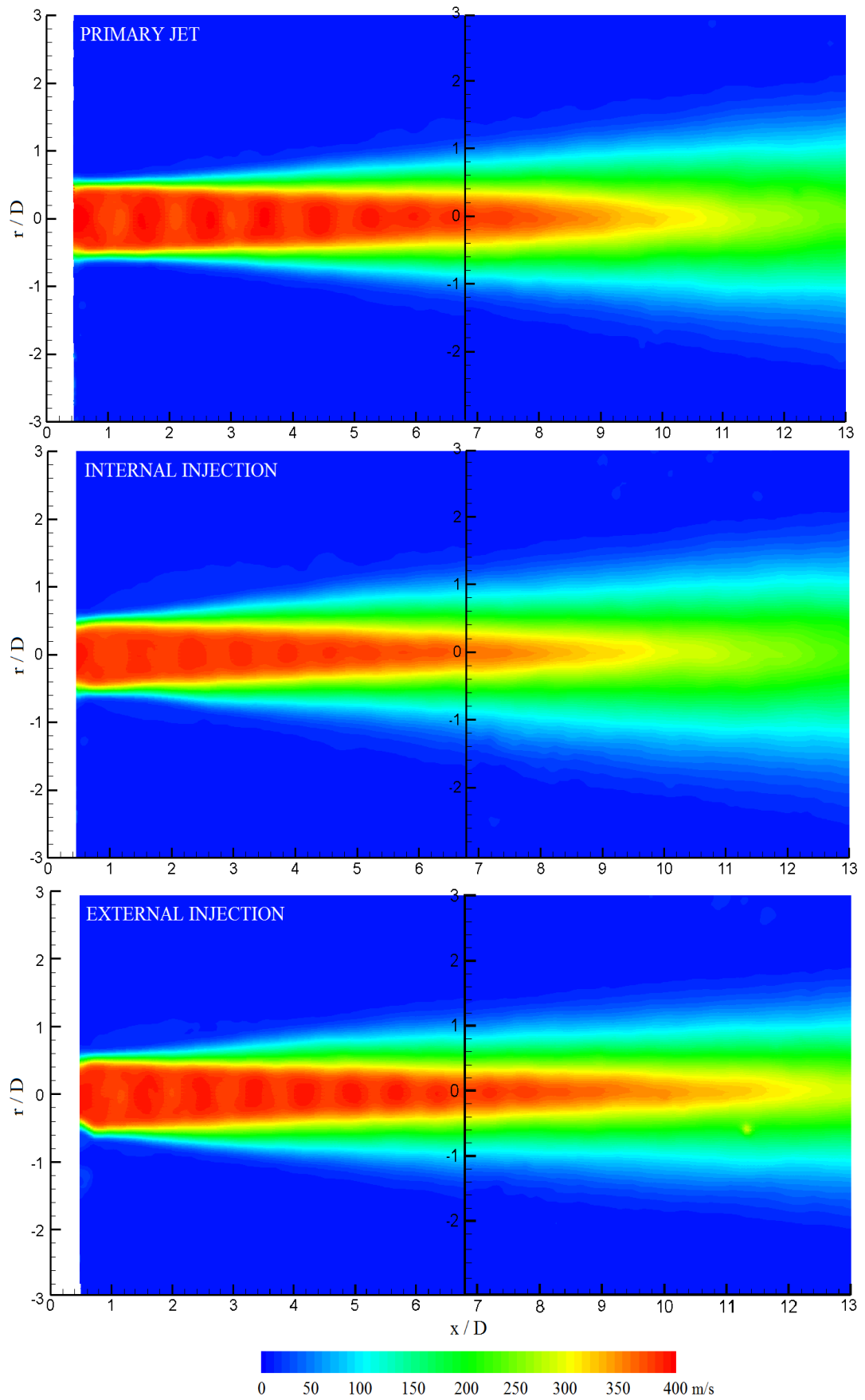


Figure 5.6: Comparison of axial velocity contours between the primary jet, internal tangential air injection at 40% mass flow ratio and external tangential air injection at 1% mass flow ratio.

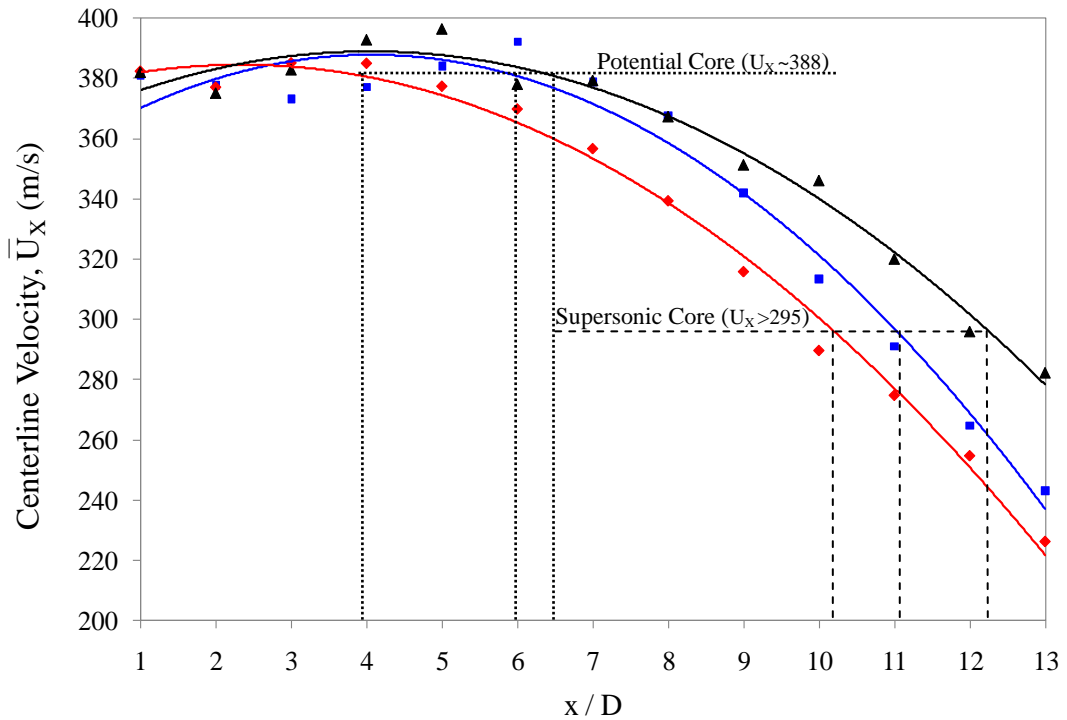


Figure 5.7: Comparison of axial velocity profiles at various streamwise locations for primary jet (■), internal injection at 40% IMFR (◆) and external injection at 1% IMFR (▲). Second order polynomials have been used to demonstrate the trend of data points.

Figure 5.8 shows contours of axial velocity obtained from the 3D PIV measurements. The end-on view provides another angle from which the transformations of the critical shear layer can more clearly be observed. For the cross-section of the primary jet, the shear layer thickness can be estimated by measuring the distance over which the velocity gradient operates, $0.45 < r/D < 0.6$, equating it to $0.15D$ (4.5mm). Introducing ITI at 40% IMFR, results in the reduction of peak jet velocities towards the edges of the jet along with a slight thickening of the shear layer. Despite the IMFR of the ETI technique being only a fraction of that for ITI, the impact upon the cross-section of the jet is evidently superior. A thicker shear layer, measuring $0.2D$ (6mm) is observed extending from $0.45 < r/D < 0.65$ with the imprint of the external tangential injectors in the form of eight distinct peaks and troughs equally spaced azimuthally around the cross section of the jet. Despite the injection angle being tangential, there seems to be a radial penetration into the jet core by up to $0.07D$ (2.1mm), which is most likely due to the production of axial vorticity. The corresponding contour lines that are equally spaced at intervals of 20m/s also illustrate this effect.

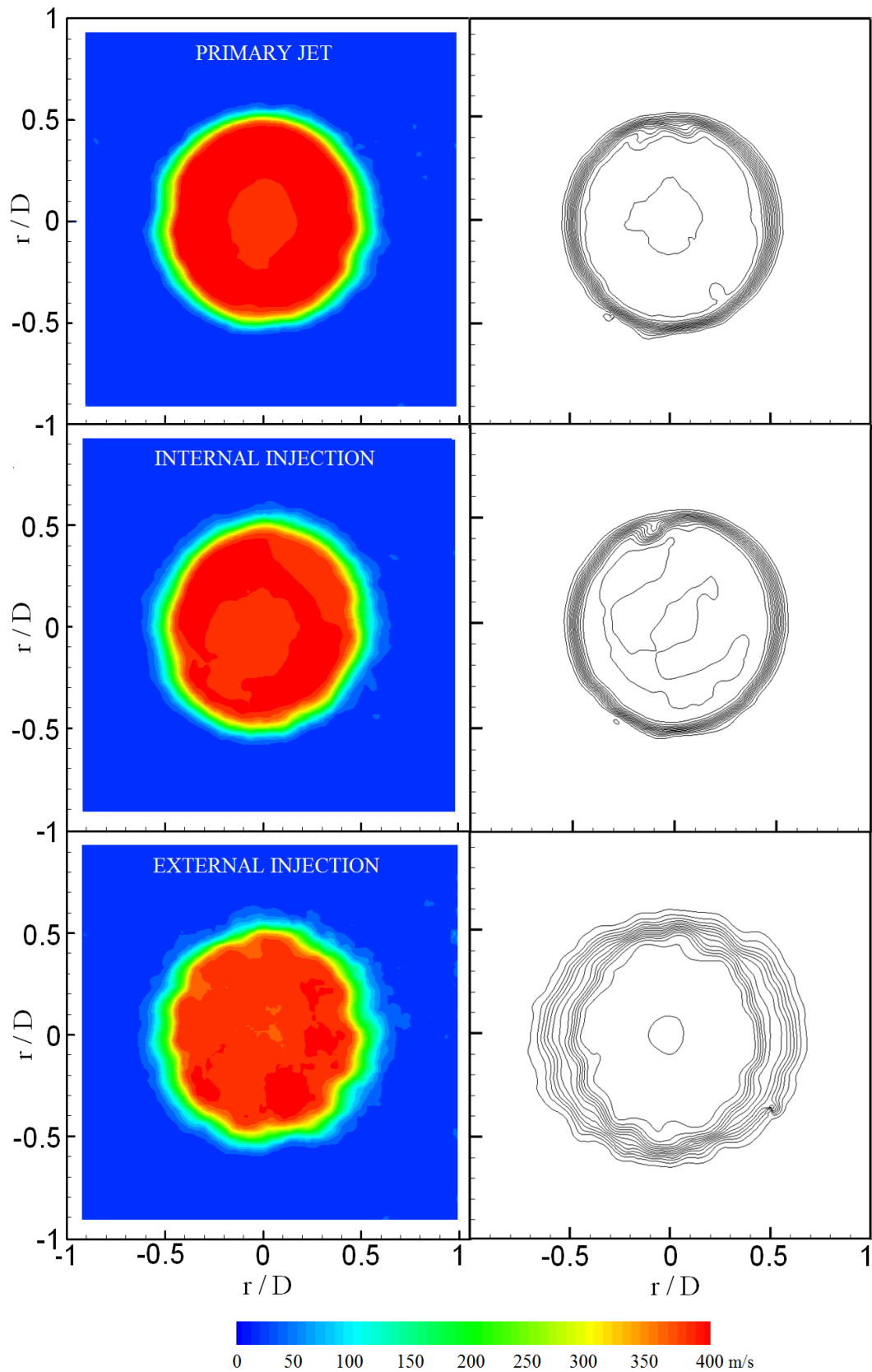


Figure 5.8: Comparison of axial velocity contours from 3D stereoscopic PIV at $x/D=0.6$ for the primary jet, internal tangential injection at 40% mass flow ratio & external tangential injection at 1% mass flow ratio. The corresponding contour lines are spaced at regular intervals of 20 m/s.

5.2 Tangential Velocity

Another advantage of the 3D PIV measurements is that they enable us to extract details on the degree of swirl introduced by the injection techniques by observing the tangential component, U_θ , of jet's velocity. Figure 5.9 compares the tangential velocity profiles between various IMFR's of ITI. The profile for the primary jet is shown for comparison and is seen, as expected, to remain fairly close to zero across the diameter of the jet. An IMFR of 10% introduces a rotational component of 58m/s, peaking inside the jet at $r/D=0.45$. The rate at which U_θ increases to 80m/s, by increasing the IMFR to 40%, is much lower compared to the first interval. With a 50% IMFR, U_θ is further increased to 85m/s confirming the reduced effectiveness of raising the IMFR beyond 40%.

Figure 5.10 shows little difference in increasing the IMFR from 0.7% to 1% for ETI, measuring 15m/s and 18m/s respectively. However, at 1.3% IMFR, U_θ is more than doubled to approximately 40 m/s, showing greater effectiveness in increasing the IMFR beyond 1%.

In a swirling jet the axial flux of angular momentum is conserved and can be defined as the integral of the angular momentum across the face of the jet as shown in equation (5.1) (Beer & Chigier, 1972). The swirl number is a parameter used to indicate the contribution of the tangential swirling component in a mostly axial flow and can be defined as the ratio of the rotational momentum to the axial momentum as shown in equation (5.2) (Beer & Chigier, 1972). Table 5.3 shows the swirl numbers, S_N , generated by ITI to be significantly higher than those seen for ETI. At an IMFR of 40% for ITI, S_N measures at 0.086, which is nearly 7 times greater than the 0.013 attributed to an IMFR of 1% for ETI.

$$G_\theta = \int_0^R (U_\theta r) \rho U_x 2\pi r \partial r \quad (5.1)$$

$$S_N = \frac{G_\theta}{T_x R} = \frac{2\pi\rho \int_0^R U_x r U_\theta r \partial r}{2\pi\rho R \int_0^R U_x^2 r \partial r} \quad (5.2)$$

Table 5.3: Swirl Numbers Generated by each Tangential Air Injection Technique

Injection Technique	Internal Tangential			External Tangential		
	10%	40%	50%	0.7%	1.0%	1.3%
Injection mass flow ratio						
Swirl Number, S_N	0.070	0.086	0.091	0.009	0.013	0.022

Figure 5.11 compares the tangential velocity profiles for the best performing configurations of each technique, in terms of OASPL reduction, against the primary jet. There are several differences between the injection techniques, the most obvious of which is the magnitude of velocities, measuring 20% and 5% of that of the primary axial component, U_x (388m/s); for IMFR's of 40% and 1% respectively. Secondly, the velocities are found to peak at different radial locations. Since ITI occurs within the nozzle, U_θ is found to peak within the jet diameter at $r/D=0.45$. The external tangential injectors are targeted precisely at the edges of the jet and so U_θ , for ETI, is seen to consequently peak at the edge of the jet at $r/D=0.5$. Thirdly, the velocity profiles for ITI are much broader, spanning from $0.3 < r/D < 0.55$ at 18m/s, compared to localised peak for ETI at the same velocity. Since the tangential velocity profiles were measured at a streamwise location of $x/D=0.6$, the swirl component generated by ITI had nearly 7 nozzle diameters from the point of injection to properly mix with the axial flow, before being recorded at the PIV laser plane (Figure 3.3). This is much greater compared to only $0.6D_j$ for ETI. Hence, the higher rates of mixing within the nozzle have allowed the tangential component of velocity to penetrate further into the core, thus resulting in broader peaks in the velocity profiles. Previous numerical experiments by Tucker et al. (2003) have shown swirl velocities to decay rapidly with axial distance due to flow mixing; however this cannot be confirmed for the techniques being investigated in the study unless end-on PIV measurements are made at further downstream locations along the streamwise axis. This will be presented as a suggestion for future work in Chapter 7. It is also interesting to note the slight reversal of flow, measuring 10m/s at $r/D=0.5$ for ETI at 1% IMFR. This flow reversal may be evidence for small, axially aligned vortices generated by each external injector, as is common with mechanical chevrons (Callender et al., 2007).

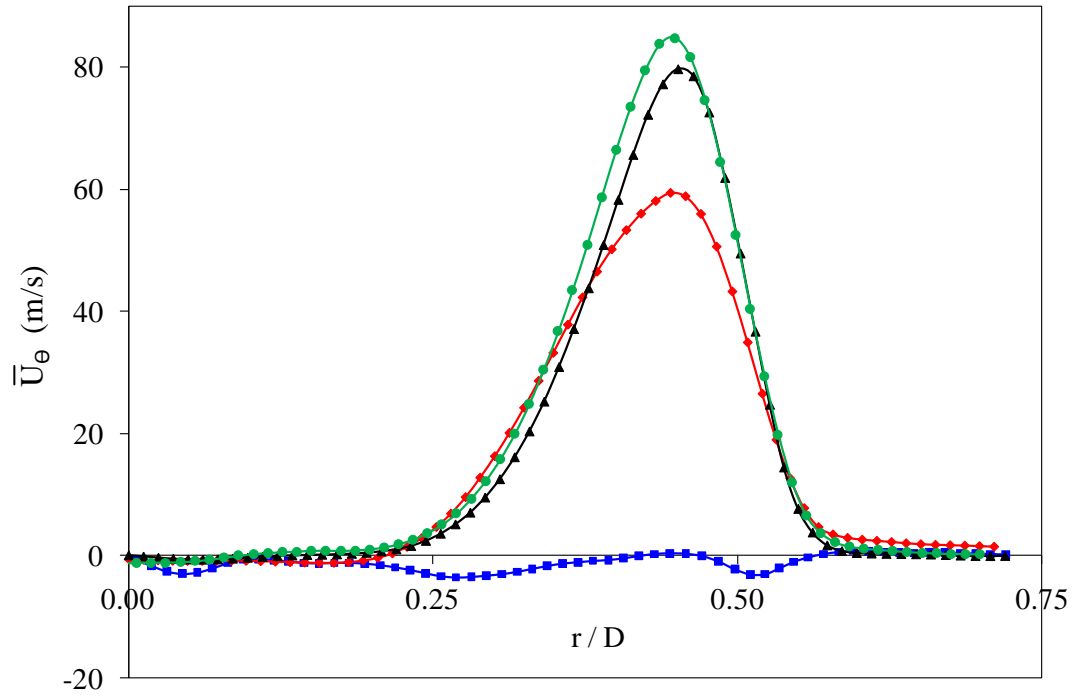


Figure 5.9: Comparison of tangential velocity profiles at $x/D=0.6$ for internal tangential injection at mass flow ratios of 0% (■), 10% (◆), 40% (▲) & 50% (●).

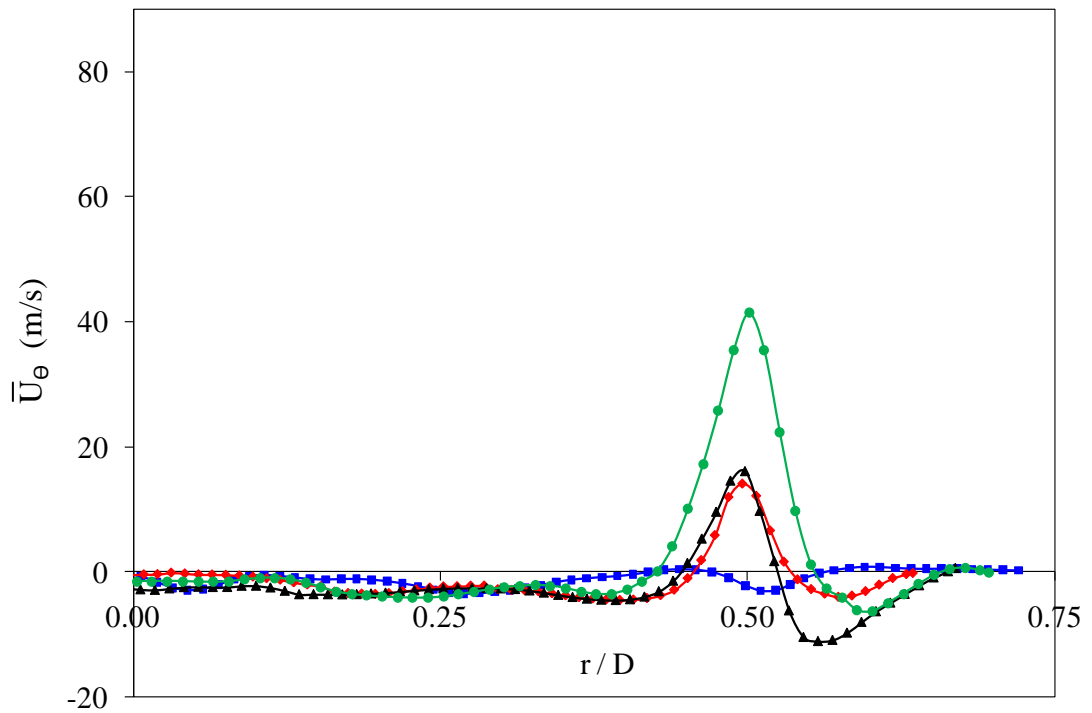


Figure 5.10: Comparison of tangential velocity profiles at $x/D=0.6$ for external tangential injection at mass flow ratios of 0% (■), 0.7% (◆), 1% (▲) & 1.3% (●).

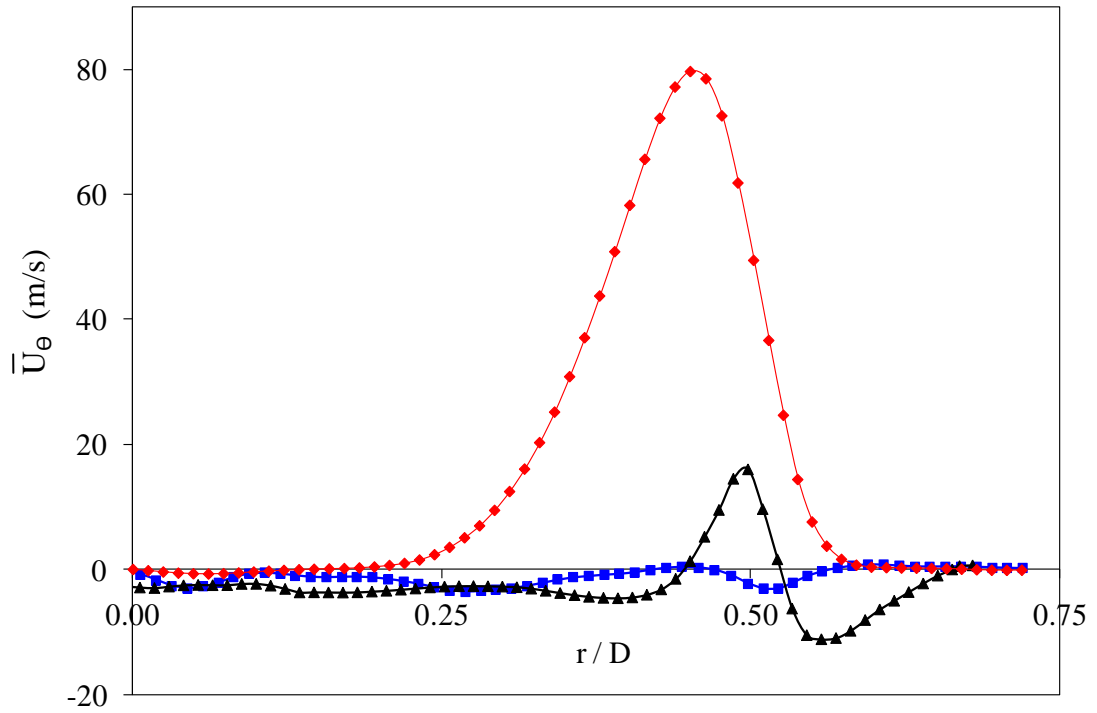


Figure 5.11: Comparison of tangential velocity profiles at $x/D=0.6$ between the best performing configurations; internal tangential injection at 40% IMFR (\blacklozenge), external injection tangential at 1.0% IMFR (\blacktriangle) against the primary jet (\blacksquare).

5.3 Turbulence Intensity

The degree of axial instability in a jet has been shown to be related to the mechanisms that cause jet noise reduction. Turbulence intensity, T_I , is the ratio of the local velocity fluctuation to the local time averaged velocity as shown in equation (5.3).

$$T_I = \frac{u'_{x rms}}{\overline{U}_x} \quad (5.3)$$

$$u'_{x rms} = \sqrt{\frac{\sum_1^N (u'_{x_n})^2}{N}} \quad (5.4)$$

Figure 5.12 shows an increase in axial turbulence intensity, T_I , with streamwise distance, for the unperturbed primary jet. The peak value of 0.16 at $x/D=7$ compares well to the value of 0.14 measured for a transonic jet (Arakeri et al., 2003). The T_I magnitudes gradually decay beyond $x/D=9$. In terms of the cross-section of the jet, the location of the T_I peak is preserved at the edge of the jet ($r/D=0.5$), irrespective of the streamwise location, suggesting that the shear layer of the jet is highly fluctuating compared to the core. Once again, the increasingly broad profiles indicate mixing of the shear layer with the core of the jet, making the centreline flow increasingly unstable at the downstream locations, particularly beyond the potential core. With the introduction of ITI, T_I is increased at locations immediately downstream of the nozzle ($1 < x/D < 4$), with the peak occurring further upstream ($x/D=4$) than in the primary jet case. While ITI shows reductions in T_I only at the downstream angles, ETI gives evidence of broadband reductions with the peak of 0.135 occurring at $x/D=5$.

Figure 5.13 allows for a more detailed comparison of the variation of T_I across the jet at three specific streamwise locations. At $x/D=1$, ITI shows a 30% increase in T_I with ETI showing no effect. Both injection techniques slightly widen the profiles towards the inner, high-speed side of the shear layer. At $x/D=6$, ETI shows reductions in T_I at locations $r/D < 0.9$, with the peak reduction of 18% occurring at $r/D=0.5$. ITI continues to show increased instability across most of the jet, with up to 25% higher T_I levels at $0.4 < r/D < 0.8$. Towards the end of the supersonic core, $x/D=12$, the peaks have become increasingly flat, with both techniques showing reductions in turbulence intensity across the jet, especially ETI. Fluidic injection through 45° axially impinging microjets has been shown to reduce the turbulence intensity level associated with transonic jet shear layer, by up to 15% (Arakeri et al., 2003). However, enhancements in turbulence intensity by up to 10% have also been recorded near the low-speed outer edge of the shear layer (Alkislar et al., 2007). Both of these trends have been observed, qualitatively, for external tangential injection around a supersonic jet at $x/D=6$ in Figure 5.13.

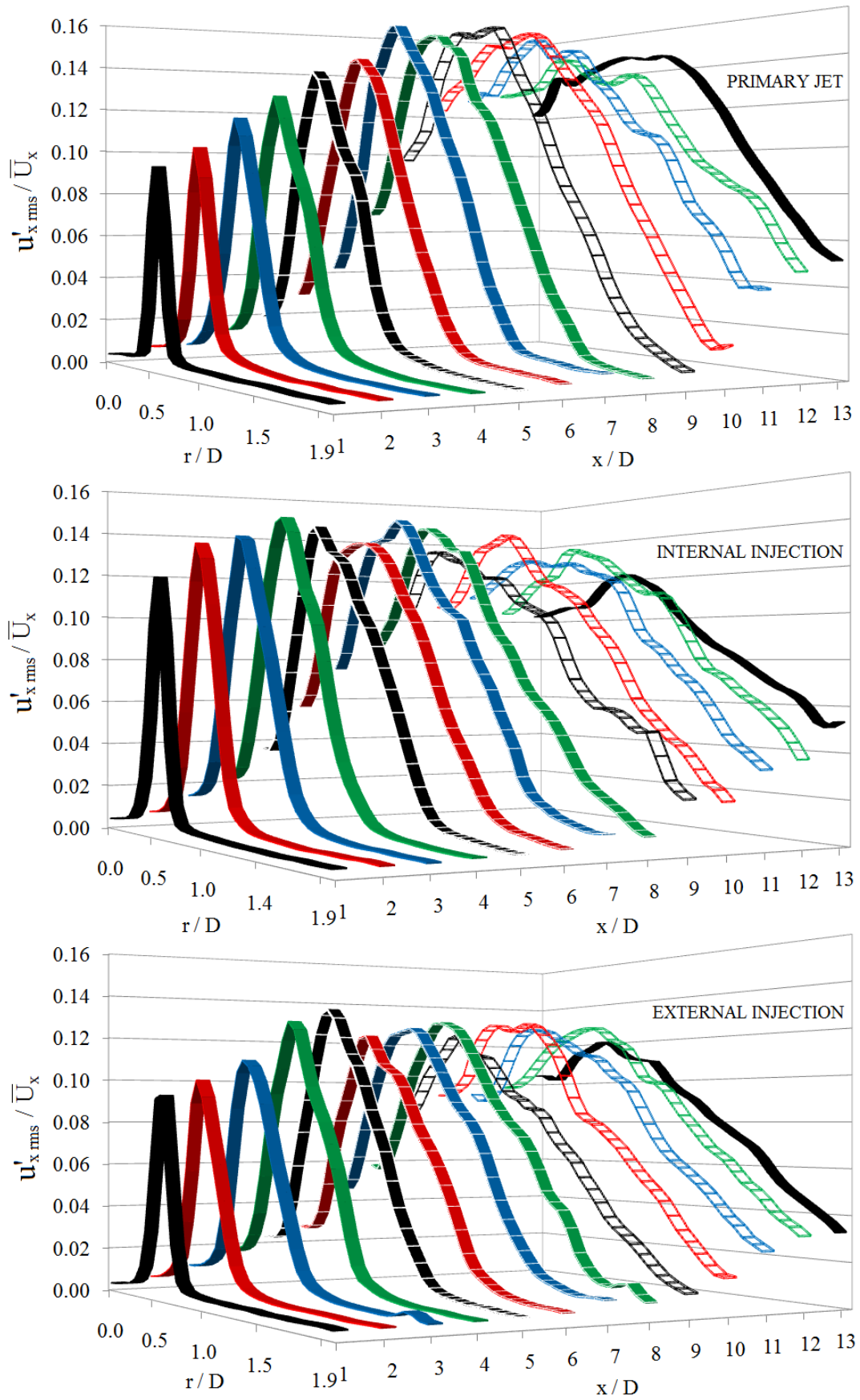


Figure 5.12: Variation in normalised turbulence intensity with streamwise distance from the nozzle exit for the primary jet (top), internal injection at 40% IMFR (centre) and external injection at 1% IMFR (bottom).

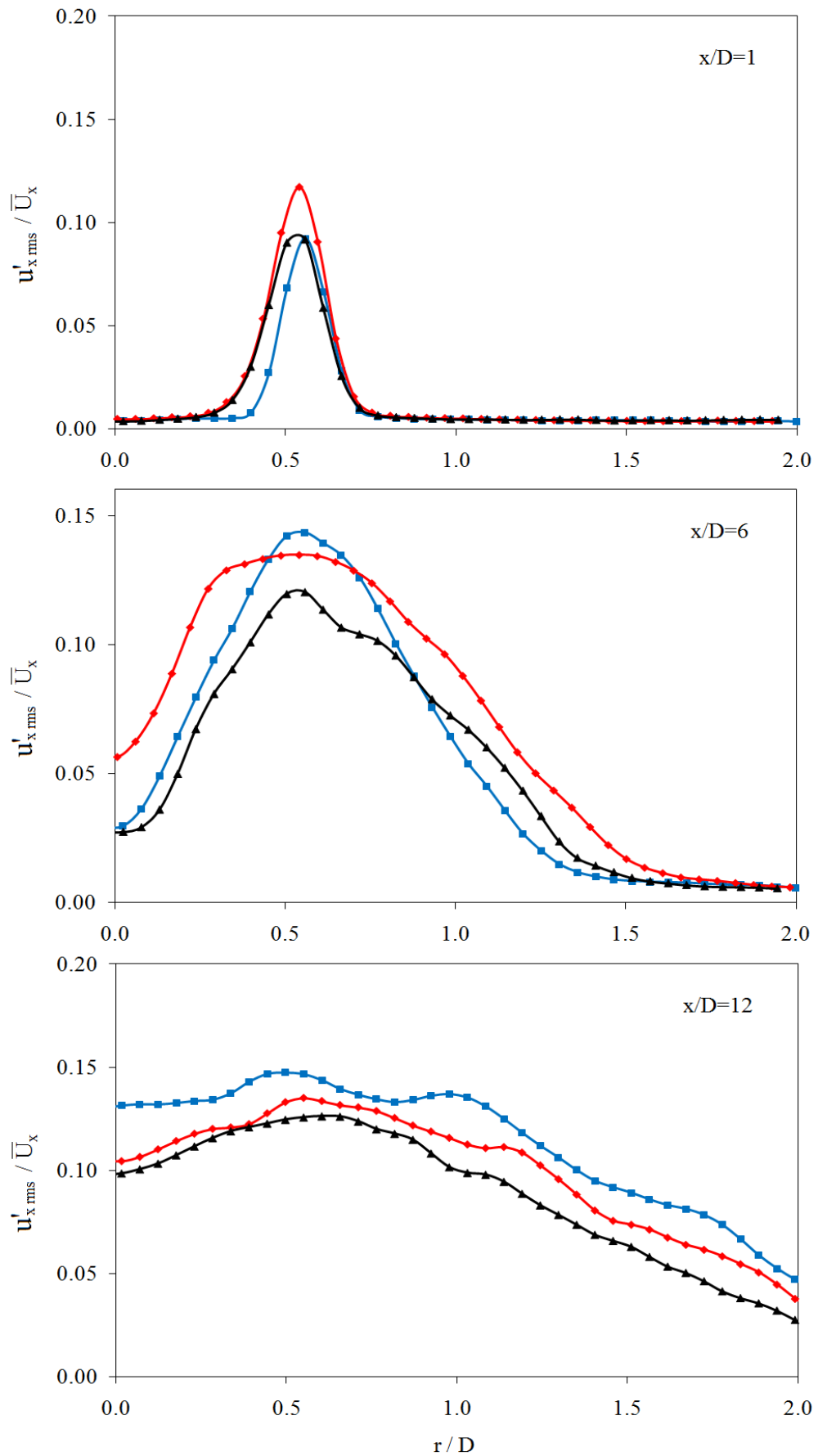


Figure 5.13: Comparison of axial turbulence intensity profiles at various streamwise locations for primary jet (■), internal injection at 40% IMFR (◆) and external injection at 1% IMFR (▲).

5.4 Reynolds Stress

The Reynolds Stress, R_S , is defined as the product of the axial (u_x) and radial (u_r) component fluctuations of velocity as shown in equation (5.5), with a fluctuation defined as a deviation from the mean velocity in equation (5.6) (Arakeri et al., 2003).

$$R_S \left[\frac{m^2}{s^2} \right] = -\overline{u'_x u'_r} \quad (5.5)$$

$$u'_x = u_x - \overline{U}_x \quad (5.6)$$

Figure 5.14 shows low levels of normalised Reynolds Stress, R_S / U_J^2 , at streamwise locations close to the nozzle for the unperturbed primary jet. This quantity is found to increase gradually up to a maximum of 0.0095 at $x/D=7$, which is higher than the 0.006 recorded at the same location for a transonic jet (Arakeri et al., 2003). A gradual decay is observed beyond the end of the potential core. The Reynolds stress peak is found to occur within the shear layer, towards the edge of the jet's cross section ($r/D > 0.5$) at most streamwise locations. For ITI significant increases in R_S / U_J^2 are observed close to nozzle exit up to a streamwise location of $x/D=5$, beyond which reductions are recorded as compared to the primary jet. ETI shows broadband reduction in R_S / U_J^2 , with a flatter axial distribution that is void of any obvious peaks.

Figure 5.15 allows for a more detailed comparison of the variation of normalised Reynolds stress across the jet at three specific streamwise locations. At $x/D=1$, ITI shows a significant 500% increase in R_S / U_J^2 with ETI returning a relatively modest 100% increase. Both these enhanced R_S / U_J^2 peaks occur at $r/D=0.5$; closer to the core of the jet than for the primary jet ($r/D=0.6$). At $x/D=6$, the Reynolds stresses are much higher than at upstream locations. ITI shows a 25% increase in R_S / U_J^2 compared to the primary jet, with the location of the peak preserved at the edge of the jet. At this same location, ETI causes a 25% decrease in R_S / U_J^2 , with the peak translated to the outer-lower velocity side of the shear layer ($r/D=0.6$). This shows agreement to the 40% reduction in Reynolds stress recorded by Arakeri et al. (2003) with the use of axially impinging microjets. At the extreme downstream location of $x/D=12$, both techniques show reduced levels of Reynolds stress with the profiles becoming broader, due to enhanced mixing with, and entrainment from, the surrounding ambient air. The radial locations of the R_S / U_J^2 peaks are also found to be displaced away from the jet core.

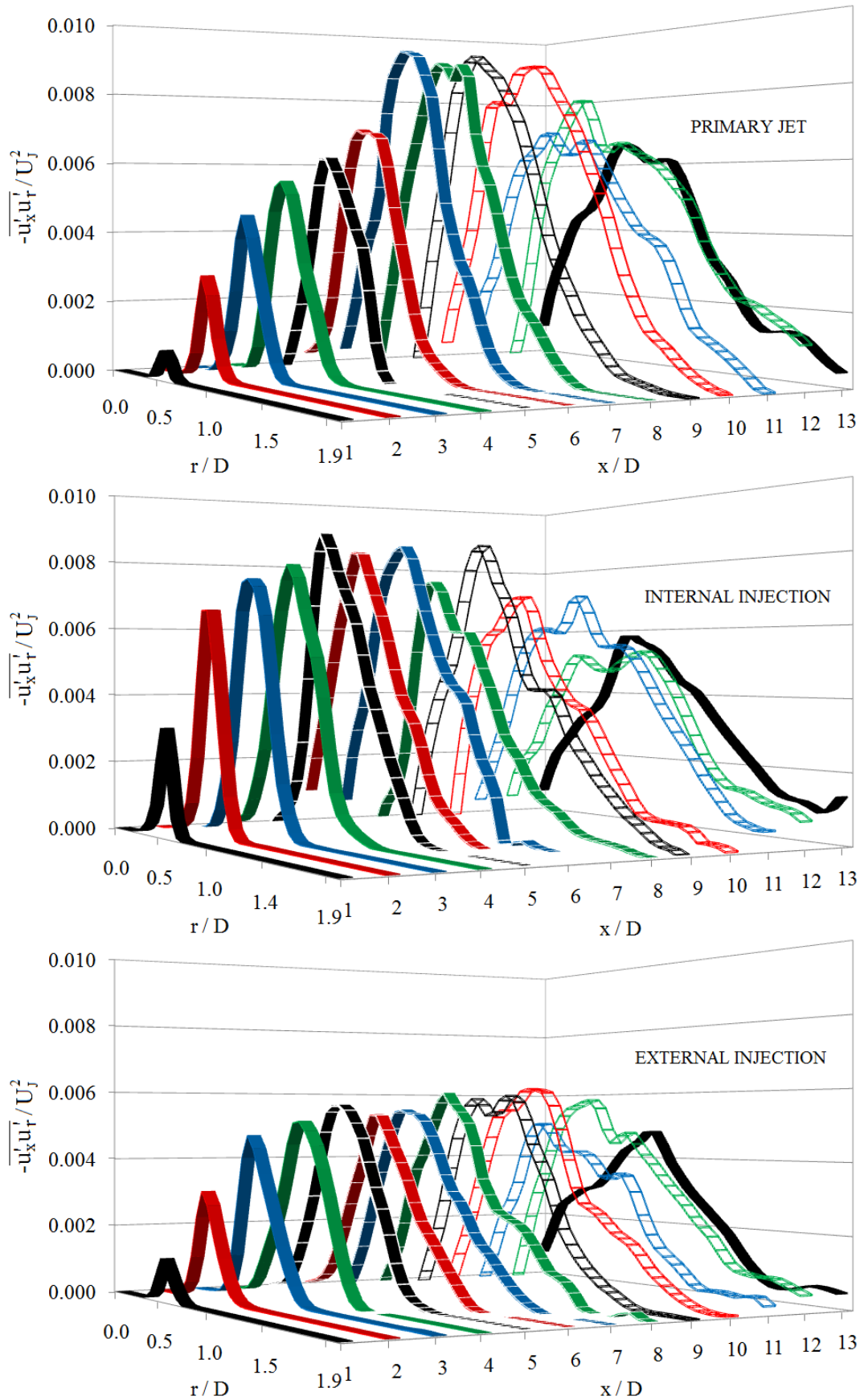


Figure 5.14: Variation in normalised Reynolds Stress with streamwise distance from the nozzle exit for the primary jet (top), internal injection at 40% IMFR (centre) and external injection at 1% IMFR (bottom).

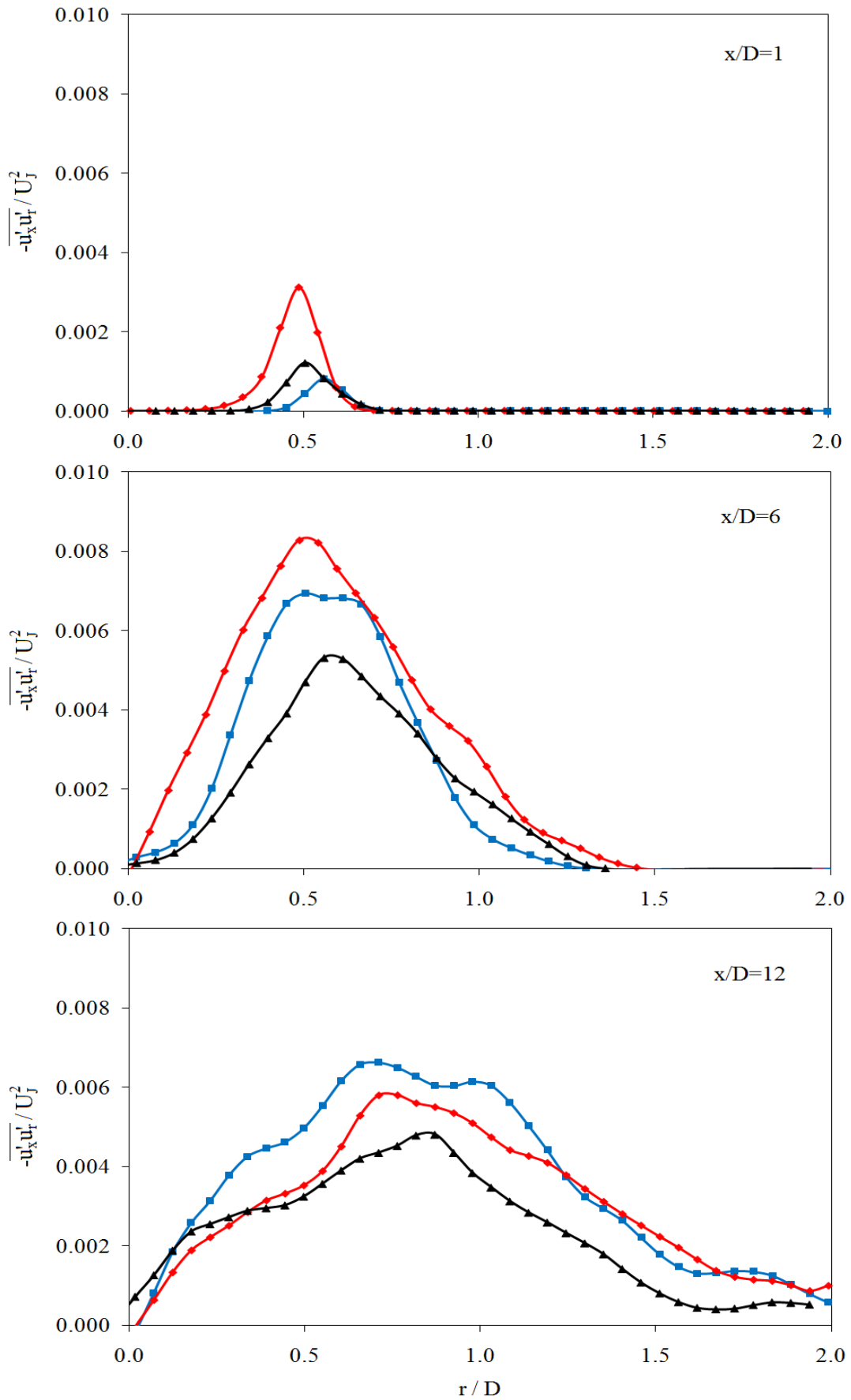


Figure 5.15: Comparison of normalised Reynolds Stress profiles at various streamwise locations for the primary jet (■), internal injection at 40% IMFR (◆) and external injection at 1% IMFR (▲).

5.5 Vorticity

Vorticity is a parameter used to describe the rate of rotation in a fluid. The axial and tangential components are defined in equations (5.7) & (5.8) respectively.

$$\omega_x \left[\frac{1}{s} \right] = \frac{\partial u_\theta}{\partial r} - \frac{1}{r} \frac{\partial u_r}{\partial \theta} \quad (5.7)$$

$$\omega_\theta \left[\frac{1}{s} \right] = \frac{\partial u_r}{\partial x} - \frac{\partial u_x}{\partial r} \quad (5.8)$$

Figure 5.16 shows contours of time averaged, non-dimensionalised out-of-plane vorticity, $\omega_x D_J / U_J$, across the jet at $x/D=0.6$. For the primary jet flow, the axial vorticity should be close to zero. However, the measurement of weak levels of vorticity can be attributed to possible calibration errors, due to misalignment between cameras and laser light-sheet. Hence a slight shift between the cameras should result in the cancelation of the offset vorticity rings. For ITI at an IMFR of 40%, regions of strong annular vorticity of opposing sign are visible. This uniform pattern is dominated by the effects of the tangential velocity gradient, the first term in equation (5.7), which is only significant within $0.35 < r/D < 0.55$. A small defect near the top edge of the jet can be ignored as a region of glare in the images caused by a laser reflection from the nozzle, resulting in a localised erroneous correlation measurement. The out-of plane vorticity levels for ETI at 1% IMFR have a considerably weaker and less uniform distribution compared to ITI. Enhanced levels of mixing have induced a break-up of the sensitive shear layer. Each of the eight tangential external jets has produced a pair of counter rotating vortices, which have in turn increased the rate at which the shear layer expands. This spreading is more clearly illustrated by the axial velocity contour lines in Figure 5.8. A slight asymmetry in the distribution could be due to an uneven mass flow from the external jets, as balancing pressure losses from all eight injector nozzles is difficult. The peak vorticity levels of 2 are twice as high as those achieved with axially impinging microjets and chevrons, suggesting ETI to be more effective in generating swirl (Alkisar et al., 2007). It must be noted that InSight 3G (2008), calculates the out-of-plane vorticity using the Cartesian equivalent of the in-plane vectors shown in equations (5.7) & (5.8). The change in sign is due to the software selecting the default zero-axis at the top left of the vector field.

Figure 5.17 shows a three-dimensional view of the out-of-plane vorticity. The vorticity induced by ITI has a greater penetration towards the core of the jet than ETI, whereas the definitive peaks and troughs created by ETI shows it to be the more effective technique for disturbances localised to the annular shear layer.

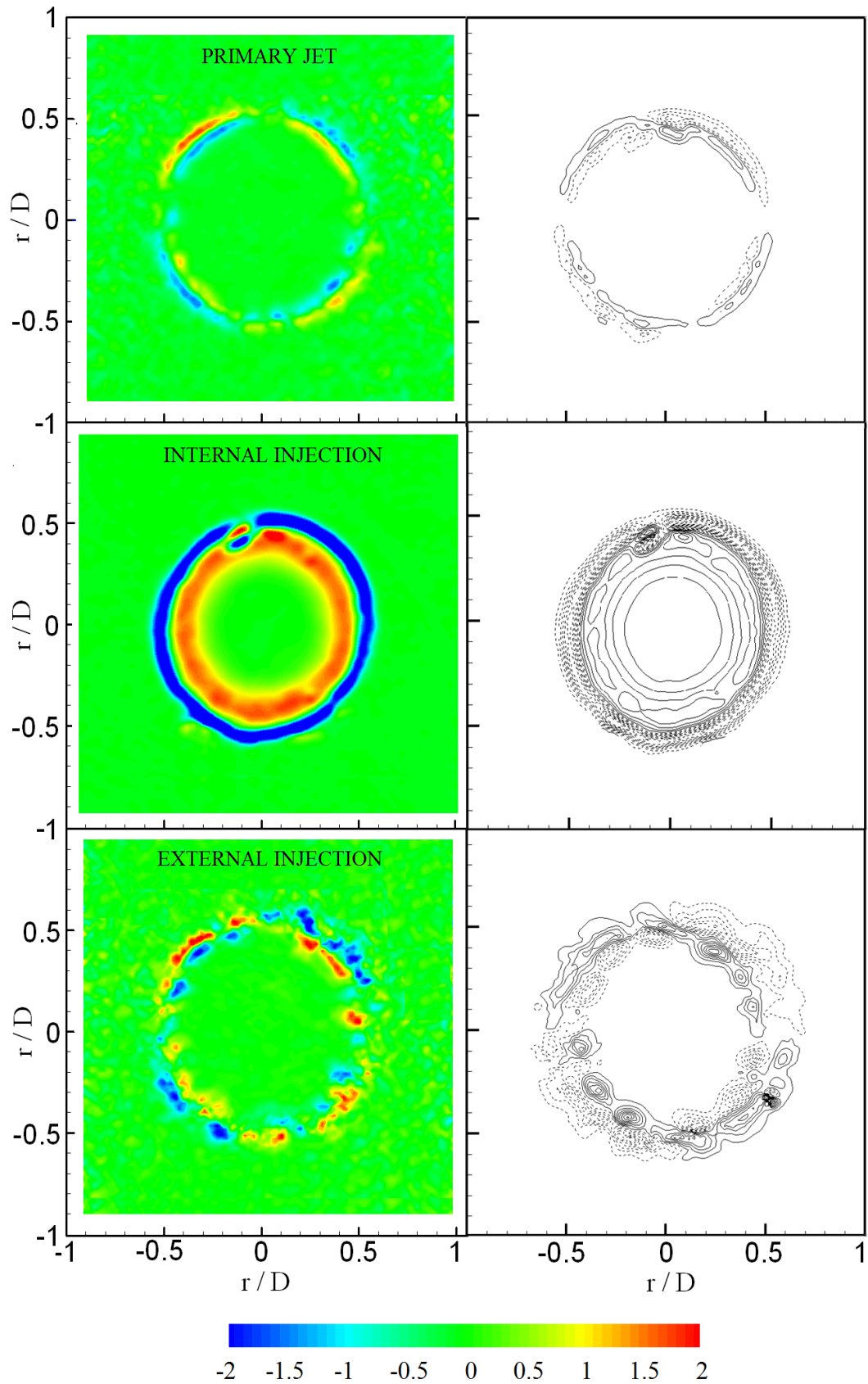


Figure 5.16: Contours of time averaged, non-dimensionalised out-of-plane vorticity, $\omega_x D_J / U_J$, from stereoscopic PIV at $x/D=0.6$ of the primary jet (top), internal tangential injection at 40% IMFR (centre) & external tangential injection at 1% IMFR. Lines are spaced at intervals of 0.5 for positive (—) & negative (···) values.

Figure 5.18 shows the out-of-plane, tangential component of vorticity. The fragmented contours are evidence for the presence of “*three-dimensional large-scale coherent vortical structures*” (Alkislar et al., 2003). Azimuthal vorticity, exclusive to the shear layer, is shown to be reduced considerably by both techniques beyond $x/D=6$.

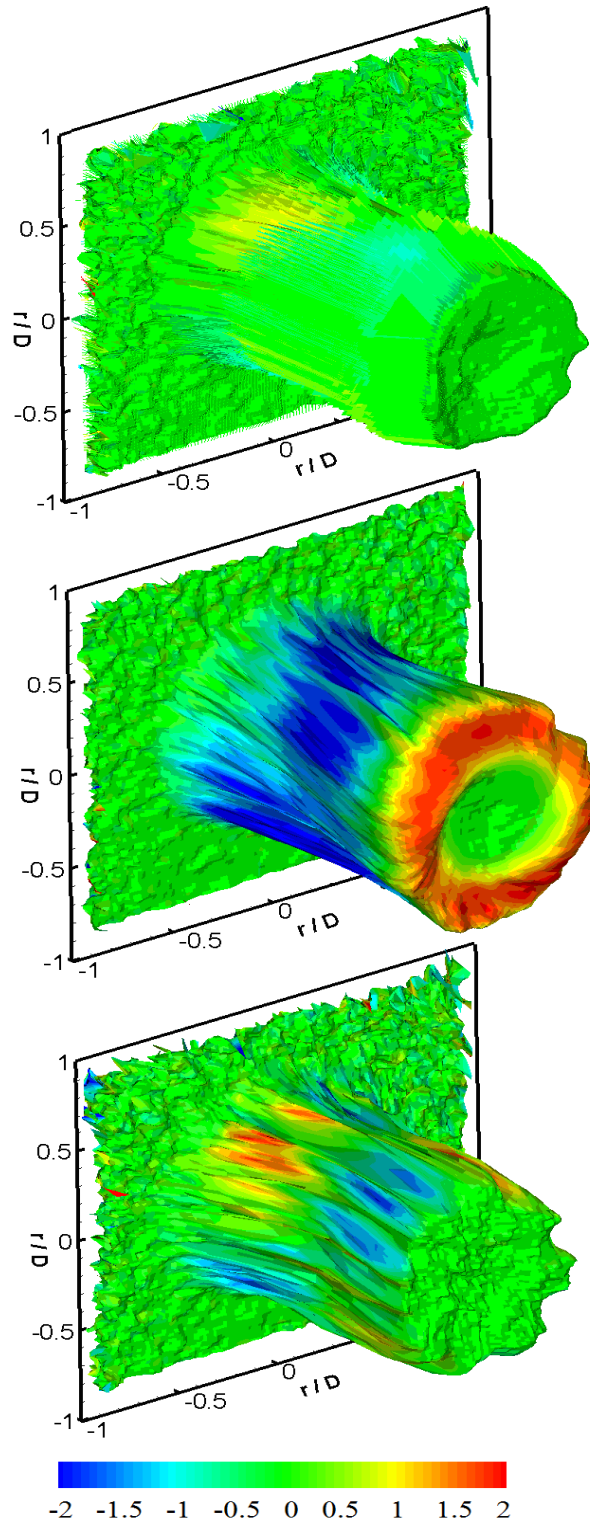


Figure 5.17: Three-dimensional view of non-dimensionalised out-of-plane vorticity, $\omega_x D_J / U_J$, for the primary jet, internal injection at 40% IMFR & external injection at 1% IMFR.

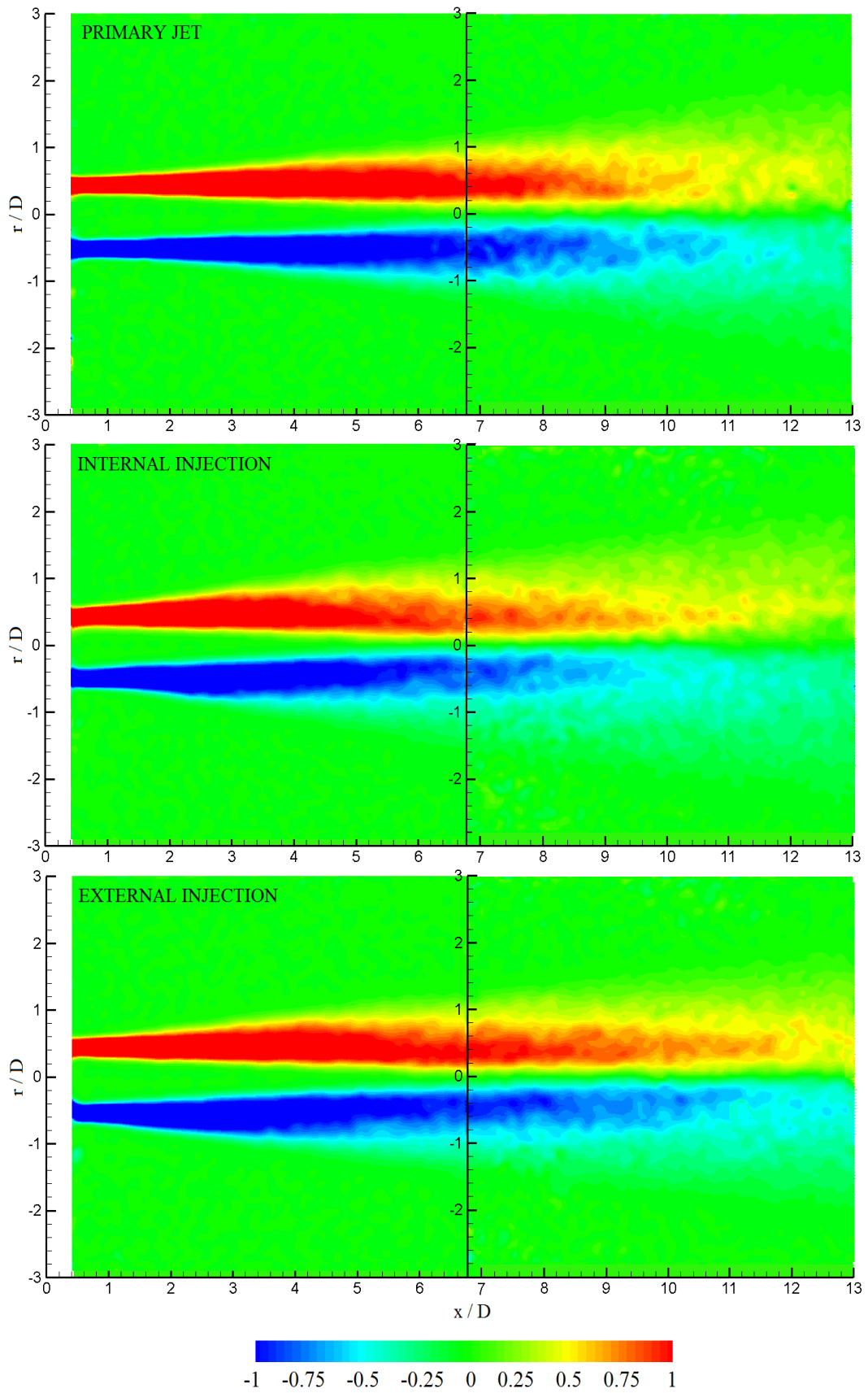


Figure 5.18: Contours of time averaged, non-dimensionalised out-of-plane vorticity, $\omega_e D_J / U_J$, from 2D mono PIV of the primary jet (top), internal injection at 40% IMFR (centre) & external injection at 1% IMFR (bottom).

5.6 Summary of Flow-Field Results

The main findings from the experimental PIV measurements of the modified and unmodified jet flow are summarised below.

Primary Jet

1. Peak axial jet velocity, U_x , measured at 388m/s as compared to 384m/s, which was derived assuming uniform flow across the jet.
2. Potential and supersonic core lengths were 6 and 11.1 nozzle diameters respectively
3. Integral of velocity profile yields 165N, with 168N calculated for isentropic flow.
4. Turbulence Intensity, T_1 , increases with streamwise direction, peaking at 0.16 at $x/D=7$
5. Normalised Reynolds Stress, R_S/U_J^2 , peaks at 0.01 at $r/D=0.5$ for $x/D=7$.
6. Low levels of out-of-plane (axial) vorticity, $\omega_x D/U_J$, across the jet at $x/D=0.6$

Internal Tangential Injection at 40% IMFR

1. ITI accelerates flow tangentially in the nozzle causing deceleration of axial velocity through adverse pressure gradients.
2. Potential and supersonic core lengths are reduced to $4D_J$ & $10.2D_J$ respectively
3. Thrust is reduced by 5% with peak U_θ (80m/s) contributing to a swirl number of 0.086
4. Shear layer instability induced by higher T_1 at $1 < x/D < 6$, with reductions beyond
5. 25% increase in R_S/U_J^2 in shear layer at $x/D < 6$, with reductions downstream
6. Amplified out-of-plane (axial) vorticity within the shear layer, $0.35 < r/D < 0.55$
7. Low frequency noise reductions by ITI are coupled with penalties in thrust

External Tangential Injection at 1% IMFR

1. Slight axial deceleration initially at edges of jet, otherwise increased axial velocities
2. Potential and supersonic core lengths are increased to $6.5D$ & $12.3D$ respectively
3. Thrust increased by 0.8% with peak U_θ (15m/s) contributing to swirl number of 0.013
4. Enhanced stability, with reductions in turbulence intensity at most values of r/D & x/D
5. Enhanced shear layer stability, with 25% reduction in R_S/U_J^2 at $6x/D$ & 85% at $12x/D$
6. Effective break-up of shear layer with counter-rotating vortical pairs from injectors
7. Minimal performance penalties imposed by ETI at relatively low IMFR of 1%.

6 DISCUSSION

6.1 Shock Associated Noise Reductions

It has been previously established that screech noise is a product of turbulent structures, induced at the nozzle exit, interacting with the shock cell structure of a supersonic jet (Powell, 1953). The existence of shock cell structures in the potential core implies that the jet is imperfectly expanded and serve the purpose of balancing the difference of pressure between the jet and ambient air (Tam, 1999). The presence of the shock cells in the jet plume results in multiple components of shock associated noise in addition to mixing noise. Both screech and broadband shock noise were detected at the sideline SPL spectra of the cold Mach 1.3 jet in Figure 4.1, confirming its imperfectly expanded state.

The centreline axial velocity of the primary jet was measured to be 375m/s at a streamwise location of $x/D=0.6$, as shown in Figure 5.3. However, the major part of the jet's cross-section was measured to have an axial velocity of 388m/s. These peak velocities towards the edge of the jet are more representative of the overall jet velocity since they cover a greater annular area than those at the centreline. Hence, in order to obtain a better estimate of the global jet velocity we can integrate the axial velocity profile across the jet radius as shown in equation (6.1):

$$\pi R^2 U_j = 2\pi \int_0^R U_x r dr \quad (6.1)$$

As the jet develops in the downstream direction ($x/D=0.6$), entrainment with the surrounding ambient air results in a slightly wider jet profile as shown in Figure 5.3. Hence, in order to estimate the global jet velocity at the nozzle exit ($x/D=0$) the entrained flow will be omitted from the integration. Finally, integrating from $r=0$ to $R \sim 0.015$ yields a weighted axial jet exit velocity of 380m/s. This compares to within 1% of the 384m/s derived from isentropic flow relations, which is of the order of the accuracy of the PIV measurements. The close match between experimental and theoretical values indicates only a slight degree of under expansion when the jet is operating at design condition. For supersonic regimes, the diverging section of the nozzle is designed to accelerate the flow whilst gradually reducing its static pressure to the level of the atmosphere. The fifth order polynomial used to profile the shape of the converging section of the nozzle aims to reduce the internal boundary layer thickness whilst maintaining a uniform velocity profile (Bell et al., 1988). However, the method of characteristics, used to design the diverging section, is an inviscid calculation and so only accounts for the reductions in shock wave reflections within the nozzle (Zucrow & Hoffman, 1976). Hence, the existence of a boundary layer within the nozzle effectively reduces the exit diameter of the jet, resulting

in a slightly underexpanded jet. The boundary layer thickness, δ_{BL} , can be estimated by the finite distance over which the steep velocity gradients operate towards the edge of the jet cross section in Figure 5.3. At a streamwise location of $x/D=0.6$, the primary jet boundary layer is approximately 2mm thick ($0.47 < r/D < 0.54$) and so is expected to be slightly lower at the nozzle exit ($x/D=0$). This measurement compares well to that of Samimy (2010) who used a 25.4mm exit diameter converging-diverging nozzle with a similar contraction ratio (3:1) to the nozzle being investigated in this study (2.7:1). For the high Reynolds number (1.1×10^6) Mach 1.3 jet configuration, the boundary layer was thought to be turbulent and estimated to be approximately 1mm thick.

With the jet operating very close to a perfectly expanded state, the difference between the jet and ambient atmospheric pressures is minimal. Hence, the omission of the back pressure term in equations (3.11) & (3.48) for the isentropic and experimentally approximations of jet thrust, is justified. Figure 5.3 and Figure 5.7 show ETI at 1% IMFR to have an almost identical centreline velocity as compared to the primary jet with slight reductions towards the edges of the core, resulting in a weighted global jet velocity, U_J , of 379m/s. Hence the omission of the back pressure term is also a fair approximation for this configuration. For ITI at an IMFR of 40%, adverse pressure gradients due to the swirling flow components resulted in a decayed velocity profile towards the edges of the jet, with a slight increase in centreline velocity, as shown in Figure 5.3. Using equation (6.1) the global axial jet velocity for this specific ITI velocity profile is approximately 360m/s. In this underexpanded case, the ambient air pressure is lower than that of the jet. Thus the absence of a back pressure force would serve to further increase the jet thrust, resulting in a lower than estimated thrust penalty of 5% that was shown in Table 5.1.

The harmonic screech tone was recorded at $St=0.74$ ($f=9.6\text{kHz}$) for the 90° SPL spectra of the primary jet in Figure 4.1, whereas the downstream propagating fundamental component occurred at $St=0.49$ (6.3kHz) at 15° . Equation (2.10) quantifies the frequency of the fundamental component of screech with respect to the convective speed of the eddies, U_C , and shock cell spacing, s , (Powell, 1953). The harmonic component, through equation (2.12), can be estimated as being twice that of the fundamental component. Equation (2.10) however, is heavily dependent on the shock cell spacing, which from PIV data in Figure 5.6 is shown to vary between adjacent cells with respect to streamwise location. A mean value of $0.85D_j$ is a reasonable representation of the spacing between the third and fourth shock cells, the region from which screech noise originates (Kaji et al., 1996; Raman, 1999). It matches to within 2% of the $0.87D_j$ predicted numerically using the Prandtl-Pack shock cell spacing formula shown in equation (2.11). Approximating the convective speed of the hydrodynamic structures to be within 60-70% of that of the jet (Bishop et al., 1971; Tam, 2009), the theoretical

frequency of the harmonic component of screech noise is between 10.2kHz and 11.1kHz respectively. The experimental value (9.6kHz) compares more favourably, with a 5% error, to the theoretical value (10.2kHz) derived from the lower convective jet speed ($0.6U_j$).

All three tangential air injection techniques proved successful in eliminating the fundamental and harmonic components of screech noise as shown in Figure 4.19. Enhanced shear layer mixing induced by the air injectors is thought to be the mechanism that disrupts the resonant feedback loop around the nozzle exit from the turbulence-shock interaction process. This is consistent with previous findings that showed swirling velocity components reduce screech noise through impeding the formation of shock waves (Neemah, 1999). An improved design consisting of a reduced nozzle lip thickness has also proven to be an effective technique for passive screech noise control by reducing the sound reflecting surfaces that amplify the acoustic feedback loop from the shock cells (Norum, 1983).

6.2 Turbulent Mixing Noise Sources and Structures

The contrast between the shape and nature of the acoustic spectra at the different observer angles in Figure 4.3 validates the existence of multiple noise source structures and mechanisms in the jet, which radiate and dissipate at varying angles and speeds. The acoustic spectra at the sideline and mid-range angles of 90° - 50° are characterised by flat, low intensity SPL curves that Conform to Tam's (1996) similarity *G-spectra* for fine-scale turbulence noise. In contrast, the downstream SPL spectra conform to Tam's (1996) similarity *F-spectra*, characteristic of large-scale turbulence noise. The normalised autocorrelation results in Figure 4.22 also support this view. The shape of the autocorrelation from all ten microphones can be systematically divided into the two groups. The sideline and mid-range angles of 90° - 50° are characterised by narrow, peak negative correlation widths ($2\tau_{max}$), whereas those from the downstream angles of 30° - 15° are much wider. Using the peak negative normalised autocorrelation width, the noise source structure sizes were estimated in table 11. The results confirm that the axisymmetric jet has two spatial length scales (Samimy, 2010), with the acoustic waves propagating towards the sideline direction having wavelengths of the order of the boundary layer thickness ($0.1D_j \sim 3\text{mm}$) and those radiating towards the downstream direction being of the order of the nozzle exit diameter ($\sim 3D_j$).

The normalised cross-correlation between adjacent microphone pairs was used to obtain important information on the source location of the two distinctly different noise emitting structures. It is well known that higher frequency mixing noise from fine-scale turbulent structures originates from the instabilities in the shear layer close to the nozzle

exit, whereas lower frequency noise from large-scale turbulent structures originates from further downstream towards the end of the potential core (Bishop et al., 1971). Figure 4.28 shows that the low frequency preferred modes of the jet ($St=0.17, f=2\text{kHz}$) originate close to the end of the supersonic core of the jet ($x/D>12$) with Figure 4.30 showing the higher frequency noise ($St=0.74, f=9.6\text{kHz}$) to be instigated closer to the nozzle exit ($3<x/D<5$). The agreement of these experimental results with established ideas places a degree of confidence in the results from Figure 4.28 to Figure 4.31, which shed light on how the three distinct air injection techniques alter the locations of the jet's noise sources.

The cross-correlation data was also used in understanding the nature of the noise emitting structures. Low levels ($R_{CC}<0.1$) of normalised cross-correlation between adjacent microphones in the sideline direction (90° - 80° in Figure 4.24) indicate the random and incoherent nature of the noise structures radiating in that direction, much like the volatile shear layer region from which they originate. However, at downstream locations the cross-correlation between pressure signals from microphones at 25° - 30° was as high as 0.8 (Figure 4.26) despite the distance between them being greater than those at the sideline. This indicates that the low frequency noise emitted from the large-scale structures has a more organized and coherent nature (Tam 2009). The type of tangential air injection is shown to have minimal effect on the normalised autocorrelation and cross-correlation peaks (positive and negative), indicating a limited influence on the size and nature of the noise generating turbulent flow structures. However, there is evidence to suggest that it displaces their origins in Figure 4.28 to Figure 4.31.

The near-field region of the jet, $30<x/D$, is dominated by non-linear and non-spherical propagating hydrodynamic modes, yet it is surprising how well the noise source locations based on contours of near-field SPL in Figure 4.33 to Figure 4.36 match those derived from far-field cross-correlations. The noise source locations derived from the near-field SPL data showed strikingly similar characteristics to the extended near-field SPL measurements of a cold Mach 1.5 jet by Yu (1971). They confirmed low frequency noise to have an array of sources extending beyond the supersonic core of the jet ($x/D>12$), with the higher frequency noise sources ($f>10\text{kHz}$) being fairly localised at $x/D=4$.

6.3 Mechanisms for Low Frequency Noise Reductions

The shear layer is known to be sensitive to perturbations over a wide range of frequencies (Zaman & Hussain 1981) and hence it has been of considerable interest to researchers seeking to reduce jet noise through impinging microjets promoting streamwise vorticity (Arakeri et al., 2003; Callender et al., 2007; Alkislar, 2007; Castelain et al., 2008). The steady tangential air injection techniques (ITI & ETI) explored in this

study have also been successful in reducing low frequency ($St < 1$, $f < 13\text{kHz}$) as shown in Figure 4.19. The 2kHz pulsating tangential air injection technique (PTI) also showed reductions in low frequency noise through targeting the jet's preferred mode, which is also known to be '*unstable to perturbations*' over a wide range of frequencies (Samimy, 2010). Figure 4.4 shows the OASPL of the Mach 1.3 primary jet of nozzle pressure (P_J/P_o) and temperature (T_J/T_o) ratios of 0.36 and 0.75 respectively. The Mach 1.3 jet's directivity compares well to that of a Mach 1.36 jet of temperature ratio unity (Viswanathan, 2010), with a flat distribution at the sideline angles (90° - 70°) followed by a gradual and constant increase across the midrange angles (60° - 40°) towards the peak radiating downstream angle of 30° - 25° . The greatest OASPL benefits from ITI and ETI were recorded at the extreme downstream angles beyond 30° as shown in Figure 4.21. The large-scale coherent structures responsible for emitting low frequency noise towards downstream angles, have been identified to go through three vital stages of spatial development from the point of birth near the shear layer; '*the growing, saturation and decay phases*' (Samimy, 2010). However, it is very difficult to weigh up their respective contributions towards the peak noise levels of the jet and to conclude which is most significant.

The tangential velocity profiles in Figure 5.11 show that ITI accelerates the flow tangentially within the nozzle causing a deceleration in the axial direction previously shown in Figure 5.5. This subsequently reduces the potential and supersonic cores by as much as 2 nozzle diameters as compared to the primary jet in Figure 5.7. The potential core length for the primary jet was found to match exactly to the $6D_J$ derived theoretically from Witze (1974) formula based on the ambient to jet density ratio, ρ_a/ρ_J , of 0.77 and Kleinstein constant $k=0.067$ from equations (2.5) & (2.6). This not only adds confidence in the experimental results, but is another indicator that the jet is operating near its perfectly expanded state. The existence of swirl in an axial jet is known to increase the dominance of helical instability modes over the preferred modes of the jet (Liang et al., 2005). This could be the phenomenon causing the axial deceleration of the flow. The peak swirl number of 0.086, generated by ITI at 40% IMFR, is comparably small to those previously achieved using passive methods. Knowles and Carpenter (1988) managed $S_N=0.15$, whilst Gilchrist & Naughton (2005) more recently recorded levels up to $S_N=0.3$. However these experiments, as detailed in § 2.5.1, were on incompressible, subsonic jets and so the swirl numbers by definition were not limited by the square of the jet velocity in the denominator term of equation (5.2). Neemah et al. (1999) used a vortex chamber to generate swirl in a supersonic Mach 1.3 jet. In that study the contribution of the tangential component of velocity was defined using the Swirl Mach number, $M_S=U_\theta/a_\infty$, typically around 0.3. Using his definition, the Swirl number of 0.086 generated by ITI in this study,

corresponds to a Swirl Mach number of 0.27 ($M_s = 80/295$), which compares well to the value of 0.3 recorded by Neemah (1999).

The pressure transducer upstream of the nozzle serves the purpose of maintaining the plenum pressure. An increase in the mass flow rate from the internal injector ports into the plenum is compensated by an instantaneous reduction of flow entering the settling chamber via the gate valve, hence keeping the total mass flow rate through the nozzle constant. Despite this measure it seems that the swirling velocity component has a net effect of reducing the axial jet velocity and thrust, and could be the reason for the lower downstream spectral noise levels when compared to the undisturbed flow. Contours of axial velocity and vorticity derived from stereoscopic PIV measurements in Figure 5.8 & Figure 5.16 indicate ITI to induce strong levels of swirl in the shear layer, while ETI proves more effective in mixing and breaking up the shear layer. It can be argued that these disruptions at the initial ‘*growth*’ stages limit the spatial extent to which the large-scale coherent structures grow, which subsequently translates to low frequency noise reductions.

To better understand these aeroacoustic benefits, the fluid dynamic interaction between the jet and tangential air injectors must be considered. Figure 5.13 & Figure 5.15 both show ETI to have reduced turbulence intensity, T_t , and normalised Reynolds stress, R_s/U_j^2 , levels by up to 18% and 25% respectively, in the critical shear layer region of the jet beyond $x/D=6$. Water injection at an IMFR of 5% to that of a Mach 1.4 jet has also been shown to reduce turbulence levels within a jet. This subsequently led to reduction in jet noise, which was thought to be driven by the process of water particle break-up upon interaction with the main jet (Krothapalli et al., 2003). Lighthill (1952) in his pioneering theory pointed towards Reynolds stresses as being the major contributor to jet noise, as shown in equation (2.2). Based on this understanding, the aerodynamic mechanism through which ETI achieves the low frequency noise reductions is evident. ITI, on the other hand, demonstrates contrasting fluid dynamic effects on the primary jet. At streamwise locations close to the nozzle exit ($1 < x/D < 6$) both turbulence intensity and Reynolds stress are increased. Based on Lighthill’s equation this should translate to an increase in noise, which is exactly the case in Figure 4.20 for the midrange angles of 70°-40°. Similar to ETI both turbulence intensity and Reynolds stress are reduced between the potential and supersonic cores for ITI (Figure 5.13 & Figure 5.15), the region in which large-scale structures are most dominant, and so explain the low frequency SPL and OASPL reductions in Figure 4.19 & Figure 4.20.

6.4 Mechanisms for Increased High Frequency Noise

The low frequency noise reductions induced by both steady ITI and ETI techniques are coupled with an SPL cross-over into higher frequency bands as shown in Figure 4.19 and Table 4.1. However, this phenomenon is more predominant at the sideline and midrange angles, suggesting it is linked to the small-scale turbulent noise structures radiating in that direction. This counter-balancing effect is consistent with the law of conservation of energy, with energy neither being created nor destroyed, but subsequently transferred to levels beyond the human audible range of 20-20,000 Hz (Cutnell, 1998).

The use of circumferential control jets on a primary jet flow has been shown to weaken the formation of large-scale flow structures in the near-field, resulting in the destabilisation of the shear layer and enhanced formation of small-scale turbulent structures (New and Tay, 2004). The deflection of the injected fluid from the primary jet core was thought to have produced a pair of counter rotating vortices, the mechanism for enhanced mixing and small-scale turbulence noise (New and Tay, 2004). A more recent experimental investigation on the use of microjets for impinging fluidic injection into the shear layer concluded similar mixing effects, with a transfer of acoustic energy into higher frequency bands (Callender, 2007).

In terms of the fluid dynamic effect of internal tangential injection at 40% IMFR, an increase in both T_l and R_s is observed close to the nozzle at $x/D=1$ in Figure 5.13 and Figure 5.15. This increased fluctuation is promoted by the tangential velocity components in the shear layer resulting in the peak recorded swirl number of the order 0.086. The increased mixing may be causing a rapid decomposition of fine-scale structures, enhancing viscous dissipation. This may be linked to the pattern of increased high frequency noise. However, for ETI the increase in T_l and R_s close to the nozzle exit is not as significant and hence there must be another mechanism behind the high frequency SPL cross-over in the acoustic spectra shown in Figure 4.19.

External tangential injection targets the sensitive shear layer by introducing a net swirling component of velocity. In doing so, the injection plane of all eight injectors is parallel to the sideline direction. Control jets external to the jet nozzle have been shown to contribute to the overall increase in high frequency noise through ‘*self-noise*’ (Callender, 2007). In order to better understand this undesired parasitic noise, the external injectors can be considered in isolation as sub-scaled jets characterised by the same acoustic spectra and directivity patterns as the main primary jet. Using the isentropic relations, at an IMFR of 1% the exit velocity of each of the eight external injectors (which are not designed to be perfectly expanded) is of the order of 272 m/s ($M_E = 0.8$ in table 4). The mean flow features of free microjets have recently been shown to be similar to larger supersonic jets operating at higher Reynolds numbers (Phalnikar et al., 2008). Tanna

(1977) first established the Strouhal number of 0.19 as the value for peak jet noise. Assuming that the injector jets also exhibit peak noise at $St=0.16-19$, with an injector diameter and fluid velocity of 1.5mm and 272m/s respectively, peak injector self-noise is expected to occur at approximately 29kHz-34kHz based on the Strouhal relation shown in equation (3.22). The smaller diameter scales of the injectors exhibit smaller noise structures and hence introduce higher frequency noise to the main jet's acoustic field. Isolated background measurements of 1.65 μ m diameter microjets showed self-noise to peak in the range of 20-32kHz (Callender, 2007). This value is consistent with the present self-noise estimate as well as the measured high frequency noise cross-over that occurs at a $St=2.5$ (32kHz) in the 90° SPL spectra (Figure 4.10). The high f cross-over is more pronounced and initiates at much lower frequencies ($St\sim 0.9$, $f\sim 12$ kHz) at the downstream angle of 30° as compared to the sideline observer angle. At 30° the SPL peaks (132dB) and begins to drop off at $St=0.18$. At the high f cross-over point of $St=0.9$ the SPL has already decayed to 114dB, whereas the injector self noise is still climbing up to its peak of approximately 30kHz. Hence at downstream angles the injector self noise has a more profound overall effect on the acoustic spectra than at the upstream angles, which begin to decay at much higher ultrasound frequencies. In conclusion, unlike the low frequency noise benefit, the amplification of high frequency noise is not just due to fluid dynamic mixing effects between the primary jet and external injectors, but also the control jet noise itself. Callender (2007) subtracted the self-noise spectra from that of the modified primary jet and found the cross-over effect to be eliminated, revealing SPL reductions even at higher frequencies that were previously veiled. This method of parasitic noise subtraction could be used to calculate the noise reduction purely due to the fluid dynamic effects of shear layer mixing. However, in reality the parasitic noise from the injectors is part of the overall mechanism for jet noise reduction and hence will not be subtracted from the acoustic spectra presented in this study.

ETI shows OASPL benefits across all observer angles as compared to the primary jet in Figure 4.20. This puts forward evidence for the low frequency SPL reductions to be much more significant than any higher frequency amplifications.

The 2kHz pulsating tangential injection configuration at an IMFR of 0.7% did not show evidence for the high f noise cross-over effect as seen for both ITI and ETI. In terms of its physical set-up it is identical to ETI, and so the pulsating nature or the lower exit velocities of the injector fluid may be part of the reason.

6.5 Error and Uncertainty

In order to gain an estimate of the random acquisition errors involved in the acoustic measurements, the OASPL of the primary jet was calculated from five separate samples, each recorded over a period of 3 second at a sampling frequency of 140kHz. The standard deviation in OASPL's derived from the multiple samples was found to be lower than 0.02dB and 0.08dB at the sideline (90°-70°) and mid-range (60°-30°) observer angles respectively. The standard deviation in the samples was found to be slightly higher, between 0.15-0.2dB for the downstream observer angles (25°-15°), equating to less than 0.18% of the rms of the peak OASPL. Hence, all magnitudes of noise reduction recorded for each respective air injection technique are expected to be accurate to within 0.2 dB (<1%). A plot of the variation in OASPL's from the five samples is shown in Figure 4.4. In terms of the possible systematic errors in the acoustic measurements, an indication is given by the variation in sensitivity amongst all ten free-field condenser microphones. The sensitivities, s , typically ranged from 3.45mV to 3.67mV, yielding a standard deviation of 0.08mV which is approximately 2.3% of the s_{rms} . The variation in free-field response with respect to the microphone's directivity to the noise source begins at frequencies beyond 10kHz with a measurement uncertainty of 1dB up to 40kHz (G.R.A.S, 2003). This suggests that the response of a microphone is omnidirectional at low frequencies (Viswanathan, 2006), hence making the acoustic measurements for lower frequency noise more accurate.

With respect to the flow-field data acquired through PIV, the measurement uncertainty has been shown to vary with seeding particle size on the image plane. Maintaining an average particle size greater than 3×3 pixels on an interrogation window size of 64x64 pixels is a sufficient criterion in keeping rms random errors associated with displacement vectors below 1% (Raffel, 1998). The error increases gradually to over 1.5% for particle image diameters of 4 and 5 pixels but increases more sharply for those smaller than 3 pixels. When the particle image size becomes too small, there is an introduction of peak locking, where the vector displacements are rounded to integer values, and hence bias errors are increased. A more detailed account of the measures taken to reduce velocity measurement errors is given in § 3.8. The peak jet velocity measured at 388m/s gives an error of 1% with respect to the 384 m/s derived theoretically through isentropic flow relations. Hence, the increase in thrust by 0.8% recorded for ETI at an IMFR of 1% is of the order of the accuracy of the PIV measurements.

6.6 Optimal Noise Reduction Technique

The external tangential injection configuration is evidently the more efficient technique for reducing jet noise, especially at the sideline and downstream observer angles (Figure 4.20). All three air injection techniques possess their own strengths and weaknesses, which in terms of their acoustic performance are summarised in table 10. At the extreme downstream angle of 15° , ITI yields a greater OASPL benefit of 6.3dB as compared to the 4.7dB by ETI. However, the IMFR of 1% used by ETI is only a fraction of to 40% being discharged by ITI. The effectiveness of ETI becomes more apparent when the performance parameter of thrust is considered. A penalty in thrust levels of more than 5% with ITI would have severe consequences on the specific fuel consumption of aircraft engines, proving detrimental to airline economics. On the other hand, the additional mass injected by ETI equates to a 0.8% increase in thrust levels. The 2kHz PTI configuration returned much higher SPL benefits (~ 1 dB) across the mid-range observer angles of 70° - 40° , as compared to the other two techniques (< 0.5 dB). However, the complicated system used to pulse the flow at such high frequencies is relatively inefficient. In order to obtain an IMFR of 0.7% at the injector outlets, an upstream supply gauge pressure greater than 5bar (506kPa) is required. This gives some measure of the pressure and frictional losses across the aluminium and PTFE Teflon slip surfaces, given that the main jets gauge plenum pressure is only 1.75bar. Unless a more efficient and economically viable method for pulsing the injector fluid is made available, PTI as an overall technique cannot be considered effective.

The external tangential air injection technique is unique in the sense that it has a net swirl effect on the jet's shear layer, unlike the axially impinging microjets and mechanical chevrons, which have been the areas of most interest to researchers in the recent past. A time averaged tangential velocity component of almost 20m/s contributes to a jet swirl number of 0.013, as shown in Figure 5.9 and Table 5.3 respectively. The swirl number, S_N of 0.013 corresponds to Swirl Mach number, $M_S = U_\theta / a_\infty$, equal to 0.07. Even the minute IMFR of 1% tangentially into the axial jet produces both radial and axial vorticity, proving it to be an effective method for promoting rapid and possibly premature roll-up (early transition to decay) of vortices associated with the shear layer. The Schlieren Images captured by Luff et al., (2008) show internal swirl to promote enhanced mixing closer to the nozzle whilst inducing the premature roll-up of vortical structures by up to a nozzle diameter, as shown in Figure A.1 in Appendix A. PIV studies have shown radially impinging microjets to produce counter-rotating vortices near the high speed inner side of the initial shear layer (Alkislar et al., 2007). However, due to the non-impinging nature of the tangential injection, the PIV contours from this study show that the vortical structures exist closer to the low speed outer-side of the shear layer at a jet

radius $r/D=0.5$ in Figure 5.16. The location of these flow structures is confirmed by the flow reversal pattern observed at $0.5 < r/D < 0.55$ in the tangential velocity profiles of Figure 5.11, which is additional evidence of small axially aligned vortices being generated by the external injectors.

In terms of the fluid dynamic effects, the potential and supersonic cores of the primary jet were increased by $0.5D_j$ and $1.2D_j$ with ETI to their new lengths $6.5D_j$ and $12.3D_j$ respectively. This observation agrees qualitatively to that of Arakeri et al. (2003), who also reported the lengthening of the potential core from $x/D=6$ to $x/D=7.5$ with the use of microjets. Figure 5.13 & Figure 5.15 both show ETI to have reduced peak levels of turbulence intensity, T_i , and normalised Reynolds stress, R_s/U_j^2 , by up to 18% and 25% respectively, in the critical shear layer region of the jet beyond $x/D=6$. These experimental results also show agreement to the axially impinging microjet studies of Arakeri et al., (2003) who reported reductions in turbulence intensity and Reynolds stresses by up to 15% and 40% respectively. These alterations in the instability characteristics of the initial shear-layer have shown to greatly influence the acoustic far-field of the jet, playing a critical role in the noise reductions presented in Figure 4.12. The peak non-dimensionalised out-of-plane (axial) vorticity levels (~ 2) recorded in Figure 5.16 are almost twice as high as those previously achieved with axially impinging microjets and mechanical chevrons (Alkisslar et al., 2007), proving the swirl generated by ETI to be more effective in promoting shear layer mixing. The smaller and more rapidly decomposing vortical structures induced by ETI may explain the increased SPL at the higher frequency bands observed in Figure 4.10. Azimuthal (tangential) vorticity, exclusive to the shear layer, is shown to persist further downstream of the potential core with the external injectors in Figure 5.18. This, in addition to the thicker shear layers can contribute towards higher levels of shear refraction, widening the cone of silence to include the microphone at 15° , hence explaining the substantial OSAPL reductions.

The pitch of the external injectors has been shown to play a critical role in its ability to effectively reduce jet noise (Callender, 2007). For a set injection pressure ratio, an injector pitching angle of 60° to the primary jet flow yielded up to three times greater noise reductions than a purely streamwise (axial) injection of pitch 0° (Callender, 2007). This pattern was observed at both sideline and downstream acoustic spectra and OASPL. This result was explained by the fact that the steeper pitched injectors penetrate deeper into the jet shear layer and core, hence maximising the effects of any mass or momentum transfer. These findings justify the use, and explain the effectiveness of the present 90° pitch, tangential injectors, given that noise reduction through shear layer disturbance is a primary aim.

Apart from the physical geometrical configuration, the injectant mass flow is also vital. Increasing the IMFR by as little as 0.3% from the optimal 1% begins to undo the noise reductions previously achieved, as shown in Figure 4.12. For radial microjet injection, New and Tay (2004) concluded that an over pressure in fluid injection, results in the counter-rotating vortices from the fluid interaction penetrating too far into the main jet's core, hence reducing the overall effectiveness. It seems this trend is transferable to the tangential injectors as higher IMFR's result in deeper penetration and swirl numbers associated with the shear layer, thus reducing the success of ETI.

In terms of application on existing aircraft turbofan engines, ETI by nature of its design and performance parameters should have a simpler implementation compared to ITI and PTI. A mass flow ratio of the order 1% to that of the primary exhaust can sensibly be bled through an external pressurised tank, which can be replenished if required by the engine compressors. Alternatively, the external injector flow could be bled directly from the intermediate stage compressor of a civil aircraft engine, as is usual done to maintain cabin pressure (Rolls Royce, 1986). The intermediate stage compressor of aircraft turbofan engines typically provides pressure ratios 8 times than of the atmosphere (Rolls Royce, 1986), which is more than sufficient given the supply pressure required for ETI operation. One of the primary justifications for using active jet noise control methods was having the ability to disengage the injectors during phases of the flight envelope where noise pollution is not an issue, i.e. high altitude cruise. Hence operation during the short but critical take-off, climb and landing manoeuvres should not over-exert the engines resources. The actual external injectors could be housed within the nacelle leading up to the point of injection from within the nozzle lip. A design that blends the injectors within the streamlined shape of the nacelle would be highly desirable to minimise penalties such as parasitic drag that is currently common with mechanical chevrons. However, these suggestions are general and any serious attempt to implement the ETI system will require extensive research on the actual temperature and pressure ratios within co-flow regimes whilst considering upstream geometrical features such as the wing pylon.

6.7 Back to the Beginning

In order to draw links to the earlier discussion on Lighthill's Acoustic Analogy an estimate of the resultant change in acoustic intensity through ETI will be made using flow-field turbulence data obtained from PIV. Goldstein (1976) presented an expression that relates the acoustic Intensity, I , per unit length of a subsonic jet to its time averaged axial velocity fluctuations, u' , as shown in equation (6.2);

$$\bar{I}(r) \cong \frac{K\rho_o u'^4 l^3 A(x)}{16\pi^2 a_o^5 \tau_\xi^4 (1 - M_C \cos \theta)^5 r^2} \quad (6.2)$$

where K is a dimensionless constant, τ_ξ is the turbulent delay time for the second-order correlation to fall to $1/e$, l is the turbulence length scale, M_C the convective Mach number and $A(x)$ the cross sectional area of the jet. Using the following substitutions as defined by Goldstein (1976); $A(x) = 1/4\pi Dx$, $l = l_1 \approx 0.2U_J$, $\tau_\xi \approx 0.1x$ and $M_C = U_C / a_o$ where $U_C = 0.6U_J$, equation (6.2) can be re-written as equation (6.3).

$$\bar{I}(r) = \frac{5.79 \times 10^{-5} K \rho_o}{\pi a_o} \frac{M_C^4}{(1 - M_C \cos \theta)^5} \frac{u'^4}{r^2} \quad (6.3)$$

Hence, apart from the obvious constants, K , ρ_o and a_o , if M_C and the correlation length, l , are not affected by the noise control then the effect of ETI on the acoustic intensity is through the square of the turbulent kinetic energy, T.K.E, where $T.K.E = 1/2(u'^2)$. From Figure 5.5 we can deduce that ETI has no effect on the jet's centreline velocity at $x/D=0.6$, with a slight 10m/s increase at $x/D=6$. Given the likelihood that the jet temperature is unaltered by the introduction of ETI, the effect of this small (10m/s) velocity increase can be approximated as being negligible (2%) on the jet's convective Mach number. Using the auto-correlation data in Figure 4.22 it has already been established that neither of the air injection techniques has an effect on the correlation length scale of the jet, only the depth of the negative correlation peaks are effected, which indicates the contribution from the large scale turbulent structures in the flow towards noise generation (Tam, 2008).

Given that the change in the acoustic intensity is proportional to the change in the square of the acoustic pressure, $I=P^2/\rho a_0$ (Kinsler, 2000), equation (3.21) can be used to relate the OASPL (dB) to the acoustic intensity, shown in equation (6.4);

$$OASPL = 10 \log_{10} \left(\frac{P^2}{P_{ref}^2} \right) = 10 \log_{10} \left(\frac{I}{I_{ref}} \right) \quad (6.4)$$

Thus, the change in the overall sound pressure level, $\Delta OASPL$, as a result of introducing ETI, can be predicted by implementing our earlier derivation, that I is proportional to $(T.K.E)^2$, as shown in equation (6.5):

$$\Delta OASPL = 10 \log_{10} \left(\frac{I_2}{I_1} \right) = 10 \log_{10} \left(\frac{u_2'^4}{u_1'^4} \right) = 40 \log_{10} \left(\frac{u_2'}{u_1'} \right) \quad (6.5)$$

Having confirmed the nature of the constant terms, the variables can now be investigated. It is widely accepted that turbulent mixing noise originates from downstream of the potential core (Bishop et al., 1977; Tam, 1995; Panda et al., 2002). In this study, this has already been shown experimentally using both the far-field cross-correlation and near-field SPL measurement techniques. Hence let us consider the turbulence intensity, T_I , across the jet at an axial plane of $x/D=6$ in Figure 5.13. The peak T_I occurs at $x/D=6$ and $r/D=0.5$ for the primary jet and is reduced by ETI from 0.14 to 0.12. Multiplying T_I by the jet velocity ($U_J=384\text{m/s}$) gives us the corresponding turbulent velocity fluctuations, u_1' of 54m/s and u_2' of 46 m/s for the primary jet and ETI control respectively. This yields a ratio of $(u_2'/u_1')=0.85$. However in order to obtain a more accurate representation of the change in turbulent velocities, we will consider a greater cross-section of the jet, $0 < r/D < 1.5$, rather than just a single location as, $r/D=0.5$. Using the mean ratio of velocities fluctuations, $(u_2'/u_1')_{mean} = 0.92$ the expected noise reduction can be quantified as 1.45dB using equation (6.5).

The dominant component of turbulent mixing noise from large scale fluctuating structures is known to propagate towards the downstream arc of an axisymmetric jet (Tanna 1977; Tam 1996; Hileman et al., 2002), whilst supersonic components such as screech and broadband shock noise dominate the sideline (Powel, 1953; Raman 1999). Hence the comparison between the predicted and experimental OASPL noise reductions

will also be made in this specific region. Figure 4.20 and Figure 4.21 illustrate how the peak OASPL of the primary jet, which occurs at an observer angle of 25° , is reduced by 1.35dB from 120.6dB to 119.1dB. This is fairly close to the predicted 1.45dB. However, if we consider the average OASPL reduction across the downstream observer angles of 40° - 15° the comparison is near exact at 1.43dB. Hence it can be concluded that the change in the acoustic intensity is proportional to the change in the square of the *T.K.E*, implying that the underlying physics of the ETI technique are governed by the same principles outlined in the Acoustic Analogy.

The near-field SPL contours in Figure 4.33 show low-frequency noise to originate from beyond the supersonic core at $10 <x/D> 12$. Such findings have previously been documented both experimental (Yu, 1971) and numerically (Self, 2004). Hence, if we consider the mean ratio of turbulent velocity fluctuation, $(u'_2 / u'_1)_{mean} = 0.77$, across the jet ($0 > r/D < 1.5$) at $x/D = 12$ as shown in figure 5.13, the expected OASPL reduction is 4.45dB. Although this is in close agreement with the isolated noise benefit of 4.7dB at 15° using ETI, the close match is thought to be more of a coincidence than of any physical meaning. The unusually high noise reduction observed at 15° is probably affected considerably by the cone of silence and atmospheric attenuation along the relatively greater propagation distance. This aspect can be investigated by accounting for the propagation distance (of sound waves radiating towards 15°) within the jet flow. Using simple trigonometry, the propagating distance within the jet is found to be equal to $R \sin(15) = 5.8\text{cm}$, hence all frequencies above the fundamental component of screech, 6.3kHz ($St = 0.49$), have wavelengths smaller than 5.8cm and thus are subject to shear refraction outside the cone of silence (Lilley, 1974).

7 CONCLUSIONS & FUTURE WORK

7.1 Conclusions

An investigation of the reduction in noise emitted from an unheated, circular Mach 1.3 jet with the introduction of a tangential component to the flow has been presented. Three distinctly different techniques of tangential air injection were considered and the results were compared to the undisturbed primary jet.

The primary jet was found to be slightly under-expanded with the peak and cross-sectionally weighted jet exit velocities of 388m/s and 380m/s measured from PIV, agreeing to within 1% of the 384m/s derived theoretically from isentropic flow relations. The under-expanded nature of the jet, due to the formation of a boundary layer within the diverging section of the nozzle (~1mm), resulted in a shock cell structure of mean cell spacing of 0.85 nozzle diameters. This resulted in a sharp SPL peak of 118dB at a $St=0.74$ (9.6kHz) in the sideline (90°) acoustic spectra of the jet, and was identified as being the harmonic component of screech noise. An isolated spectral peak at the downstream angle of 15° was most likely a reflection of the upstream propagating fundamental component of screech noise, off the jet nozzle. Broadband shock noise was also evident at the sideline observer angles, peaking at $St=1$ (13kHz). A study of the jet's directivity highlighted its peak radiation angle in the downstream direction (30°-25°) at an OASPL of 121dB. The preferred modes of the jet radiated at $St=0.17$ (2kHz), signified by a spectral peak of 132dB. All acoustic measurements were scaled to a distance of 40 nozzle diameters from the jet exit.

Validation through Tam's (1996) similarity spectra supports the view that fine-scale turbulent structures radiate low-amplitude, high frequency, noise in the sideline direction with the large-scale turbulent structures propagating low-frequency major noise events towards the downstream angles. The normalised autocorrelation results quantified the sizes of these fine and large-scale turbulent noise structures to be of the order of the boundary layer thickness (~0.1 D_j) and the nozzle diameter (~3 D_j) respectively. Normalised cross-correlation between adjacent microphone pairs was used to derive the time lag for maximum correlation and was subsequently used to approximate the origins of the noise sources based on their radiating frequencies. Low frequency noise coinciding with the preferred modes of the jet ($St=0.17$, $f=2$ kHz) were found to originate beyond the potential core ($x/D=6$), close to the end of the supersonic core ($x/D>11$). High-frequency screech ($St=0.74$, $f=9.6$ kHz) and broadband shock noise ($St=1$, $f=13$ kHz) were found to originate closer to the nozzle at streamwise locations of $3<x/D<6$. The noise source locations based on contours of near-field OASPL showed a surprisingly close match to those derived from far-field cross-correlation data.

Internal Tangential Injection (ITI) at an injection mass flow ratio of 40% was found to induce a swirl number of the order of 0.086 in the jet, which corresponded to a swirl Mach number of 0.27. However, the confined swirl induced adverse pressure gradients within the nozzle resulting in a deceleration of the axial velocity and reduction in the jet's potential core from 6 to 4 nozzle diameters. This subsequently resulted in a thrust penalty of 5%. A pressure transducer and gate valve were used in conjunction to maintain plenum pressure, such that an increase in mass flow from the tangential injectors would be compensated by an instantaneous decrease of mass flow into the plenum via the main reservoir. Acoustically, ITI was found to be most successful at the extreme downstream angle of 15°, yielding an OASPL benefit of 6.3dB at an optimal IMFR of 40%. At 30° an OASPL noise reduction of 1.3dB was recorded. ITI was also successful in reducing spectral SPL levels of screech (6.4dB) and broadband shock noise (4.9dB). A high-frequency noise cross-over observed at most angles was attributed to the promotion of rapid mixing with the surrounding flow, and hence a faster decomposition of the shear layer, shifting sound pressure levels to higher frequency bands. The internal swirl was found to have a destabilising fluid dynamic effect on the main jet, with a 25% increase in turbulence intensity levels in the initial shear layer, immediately downstream of the nozzle exit. There was also a 25% increase in Reynolds stress at a streamwise location of $x/D=6$.

External Tangential Injection (ETI) immediately downstream of the nozzle exit was found to induce a swirl number of the order of 0.013 in the main jet ($M_S \sim 0.07$). An increase in centerline velocity was recorded at the expense of a slight deceleration towards the jet edges. Both the potential and supersonic cores were lengthened to $6.5D_J$ and $12.3D_J$ respectively with the slight increase in thrust levels, 0.8%, being of the order of the accuracy of the PIV measurements (1%). For ETI the greatest OASPL noise benefit of 4.7dB was recorded at 15° at an optimal IMFR of 1% to that of the primary jet. At 30° an OASPL reduction of 1dB was recorded. Shock associated broadband and harmonic screech peaks were also significantly reduced by 3.7dB and 7.5dB respectively. Both turbulence intensity and Reynolds stress, in contrast to ITI, were found to be reduced by up to 25% at all streamwise locations from $1 < x/D < 13$, which is evidence for a stabilizing effect on the jet. The increase in the high frequency noise cross-over was credited to the parasitic self-noise from the eight, 1.5mm, diameter air injectors themselves. Swirl introduced into the shear layer outside of the nozzle has shown to be more effective than that initiated upstream, within the nozzle.

The 2kHz pulsating tangential air injection technique (PTI), was specifically targeted at perturbing the dominating preferred modes of the jet. It proved to be the most successful amongst the three for the mid-range observer angles of 70°-40° with an

OASPL benefit of 1dB at the optimal IMFR of 0.7%. However, it was not as successful as ITI and ETI at the downstream angles, returning an OAPSL reduction of only 0.7dB at 15°. Due to time constraints, it was not possible to conduct PIV measurements for PTI flow-field data; hence this result could not be fully explored. Another unusual finding was the absence of the high frequency noise cross-over at any of the microphone locations. An improved siren design that reduces the pressure and frictional losses at the aluminum to PTFE-Teflon slip surfaces, may make PTI a more efficient control method. Recommendations of future work in regards to this technique have been proposed in the following section, in the light of the shortcomings of this study.

The additional flow injected by ETI around the axial jet, at only a fraction of that of ITI, proved to be very successful in promoting rapid and possibly premature roll-up (early transition to '*decay phase*') of vortices associated with the shear layer, hence limiting the spatial extent of their growth. This proposition supports the acoustic trends of low-frequency noise benefits at the expense of increased high-frequency noise. Unlike radially impinging microjets that have been of major interest to previous researchers, the tangential injectors present an overall net swirling effect to the shear layer. The non-impinging nature of this type of injection results in counter-rotating vortical structures that exist near the low-speed outer-side of the shear layer, unlike microjets, chevrons and ITI. Several design parameters, such as the number, axial and circumferential location of the external jets, as well as the physical properties of the injected gas have yet to be optimised. Only the injection mass flow ratio was varied in this study.

To conclude, stereoscopic PIV measurements of the axial and tangential flow components have confirmed that small changes to the jet flow structure have a significant effect on its noise levels.

7.2 Future Work

The following are recommendations for future work.

- It would be interesting to investigate the acoustic and flow-field effects of the tangential air injection techniques on a transonic, Mach 0.9, and higher supersonic Mach 2 regime where the noise contribution from Mach wave radiation is more significant.
- Simulating co-axial flow regimes with the use of helium gas or a fan heated core flow will raise the commercial perspective of future investigations.
- The external tangential air injection technique has not been optimised in this study. Hence, it would be interesting to investigate the following parameters; the number of injectors, out-of-phase injection, axial location of injectors, physical properties of the injected gas and injector diameter with the purpose of reducing exhaust injector velocity and hence its associated high-frequency parasitic self-noise.
- The effectiveness of the external tangential injection technique in reducing the jet's near and far-field sound pressure levels whilst having minimal undesired effect on thrust levels has inspired the idea of a mass-less injection system. The existing 8 tangential injectors spaced circumferentially around the nozzle could be sourced by an oscillating medium, resulting in synthetic jets. This concept would eliminate the need for a secondary flow input. A speaker connected to an air-tight 8-way manifold was initially considered in this study, but the danger of rupturing the speaker diaphragm was highlighted due to adverse pressure gradients through the injectors.
- Due to the time constraints, it was not possible to acquire flow field PIV data for the 2kHz pulsating tangential injection. This additional information may help in better understanding the absence of the high frequency cross-over effect in the acoustic results. Investigating 2.5kHz or 3kHz pulsating tangential injection will help to conclude whether or not 2kHz is the optimal pulsating frequency.
- Synchronised acoustic and flow measurements have in the past been used to locate the source mechanisms responsible for jet noise. Major noise events in the signal

time history can be used to identify the contribution of certain flow structures towards jet noise.

- Near-field SPL data for both internal and pulsating tangential injection configurations will give information on how they affect the noise source locations with respect to frequency and will make an interesting comparison with the far-field cross-correlation data.
- The aerodynamic interaction between the tangential injectors and primary jet should be validated or perhaps further explained through computational studies. This may also aid in identifying the optimum conditions for the effectiveness of the injectors. DNS (Kollmann et al., 2001), RANS and LES studies (Tucker et al., 2003; Puneekar et al., 2010) have been shown to be capable of predicting the radiated noise levels from high subsonic and supersonic jets. It would therefore be of interest to see if such computations demonstrate significant noise benefits from the novel air injection techniques presented in this study.

REFERENCES

Ahmad, A., Cater, J., Avital, E., and Lawn, C., “Experimental Aeroacoustics Study on Jet noise Reduction Using Tangential Air Injection”, *Proc. of 3rd European Postgraduate Fluid Dynamics Conference*, University of Nottingham, 13-16 July 2009, pp.3.

Ahmad, A., Cater, J., Avital, E., and Lawn, C., “Aeroacoustics Study on Jet noise Reduction Using Tangential Air Injection”, *Proc. of 4rd European Postgraduate Fluid Dynamics Conference*, ESPCI Paris Tech, 3-7 July 2010.

Ahmad, A., Avital, E., Lawn, C., and Cater, J., “Tangential Air Injection for Jet Noise Reduction”, *Submitted to the AIAA Journal*, 2011.

Ahmad, A., Avital, E., Lawn, C. and Cater, J., “Low Supersonic Jet Noise Reduction using Tangential Air Injection Techniques”, *Proc. of 18th International Congress on sound & Vibration*, ICSV18, Rio De Janeiro, Brazil, 10-14 July 2011.

Ahuja, K. K., “An experimental study of subsonic jet noise with particular reference to effects of upstream disturbances”, *MPhil Thesis*, University of London, June 1972.

Alkislar, M.B., Krothapalli, A., and Lourenco. L. M., “Structure of a screeching rectangular jet: a stereoscopic particle image velocimetry study”, *Journal of Fluid Mechanics*, Vol. 489, 2003 pp. 121–154. DOI: 10.1017/S0022112003005032

Alkislar, M. B., Krothapalli, A., Butler, G. W., “The effect of streamwise vortices on the aeroacoustics of a Mach 0.9 Jet”, *Journal of Fluid Mechanics*, Vol. 578, 2007, pp. 139-169.

Alkislar, M. B., “Aeroacoustics of a Mach 0.9 Jet with Chevron-Microjet Combination”, *AIAA 2008-3041*, 14th AIAA/CEAS Aeroacoustics Conference (29th AIAA Aeroacoustics Conference) 5 - 7 May 2008, Vancouver, British Columbia Canada

Alonso, M., and Avital, E. J., “Study of sound generated by large-scale structures in low speed coaxial jets”, *International Journal of aeroacoustics*, Vol. 8, No.3, 2009, pp. 261-282.

Arakeri, A., Krothapalli, A., Siddavaram, V., Alkislar, M., and Lourenco L., "On the use of microjets to suppress turbulence in a Mach 0.9 axisymmetric jet," *Journal of Fluid Mechanics*, Vol. 490, 2003, pp. 75-98.

Atvars, J., Schubert, L.K., and Ribner, H.S., "Refraction of sound from a point source placed in an air jet", *Journal of Acoustic Society*, Am 37, 1965, pp168–170.

Avital, E. J., Alonso, M., and Supontisky, V., "Computational aeroacoustics: The low speed jet", *The Aeronautical Journal*, Vol. 112, No.1133, July 2008, pp.405-414.

Bell, J.H. and Mehta, R.D., "Contraction design for small wind tunnels", NASA Contractor report No. 177488, NASA, Washington DC, 1988.

Beer, J. M. and Chigier, N.A. "Combustion Aerodynamics", 1972 Applied Science Publishers LTD.

Bishop, K. A., Fowcs-Williams, J. E. and Smith, W., "On the noise sources of the unsuppressed high-speed jet", *Journal of Fluid Mechanics*, Vol. 50, No. 1, 1971, pp. 21-31.

Callender, B., Gutmark, E., and Martens, S., "A comprehensive study of fluidic injection technology for jet noise reduction", AIAA 2007-3608, 13th AIAA/CEAS Aeroacoustics conference (28th AIAA Aeroacoustics conference).

Carpenter, P. W. and Johannesen, N. H., "An extension of one-dimensional theory to inviscid swirling flow through choked nozzles," *Aeronautics Quarterly*, Vol. 26, 1975, pp. 71-87.

Castelain, T., Béra, J-C., and Sunyach, M., "Noise reduction of a Mach 0.7–0.9 jet by impinging microjets", Elsevier, C. R. Mecanique 334, 2006, pp.98–104.

Cooley, J. W., and Tukey, J. W., "An algorithm for the machine calculation of complex Fourier series", *Math. Comput.*19, 1965, pp.297–301.

Charron, S., and Botte, M. C., "Frequency-selectivity in loudness adaptation and auditory fatigue", *Journal of the Acoustical Society of America*, 83(1), 1988, pp.178-187.

Crighton, D. G., “Basic principles of aerodynamic noise generation”, *Prog. Aerosp. Sci.*, Vol. 16, No. 1, 1975, pp. 31-96.

Crighton, D. G., “Orderly structure as a source of jet exhaust noise”, *Proceedings of the Symposium on Turbulence*, Lecture Notes in Physics, Vol. 76, 1977, pp. 154-170.

Crow, S.C., and Champagne, F.H. “Orderly Structure in Jet Turbulence”, *Journal of Fluid Mechanics*, 48, 1971, pp.547–591.

Cutnell, J. D. and Johnson, K. W., “Physics”, 4th edition, Wiley, New York, 1998.

European Commission for Research: European Aeronautics “A Vision for 2020”, Meeting Society’s needs and winning global leadership”, Luxemburg, January 2001.

Farokhi, S., Taghavi, R., and Rice, E., “Effect of Initial Swirl Distribution on the Evolution of a Turbulent Jet”, *AIAA Journal*, Vol. 27, No. 6, 1989, pp. 700–706.

Fincham, A. and Delerce, G., “Advanced optimisation of correlation imaging velocity algorithms”, *Experiments in Fluids*, 29, 2000, pp. S13-S22.

Ffowcs-Williams J. E., “The noise from turbulence convected at high speed”, *Phil Trans R Soc*, A 255, 1963.

Frank, J. E. and Taghavi, R. “Supersonic rectangular jets with swirling shear layers”, In ASME FED, high speed jet flows (Eds S. Kaji, G. Raman, and C. J. Freitas), Vol. 214, pp. 77–82, Hilton Head, SC, USA, 13–18 August 1995.

Gilchrist, R., and Naughton, J., “Experimental Study of Incompressible Jets with Different Initial Swirl Distributions: Mean Results”, *AIAA Journal*, Vol. 43, No. 4, 2005, pp. 741–751.

Goldstein, M.E., “Aeroacoustics”, *Mc Graw-Hill*, New York, 1976.

G.R.A.S Sound and Vibration, “1/4-inch Free-Field Microphone Type 40BF”, Product and Data specifications, version 10-12-2003.

Greska, B. J., "Supersonic jet noise and its reduction using microjet injection", *PhD Thesis*, The Florida State University, 2005.

Gupta, A.K., Lilley, D.G and Syred, N., "Swirl Flows", Energy and Engineering Science Series, Abacus Press Cambridge, 1984.

Harper-Bourne, M. and Fisher, M., "The noise from shockwaves in supersonic jets", Proceedings of AGARD conference on Noise Mechanisms, AGARD, 1973.

Henderson, B. S. and Norum, T. D., "Impact of azimuthally controlled fluidic chevrons on jet noise" AIAA 2008-3062, 14th AIAA/CEAS Aeroacoustics Conference (29th AIAA Aeroacoustics Conference), 5 - 7 May 2008, Vancouver, British Columbia Canada,

Hileman, J. I. and Samimy, M., "Turbulence structures and the acoustic far field of a Mach 1.3 Jet", *AIAA Journal*, Vol. 39, No. 9, 2001, pp. 1716-1727.

Hileman, J. I., Thurow, B. and Samimy, M., "Exploring noise sources using simultaneous acoustic measurements and real-time flow visualization in jets", *AIAA Journal*, Vol. 40, No. 12, 2002, pp.2382-2392.

Hileman, J. I., Thurow, B. and Samimy, M., "Development and evaluation of a 3-D microphone array to locate individual acoustic sources in a high-speed jet", *Journal of Sound and Vibration*, Vol. 276, 2004, pp.649–669.

Høst-Madsen, A. and Nielsen, A.H., "Accuracy of PIV measurements in turbulent flows", Proceedings of the ASME/JSME Fluids Engineering Conference, Hilton Head, ASME, Vol. 229, 1995, pp. 481-488.

InSight 3G, "Data Acquisition, Analysis and Display Software Platform", User's Guide, P/N 1980511, Revision G, TSI, January 2008

Jenkinson, L. R., Simpkin, P., and Rhodes, D. "Civil jet aircraft design", Butterworth-Heinemann, 1999.

Jordan, P., and Gervais, Y., "Subsonic jet aeroacoustics: associating experiment, modelling and simulation", *Experimental Fluids* 44, 2008, pp.1-21.

Kaji, S., and Nishijima, N., “Pressure Field around a Rectangular Supersonic Jet in Screech”, *AIAA Journal*, Vol. 34, No. 10, 1996, pp. 1990–1996.

Keane, R.D. and Adrian, R.J., “Optimisation of particle image velocimeters: PartII Multiple pulsed systems”, *Measurement Science and Technology*, Vol. 2, 1991, pp. 963-974.

Kinsler, L. E., Frey, A. R., Coppens, A. B., and Sanders, J. V. “Fundamentals of acoustics”, Fourth Edition. John Wiley & Sons, Inc. 2000.

Knowles, K. and Saddington, A. J., “A review of jet mixing enhancement for aircraft propulsion applications”, Proceedings of IMechE 220 Part G: *Journal of Aerospace Engineering*, 2005, pp. 103-127.

Kollmann, W., Ooi, A. S. H., Chong, M. S. and Soria, J., “Direct numerical simulations of vortex breakdown in swirling jets,” *Journal of Turbulence*, Vol. 2, 2001, pp. 1-17.

Krothapalli, A., Venkatakrishnan, L. and Lourenco, L., “Crackle: A dominant component of supersonic jet mixing noise”, *AIAA 2000-20024*, 6th AIAA/CEAS Aeroacoustics conference, 12-14 June 2000, Lahaina, Hawaii.

Krothapalli, A., Venkatakrishnan, L., Lourenco, L., Greska, B., and Elavarasan, R., “Turbulence and Noise Suppression of a High-Speed Jet by Water Injection”, *Journal of Fluid Mechanics*, Vol. 491, 2003, pp. 131–159.

Kumar, V., Alvi, F.S., “Use of high speed microjets for active separation control in diffusers”, *AIAA Journal*, Vol. 44, No. 2, 2006, pp.273–281

Liang, H. and Maxworthy, T., “An experimental investigation of swirling jets”, *Journal of Fluid Mechanics*, Vol. 525, 2005, pp. 115-159.

Lighthill, M.J., “On Sound Generated Aerodynamically: I. General Theory”, *Proc. Roy. Soc. London Ser. A* 211, 1952, pp.564–581.

Lighthill, M.J., “On Sound Generated Aerodynamically: II. Turbulence as a Source of Sound”, *Proc. Roy. Soc. London Ser. A*, 222, 1954, pp.1–32.

- Lilley, G. M. "On the noise from air jets", *A.R.C.* 20376, F.M. 2724, 1958.
- Lilley, G.M., "On the noise from jets", *AGARD*, Conference proceedings, No. 131, paper 13, 1974.
- Lilley, D. G., "Swirl flows in combustion: a review", *AIAA Journal*, Vol. 15, No. 8, 1977, pp.1063–1078.
- Lou, H., Alvi, F.S., and Shih, C. "Active and adaptive control of supersonic impinging jets", *AIAA Journal*, Vol.44, No.1, 2006, pp.58–66.
- Luff, D.S., Ahmad, A. and Cater, J. E., "An investigation of noise reduction in a Mach 1.3 round jet using tangential blowing", *AIAA 2008-2837*, 14th AIAA/CEAS Aeroacoustics Conference (29th AIAA Aeroacoustics Conference), 5 - 7 May 2008, Vancouver, British Columbia Canada.
- Lush, P. A., "Measurements of subsonic jet noise and comparison with theory", *Journal of Fluid Mechanics*, Vol. 46, 1971, pp. 477-500.
- Mehta, R. D. and Bradshaw, P., "Design rules for small low speed wind tunnels", *Aeronautical Journal*, Vol. 73, 1979, pp. 443-449.
- Melling. A., "Tracer particles and seeding for particle image Velocimetry", *Measurement Science Technology*, 8, 1997, pp.1406–1416.
- Morfey, C. L., "Sound radiation due to unsteady dissipation in turbulent flows", *Journal of Sound and Vibration*, Vol. 48, No.1, 1976, pp. 95-111.
- NASA, "Proceedings of the Jet Noise Workshop", *NASA/CP-2001-211152*, 2001.
- Neemah, R., AlGattus, S., and Neemah, L., "Experimental investigation of noise reduction in supersonic jets due to jet rotation", *Journal of Sound and Vibration*, Vol. 221, No. 3, 1999, pp 505-524.
- New, T.H. and Tray, W.L., "Effects of circumferential microjets on the near field behaviour of a round jet", *AIAA Paper 2004-0923*.

New, T.H. and Tray, W.L., “Cross stream radial fluid injection into a round jet”, *AIAA Paper* 2004-2403.

Norum, T.D and Seiner J.M., “Measurements of static pressure and far field acoustics of shock-containing supersonic jets”, *NASA TM* 84521,1982a.

Norum, T.D., “Screech suppression in supersonic jets”, *AIAA Journal*. 21:235-40, 1983.

Panda, J., “An experimental investigation of screech noise generation”, *Journal of Fluid Mechanics*, 378, 1999, pp.71-96.

Panda, J. and Seasholtz, R.G., “Experimental investigation of density fluctuations in high-speed jets and correlation with generated noise”, *Journal of Fluid Mechanics*, Vol. 450, 2002, pp. 97-130.

Panda, J. Seasholtz, R. G. and Elam, K. A., “Investigation of noise sources in high-speed jets via correlation measurements”, *Journal of Fluid Mechanics*, Vol. 537, 2005, pp. 349-385.

Petitjean, B. P. and McLaughlin, D. K., “Experiments on the nonlinear propagation of noise from supersonic jets”, *AIAA Journal* 2003-3127, 9th AIAA/CEAS Aeroacoustics Conference and Exhibit, 12-14 May 2003, Hilton Head, South Carolina.

Petitjean, B. P. and Viswanathan, K., and McLaughlin, D. K., “Acoustic pressure waves measured in high speed jets experiencing nonlinear propagation”, *International Journal of Aeroacoustics*, Vol. 5, No. 2, 2006, pp. 193-215.

Phalnikar, K.A., Kumar, R., and Alvi, F.S., “Experiments on free and impinging supersonic microjets”, *Experimental Fluids* 44, 2008, pp.819–830.

Powell, A., “On the noise emanating from a two-dimensional jet above the critical pressure”, *Aeronautical Quarterly* 4, 1953, pp.103-122.

PCB Piezotronics, “Microphone Handbook, Test and Measurement Microphones”, NY, USA, 2009.

Prasad, A.K., Adrian, R.J., Landreth, C.C. and Offutt P.W., “Effect of resolution on the speed and accuracy of particle image velocimetry interrogation”, *Experiments in Fluids*, 13, 1992, pp.105-116.

Press, W.H., Teukolsky, S.S., Vetterling, W.T. and Flannery B.P., “Numerical recipes in Fortran, the art of scientific computing”, 2nd Ed., Cambridge University Press, 1992.

Punekar, J., Avital, E. J. and Musafir, K.E., “Computations of Nonlinear Propagation of Sound Emitted from High Speed Mixing Layers”, *Open Acoustics* 3.3, 2010, pp11-20.

Raffel, M., Willert, C. E., Wereley, S.T., and Kompenhans, J., “Particle Image Velocimetry: A Practical Guide”, Second Edition, Springer, 1998.

Raman, G., “Supersonic jet screech: Half-century from Powell to the present”, *Journal of Sound and Vibration*, Vol. 225, No.3, 1999, pp.543-571.

Ribner, H. S., “Aerodynamic sound from fluid dilatations”, *UTIA*, report No. 86, AFOSR TN 3430, 1962.

Ribner, H. S., “Quadrupole correlations governing the pattern of jet noise”, *Journal of Fluid Mechanics*, Vol. 38, No. 1, 1969, pp.1-24.

Rolls-Royce, “The jet engine”, fifth edition, Rolls-Royce plc 1986.

Royal Aeronautical Society, “Aviation and the environment, Reference Sheets”, Greener by Design, January 2004.

Royal Aeronautical Society, “Air Travel-Greener by Design”, Annual Report 2004-2005, March 2005.

Samimy, M., Kim, J.H., Kearney-Fischer, M., and Sinha, A., “Acoustic and flow fields of an excited high Reynolds number axisymmetric supersonic jet”, *Journal of Fluid Mechanics*, Vol. 656, 2010, pp. 507-529.

Self, R.H., “Jet noise prediction using the Lighthill acoustic analogy”, *Journal of Sound and Vibration*, Vol.275, 2004, pp.757–768.

Schwartz, I. R., “Minimisation of jet and core noise of a turbojet engine by swirling the exhaust flow”, *AIAA 2nd Aero-Acoustics conference*, Hampton, VA., March 24-26, 1975, pp380-397.

SCITEK, “SCITEK LS-10 Remote Operation Liquid Droplet Seeder”, Scitek Consultants Ltd, Derby, 2006.

Seiner, J. M., and Reethof, G. “On the distribution of source coherency in subsonic jets”, *AIAA Paper*, Vol.74, No.4, 1974.

Shields, F. D., & Bass, H. E., “Atmospheric Absorption of High Frequency Noise and Application to Fractional-Octave Band”, *NASA CR 2760*, 1977.

Shiri, A., George, W. K., and Naughton, J. W., “Experimental Study of the Far Field of Incompressible Swirling Jets”, *AIAA Journal*, Vol. 46, No. 8, August 2008,

Singh, A. and Chatterjee, A., “Numerical Prediction of Supersonic Jet Screech Frequency”, *Shock Waves* 17(4), 2007, pp.263-272

Smith, M. J. T., “Aircraft Noise”, *Cambridge Aerospace Series*, Cambridge University Press, Paperback Edition, 2004.

Smits, A. J., “Flow Visualization : Techniques and Examples”, *Imperial College Press*, 2000.

Tam, C. K.W., and Chen, P., “Turbulent Mixing Noise from Supersonic Jets”, *AIAA Journal*, Vol. 32, No. 9, 1994, pp. 1774–1780.

Tam, C. K. W., “Supersonic Jet Noise”, *Annual Review in Fluid Mechanics*, Vol. 27, 1995, pp.17-43.

Tam, C. K. W., Golebiowski, M., and Seiner, J. M., “On the Two Components of Turbulent Mixing Noise from Supersonic Jets”, *AIAA Paper* 96-1716, May 1996.

Tam, C. K. W., “Jet noise since 1952”, *Theoretical and Computational Fluid Dynamics*, Vol. 10, 1998, pp. 393-405.

Tam, C. K. W., “Influence of Nozzle Geometry on the Noise of High-Speed Jets”, *AIAA Journal*, Vol. 36, No. 8, 1998, pp.1396–1400.

Tam, C. K. W., and Auriault, L., “Jet Mixing Noise from Fine-Scale Turbulence”, *AIAA Journal* Vol. 37, No. 2, February 1999.

Tam, C. K.W., Pastouchenko, N. N. and Viswanathan, K. “Broadband Shock-Cell Noise from Dual Stream Jets”, *AIAA 2008-2833*, 14th AIAA/CEAS Aeroacoustics Conference 5-7 May 2008, Vancouver, British Columbia Canada.

Tam, C.K.W., Viswanathan, K., Ahuja, K.K., and Panda, J., “The sources of jet noise: experimental evidence”, *Journal of Fluid Mechanics*, Vol. 615, 2008, pp. 253-292, Cambridge University Press, doi:10.1017/S0022112008003704

Tanna, H. K. and Dean, P. D., “An experimental study of shock-free supersonic jet noise”, *Progress in Astronautics and Aeronautics*, Vol. 43, 1975, pp. 203-236.

Tanna, H. K., “An experimental study of jet noise Part 1: Turbulent mixing noise”, *Journal of Sound and Vibration*, Vol. 46, No. 3, March 1977, pp 405-428.

Tinney, C.E., Hall, A., and Glauser, M. N., Lawrence, S. U., and Coughlin, T., “Designing an Anechoic Chamber for the Experimental Study of High Speed Heated Jets”, *AIAA 2004-10*, 42nd AIAA Aerospace Sciences Meeting and Exhibit, Nevada.

Tucker, P. G., “Novel MILES computations for jet flows and noise”, *International Journal of Heat and Fluid Flow*, Vol. 25, 2003, pp. 625-635.

Viswanathan, K., “Nozzle Shaping for Reduction of Jet Noise from Single Jets”, *AIAA Journal*, Vol. 43, No. 5, 2005, pp. 1008–1022.

Viswanathan, K., “Instrumentation considerations for accurate jet noise measurements”, *AIAA Journal*, Vol. 44, No. 6, 2006, pp. 1137-1149.

Viswanathan, K., “Investigation of Noise Source Mechanisms in Subsonic Jets”, *AIAA Journal* Vol. 46, No. 8, August 2008.

Viswanathan, K., “Does a Model Scale Nozzle Emit the Same Jet Noise as a Jet Engine”, *AIAA Journal*, Vol. 46, No. 2, 2008, pp. 336–355. doi:10.2514/1.18019

Westerweel, J., “Digital Particle Image Velocimetry, Theory and Application”, *Thesis*, Delft University Press, 1993.

Westerweel, J., “Efficient detection of spurious vectors in particle image velocimetry data”, *Experimental Fluids* 16:236–247, 1994.

Westerweel, J., Dabiri, D. and Gharib, M., “The effect of a discrete window offset on the accuracy of cross-correlation analysis of digital PIV recordings”, *Experiments in Fluids* 23, 1997, pp.20-28.

White, F. M., “Fluid Mechanics”, Fifth edition, McGraw-Hill International Edition, 2003.

Witze, P. O., “Centreline velocity decay of compressible free jets”, *AIAA Journal* Vol.12, No.4, April 1974, pp 417-418.

Yu, J. C., “Investigation of the noise fields of supersonic axisymmetric jet flows”, *PhD. Thesis* Syracuse Univ., Syracuse, NY, 1971.

Zaman, K. B. M. Q. and Hussain, A. K. M. F. “Turbulence suppression in free shear flows by controlled excitation”, *Journal of Fluid Mechanics* 103, 1981, pp.133–159.

Zaman, K. B. M. Q., Bridges, J. E., and Brown, C. A., “Excess Broadband Noise Observed with Over expanded Jets”, *AIAA Journal* Vol. 48, No. 1, 2010, pp.202-214.

Zucrow, M. J. and Hoffman, J. D., “Gas Dynamics”, John Wiley & Sons, 1976.

APPENDIX A

Schlieren Images

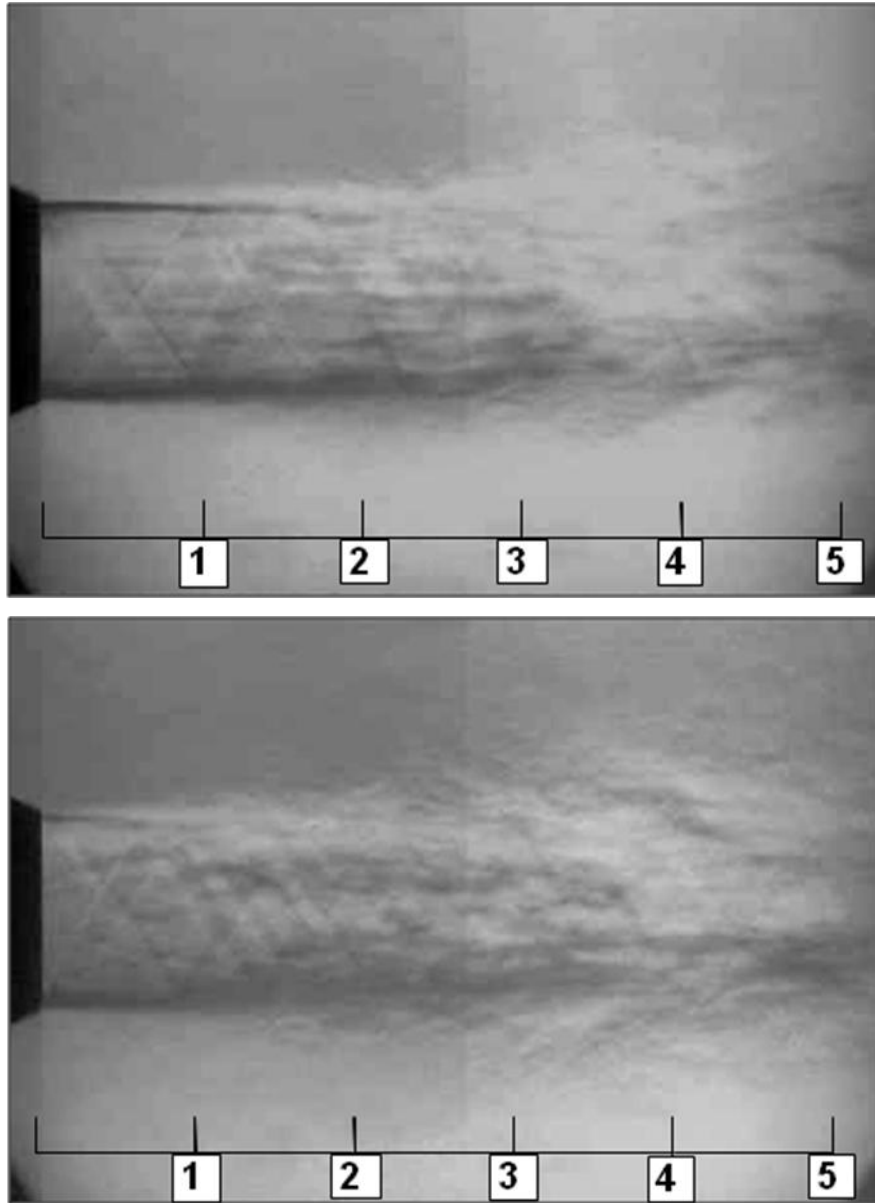


Figure A.1: Schlieren Images captured by Luff et al., (2008), showing vortex roll-up to occur at $x/D \sim 2$ for the primary jet (top), with ITI at 40% IMFR inducing premature roll-up of vortices at $x/D \sim 1$. Enhanced mixing is shown to break up the shear layer.

APPENDIX A

PTI Pulsating Injection Frequency Validation

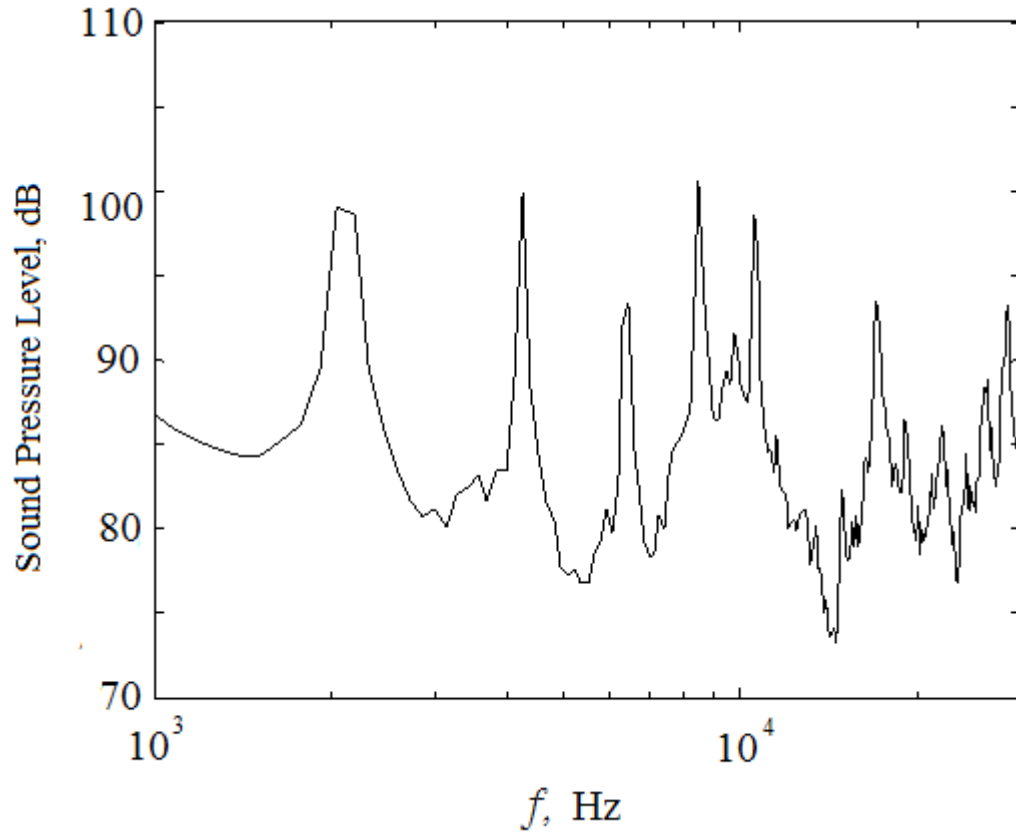


Figure A.2: Acoustic spectra, showing the background parasitic self-noise from an isolated pulsating tangential injector (PTI). The microphone was placed at an observer angle of 30° at a radial distance $r/D=100$ from the PTI injector of exit diameter 1.5mm. A relatively broad SPL peak is clearly visible at 2.2kHz with harmonics at 4.4kHz, 6.6 kHz, 8.8 kHz & 11kHz, giving evidence in support of PTI operating close to its design frequency of 2kHz.